THE VERY HIGH ENERGY GAMMA-RAY SPECTRA OF AGN

by

Martin Schroedter

A Dissertation Submitted to the Faculty of the

DEPARTMENT OF PHYSICS

In Partial Fulfillment of the Requirements
For the Degree of

DOCTOR OF PHILOSOPHY

In the Graduate College

THE UNIVERSITY OF ARIZONA

2 0 0 4

Get the official approval page
from the Graduate College
before your final defense.

STATEMENT BY AUTHOR

This dissertation has been submitted in partial fulfillment of requirements for an advanced degree at The University of Arizona and is deposited in the University Library to be made available to borrowers under rules of the Library.

Brief quotations from this dissertation are allowable without special permission, provided that accurate acknowledgment of source is made. Requests for permission for extended quotation from or reproduction of this manuscript in whole or in part may be granted by the head of the major department or the Dean of the Graduate College when in his or her judgment the proposed use of the material is in the interests of scholarship. In all other instances, however, permission must be obtained from the author.

SIGNED: _____

ACKNOWLEDGMENTS

This work would not have been possible without the encouragement and support of so many. This is my time to say thank you to you all.

Danke, Mutti und Papa für Euere treue Unterstützung.

Thank you, Trevor. You have made this, what I believe to be, the most pleasant way to earn a Ph. D. From the very quick turn-around in reading drafts of this thesis, to sending me all over the world, to always taking time to answer my most elementary questions patiently. Thank you.

My colleagues at Iowa State, especially Dave Carter-Lewis and Frank Krennrich with whom I had (and will again have!) the pleasure of working.

My friends here in Tucson, Lee, Shoshana, and Dree, who have made life so much more pleasant and interesting.

Steve, thanks for dropping everything the minute I step in your office (except on time when you had a final exam within 5 minutes :), for saving me years of frustrating time on the computer, for reading my thesis, etc. etc. etc.

All the people at base camp for always helping me or entertain me when I was bored: Ken, Steve, Gene, Ginnee, Cezar, Grace, Karen, and Danny.

Also, thank you Roger Haar, for being my friend and mentor; the long hours in advanced lab will not be forgotten.

Zuzu, what can I say. My best friend.

TABLE OF CONTENTS

TABLE OF CONTENTS—*Continued*

TABLE OF CONTENTS—*Continued*

TABLE OF CONTENTS—*Continued*

LIST OF TABLES

LIST OF TABLES—*Continued*

LIST OF FIGURES

LIST OF FIGURES—*Continued*

LIST OF FIGURES—*Continued*

LIST OF FIGURES—*Continued*

LIST OF FIGURES—*Continued*

LIST OF FIGURES—*Continued*

LIST OF FIGURES—*Continued*

LIST OF FIGURES—*Continued*

LIST OF FIGURES—*Continued*

LIST OF FIGURES—*Continued*

ABSTRACT

A total of six extragalactic objects have been detected so far at very high energies (VHE). They are BL Lac objects, a sub-group of active galactic nuclei characterized by intense non-thermal radiation. The VHE spectra of two of these, 1ES 1959+650 and 1ES 2344+514, were measured in this work. Similar to the other four BL Lacs detected, their VHE spectrum and flux level is highly variable and shows a broadband spectrum characterized by two emission peaks: one in X-ray, the other at GeV to TeV energies. For one of these, 1ES 1959+650, simultaneous observations were carried out at other wavelengths and for the first time, a VHE flare without increased X-ray flux level was recorded. For the other object, 1ES 2344+514, no simultaneous X-ray observations were taken, making further modeling impossible.

VHE gamma-ray astronomy can establish important upper limits on the density of the extragalactic background light (EBL). If one can somehow guess what the source spectrum is, then one can infer the EBL density from the measured attenuation in the spectra. As the VHE spectra of BL Lac object are very similar, the zeroth order assumption was made (and justified) in this work that they are actually the same; differences in attenuation arising solely due to the different distances to the objects. The upper limits derived here are not very constraining, but they do question one particular set of EBL measurements that are very high in the near infrared waveband. Galaxy formation models are typically not able to reproduce this high density.

The analysis of VHE spectra is still being developed; in part because of the new array of four telescopes, VERITAS, being built at the moment. Monte-Carlo simulations are used in this work and changes in the simulation software had not seen a comparison to the previous version until this work. Differences were identified that impact the energy reconstruction. A method was developed to calibrate the absolute energy scale by automatically identifying cosmic-ray muons recorded by the telescope.

THE VERY HIGH ENERGY GAMMA-RAY SPECTRA OF AGN

Martin Schroedter, Ph.D.
The University of Arizona, 2004

Director: Trevor Weekes

A total of six extragalactic objects have been detected so far at very high energies (VHE). They are BL Lac objects, a sub-group of active galactic nuclei characterized by intense nonthermal radiation. The VHE spectra of two of these, 1ES 1959+650 and 1ES 2344+514, were measured in this work. Similar to the other four BL Lacs detected, their VHE spectrum and flux level is highly variable and shows a broadband spectrum characterized by two emission peaks: one in X-ray, the other at GeV to TeV energies. For one of these, 1ES 1959+650, simultaneous observations were carried out at other wavelengths and for the first time, a VHE flare without increased X-ray flux level was recorded. For the other object, 1ES 2344+514, no simultaneous X-ray observations were taken, making further modeling impossible.

VHE gamma-ray astronomy can establish important upper limits on the density of the extragalactic background light (EBL). If one can somehow guess what the source spectrum is, then one can infer the EBL density from the measured attenuation in the spectra. As the VHE spectra of BL Lac object are very similar, the zeroth order assumption was made (and justified) in this work that they are actually the same; differences in attenuation arising solely due to the different distances to the objects. The upper limits derived here are not very constraining, but they do question one particular set of EBL measurements that are very high in the near infrared waveband. Galaxy formation models are typically not able to reproduce this high density.

The analysis of VHE spectra is still being developed; in part because of the new array of four telescopes, VERITAS, being built at the moment. Monte-Carlo simulations are used in this work and changes in the simulation software had not seen a comparison to the previous version until this work. Differences were identified that impact the energy reconstruction.

A method was developed to calibrate the absolute energy scale by automatically identifying cosmic-ray muons recorded by the telescope.

CHAPTER 1

INTRODUCTION

Astrophysical observations of the electromagnetic spectrum beyond the visible range began with the discovery of the universal radio and microwave backgrounds. Since then, many techniques have been used to uncover the photon spectrum with energies from radio to PeV; they depend on frequency and flux level. At photon energies higher than a few eV, corresponding to visible light, the Earth's atmosphere is opaque and observations must be carried out either from satellites or indirectly with optical telescopes or particle detectors on the ground. The ground-based detectors measure secondary radiation produced as the primary gamma rays are absorbed in the atmosphere. From the infrared to radio frequencies above 30 GHz, the atmosphere emits and absorbs radiation strongly. Thus, the atmosphere presents both an obstacle and an opportunity for observational astrophysics.

1.0.1 Imaging Atmospheric Cherenkov Technique

Gamma rays with energies up to 40 GeV have been observed by the EGRET satellite, but at higher energies the flux is so low that the small detector area does not collect enough photons for a meaningful measurement. In addition, at these higher energies, the secondary cascade caused by gamma rays in the detector on the satellite are not contained fully, so that the gamma-ray energy cannot be determined accurately. Fortunately, at these very high energies (VHE), gamma rays produce particle showers in the atmosphere that can be detected from the ground by their emitted Cherenkov radiation, see App. B. These detectors are called atmospheric Cherenkov telescopes and have large collection areas on the order of 100,000 m^2, much larger than the 0.1 m^2 of the largest high-energy satellite, EGRET, flown to date.

By directly imaging the Cherenkov light produced in particle air showers, imaging

atmospheric Cherenkov telescopes (IACT) have the capability to distinguish between the compact images produced by primary gamma rays and the fragmented images produced by the much more numerous cosmic rays[1]. This is illustrated in Fig. 1.1 where the particle air shower development for an initial gamma ray and an initial proton are shown. Charged particles moving through the atmosphere with a speed greater than the local speed of light[2] produce Cherenkov light. The Cherenkov light is emitted in a narrow cone pointing along the direction of the charged particle. The opening angle increases with the density of air and reaches $1.4°$ at sea level. The Cherenkov light from all particles in the shower is imaged by a telescope on the ground. The image in the white circle (Fig. 1.1) represents the picture produced on the focal plane of the telescope, where the Cherenkov light is color coded according to particle species that produced it. The images were produced by a Monte-Carlo computer simulation of the air shower development, Cherenkov light emission, and imaging by the telescope. As there is no man-made particle accelerator in space that can produce gamma rays with those energies, simulations are an essential tool in relating what is measured on the ground with the initial particle type, direction, and energy.

The imaging of Cherenkov light from air showers makes it possible to discriminate gamma rays from cosmic rays based on the shape and other information such as timing of the shower front. Cosmic rays are much more numerous than gamma rays; they represent a background about 500 times as large as the rate of gamma rays detected from a strong source such as the Crab Nebula. This source is so well studied that is has become regarded as the "standard candle" in VHE gamma-ray astronomy. Imaging also makes it possible to produce a map of the arrival direction of gamma rays. Each photon can be reconstructed with about $0.1°$ directional accuracy and with sufficient statistics, the source location and size can be measured with an accuracy surpassing that of any other high energy detector, such as those on satellites or ground-based air shower arrays.

Another key feature of IACTs is their capability to reconstruct the energy of the pri-

---

[1] In this work, cosmic rays include protons, atomic nuclei, and electrons, but not gamma rays.

[2] The local speed of light is the speed of light in vacuum divided by the index of refraction.
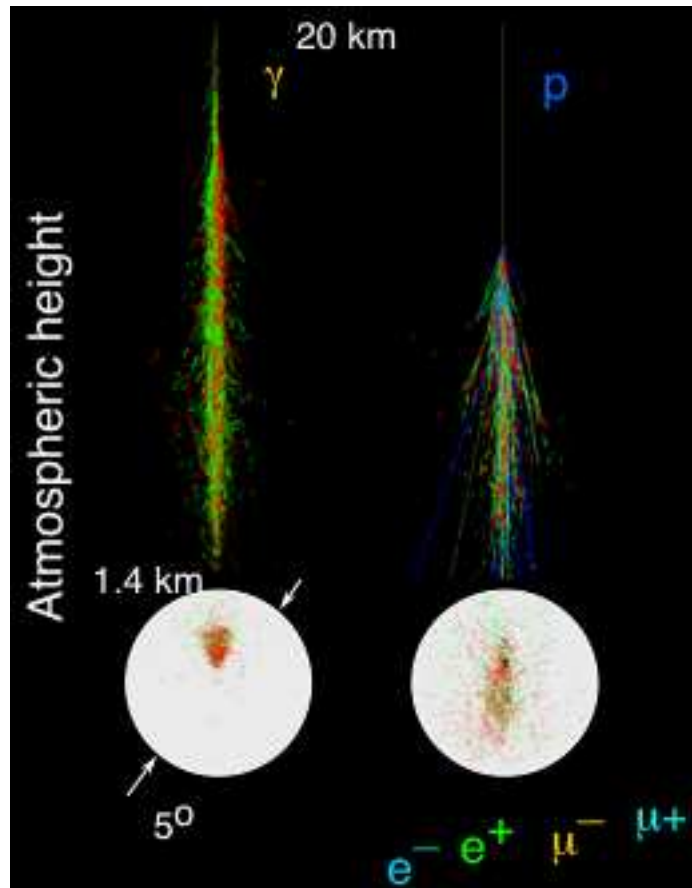
FIGURE 1.1. Particle air shower produced by a gamma ray (*left*) and by a proton (*right*). The angular distribution of Cherenkov light on the ground is shown in the white circle. The Cherenkov light is color coded according to which particle species produced it. The energy of the gamma-ray is roughly 1 TeV, that of the proton about 0.5 TeV.

mary particle with the help of Monte Carlo simulations. This makes it possible to measure the gamma-ray spectrum and is of great importance in understanding the mechanism that produces VHE gamma rays. Spectral variability has been measured on time scales as short as 30 minutes.

Easier than measurements of spectral variability, however, are measurements of the absolute gamma-ray brightness of a source, which, when made over a prolonged period of time, produce a light curve of the object. The rapid variability seen from some types of

active galactic nuclei, called blazars, still awaits a full explanation.

1.0.2 History of VHE Astronomy at Whipple

The method of detecting VHE gamma rays with an IACT was established with the detection of the Crab Nebula (Weekes et al., 1989). Measurements of the VHE emission from the Crab Nebula by many experiments are consistent with each other and no time variability has been found. It is lucky that the first VHE gamma-ray source to be detected with this new method was the Crab Nebula; what would the reaction from the astronomical community have been if a blazar had been claimed as the first detection with its rapid on/off flaring activity?

Blazars are extragalactic super-massive black holes with two opposing jets of high energy particles. One of these jets is directed at us and produces the VHE gamma rays through an unknown mechanism. One example is Mrk 421; it had been detected by the high-energy satellite experiment EGRET and was considered a good candidate for detection in VHE gamma rays. It was discovered at these energies with the 10 m telescope at the Fred Lawrence Whipple observatory (Punch et al., 1992), and significant variability of the lightcurve has been found on time scales as short as 15 minutes. A second blazar, Mrk 501, from which VHE gamma rays were discovered, (Quinn et al., 1996), was not seen initially by EGRET. This established VHE gamma-ray astronomy as an independent field.

VHE gamma-ray spectral analysis began with the measurement of the Crab Nebula (Vacanti et al., 1991). This established the production mechanism of VHE gamma-rays as a combination of acceleration of electrons to energies up to 10^{15} eV followed by Compton up-scattering of infrared/optical seed photons to the VHE regime of 10^{12} eV and above. This general mechanism is the most widely used explanation for the VHE gamma-ray production.

1.0.3   Present Status and Outlook

Presently, only four major IACTs are in operation worldwide: the Whipple 10 m telescope, HESS, CANGAROO III, and MAGIC. The capabilities, as well as the scientific goals, of these instruments overlap; however they are physically located in different parts of the world and not in direct competition with each other. HESS and CANGAROO cover the southern hemisphere, while MAGIC and Whipple observe the northern hemisphere. The sensitivity of some of these instruments is shown in Fig. 1.2.

Observations are being carried out on galactic and extragalactic sources. Known VHE sources include active galactic nuclei, supernova remnants, and an X-ray binary system. Simultaneous observations at other wavelengths are regularly scheduled to provide a more detailed look at the broad energy spectra of these sources. The search for new sources is a slow process because of the small field of view (FOV) that these instruments have. Nevertheless, two objects have been discovered by IACTs that are not seen at lower energies.

The next (third[3]) generation of IACTs is now coming online. These consist of a few IACTs operating together in an array and combine the proven concepts of large optical telescope, imaging camera, and stereoscopic observations. Improvements have been made in the optics (larger field of view, improved angular resolution) and in the electronics (FADC, 10-50 times higher data rates). The additional information gained by stereoscopic observations of air showers improves the energy reconstruction of gamma-ray showers and provides enhanced differentiation between gamma-ray and cosmic-ray primaries. The increased background rejection, especially of the cosmic-ray muon component, improves the low energy sensitivity of these instruments; a 50 GeV threshold might be possible. The GLAST satellite, to be launched in 2006, will cover the energy from 0.1-100 GeV. This will allow simultaneous measurements of energy spectra over 6 complete decades.

HESS and CANGAROO are the first operational examples, each with an array of four - 12 m telescopes. VERITAS, currently being built, will be essentially of the same design.

---

[3]The first generation were non-imaging Cherenkov telescopes, while the current Whipple 10 m telescope is a second generation system that uses a high resolution camera.

HESS is already showing that more exciting new discoveries will be made in this field. Upgrade plans for these third generation instruments are already considered to decrease the energy threshold and flux sensitivity even further.
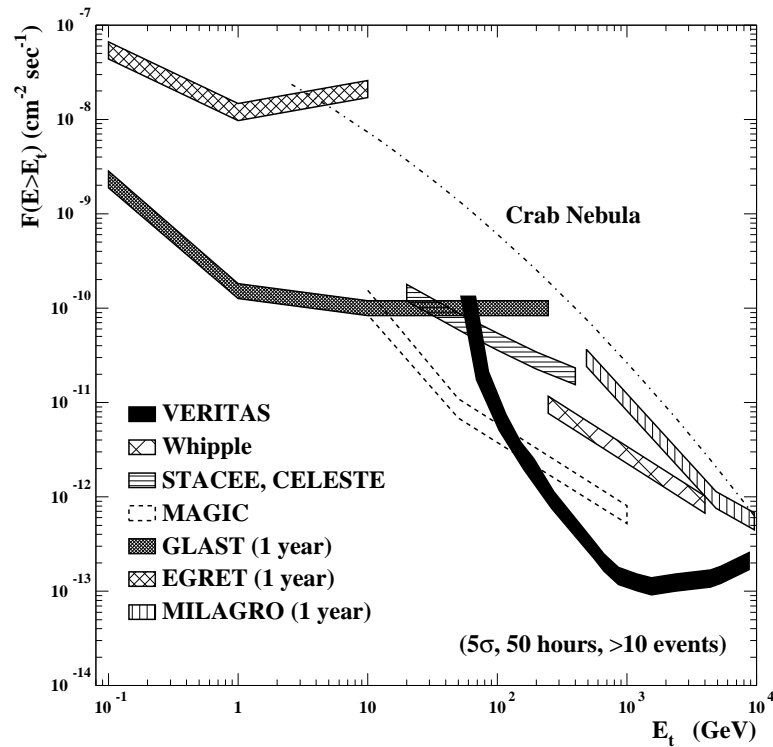
FIGURE 1.2. Sensitivity of some past, current, and future VHE gamma-ray observatories. Figure from Weekes (2003a).

1.0.4 Organization of the Thesis

The rest of the Introduction gives a short outline of major high-energy astronomy experiments, results, and challenges. The Whipple 10m telescope is described in chapter 2. This is followed by a discussion of the spectral analysis method in chapter 3 together with a comparison of the Crab Nebula spectrum during different observing seasons. The VHE gamma-ray spectra for two blazars, 1ES 1959+650 and 1ES 2344+514, are derived in chapters 4 and 5, respectively. A discussion of the extragalactic infrared background is

presented in chapter. 6 together with derivation of upper limits on the optical and infrared EBL density.

1.0.5 A Note on Units

SI and cgs units will be used throughout with the speed of light set to 1 when convenient. Spectral energy distributions will be presented in a νI_ν or equivalently, $E^2 \frac{dN}{dE}$, representation.[4] In this representation the spectrum results in a flat curve when the energy density per logarithmic energy bin is constant. To illustrate this, let the particle density be $\frac{dN}{d(\log E)}$, then the energy density $\mathcal{E}$ per decade of energy is $\frac{E\ dN}{d\log(E)} = \frac{E\ dN}{1/(E\ \ln(10))dE} = \ln(10)\ E^2 \frac{dN}{dE}$. This commonly employed way of displaying the spectrum rests on the observation that most astrophysical processes scale logarithmically with energy.

1.1 Gamma-Ray Observatories

The term gamma ray is generic and describes photons of energy from about 100 keV to well above PeV, or 10^{18} eV. To explore this wide energy range, various types of detectors are used; it is these detectors which define the energy regimes. Tab. 1.1 shows the energy range and corresponding detector type. Throughout the entire energy range of observational gamma-ray astronomy, the interest lies in galactic and extragalactic sources some of which have relativistic outflows.

Differences in the scientific objectives arise over this large energy range because LE to ME gamma rays are produced mainly from nuclear emission, while HE to VHE gamma rays are produced by astrophysical particle accelerators such as black holes and pulsars. Another subject covered throughout the entire gamma-ray range is the origin of the diffuse extragalactic background radiation. In the X-ray regime, it has been measured with high precision and a significant amount of the radiation can be explained as coming from

---

[4]I_ν is the spectral radiation intensity, it is related to the spectral energy density u_ν by $I_\nu = \frac{c}{4\pi}u_\nu = \frac{c}{4\pi}\frac{de}{d\nu}$, which for a thermal source equals $\frac{c}{4\pi}\frac{8\pi h}{c^3}\frac{\nu^3}{e^{\frac{h\nu}{kT}}-1}$. The representations νI_ν, λI_λ, and $\epsilon^2 n_\epsilon$ are equivalent.

Band	Abbreviation	Energy Range	Detector
Low/medium	LE / ME	0.1-30 MeV	Satellite
High	HE	0.03-100 GeV	Satellite
Very High	VHE	0.1-100 TeV	Ground-based:
			- Cherenkov telescope
			- Air shower array > 10 TeV
Ultra High	UHE	>0.1 PeV	Ground-based:
			- Air shower array
			- Fluorescence detector

TABLE 1.1. Gamma-ray energy bands and method of detection. Adapted from Weekes (2003b).

discrete objects in the universe. At higher energies, the uncertainties in the measurements are larger(or non-existent) and it is not known whether discrete and diffuse sources that we see can account for the radiation. If a significant amount of radiation cannot be accounted for, then it leaves the possibility open for radiation to be produced by, as yet, unknown mechanisms and/or particles.

Several excellent reviews cover the field of HE/VHE gamma-ray astronomy, see for example Weekes (1988); Ong (1998); Weekes (2003b). This chapter will only give a brief review of the most important observational techniques that are used in the field of gamma-ray astronomy. Observations of cosmic rays are not interesting in the context of astronomy because charged particles lose their directional information in interaction with the galactic and extragalactic magnetic fields. However, the techniques used to detect energetic cosmic rays and gamma rays are the same and hence will be mentioned.

The Earth's atmosphere is opaque to most forms of radiation; apart from the radio band there is only a small window in the optical where it is almost completely transparent. The column density of the atmosphere is about 1040 g/cm^2 to sea level; this is equivalent to almost 1 m of lead. In describing interactions of gamma rays, a convenient distance measure is the radiation length. This is the mean distance over which a high energy gamma ray or electron loses all but 1/e of its energy due to pair production or bremsstrahlung.

One radiation length in air is 37 g/cm^2; thus the atmosphere is about 28 radiation lengths thick. Fig. 1.3 shows a simplified model of an electromagnetic shower. Fluctuations in the energy distribution and the interaction length are ignored in the cartoon model. An electromagnetic shower develops by successive interactions of secondaries produced either through pair production of gamma ray interacting with the radiation field of a nucleus, or through bremsstrahlung radiation from the charged electrons and positrons. Increasing numbers of particles are produced in the shower until the energy of the secondaries drops below the pair production threshold of $2m_e^2$. This makes the atmosphere a good calorimeter
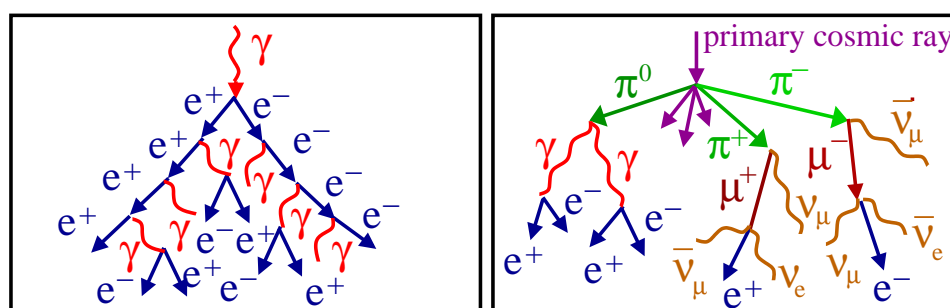
FIGURE 1.3. *Left:* Development of an electromagnetic shower. *Right:* Possible ways a particle shower can develop from a hadronic primary. Figure taken from Horan (2001).

because an initial gamma ray will deposit all its energy in the atmosphere by production of secondary particles which subsequently produce radiation that can be detected on the ground. Fig. 1.4 shows the various ways by which gamma rays can be detected; these will be elaborated on in the following sections.

In contrast to the simple particle production occurring in electromagnetic showers, hadronic showers produce a myriad of particles, see Fig. 1.3. A cosmic ray (CR), usually a proton, interacts in the atmosphere, producing many neutral and charged pions. A π^0 decays almost immediately into a pair of photons that initiate an electromagnetic shower. The $\pi^{+,-}$ participate in nuclear interactions and produce muons, neutrinos, and electrons. Due to the cross sections for these interactions, the shower becomes much broader than EM showers and, in addition, they have a significant component of penetrating muons.
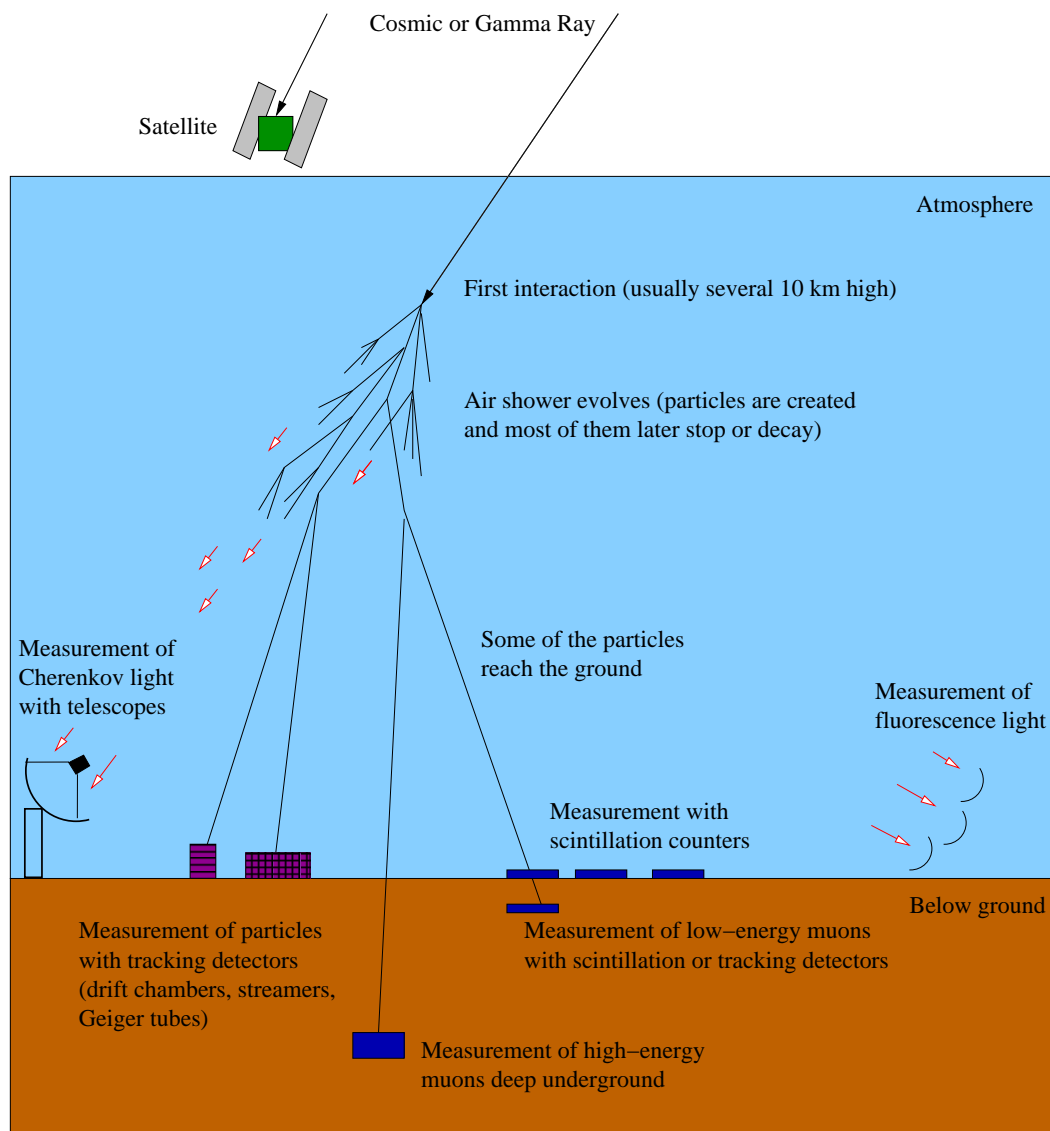
FIGURE 1.4. Methods of measuring cosmic and gamma rays. Figure adapted from Bernlöhr (1999).

1.1.1 Satellites

At energies below 10 GeV, gamma rays produce air showers with insufficient amounts of secondary radiation to be detected on the ground. Hence, observations must be carried out with detectors above the atmosphere. The energy range covered by satellites is generally

0.1 keV to 10 GeV. At higher energies the photon flux is so low that the detector size becomes impractically large for satellites.

Commonly used methods for detection of gamma rays with satellites are

- Proportional counters (0.1 - 100 keV). Gas-filled chambers that measure the amount of ionization produced by particles passing through them. The particles can be tracked by arranging the chambers in an array.

- Spark chambers (30 MeV - 10 GeV): Gamma rays produce e^+/e^- pairs in a lead absorber and these produce ionization trails in a gas filled chamber. Alternating layers of absorber and ionization chambers allow reconstruction of the particle direction to within $1°$. A calorimeter, located at the final stage, measures the total amount of energy from the secondaries.

In addition, satellites are shielded by a scintillation detector which allows them to reject triggers caused by charged primaries passing through the detector. A few satellites are mentioned below from which data is used in following chapters.

The Compton Gamma Ray Observatory (CGRO) was launched in 1991 and was operated for nine years. Four instruments on board had an order of magnitude improvement in sensitivity over previous telescopes and covered the electromagnetic spectrum from 30 keV to 30 GeV. In order of increasing energy these are: Burst And Transient Source Experiment (BATSE), Oriented Scintillation Spectrometer Experiment (OSSE), the Imaging Compton Telescope (COMPTEL), and the Energetic Gamma Ray Experiment Telescope (EGRET). EGRET was the largest gamma-ray telescope with an effective collection area of about 1600 cm^2, i.e. 15 in by 15 in. EGRET detected two classes of object: pulsars and AGN. However, the legacy of EGRET is a large number (170) of unidentified objects for which no firm counterpart at other wavelengths could be established.

At X-ray energies, NASA in 1978 launched the second High Energy Astrophysical Observatory (HEAO-2). It was renamed Einstein after launch and lasted until 1981. It was the first imaging X-ray telescope with arc-second resolution and a field of view of tens of
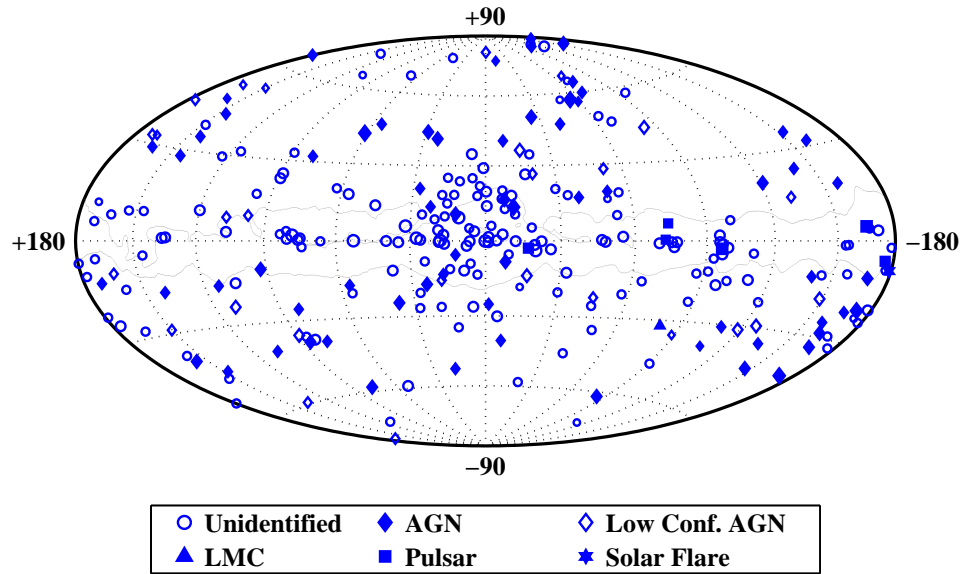
FIGURE 1.5. Sources detected by EGRET. Figure courtesy of Fegan (2004).

arc minutes. The sensitivity of its four instruments, covering the energy range from 0.2 -
20 keV, was several 100 times better than previous instruments. It was used to image faint
and extended sources. The Einstein Slew Survey (Elvis et al., 1992) was constructed with
data from the Imaging Proportional Counter (0.1-4 keV) when the telescope was slewing
from one source to the next. The final catalog was completed in 1992 and covered 50% of
the sky.

The ROSAT (Röntgen Satellite) X-ray observatory was launched in June 1990 and
lasted until February 1999. It completed a sky survey as well as a series of pointed ob-
servations. It carried two coaligned instruments: an X-ray telescope with position sensitive
proportional counter (0.5-3 keV, $2°$ FOV) and the Wide Field Camera (0.2 keV, $5°$ FOV).

1.1.2 Atmospheric Cherenkov Light Telescopes

That Cherenkov light produced by cosmic-ray particle showers contributes 10^{-4} of the
light of the night-sky was first noted by Blackett (1948). A short explanation of Cherenkov
radiation is given in App. B. Cherenkov radiation produced by a gamma-ray shower looks

similar to the short trail of a meteor burning up in the night sky; except that one has to be very close (120 m) to the impact point on the ground and use fast detectors (about 3 ns) to see it.

The first measurements of the Cherenkov light associated with extensive air showers were done by Galbraith and Jelley (1953a) using a single PMT at the focal point of a small parabolic mirror and microsecond electronics. They later found that the properties of the detected light were consistent with Cherenkov radiation[5] : i.e. a broad lateral light distribution on the ground, with density peaked at around 40 m and extending over 125 m from the shower core (Jelley and Galbraith, 1953), that the light is concentrated in a narrow angular cone of about $2°$ that it is polarized, and a light spectrum that peaked in the blue (Galbraith and Jelley, 1953b).

The first images of Cherenkov light produced by extensive atmospheric air showers were taken by Hill and Porter (1961) using image intensifiers coupled to photographic plates. The energy threshold of their detector was about 500 TeV and no sources were detected. Jelley (1967) gives an extensive review on the measurements of Cherenkov radiation from air showers at that time.

Today, the most successful ground-based gamma-ray detectors are imaging atmospheric Cherenkov telescopes (IACT), which directly record the images of Cherenkov light and can discriminate electromagnetic from hadronic shower with $>99.5\%$ efficiency. A list of some IACTs is given in Tab. 1.2. Details of IACTs can be found in the reviews by Aharonian and Akerlof (1997); Catanese and Weekes (1999) and references therein. IACTs have a small field of view, $<5°$, and low duty cycle of only about 15% because observations can only be made during clear moonless nights (about 1300 hours/year). IACTs have a large collection area of about 100,000 m^2, high angular resolution, $<0.1°$, and an energy

---

[5]Other possibilities are bremsstrahlung radiation and radiation associated with recombination following ionization (fluorescence). Galbraith and Jelley (1953b) found that bremsstrahlung radiation is similar in its angular distribution and polarization to Cherenkov light, but that it is only 10^{-5} in intensity. Photons from fluorescence are emitted isotropically, are not polarized, and the total amount of radiation produced is only 10^{-2} compared to Cherenkov radiation (Galbraith and Jelley, 1953b).

resolution ($\Delta E/E$) of about 50%.

A single IACT is limited at low energies (< 50 GeV) by the cosmic diffuse electron background that produce electromagnetic showers identical to gamma rays and by muons produced by cosmic rays. Arrays of IACTs can successfully eliminate the local muon background, and achieve higher energy resolution ($\approx 10\%$) and better angular resolution. The first operational examples of IACT arrays were HEGRA and the 7 Telescope Array. Currently operational systems are HESS and CANGAROO, while the future VERITAS array is under construction.

Another type of non-imaging Cherenkov detector are arrays of telescopes which measure the density and temporal distribution of Cherenkov light on the ground. These are usually converted Solar furnace facilities and have a very low energy threshold, around 50 GeV. Examples of this type are STACEE and CELESTE. However, γ/hadron separation is difficult to achieve with these instruments and therefore they have low sensitivity to gamma rays.

1.1.3 Extensive Air Shower Experiments

Extensive air showers, so called because of the wide distribution of secondary particles arriving on the ground, can be detected directly on the ground by different kinds of instruments; some examples are shown in Fig. 1.4. They all require a coincidence of several particle detectors to discriminate large showers from the many hundreds of single uncorrelated particles arriving on the ground. The area over which the secondary particles from an air shower are spread grows with energy. Therefore, depending on the energy, hundreds of detectors are spaced tens to hundreds of meters apart.

Advantages of these detectors over IACTs are their 1 sr field of view and almost 100% duty cycle. However, compared to IACTs their energy threshold is high and hadron rejection is poor. Particle detectors, especially those with a threshold around 1 TeV, have potential advantages in the detection of gamma-ray bursts and unexpected sources.

Group	Lat. [°]	Long. [°]	Altitude [m]	Operating Period	E_{thresh} [TeV]
Whipple 10 m	32N	111W	2320	1967-	0.3
Whipple 11 m	32N	111W	2320	1994-5	0.5
HEGRA CT-1	29N	18W	2200	1992-2002	0.5
HEGRA	29N	18W	2200	1998-2002	0.5
CANGAROO I	31S	136E	160	1992-99	1.5
CANGAROO II	31S	137E	160	1999-2004	0.4
CANGAROO III	31S	137E	160	2004-	
Durham Mark-6	31S	145E	260	1995-2000	0.25
CAT	42N	2E	1650	1996-2001	0.25
CELESTE[a]	42N	2E	1650	1995-2004	0.03
CrAO GT-48	45N	34E	600	1975-	1.0
Telescope Array	40N	113W	1600	1996-2000	0.6
STACEE[a]	35N	105W	1700	1995-	0.1
HESS	23S	15E	1800	2004-	0.1
MAGIC	29N	18W	2200	2004-	
VERITAS	32N	112W	1800	2006?	0.1

TABLE 1.2. A list of some Cherenkov telescopes. All, except those denoted with [a] have imaging cameras. The energy threshold is usually stated for zenith observations, but the definition of threshold varies somewhat.

The TIBET air shower array has measured the Crab Nebula spectrum (Amenomori et al., 1999) above 3 TeV. The Milagro detector operating at an energy threshold between 5 - 15 TeV has detected the Crab Nebula as well(Atkins et al., 2004). Both arrays have also detected emission from Mrk 421.

1.1.4 Air Fluorescence Detectors

Extensive air showers that are spread over a very large area can be detected by the UV and visible scintillation light which is emitted by nitrogen molecules in the atmosphere when charged particles pass near by. The light tracks are imaged by telescopes with cameras made of PMTs. This method has been used by the Fly's Eye experiment (Matthews et al., 1991), and by a later version, HiRes, to search for gamma rays above 200 TeV. The Auger project also operates fluorescence detectors in parallel to its extensive array of particle detectors.

1.1.5 Future VHE Observatories

Some of the goals for the next generation of VHE observatories are clear: improved sensitivity, wider energy range, wider field of view (FOV). However, not all of these goals can be combined cost-effectively into one telescope. To build a large FOV IACT is very expensive, both in terms of the physical size of the telescope required to achieve good optical quality and in terms of the camera required. For this purpose, low energy threshold extensive air shower arrays are superior as they can monitor the whole sky with almost 100% duty cycle. One such proposed system is the High Altitude Water Cherenkov array (HAWC) that would have a 50 GeV energy threshold (Sinnis et al., 2004).

To extend the energy range even lower, an array of IACTs with 5 GeV threshold located at high altitude (5 km) is proposed (Aharonian et al., 2001). This detector would complement the energy range covered traditionally by satellites (up to 40 GeV) with that of the IACTs currently coming online (HESS, VERITAS, CANGAROO).

At higher energies, extensive air shower arrays will be seeking to improve their sensitivity in the PeV regime. So far only the charged cosmic-ray component have been measured in this energy region.

1.2   VHE Gamma-Ray Sources

VHE gamma rays are produced near the most violent astrophysical regions in the universe. These are the environments of black holes, neutron stars, binary systems, and most recently discovered, the center of the Galaxy. Several types of VHE gamma-ray sources have been detected: blazars, pulsar wind nebula, and an X-ray binary system. The firmly established sources are listed in Tab. 1.3 and shown on a galactic sky map in Fig. 1.6.

For most sources, VHE gamma emission can be described either by leptonic models, such as the Synchrotron Self-Compton (SSC) model (Maraschi et al., 1992) or by hadronic ones. For example, proton-initiated cascades (Mannheim, 1993) and proton-synchrotron radiation (Mücke and Protheroe, 2001) are used to explain the VHE emission component of AGN. Measurements of VHE energy spectra are necessary to differentiate between these models.

In leptonic models, a source of ultra high energy electrons and positrons is assumed to exist. The interactions that produce VHE photons are (1) emission of bremsstrahlung photons during scattering in the surrounding (hadronic) medium, (2) inverse Compton scattering of low-energy seed photons, and (3) emission of synchrotron radiation by deflection by a magnetic field (Blumenthal and Gould, 1970). The particular geometry and order of these processes sets the models apart. The simplest SSC model assumes a single power-law electron spectrum that extends from keV to PeV energies. The electrons produce synchrotron photons in randomly oriented magnetic fields. The synchrotron photons, generally in the optical to X-ray band, are then scattered to TeV energies through inverse Compton scattering by TeV to PeV electrons. More complex models use multi-component electron spectra and time dependence, see for example (Krawczynski et al., 2002). Optical seed photons

Dist[a]	Object	Type[b]	Detections[c]
1 kpc	RX J1713-394 6	SNR	C[d], HESS
1.5 kpc	PSR B1259-63	Bin/SNR	HESS
2 kpc	Crab Nebula	SNR/PWN	W, HEGRA, CAT, C, Cr, 7T, HESS, S
8 kpc	SGR A*	SNR?	C[d], W, HESS
0.030	Mrk 421	HBL	W, HEGRA, C, HESS, CAT, S
0.034	Mrk 501	HBL	W, HEGRA, CAT, 7T
0.044	1ES 2344+514	HBL	W, HEGRA
0.047	1ES 1959+650	HBL	7T[e], W, HEGRA
0.116	PKS 2155-304	HBL	D, C?? CHECK FLUX, HESS
0.129	H 1426+428	HBL	W, HEGRA
?	TeV 2032+413	un. id.	Cr[d], HEGRA, W
?	VHE J1303-63	un. id.	HESS

TABLE 1.3. Definite sources of VHE gamma rays detected by Cherenkov telescopes. Adapted from Horan and Weekes (2004). These sources have either been detected by two independent observatories or are detections by HESS

[a] Redshift or distance in indicated units.

[b] Type: HBL = high frequency peaked blazar, SNR = supernova remnant, PWN = pulsar wind nebula.

[c] Detection at > 5-σ unless otherwise stated. W=Whipple, C=CANGAROO, Cr=Crimea, D=Durham, 7T=7 Telescope Array, S=STACEE

[d] Not compatible with other measurements.

[e] Detection at < 5-σ.

could also come from nearby hot dust clouds.

Over the past three decades, the field of VHE gamma-ray astronomy has experienced a number of false source claims that have cast some doubt over the credibility of the detections. However, now with improved telescopes and increased understanding of the technique, the field has entered a time when astronomy can readily be done, without the need for an independent confirmation. The system of stereoscopic telescopes, HESS, is the first operational example and has produced two unexpected results. The first is the serendipitous detection of an unidentified TeV source in the field of view during observations of the binary system PSR B1259-63. The second is a map of the VHE emission of the supernova remnant RX J1713-39; showing for the first time the shell structure at these high energies.
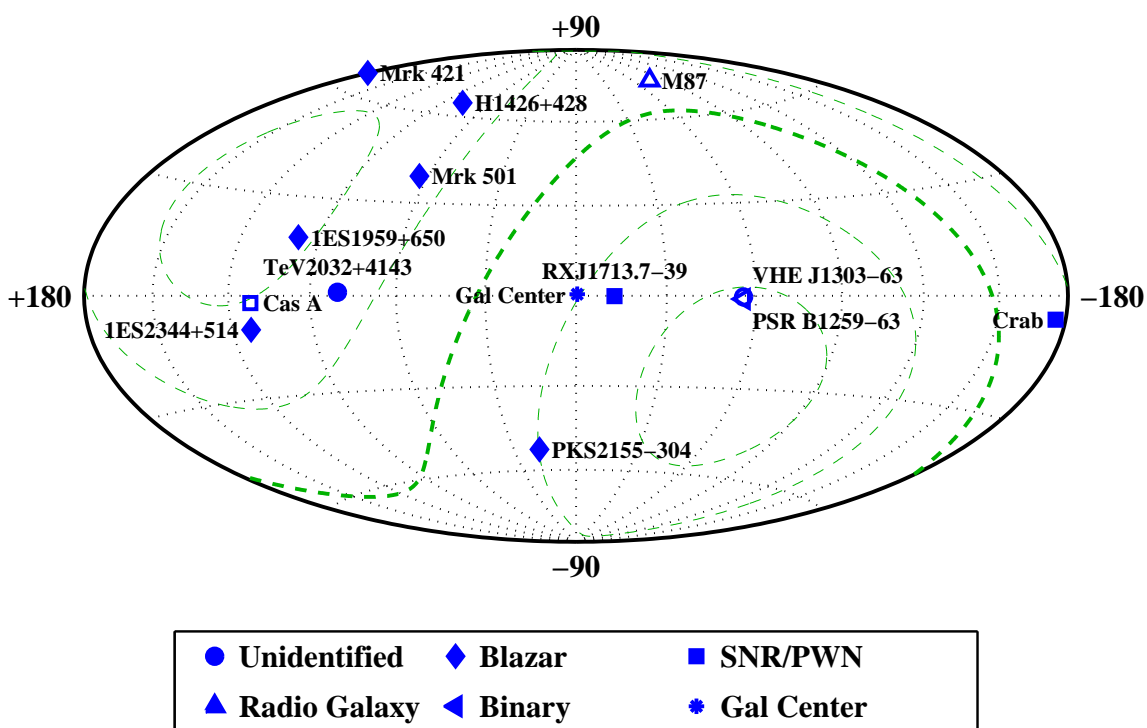
FIGURE 1.6. Catalog of VHE sources. *Solid* points indicate confirmed detections, while *open* symbols denote possible sources. The separation between the northern and southern hemisphere is shown with a *thick dashed line*. The 10 m telescope is at a declination of $32°$ N and can observe the galactic center. Figure courtesy of S. Fegan, modified from Horan and Weekes (2004).

1.2.1 Supernova Remnants

The Crab Nebula (Webster, 1994) is a plerion-type supernova remnant (SNR); a neutron star surrounded by the material from a supernova explosion in 1054 AD. The neutron star rotates with a period of 33 ms, it is called a pulsar, and is surrounded by a plasma of protons and electrons. The broad band energy spectrum is shown in Fig. 1.7 and explained as follows: The rotating strong magnetic field of the pulsar produces a strong electric field at the poles, creating an electric circuit in the plasma. The accelerated electrons emit synchrotron radiation as they move in the magnetic field. This is confined to a small region near the pulsar, but the exact location, whether at the polar caps (Harding, 1981) or at the

outer gap (Cheng et al., 1986), is controversial. As the pulsar is spinning, we see synchrotron radiation once per rotation. This pulsed emission extends from radio up to about 10 GeV. In addition, two types of steady emission are produced by the interaction of the energetic electron beam with the nebula. Electrons interact in a termination shock created by the outward pressure of the pulsar with the left-over material from the supernova blast. Here, shock-acceleration boosts the electrons up to a few PeV which then emit more synchrotron radiation. In addition, the electrons produce VHE gamma rays through IC scattering of low-energy synchrotron photons. No pulsed emission has been detected in the VHE gamma-ray signal above 250 GeV (Lessard et al., 2000), and the pulsed emission is less than 10% of the DC signal above 60 GeV (de Naurois et al., 2002).

As the Crab pulsar does not have a companion to feed energy into it, it gradually slows down as it is powering the emission of the Nebula. The emitted radiation is steady on the time scale of years and is used as the "standard candle" in VHE astronomy. It has been detected by eight ground based Cherenkov telescopes covering an energy range from 50 GeV to over 50 TeV (Weekes, 2003b). The spectrum can be approximated with single power-law $F = N_0 \ (E/TeV)^{-\gamma}$, where $\gamma \approx -2.5$ and $N_0 \approx 3 \times 10^{-7}$ TeV^{-1} m^{-2} s^{-1} (Weekes, 2003b).

The supernova remnant RX J1713.7-3946 was initially discovered by the ROSAT all-sky survey and claimed as a VHE gamma-ray source by CANGAROO-I and II (Muraishi et al., 1999, 2000). Muraishi et al. claimed a power law spectrum with index $-2.84 \pm_{st} 0.15 \pm_{sy} 0.20$ (statistical and systematic errors) and a source position compatible with the location of the peak X-ray emission. HESS (Berge et al., 2004) recently produced a resolved map of this SNR that shows several points of VHE gamma-ray emission. Their preliminary spectrum over the whole remnant can be fitted with a power law index of $-2.19 \pm_{st} 0.09 \pm_{sy} 0.15$. Their detailed map and follow-up observations will allow for the first time spectral measurements across the shell structure.

SN 1006 is a shell-type supernova remnant and was claimed by the CANGAROO collaboration as a VHE gamma-ray source (Tanimori et al., 2001) with a flux of 50% of the
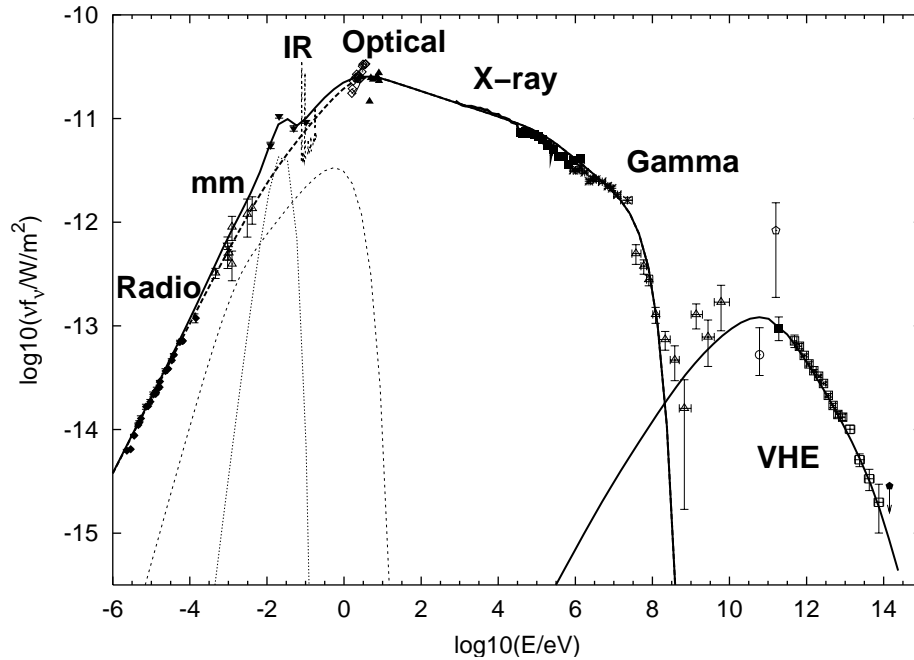
FIGURE 1.7. Spectral energy distribution of the Crab Nebula, not including the pulsed component from the Crab Pulsar. Figure from Horns and Aharonian (2004).

Crab Nebula. Subsequent observations by HESS have placed upper limits at 10% of the Crab flux (Masterson, 2004). As a side note: a point X-ray source located 9 arc min northeast of the center of SN 1006 has been spectroscopically identified as a background QSO, with a redshift of 0.335.

1.2.2 Blazars

Active galaxies, so-called because of their bright central core with a nonthermal spectra, comprise a few percent of all known galaxies in the universe. The emission originates at the nucleus of the galaxy, i.e. the active galactic nucleus (AGN), which are thought to contain super massive black holes, $10^8 - 10^9$ $M_\odot$ (Barth et al., 2003). These nuclei outshine the star light from their host galaxy across the entire waveband. The host galaxies are mostly elliptical. A generally accepted physical picture of an AGN is shown as a cartoon

in Fig. 1.8. The accretion disk is heated in the inner region by frictional losses and can radiate at ultra-violet to soft X-ray energies. Relativistically outflowing jets of particles are emitted from the polar regions of the spinning black holes (Dermer et al., 1997) and references therein. How the jet is formed and what it is made off is a matter of considerable debate. Some have speculated that the spinning black hole may coil up the magnetic fields of the galaxy and expel them along two narrow jets (Semenov et al., 2004). Alternatively, the energy might come from a small volume of space around the black hole itself, or the jets may be produced by the hot accretion disk of gas that spirals into the black hole. Only through further observations at all wavelengths will this important question be resolved.
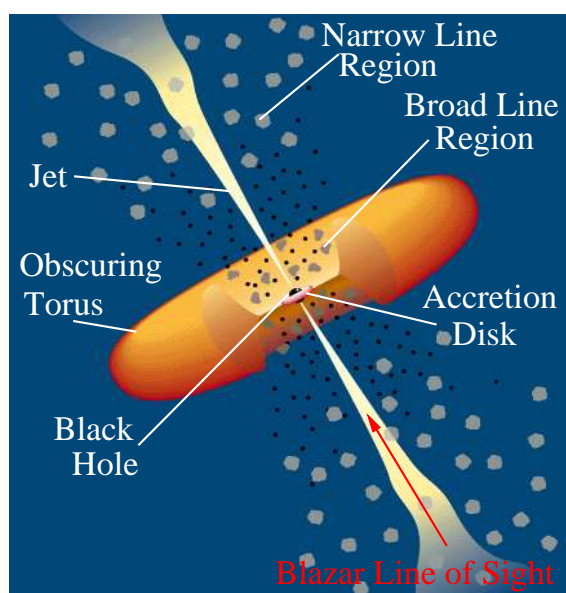
FIGURE 1.8. Model of the physical structure of AGNs. Figure courtesy of Horan (2001).

One sub-type of AGN, the BL Lac objects, named after their prototype, BL Lacertae, seem to have their jet of high energy particles aligned with our line of sight (Urry and Padovani, 1995). These AGN are all radio-loud (Stocke et al., 1990), meaning their energy output at radio wavelengths surpasses that at in the optical region. BL Lacs are characterized by rapidly variable nonthermal radiation from radio to VHE-bands, no (or very weak)

emission lines with equivalent width less than 5 Å, and a CA II "break strength" smaller than 25% (Perlman et al., 1996).

The broad band spectrum shows a double peak; commonly believed (Fossati et al., 1998; Ghisellini et al., 1998) to be produced by nonthermal Compton and synchrotron processes occurring in the jet (Dermer et al., 1997). In both components of the spectrum, strong and rapid variability has been observed. The first component extends from radio wavelengths to the UV or X-ray band and is believed to be due to synchrotron emission. It is characterized by strong radio/optical polarization on the order of 5-10%. The second component peaks at GeV to TeV energies and is commonly believed to be produced by inverse Compton up-scattering of optical seed photons by the populations of synchrotron electrons. Optical seed photons could be the synchrotron radiation, as in the SSC model, ambient photons produced by the accretion disk Dermer et al. (1992), IR photons from hot dust in the central region, or the cosmic microwave background. This means that different VHE gamma-ray spectra can be produced by the same population of electrons. See Appendix D for a study of the correlation between optical emission line variability and the VHE gamma-ray flux in Mrk 421.

BL Lacs are classified according to the location of the synchrotron peak: if it is in the far-IR to optical the object is a low-energy peak BL Lac (LBL), if the peak is higher at UV to X-rays, it is called a high-energy peaked BL Lac (HBL) (Padovani and Giommi, 1995). All AGN from which VHE radiation has been confirmed are of the HBL-type and have distinct X-ray/radio/optical colors (Perlman et al., 1996). Costamante and Ghisellini (2002) used this to predict BL Lac candidates for VHE emission.

A total of six confirmed AGN have been detected in the VHE regime, see Tab. 1.3: Mrk 421 Punch et al. (1992), Mrk 501 (Quinn et al., 1996), 1ES 2344+514 (Catanese et al., 1998), 1ES 1959+650 (Nishiyama et al., 1999), PKS 2155-304 (Chadwick et al., 1999), and H 1426+428 (Horan et al., 2002; Aharonian et al., 2002a). The spectral energy distribution (SED) of five of them together with a SSC model, is shown in Fig. 1.9. Their distance is determined from the redshift, defined by $z = \Delta\lambda/\lambda$. However, this measurement is
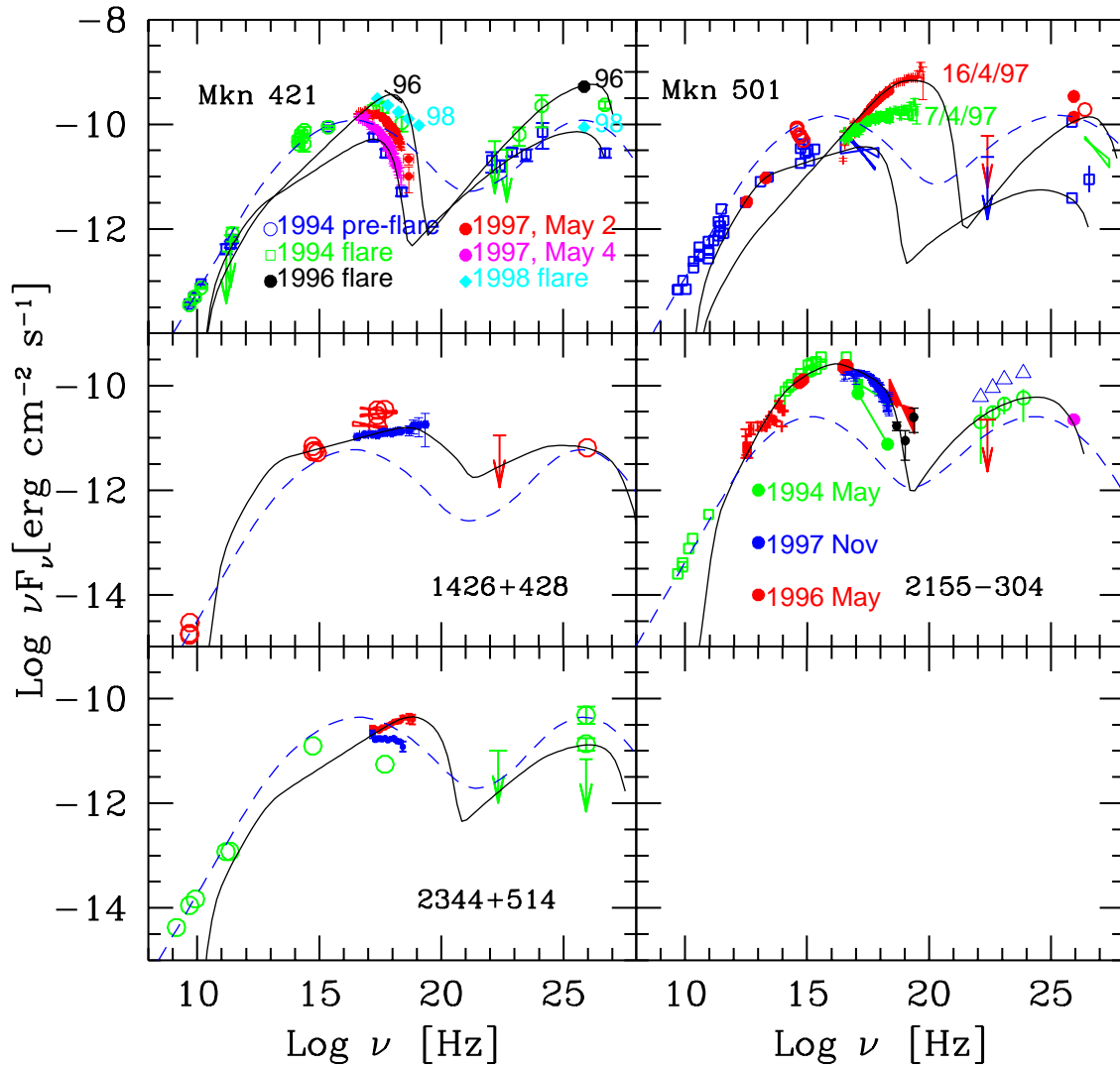
FIGURE 1.9. The spectral energy distribution of 5 BL Lac objects detected at TeV energies. The solid line shows a fit from a SSC model. Figure taken from Costamante and Ghisellini (2002). Missing from this plot is 1ES 1959+650 because the only VHE detection at the time of publication did not state a flux level.

complicated by the fact that blazars, by definition, do not have significant emission or absorption lines (but usually some weak ones can be found). For small z, the physical distance is given by $\frac{z\,c}{H_0}$, where H_0 is the Hubble constant (Weinberg, 1972). At large z,

Object	Redshift	Distance [Mpc]	[$\times 10^{24}$ m]
Mrk 421	0.031	131	3.9
Mrk 501	0.034	145	4.4
1ES 2344+514	0.044	190	5.7
1ES 1959+650	0.047	204	6.1
PKS 2155-304	0.116	535	16.5
H 1426+428	0.129	601	16.8

TABLE 1.4. Distance of VHE blazars. The distance shown is the luminosity distance, D_L, calculated with H_0=70 km/s/Mpc, $\Omega_M = 0.3$, $\Omega_\Lambda = 0.7$.

the proper distance must be found by integration using the correct cosmological model. Tab. 1.4 lists the redshift and luminosity distance[6].

1.2.3 Binary System

PSR B1259-63 (B1259) is one of only two known radio pulsars in orbit around a main sequence star, and it is the only such system from which VHE gamma rays have been detected. The Be-type companion star has a mass of about 10 $M_\odot$ and the orbital period is 3.4 years, the geometry of the system is shown in Fig.1.10. VHE gamma rays were detected from the pulsar around the time of closest approach by the HESS collaboration (Beilicke et al., 2004a). This confirmed the prediction by Kirk et al. (1999) that electrons and positrons from the shocked pulsar wind would inverse Compton scatter optical photons from the companion star near periastron.

1.2.4 Others

The Galactic Center (Melia and Falcke, 2001) harbors a super-massive black hole of 2.6×10^6 $M_\odot$, Sgr A*. Radio interferometry observations first discovered emission from the compact object in 1974. At optical wavelengths, a large accretion disk is obscuring the view of the central region. Recently, VHE gamma rays have been detected from the direction of

---

[6]The luminosity scales with luminosity distance, d_L, as $1/d_L^2$. In an expanding universe there are a few ways of defining distances, but this is the most useful in this context.

Distance:
1.5 kpc

Pulsar:
PSR B1259-63:
$M_p = 1.4 \, M_\odot$
radio freq.:
47.75 ms

companion:
SS 2883:
$M_* = 10 \, M_\odot$
$R_* = 6 \, R_\odot$

$\Rightarrow$ Very exotic geometry of system
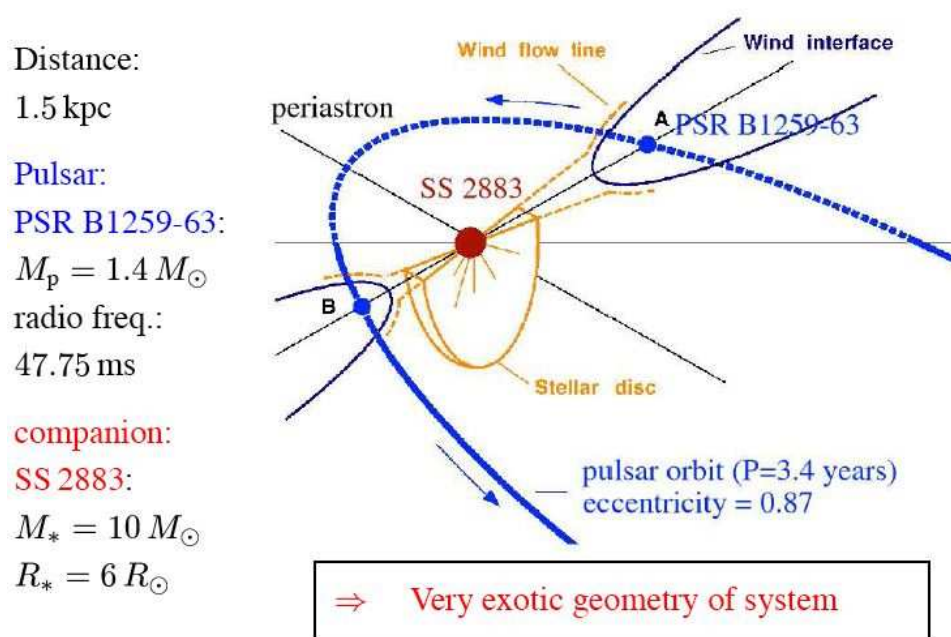
FIGURE 1.10. The pulsar PSR B1259-63 near the time of closest approach to the companion star. Optical seed photons from the companion star are inverse Compton scattered to very high energies by the electron/positron pulsar wind. Figure taken from Beilicke et al. (2004a).

Sgr A* by CANGAROO (Tsuchiya et al., 2004), Whipple (Kosack et al., 2004), and HESS (Aharonian, 2004); to pinpoint the location of the gamma-ray emission from the galactic center requires, as-yet unattained, arc-second resolution. The spectrum measured by the HESS collaboration differs substantially from the results reported by CANGAROO, while the Whipple results (after a reanalysis) are consistent with HESS.

VHE gamma rays have been detected from two objects for which no firm counterpart in other wavelengths have been established. One of these is TeV 2032+4143. It was first discovered by the Crimea Observatory (Neshpor et al., 1995), and later independently by the HEGRA collaboration during a sky survey in the galactic plane (Aharonian et al., 2002c). Observations using the Whipple 10 m telescope had been taken in 1988-90 at the location of Cygnus X-3, which is about $0.6°$ south of the unidentified source. Using this archival data, Lang et al. (2004) confirmed the location of this new source. However, the flux level

measured by the three groups is at variance: Neshpor et al. measured it to be about as bright as the Crab Nebula, Aharonian et al. measured 3% of the Crab Nebula flux, and Lang et al. measured 12% of the Crab Nebula flux. This suggests that the source is variable.

The other unidentified source, VHE J1303-63, was seen by HESS during observations of PSR J1259-63 (Beilicke et al., 2004b). It does not appear to be variable.

The giant radio galaxy M87, is the first AGN detected at VHE energies that does not belong to the BL Lac class (Beilicke et al., 2004c). Its central black hole has a mass of $2 - 3 \times 10^9$ M$_\odot$ and it is at a distance of 16 Mpc (z=0.00436). The detection was at the 4σ level with an integral flux ($E > 730$ GeV) of 3.3% of the Crab Nebula flux (Beilicke et al., 2004c). Observations with the Whipple 10 m telescope place a flux upper limit (E>400 GeV) at 8% of the Crab Nebula (Le Bohec et al., 2004).

The radio pulsar PSR 1706-44 was claimed as a VHE gamma-ray source with a flux of about 50% of the Crab (Kifune et al., 1995; Chadwick et al., 1998). Recent observations by HESS have not shown evidence for gamma-ray emission. They place an upper limit at 3% of the Crab flux (Masterson, 2004).

Lastly, some more exotic sources have been suggested in the literature:

- Dark matter annihilation in the halos of galaxies: The current best limits come from observations of the Galactic Center (Horns, 2004).

- Neutralino annihilation, see (Valle, 2004) and references therein.

- Gamma-ray bursts, see Waxman (2004); Ioka et al. (2004) and references therein. Perhaps not so exotic, as a 18 GeV photon has been already been detected from GRB940217 (Hurley, 1994).

- Primordial black holes (Halzen et al., 1991).

1.3   VHE Flares of Blazars

Over the last decade, multi-wavelength campaigns of Mrk 421, Mrk 501, and 1ES 1959+650 have shown a correlation between the X-ray and VHE flux. Flares at these energies have been observed on time scales of half-hour to weeks. During these flares, the spectrum typically hardens as the flux increases. The exact correlation is difficult to establish as there is hysteresis and simultaneous X-ray and VHE spectra are rarely measured. Multi-wavelength observations of the other VHE blazars 1ES 2344+514, PKS 2155-304, and H 1426+428 have not been as successful because the VHE flux level is very low. This will change with the improved sensitivity of IACT arrays.

The synchrotron self-Compton (SSC) model has been used in explaining the majority of observations, but the simplest model with one population of electrons fails in explaining the time-structure found in the flares. In the case of 1ES 1959, an orphan VHE flare without activity in the X-ray regime was detected during June 2002 (Krawczynski et al., 2004). It is possible that a second population of UHE electrons produced the VHE gamma-ray flare while the 3-25 keV X-ray spectrum remained unchanged. Through simultaneous multiwavelength observations, reverberation mapping (Boettcher and Dermer, 1995) can give clues on the structure of the jet and how it is connected to the accreting black-hole system.

Remarkably, the temporal and spectral X-ray and VHE emission properties of the six blazars during flares are very similar (Krawczynski et al., 2004). The X-ray synchrotron peak ranges from 10^{18} and 10^{19} Hz with a peak luminosities between 10^{43} and 10^{44} erg s^{-1} sr^{-1}. The black hole masses are also relatively similar: 10^8-10^9 M$_{\odot}$. It is possible that the reason for this similarity lies in the fact that only the brightest VHE blazars are seen by the IACTs at this time, but that there is a continuous population of blazar spectra (Costamante et al., 2001).

The following sections will describe the brightest VHE flare spectra, shown in Fig. 6.9, of four of the six blazars detected to-date. 1ES 1959+650 and 1ES 2344+514 are treated in detail in Chapters 4 and 5, respectively.

1.3.1 Mrk 421

The first VHE blazar to be detected was Mrk 421 (Punch et al., 1992) and it is the best studied of the six objects to date. Several extensive multi-wavelength campaigns have been undertaken (Macomb et al., 1995; Buckley et al., 1996; Maraschi et al., 1999). Rapid X-ray flaring in connection with VHE activity has frequently been seen (Buckley et al., 1996; Maraschi et al., 1999). Other wavebands do not show a correlation with the VHE level (Macomb et al., 1995), but see Buckley et al. (1996) for a possible correlation with the far-UV and optical bands. Such behavior could be explained by a SSC model with variable upper cut-off energy of the relativistic electron distribution. The higher energy electrons would affect emission at both X-ray and VHE simultaneously while leaving other wavelengths relatively unaffected.

The quiescent level of VHE emission from Mrk 421 above 350 GeV is around 0.2 times the steady flux from the Crab Nebula (0.3 gamma min^{-1}) (Gaidos et al., 1996). The brightest flare recorded from any source occurred on May 7, 1995, when the gamma-ray flux above 350 GeV was ten times as high as the steady flux from the Crab Nebula. During this observation, the flux doubling time was about an hour. A week later, another flare was recorded with a doubling time of less than 30 minutes (Gaidos et al., 1996).

The most detailed spectrum was measured during an exceptionally strong and long lasting flaring activity in early 2001 (Krennrich et al., 2001), see Fig. 6.9. The spectrum could be well described by a power law with exponential cut-off $F(E) \propto E^{-\alpha}e^{-E/E_c}$ with $E_c = 4.3 \pm 0.3$ TeV (Krennrich et al., 2001). The cut-off energy is attributed to gamma-ray absorption by the extragalactic medium, see Sect. 1.4.

The 2001 flare data was used to study the correlation of flux spectral index with the flux level (Krennrich et al., 2002; Aharonian et al., 2002b). It was found that a spectral hardening occurs during periods of high flux and that a power law with one fixed exponential cut-off energy results in a good fit, independent of flux level.

1.3.2 Mrk 501

Mrk 501 underwent a strong flare during February and June 1997 and the VHE spectrum derived from these flares showed, for the first time, a deviation from a power law (Samuelson et al., 1998), see Fig. 6.9. The flare spectrum reported by the HEGRA collaboration for the same time period agrees with the Whipple measurement (Aharonian et al., 1999). Similar to Mrk 421, the cut-off energy lies at $E_c = 4.6 \pm 0.8$ TeV for Mrk 501 (Krennrich et al., 2001).

1.3.3 PKS 2155-304

The HBL object, PKS 2155-304 (PKS 2155), first detected by (Chadwick et al., 1999) and confirmed by (Hinton, 2004). Recent observations by HESS (Lemiere et al., 2004) have detected PKS 2155 at a significance level of 45σ from observations in 2002/3. The light curve shows variability and the spectrum can be well fitted by a simple power law with in -3.32 ± 0.06 over the entire energy range from 0.155 TeV to 8 TeV. Lemiere et al. (2004) indicated that the shape of the spectrum did not seem to change with flux level.

1.3.4 H 1426-428

H 1426+428 (H 1426), z=0.129, is the most distant blazar from which VHE gamma rays have been detected (Horan et al., 2002; Aharonian et al., 2002a). The emission level is generally very low so that no particular flares can be identified in the data. However, as VHE emission during flaring activity is much higher than during the quiescent state, most of the photons collected may be associated with flares. It was found by (Petry et al., 2002; Aharonian et al., 2003a) that a power law with exponential cut-off does not fit the spectrum well. But this should be treated with caution because of limited statistics and systematic errors arising by combining spectra from two collaborations.

1.4 The Diffuse Extragalactic Background Radiation

The photon spectrum incident on the Earth has been measured from MHz radio waves to tens of GeV gamma rays. Once the contributions from local and galactic sources are identified and subtracted, one is left with a diffuse extragalactic background radiation (DEBRA), see Fig. 1.11. Ressell and Turner (1990) further discuss the measurements. It carries the imprint of the evolution of the universe including star formation and black holes, and its main characteristic is that it is isotropically distributed across the sky.

The most famous, strongest, and first component of the DEBRA to be detected was the cosmic microwave background (CMB). It has been measured with excellent precision to correspond to 2.725 K blackbody radiation (Fixsen and Mather, 2002), a relic of the very hot Big Bang. Cosmic rays with energy greater than 5×10^{19} eV interact with CMB photons to produce pions (Greisen, 1966; Zatsepin and Kuzmin, 1966). The resulting attenuation introduced on the spectrum of UHE cosmic rays is currently being measured by several extensive air shower experiments, see Sect. 1.1.3.

Second in intensity to the CMB, is the optical and infrared (IR) extragalactic background light (EBL). This portion of the EBL contains the imprint of galaxy evolution since the Big Bang. This includes the light produced during formation and preprocessing of stars; all are areas of active research. However, due to the bright foreground caused by our solar system, this part of the EBL spectrum is difficult to measure with optical telescopes, both from the ground and from space.

VHE astronomy is in a unique position to place limits on the optical/IR component of the EBL. Blazars are extragalactic objects and due to their much larger distance than objects in our Galaxy, the spectrum measured from the Earth is modified by interactions with the extragalactic medium. For example, if a gamma ray with 1 TeV energy collides with an ambient 1 eV optical photon, the threshold for production of an electron/positron pair is reached. If a pair is produced, then the TeV photon will not be observed, causing an attenuation of the measured spectrum at that energy. This is both a curse and a blessing,
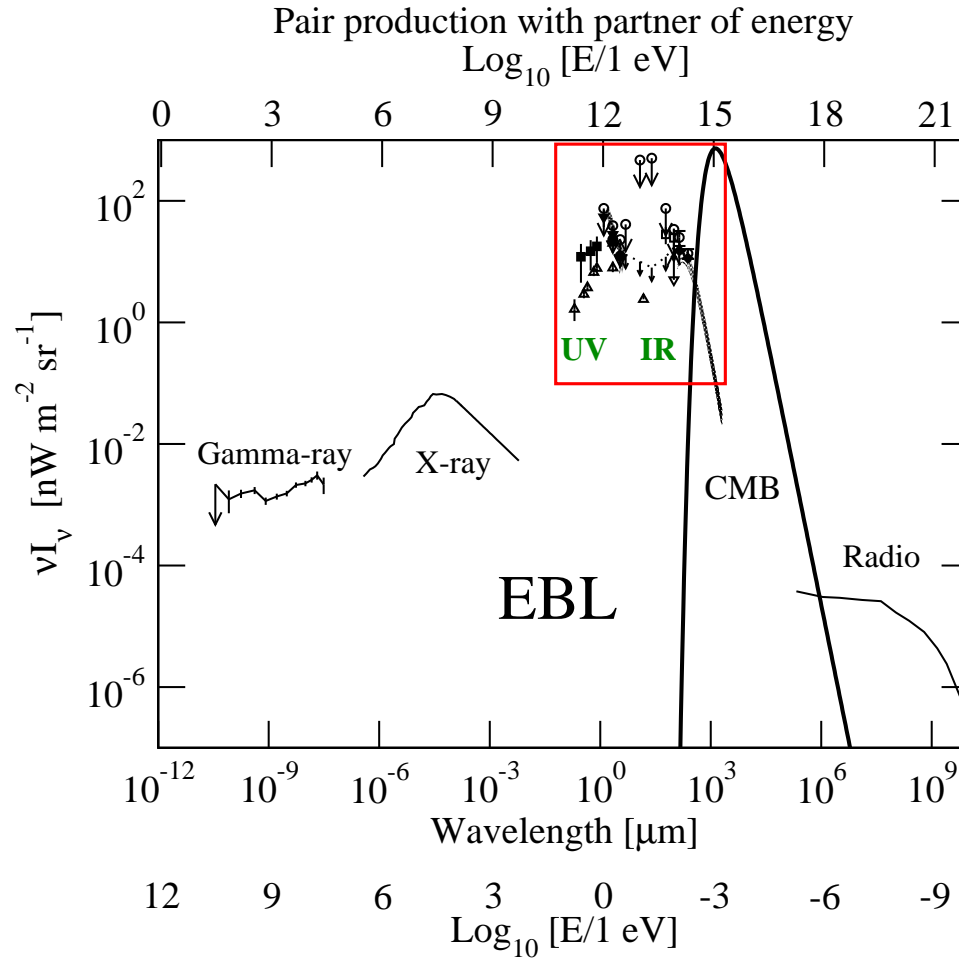
FIGURE 1.11. Spectral energy distribution of the extragalactic background light (EBL) from radio waves to gamma rays. The top axis indicates the most likely energy of the partner photon to participate in pair-production with the EBL. The radio data for normal galaxies taken from Protheroe and Biermann (1996), CMB temperature from COBE (Fixsen and Mather, 2002), infrared/optical data as described in Fig. 6.1, compilation of X-ray data from Sreekumar et al. (1998), gamma-ray measurement from Strong et al. (2004).

because this makes it difficult to determine the intrinsic blazar spectrum. But if one can somehow ascertain what the intrinsic spectrum is, then the optical photon density in the extragalactic medium can be determined from the measured attenuation. Chapter. 6 further discusses direct measurements and the limits derived from the spectra of AGN.

CHAPTER 2

THE WHIPPLE 10 M TELESCOPE

FIGURE 2.1. The Whipple 10 m telescope in its horizontal stow position.

The 10 m telescope at the Fred Lawrence Whipple observatory, Fig. 2.1, was constructed on Mt. Hopkins in 1968. It is located in southern Arizona at an elevation of 2312 m, (Lat: $31.6804°$ N, Long: $110.8790°$ W). The telescope is of a Davis-Cotton design with 240 mirror facets arranged on a spherical support structure of radius 7.3 m. All facets have the same focal length of 7.3 m. The mirrors are front-coated and have a protective anodization layer to extend the lifetime of the reflectance in ultra-violet (UV). The telescope is positioned on an elevation-azimuth mount. The camera is located at the focal point and consists of ultra-violet (UV) sensitive photomultiplier tubes (PMT). Over 35 years the camera has evolved from a single PMT with a $1°$ field of view to a high-resolution imaging detector consisting of 379 PMT each covering $0.12°$ of the sky, see Fig. 2.2.

Operation began in 1968 with a non-imaging camera that was upgraded to an imaging camera in 1982.
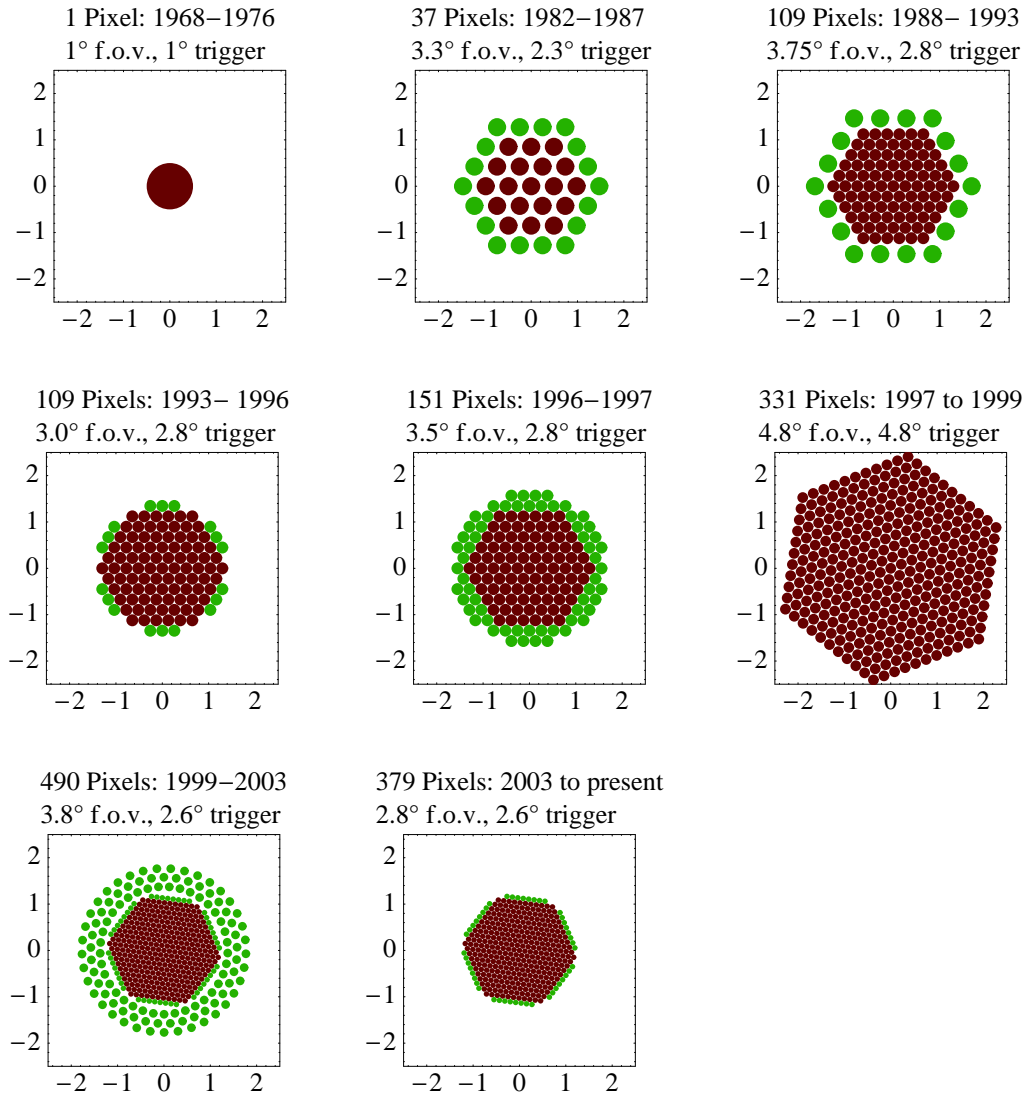
FIGURE 2.2. Layout of the PMTs on cameras used on the Whipple 10 m telescope. The PMTs contributing to the trigger (see Sect. 2.2.3) are shown in red. There were two versions of the 109 1" PMT camera. One as shown used for regular observations, the other with solar blind PMTs used during periods of bright moon light in the ARTEMIS experiment (Pomarède et al., 2000).

2.1   Types of Observations

Typically, observations with the 10 m telescope are taken with the gamma-ray source in the center of the field of view of the camera for 28 sidereal minutes. This type of observation is called an on-source (ON) run. To determine the background level, another type of type of run is taken with the source offset in right ascension (RA) by ± 30 sidereal minutes, called an off-source (OFF) run. OFF observations are taken either directly before or after the ON run and cover the same region of elevation and azimuth as the ON run, but at a slightly different time. Without the source in the FOV, OFF runs are used to measure the CR background. This background depends on the sky condition, the zenith angle of the observation, and the condition of the telescope. More details on the CR-rate is given in Sect. 2.3.

ON/OFF pairs have the most reliable background measurement and are used when the gamma-ray source is weak and when a spectrum is to be derived. However, taking pair observations results in only 50% on-source exposure time, leaving gaps in the light curve. This is especially important for variable sources, such as blazars where one would like to monitor the emission continuously. Therefore, if the gamma-ray signal is strong enough so that the statistical error in the photon rate is smaller than the systematic uncertainty in the background rate, ON observations are taken without a corresponding OFF run. These types of ON runs are then called tracking (TRK) runs. TRK observations are also taken when the night-sky is deemed by the observers to be possibly cloudy. Clouds in the field of view are noticeable from fluctuations in the CR rate. An OFF run is, in this case, not feasible because it is known that the background rate is changing.

The background level for TRK runs is estimated using a pool of OFF runs using the tracking ratio method, discussed in Sect. 2.4.4. OFF runs selected for this purpose are similar to the TRK run in elevation, $\pm 10°$, and within about two months of observation time. The latter requirement is due to the slowly decreasing light throughput of the telescope.

If only TRK runs are available for a spectral measurement, an equivalent tracking ratio

method does not work, and one specific OFF run has to be paired with each TRK. Selecting these OFF runs requires a careful balance between selecting runs that are somehow alike and maintaining an unbiased selection approach. A specific example is discussed in Sect. 4.

Another type of observation taken during a night is a 10 min. night-sky measurement with the telescope pointed at zenith, a so-called zenith run. This measures the cosmic ray rate and establishes the night-sky quality. There is a long history of zenith runs and the data has been used in long term studies of the telescope performance and recently also in a gamma-ray sky survey.

For calibration purposes, each night thousands of events are recorded with the camera illuminated by a Nitrogen arc lamp for one minute. These Nitrogen runs are used to determine the relative gains of the PMTs, see Sect. 2.4.1.

The accuracy of the telescope tracking system is checked occasionally by pointing the telescope directly at dim stars located at different elevations and azimuths. A current monitor system is used to read out the anode current in the PMTs. Ideally, only the center PMT should show a higher current, but deflection of the telescope structure and offsets during the alignment procedure may cause an offset. If a offset is measured, corrections can be implemented in the telescope tracking software.

The sky conditions during observations are rated by the observer as "A", "B", or "C", referring to clear sky, possible clouds, and definite clouds. The amount of truth in these subjective ratings has been quantified by Lebohec and Holder (2003).

2.2 The Data Acquisition System

The major components of the data acquisition system (DAQ) are shown in Fig. 2.3. Photons that are incident on the PMT may produce photo-electrons (pe). The probability for this to occur depends on the wavelength and the specific type of PMT used, see Fig. 3.18. In turn, the PMT produces an anode current linearly proportional to the number of pe. The currents are monitored and in case of over-current, the high voltage (HV) supply to that

PMT is shut down by the observer. The signal from the PMT is AC-coupled to a ten-times amplifier and then split equally between the trigger system and a charge-to-digital converter (QADC).[1] While the trigger system processes the signal, the other part of the split signal passes through a 120 ns delay cable to the QADC.

Sources of photons that produce a current in the PMTs include noise from the night-sky background (NSB), Cherenkov light from cosmic rays and gamma rays; this is discussed in Sect. 2.2.1. As the data acquisition rate is limited to about 30-40 Hz, a trigger system decides when to take a snap shot of the sky; the system is described in detail in Sect. 2.2.3. When a trigger occurs, the signal from each PMT is integrated for 20 ns and converted to digital counts (dc) by the QADC. This information, along with the time and a trigger map, is sent along the CAMAC backplane and recorded by a computer. The integration time is longer than the 3-4 ns duration of Cherenkov light(Hillas, 1982), because of a 6 ns time spread introduced by the optical geometry of the telescope, 3 ns pulse degradation in the cables, and the PMT rise and fall times.

A second trigger operating at a fixed rate of 1 Hz is supplied by a global position system (GPS) clock. Events triggered in this way are called pedestal events and are tagged in the data stream. Pedestal events are used in the data analysis to measure the dc off-set in each QADC channel. This off-set is set in hardware to a small positive value and is necessary because the AC-coupled signal produces small negative fluctuations while the QADC can only digitize positive values. The fluctuations arise from night-sky background light, discussed in Sect. 2.2.1

2.2.1 Noise and Background Light

The images acquired by the telescope contain three sources of noise: (1) night-sky glow and star light produce random fluctuations of the night-sky background (NSB), (2) electronic noise in the analog circuit, and (3) fluctuations in the gain of the PMT. The latter has not

---

[1]Another splitter was installed in Fall 2002 to supply signals to the SCARFACE experiment.
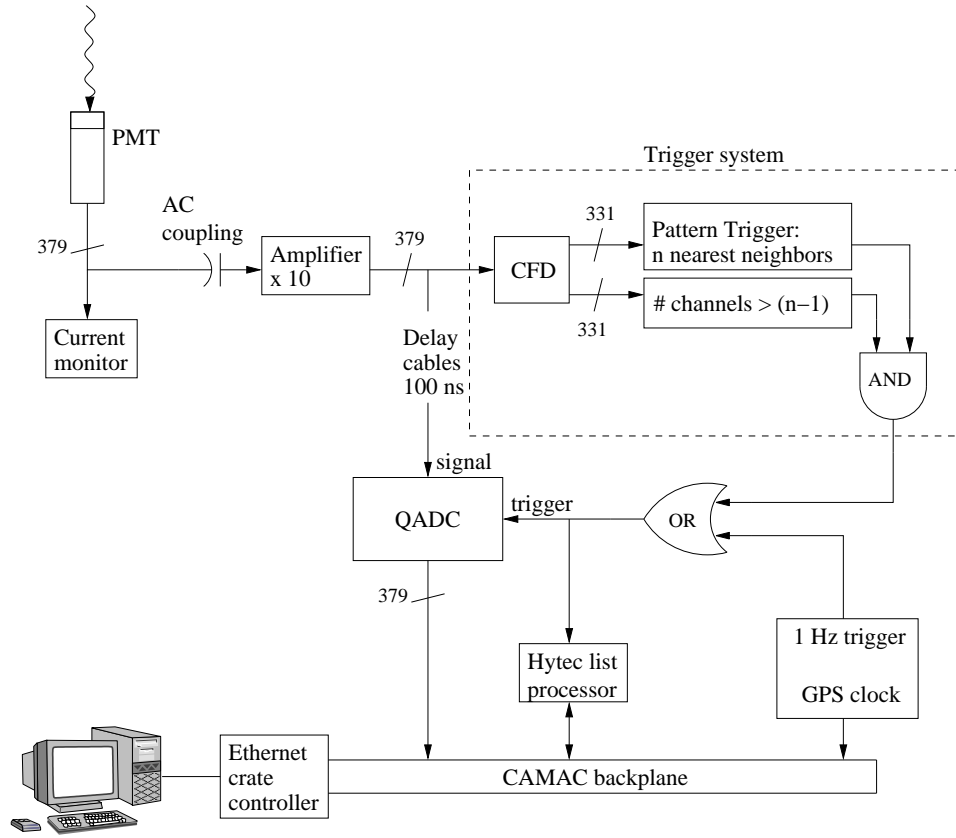
FIGURE 2.3. Schematic of data acquisition system for 379 PMT camera.

been measured but is assumed to be negligible. It is the purpose of the analysis, described in Sect. 2.4, to filter out, or account for, the noise present in the images. Contributions to the total image recorded come from Cherenkov light, S_C, the signal due to the NSB, S_{NSB}, and the signal in the absence of an analog input, i.e. the pedestal level, D:

$$S = S_C + S_{\mathrm{NSB}} + D. \tag{2.1}$$

In the absence of Cherenkov light, fluctuations about the pedestal level occur due to the NSB. Since these sources of light contribute to the final signal independently of each other, the noise is

$$\sigma_S^2 = \sigma_C^2 + \sigma_{\mathrm{NSB}}^2 + \sigma_D^2. \tag{2.2}$$

The electronics noise of the system, σ_D^2, was measured by Kwok (1989) to be 0.5 dc with an approximately Gaussian distribution.

The noise due to the NSB is measured from the variation of pedestal events. These are events for which an artificial trigger opens the QADC gate for the same duration as a normal trigger. The arrival of photons from the NSB can be described by a Poisson process[2] with mean rate α. The probability distribution for k photons to arrive during a time interval, t, is

$$p(k, t) = \frac{e^{-\alpha t}(\alpha t)^k}{k!},\tag{2.3}$$

where the mean and variance are both given by $\lambda = \alpha t$.

This means that the single pe noise rate, and therefore the NSB flux, and can also be estimated from the measured variation of the pedestal level of each PMT. For example, during March 1999 and using 1" PMTs, the average pedestal standard deviation was 4.1 dc. This, together with a conversion of 1.1 dc/pe corresponds to an average of $(4.1/1.1)^2 = 13.9$ pe per PMT per gate width. This estimate neglects the electronics noise, σ_D, and noise in the PMT resulting from the statistical nature of emission from the photocathode and the dynode chain (Engstrom, 1980). The anode noise current is increased by a factor $\sqrt{1 + 1/(\delta - 1)}$, where δ is the secondary emission ratio per dynode. Kwok (1989) determined a factor between 1.3 and 1.5 for the 37 PMT camera, resulting in $\delta = 2.2 - 1.8$. With the newer, and hopefully better, design of PMTs, the factor will be assumed to be 1.3, resulting in $(4.1/(1.1 * 1.3))^2 = 8.2$ pe. Including the gate width of 20 ns, this gives 8.2.e./20 ns = 0.41 pe ns^{-1} = 410 MHz. Estimates of the single photoelectron rate for the VERITAS telescope have been summarized by Ozlem and Ong (2002). In converting these to the Whipple 10 m telescope, the decreased collection area and larger solid angle amount to a factor of $(10/12)^2(12/7)^2 = 1.9$. With this conversion, estimates of the single pe rate are 322 MHz, 506 MHz, 575 MHz (high), and 288 MHz (low), consistent with the estimate obtained here. The night-sky background contributes the largest source of current to the

---

[2]For a Poisson process, the probability for exactly one photon to arrive during a very short time interval, t, is αt.

system.

The 10 m telescope has an effective[3] mirror area of about 69 m^2 where each 1" PMT views $\pi(2.54/730)^2 = 3.8 \times 10^{-5}$ sr of the sky; therefore the mean NSB rate at the telescope site is 1.6×10^{11} pe m^{-2} sr^{-1} s^{-1}. This value changes only slightly when the effect of the lightcones is accounted for. The measured pedestal variance without and with light cones is the same, though the collected amount of Cherenkov light increases. This indicates that the light cones are reducing the stray NSB light from nearby cities and light reflected from the ground, while increasing the solid angle subtended by each PMT.

An order of magnitude estimate of the NSB brightness can also be obtained. Assuming the energy of NSB photons triggering the 10 m is 2 eV and the PMT quantum efficiency is 25%, the brightness expressed in a νF_ν representation is $1.6 \times 10^{11}/0.25 \times 2$ eV $\times q_e = 2.5 \times 10^{-7}$ W m^{-2} sr^{-1}. Fig. 2.4 shows the sky brightness measured above the lower terrestrial atmosphere. At $0.5\,\mu$m, the flux due to zodiacal light and faint stars is about 5×10^{-7} W m^{-2} sr^{-1}, in agreement with the estimate derived here. In the optical, the NSB flux increases rapidly with wavelength (Jelley, 1967); measurements can be found in (Aharonian and Akerlof, 1997). This distribution is fortunate, as the spectrum of Cherenkov radiation increases as λ^{-2}, producing most of the light in the blue part of the spectrum.

To put the NSB in perspective, the amount of Cherenkov light from a 1 TeV gamma ray can be estimated using Fig. 3.1 as 25 photons m^{-2}. At first sight, this would appear to be undetectable; however the pulse is very short, ≈ 3 ns, and the Cherenkov photons are highly focused, $\approx 0.7°$ FWHM. Thus, the flash has a brightness of $\approx 8 \times 10^{13}$ m^{-2} sr^{-1} s^{-1}, or about 1.2×10^{-5} W m^{-2} sr^{-1} assuming Cherenkov photons of energy 2 eV. This is of sufficient brightness to be detected over the background noise. However, at a lower primary gamma-ray energy, the need is highlighted for a trigger that can distinguish between the highly collimated Cherenkov light and random photons from the NSB.

---

[3]This is the net mirror area minus obstructions and a 5% reduction in the overall reflectivity due to weathering.

A different kind of background comes from the Cherenkov light produced by the much more numerous air showers initiated by cosmic ray particles with their secondaries: N, p^+, $e^\pm$, and $\mu^\pm$. Events from these showers amount to about 99% of the data collected. Using selection criteria described in Sect. 2.4, these particles are filtered out with about 99.5% efficiency. At equal primary energy, cosmic rays produce less Cherenkov light than gamma rays on average, because CR showers contain heavier and non-charged particles. However, the CR background is not entirely unwanted; it is used in the calibration of the telescope light throughput, see Sects. 2.3, 3.3.
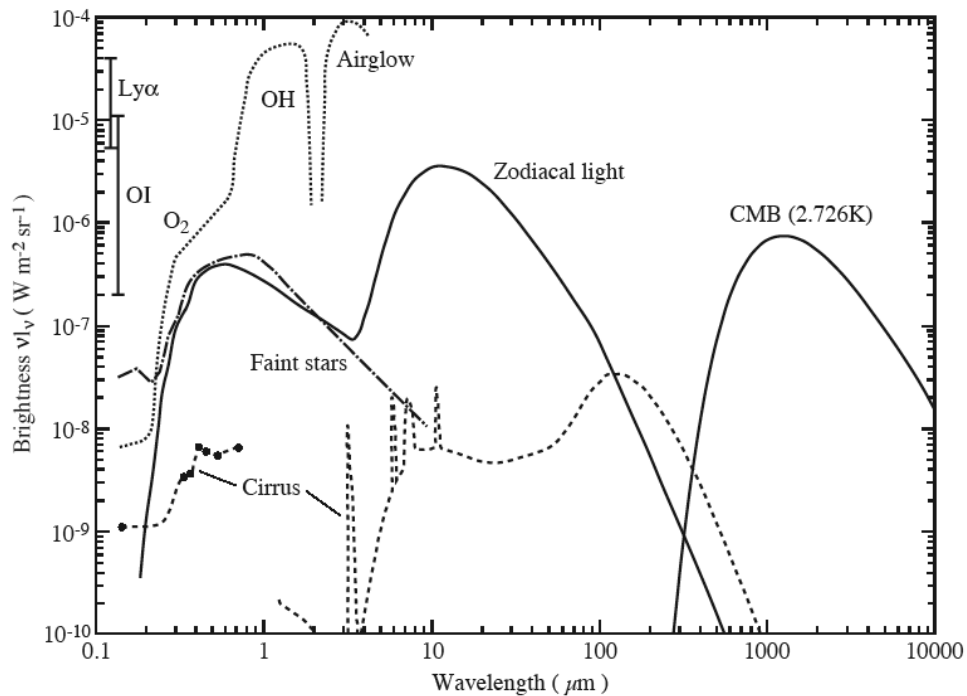
FIGURE 2.4. Overview of the sky brightness above the lower terrestrial atmosphere. Figure taken from Leinert et al. (1998).

2.2.2 Examples of Events

Fig. 2.5 shows the pulse in one PMT when a camera trigger occurred. This event is most likely due to a CR, as it is the main source of background. The intrinsic width of the

Cherenkov light front is about 3-4 ns, much shorter than the measured pulse. The broadening is caused mainly by the PMT characteristic and by the signal cable. The pulse shows a rise time of about 3 ns and a fall time of about 8-10 ns. The rise and fall time are measured for the signal to go between 10% and 90% of the maximum. Also visible is ringing stemming from the capacitive circuit in the PMT socket. To collect most of the light from one pulse, the light integration duration at the QADC is set to 20 ns.
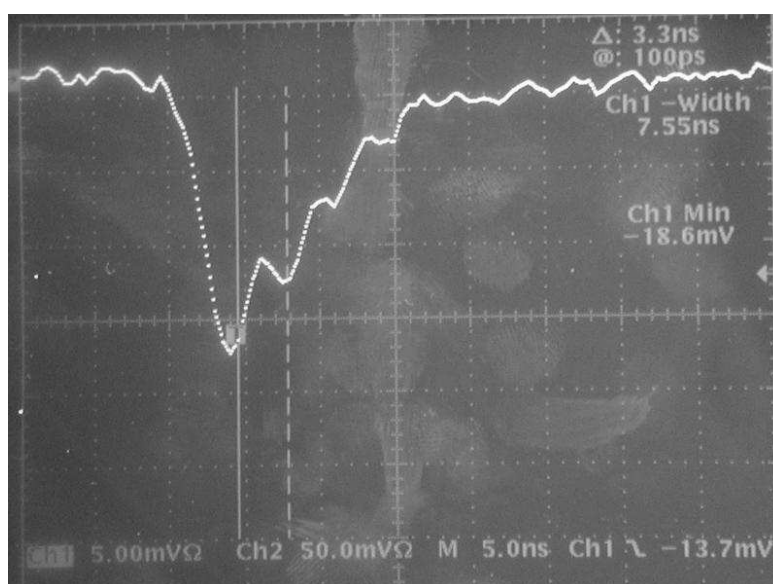
FIGURE 2.5. Example of the pulse in one PMT during a triggering event.

Fig. 2.6 shows the 4 types of events that are recorded by the telescope. At a rate of 1 Hz pedestal events are taken, shown in the *top left*. The average pedestal level calculated over the entire run is subtracted from the other events shown. The scale of the brightest pixel is given in the legend for each image by $max1$, the fraction of the area shaded in each pixel corresponds to the brightness relative to $max1$.

To distinguish genuine Cherenkov light from noise, the signal in a PMT is required to be above a noise level, see Sect. 2.4.1. The threshold is specified in terms of the pedestal variation and depends on the location of the pixel in the shower image. If a pixel is completely surrounded by other triggering PMTs it is called a "picture" threshold; if the PMT

is on the boundary of the shower image it is called a "boundary" threshold. The threshold levels have been optimized for the detection of gamma rays at the levels of 4.25 and 2.25 times the pedestal standard variation, see Sect. 2.4. Slightly different values are employed in the selection of muon events, see Sect. 3.3.2. The coloring in Fig. 2.6 indicate pixels that exceed the picture/boundary thresholds with *black*/*red*.

Also shown for each event is a fitted ellipse that has been calculated from the distribution of pixel values in the image, see Sect. 2.4. The direction of the major axis is shown by a line and indicates the most likely direction from which the shower originated. Unfortunately, with a single telescope it is difficult to break the degeneracy between the two sides from which the shower could have come. It can been done with an $asymmetry$ parameter derived by comparing the location of the geometric and weighted means of the pixel values. However, this procedure is not very efficient because the camera is small and to do better requires stereoscopic observations with at least 2 telescopes or FADCs to measure the arrival time of individual photons.

2.2.3 Trigger System

The purpose of the trigger is to discriminate between events caused by genuine gamma rays and noise or cosmic rays. One key difference between gamma-ray events and events caused by other particles is that gamma-ray images are smaller with a higher photon concentration. In addition, the NSB represents a steady source of noise that must be minimized. The trigger must be activated only when an image is likely not due to noise.

The trigger system, see Fig. 2.3, consists of constant fraction discriminators (CFD) followed by two trigger systems that operate in parallel: a multiplicity trigger and a pattern trigger. The CFD for a PMT triggers when a certain preset fraction of the total pulse height is reached. In this way, the trigger occurs independent of signal amplitude, so that small and large pulses trigger at the same time. If instead a fixed threshold trigger were employed, time jitter would be introduced from larger pulses triggering earlier than small ones. For a
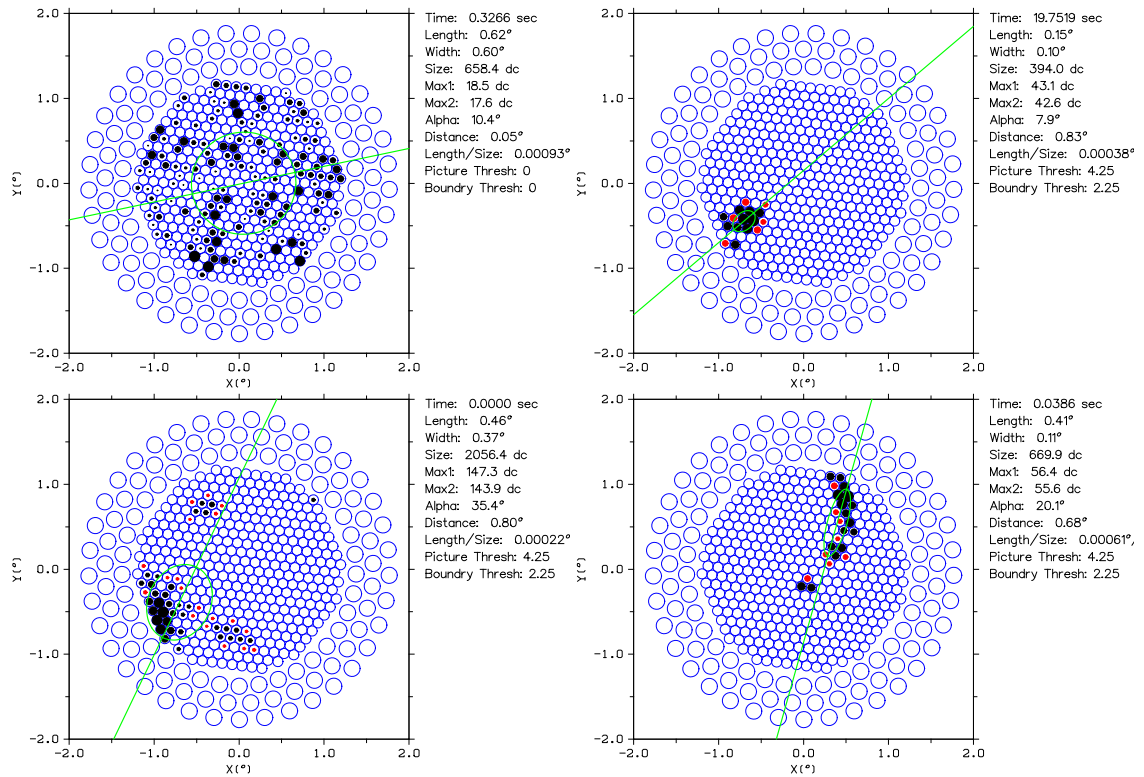
FIGURE 2.6. Examples of events taken with the 490 PMT camera, but only the inner 379 PMTs contain valid data. The light measured by each PMT measured is represented by a filled circle, such that a full circle corresponds to the brightest pixel. The amount of light in the brightest pixel is listed as the $max1$ value in the legend. See text for explanation of the colors used for pixels. The fitted ellipse from the standard analysis and the major axis are shown in *green/light grey*. *Top left*: A pedestal event, no image cleaning is applied to this kind of event, see text. *Top right*: A potential gamma-ray event that passes the $Quicklook$ cuts. *Bottom left*: A cosmic-ray event. *Bottom right*: A truncated muon event that had an impact distance outside the rim of the telescope.

more detailed description of the trigger system, see Bradbury et al. (1999).

The pattern trigger requires n adjacent PMTs above a set threshold. This threshold is set for a reasonable event rate, see Sect. 2.2.4. Gamma-ray showers are more compact than hadronic showers and produce images with light concentrated over fewer PMTs. A pattern trigger is able to increase the ratio of triggers resulting from gamma rays over hadrons. The number of nearest neighbors, n, can be set to 2, 3, or 4-fold coincidence. In the 490 PMT camera, the pattern trigger has been operated almost exclusively in 3-fold coincidence mode. One draw-back of the pattern trigger is that the timing information becomes blurred through the complex hardware in the trigger module. Therefore, a simple multiplicity trigger set to n-1 threshold is used in coincidence with the pattern trigger to provide the exact timing information for the QADC gates to opened.

NSB noise is strongly suppressed by the pattern trigger; this allows the energy threshold of the telescope to be lowered. Fluctuations in the NSB randomly raise PMTs above a fixed threshold across the field of view. At any given time, n-nearest neighbors must be above threshold for a trigger decision to be positive. For the 331 camera, the 3-fold pattern trigger reduces the accidental trigger rate over a simple 3-fold multiplicity trigger by $(215 \times 6 \times 5 + 55 \times 5 \times 4 + 61 \times 4 \times 3)/(331 \times 330 \times 329) \approx 1/4300$. The numerator counts the number of 3 nearest-neighbor combinations. This is done by adding up the nearest-neighbor combinations with 2 rings of neighbors, then those with only 1 ring on the outside, and lastly PMTs on the outer most ring of the trigger region. However, this over counts by 3! permutations because the firing order of the PMTs does not matter. The denominator counts the number of possible combinations of choosing 3 out of 331 PMTs, again over counting by 3!

Another cause of noise that is strongly suppressed by the 3-fold pattern trigger is after-pulsing in the PMT (Bradbury et al., 1999). Afterpulsing can result from a light feedback from the anode to the photocathode. The time scale for this is the transit time of the PMT, about 10 ns. Another type of afterpulsing results from the ionization of gas in the region between the cathode and the first dynode. The ions may strike the photocathode after a

while and produce secondary current equivalent to several pe (Engstrom, 1980).

2.2.4   Rates and Bias Curves

The CFD modules determine what voltage level from a PMT constitutes a real signal to be sent on to the trigger logic. For a uniform response of the camera, the same level is set for all PMTs. This requires that the PMT gain are approximately equal; a calibration is done on a yearly basis. The trigger rate is limited by the read/write speed of the computer to a maximum rate of about 30 Hz. As the reference level sets the minimum amount of light that is considered a genuine signal, it also determines the minimum energy necessary for gamma rays to cause a trigger. It is therefore necessary to set the trigger level high enough so that the computer can keep up, yet as low as possible to achieve a low energy threshold for the detection of gamma rays.

To determine the appropriate CFD threshold level, the telescope is pointed at zenith during a moonless night and the trigger rate is measured while varying the CFD threshold. In this way, the bias curve shown in Fig. 2.7 was measured on 25 June 2003. The graph shows the rate from the multiplicity trigger, set at 2-fold coincidence, and the rate of the pattern trigger, set at 3-fold near neighbor. Aside from the increase of 2-fold to 3-fold coincidence, the pattern trigger reduces the noise to a lower level. At low thresholds, the trigger is due mostly to the NSB as well as some local muons and electrons. Though the NSB noise dominates greatly at low thresholds, its spectrum is steeply falling and is surpassed at around 24 mV by cosmic rays that have a harder spectrum. This is the threshold level that one would set the trigger at. The integral slope of -1.3±0.3 in the CR-dominated region above 24 mV is remarkably close to the known CR proton spectral index of -1.7. The trigger rate decreases at lower elevations because of absorption in the atmosphere; see Sect. 2.3 for more detail on the CR spectrum measured with the 10 m under different conditions.

The horizontal axis in Fig. 2.7 is in units of mV which and is approximately linearly proportional to energy. The exact conversion to energy units requires Monte-Carlo simula-
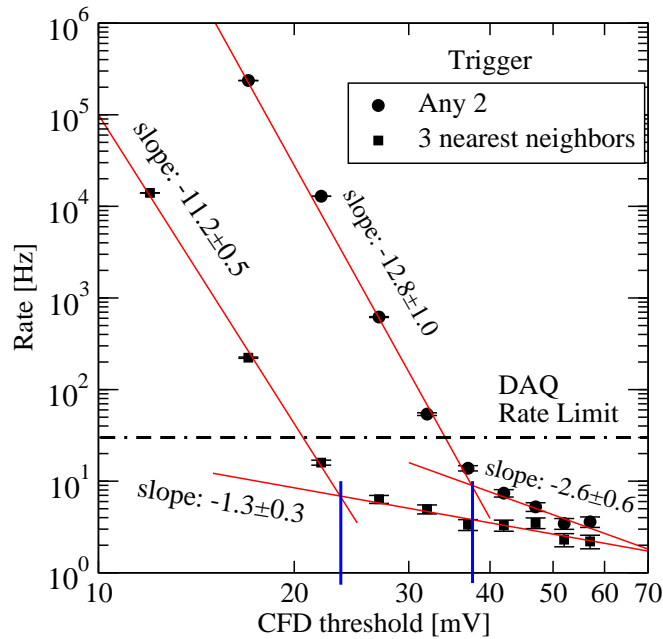
FIGURE 2.7. Trigger rate versus hardware threshold with 2-fold multiplicity trigger (*circles*) and with 3-fold nearest-neighbor trigger (*squares*). The integral power law slope is indicated for the NSB-dominated trigger region and the CR-dominated region. The trigger level would be set at the intercept of the power law fits; indicated by *blue* vertical lines, at 24 mV for pattern trigger and 38 mV for 2-fold multiplicity trigger.

tions of cosmic-ray showers. As a simpler first step, the conversion from photoelectrons to mV can be worked out from Fig. 2.8. The voltage corresponding to 1 pe is

$$V = I\,R = \frac{1\ \text{pe}}{8 \times 10^{-9}\ \text{s}} \times \frac{g\ \text{e}^-}{1\ \text{pe}} \times \frac{1.6 \times 10^{-19}\text{C}}{1\ \text{e}^-} \times 50\ \Omega \times A. \qquad (2.4)$$

This assumes a single pe pulse width of 8 ns. The dc signal from 1 pe is given by

$$1\ \text{pe} \times \frac{g\ \text{e}^-}{1\ \text{pe}} \times \frac{1.6 \times 10^{-19}\text{C}}{1\ \text{e}^-} \times A \times \frac{1\ \text{dc}}{0.25\ \text{pC}}. \qquad (2.5)$$

The combined amplifier gain, cable and signal splitter loss, A, has been measured periodically; it was 3.04 in 1995/6 and 4.68 in 2000 (Le Bohec, 2002). The PMT gain, g in e^- per pe, for the 1995 camera configuration was 0.54×10^6, derived from the 1.05 dc/pe ratio determined of Mohanty et al. (1998), and 1.1×10^6 in 2000/1, (Krennrich et al., 1999). The corresponding conversion factors are listed in Tab. 2.1.

Year	mV/pe	dc/pe
1995/6	1.6	1.05±0.10
2000/1	5.1	3.3±0.3

TABLE 2.1. Conversion factors between the analog and digital signals during the 1995/6 and 2000/1 observing season.

In going from the 1" PMTs of the 1995 camera to the 1/2" PMTs used from 2000 onwards, the gain was increased to achieve roughly the same energy threshold per PMT while the photocathode area decreased by roughly a factor of 4. A detailed study of the conversion between photons received by the telescope and the measured dc is given in Sect. 3.3 using cosmic-ray muons.
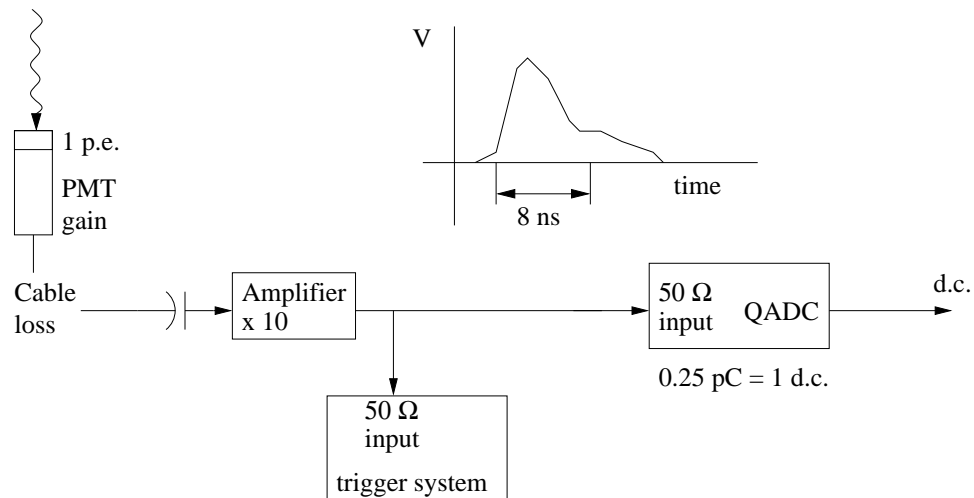
FIGURE 2.8. Diagram of the conversion of a photoelectron (pe) to the digital count (dc) output. The combined amplifier gain and cable loss was measured for the 1995 and 2000 configurations (Le Bohec, 2002).

2.3   Cosmic Ray Rate

The cosmic rays originate from outside the solar system and represent a steady flux[4]. Cosmic rays are composed of about 95% hydrogen (protons) and about 4% He. The energy spectrum of protons falls as a power law with differential index -2.7 in the energy range of the 10 m telescope. The production of Cherenkov light by showers initiated by gamma rays and cosmic rays is very similar, though essential differences exist that make a separation between the two particle types possible. Cosmic rays tend to produce a more fragmented shower with muons that easily penetrate to ground level. This means that the average depth of Cherenkov light emission is lower for protons than for gamma rays. Also, the wavefront of arriving Cherenkov photons tends to be wider. In spite of these differences, the CR background is still the closest to a calibrated beam of particles available to IACTs. The Cherenkov light produced by cosmic rays is therefore used as a calibration tool to measure the relative performance of the telescope and to measure changes in the atmospheric conditions.

Other ways to monitor the night-sky are through extinction measurements with optical telescopes, infrared radiometers to detect heat emitting from water vapor and clouds in the atmosphere, LIDAR observations to measure the distribution of pollutants in the atmosphere, and radiosonde balloons that measure atmospheric variations with altitude. Further details are given elsewhere, see for example Bernlohr (2000). All these methods have the drawback that they do not give a clear indication of how much changed conditions effect Cherenkov observations without detailed modeling. For example, a thin cirrus cloud at 20 km altitude may well be detrimental to an optical telescope, but the Cherenkov light reaching ground level originates from about 5 - 10 km altitude and is thus not effected by such clouds.

As the spectrum of high energy cosmic-rays incident on the top of the atmosphere is constant, any changes in the measured CR spectrum are a result of changes in the atmo-

---

[4]At energies below 10 GeV modulations can occur from the solar wind.

spheric absorption and/or by changes in the telescope. The cosmic ray spectrum measured by a Cherenkov telescope depends on the elevation of clouds and dust in the line of sight. If absorption occurs only close to the telescope, e.g. < 1 km, the entire CR spectrum is attenuated uniformly. A general attenuation can also be caused by telescope efficiency, caused for example by the PMTs or by degradation of mirrors. Thus, it is hard to determine exactly which parts of the telescope cause the change. However, if clouds are localized to high elevations above 10 km, low energy events that emit most Cherenkov light at those altitudes are suppressed relative to high energy CR particles.

To derive the energy calibration of the CR spectrum requires extensive Monte-Carlo simulation and the needed energy resolution is difficult to achieve with a single telescope. For a relative measurement, this is not needed and instead a simpler approach is taken here with the definition of a single factor that measures the light throughput with respect to a reference run. This "throughput" factor is a relative measure of the cosmic ray spectrum (Lebohec and Holder, 2003). It is defined as the ratio of the measured cosmic ray flux to some reference observation. Taking the power-law CR spectrum as

$$N(s) = \frac{\mathrm{d}N}{\mathrm{d}s} = (s/s_0)^{-\alpha},\tag{2.6}$$

where s denotes the brightness of Cherenkov images, $size$. It is this brightness that changes due to the atmosphere, the observing elevation, and the telescope performance. Let the reference spectrum be denoted by N_r, then the throughput factor, t, is defined by

$$N_R(s) \stackrel{!}{=} N(t\,s).\tag{2.7}$$

This means that for the size spectrum measured on a particular night to agree with the reference spectrum, an adjustment needs to be made in the $size$ scale:

$$(\frac{s}{s_R})^{-\alpha} = (\frac{t\,s}{s_0})^{-\alpha}.\tag{2.8}$$

So that the throughput is defined by

$$t = \frac{s_0}{s_R}.\tag{2.9}$$

For example, if measured images are brighter than those in the reference run, then t is a number > 1.

Unfortunately, this method cannot be implemented exactly as it is described here, because the measured $size$ spectrum is not a pure power law due to the telescope trigger and the limited FOV Instead, a χ^2-minimization routine is used to find the best fit between the reference spectrum and the measured spectrum that has the $size$ scale multiplied by t. Only the region well above the threshold is included in this fit. This is implemented by binning the $size$ spectrum linearly between 200 dc and 7000 dc in steps of 170 dc. Then, to avoid the trigger region the χ^2 difference between the counts in the run and the reference is calculated between 6 bins above the maximum, usually 1000 dc, up to a maximum of 6000 dc.

Fig. 2.9 shows the $size$ spectrum of the commonly used reference run gt016531 taken at 70° elevation in "A" weather. Also shown is a run taken at 45° elevation with a throughput factor of 0.69±0.04.
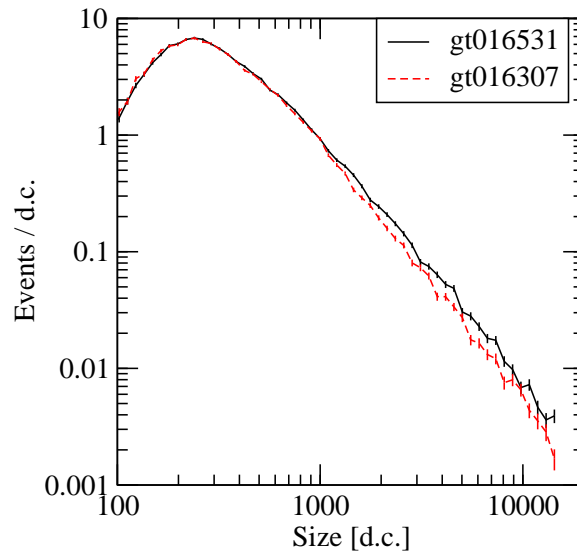
FIGURE 2.9. Measured cosmic-ray $size$ spectrum of two observations taken in the year 2000. The data labeled gt016531 is the reference run. The cosmic-ray rate of events with $size > 1000$ dc in the run gt016307 is 0.69±0.04 relative to the reference run.

2.4   Analysis Method

The imaging technique allows gamma rays to be preferentially selected out of the much larger CR background. Several techniques have been developed to process the images and reject them if they are not deemed to be caused by gamma rays. Typically, there are three steps involved in the analysis: (1) determine which pixels contain genuine signal, (2) parameterization the image, and (3) cosmic-ray discrimination.

Cleaning the image from noisy pixels has been tried using picture/boundary thresholds (Punch et al., 1991), island cleaning (Bond et al., 2003), and with wavelets(Lessard et al., 2002). Wavelet cleaning has improved sensitivity to low energy events compared to the standard 10 m analysis.

The parameterization of the shower images has been done with first, second, and third order moments, see for example (Hillas, 1985a). A different approach combining wavelets and fractals has been tried as well (Haungs et al., 1999).

For selection of gamma rays and rejection of the cosmic-ray background, usually selection criteria are applied to the parameters. These criteria are derived either empirically through optimization of the signal from the Crab Nebula or through guidance from Monte-Carlo simulations. This method is relatively easy to implement. Neural networks have also been used in the gamma/hadron separation (Reynolds and Fegan, 1995). Initially, the results were somewhat disappointing, but advances in computer speed have shown that with more parameters as input, neural nets can give greatly enhanced background rejection.

A different approach was taken by Le Bohec et al. (1998) where shower images are fitted to simulated shower profiles and the selection and energy estimate is done simultaneously. The method was applied to the CAT telescope with very good results. However, a draw-back is that the calibration of the shower profiles requires accurate Monte-Carlo simulations.

The standard method used in the analysis of data from the 10 m telescope is described below. It has been consistently successful and is the easiest to use, but new methods (neural

nets and picture look-up tables) show increased background suppression by up to a factor of two.

2.4.1 Cleaning and Flat Fielding

Pixels containing mostly noise are removed from the image by applying two sets of threshold cuts based on their signal-to-noise ratio. The noise is measured for each pixel, i, from the standard deviation, σ_i, of the signal in pedestal events. Also, at this point the mean pedestal value, ped_i, is determined and subtracted from all pixels. In the pedestal calculation pixels are required to contain a signal, s_i, less than 74 dc because it is possible that a cosmic ray coincided accidentally while a pedestal trigger occurred[5]. Only pixels that fulfill either of the following two criteria are selected as belonging to the event:

1. $s_i - ped_i > 4.25\sigma_i$, called an "image" pixel,

2. $s_i - ped_i > 2.25\sigma_i$ and it is the nearest neighbor of an image pixel; referred to as a "boundary" pixel.

All other pixels are ignored. Optimization of these thresholds was originally done a-posteriori on the gamma-ray signal from the Crab Nebula. Following the installation of a new camera, a re-optimization of these cuts was carried out. No significant difference in the thresholds has been found and they have remained the same.

In addition, PMTs are ignored if their pedestal standard deviation is less than 0.6 or more than 1.5 times of the median value. The median is calculated only for those PMTs with 0.6 dc $< \sigma_i <$ 200 dc. This procedure eliminates PMTs that were receiving excessive star light or had their HV turned off during the run to avoid light damage.

The gain of a PMT depends strongly on the supplied high voltage (HV); typically, a 1% change in HV causes a 10% change in gain. The HV for all PMTs is adjusted on a yearly basis so as to produce a uniform gain across the camera. To account for small HV changes

---

[5]All numeric values are specific to the 10 m telescope/DAQ system and have been derived empirically.

over time, the camera is illuminated uniformly with a Nitrogen flash light on a nightly basis. The bright light from the flasher triggers the DAQ to record the events. The gain of each PMT, g_i, is calculated relative to the mean brightness of each event for all PMTs that have a raw signal of less than 1024 dc, the maximum value of the QADC, and $s - ped > 50$ dc. The former restriction eliminates "hot" pixels, the latter dead pixels. PMTs are ignored completely in all events if the average gain is outside a reasonable range: $0.1 < \langle g_i \rangle < 3.5$. After turning off these PMTs, the average gain for the remaining PMTs is renormalized back to 1. The same gain correction, including the elimination of pixels, is applied to all data taken during the night.

After pedestal subtraction and flat fielding, the signal of PMTs that pass the cleaning thresholds is $v_i = (s_i - ped_i)g_i$.

2.4.2 Noise Equalization

Because images are cleaned relative to their NSB noise level, the energy threshold of each PMT depends on the sky brightness seen by it. The different cleaning thresholds also effects the selection of image pixels and can distort the Cherenkov image. In an ON/OFF analysis, a bias may occur if one region of sky is brighter than the other, because fewer events pass the cleaning thresholds in the brighter region.

To eliminate this bias, a software algorithm has been developed that injects additional noise into each image before the analysis stage (Cawley, 1993). This deteriorates the image, but eliminates bias. The noise is drawn from a Gaussian distribution and injected only into the darker pixel of the ON or OFF run.

In the analysis of Monte-Carlo simulations noise adding is performed as well. Monte-Carlo simulations are produced with a minimal amount NSB and electronics noise to make them more generally usable. After noise addition, the measured NSB fluctuations are reproduced in the simulation.

2.4.3 Parameterization

After image cleaning, flat fielding, and adding noise, images parameters are calculated that describe the shape, orientation, and brightness (Hillas, 1985a; Reynolds et al., 1993). The parameters describing the geometry are calculated from the first and second order moments of the light distribution, shown in Fig. 2.10. Parameters characterizing the brightness are the total amount of light in the image, $size$, and the three brightest pixels, $max1, 2, 3$.
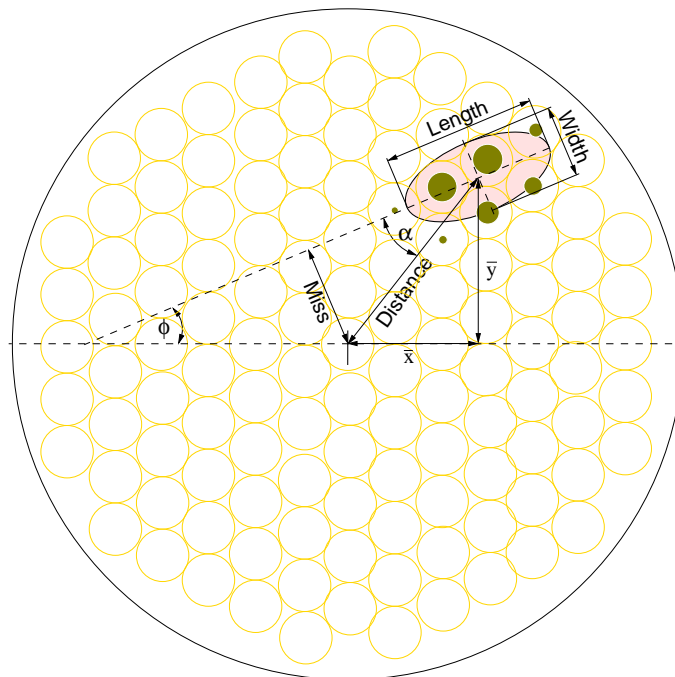
FIGURE 2.10. Illustration of an air shower event imaged by the telescope on the camera. The outline of a generic closed-packed PMT camera is shown in the background with the Cherenkov signal represented by filled circles. The shower image is elliptical and its orientation towards the center of the camera is labeled by α ($alpha$).

2.4.4 Calculation of the Gamma-Ray Rate

The evaluation of the gamma-ray rate consists of the following steps:

1. For ON/OFF pairs, trim the file length to equal lifetimes.

Parameter	$Supercuts1995$	$Supercuts2000$
$width$	0.073°... 0.15°	0.05°... 0.12°
$length$	0.16°... 0.30°	0.13°... 0.25°
$distance$	0.51°... 1.1°	0.40°... 1.0°
$alpha$	<15°	<15°
$length/size$	——	<0.0004°/dc
$size$	>400 dc	——
$max1$	>100 dc	>30 dc
$max2$	>80 dc	>30 dc
$max3$	——	>20 dc
Pict. threshold	4.25 σ	4.25 σ
Bndr. threshold	2.25 σ	2.25 σ

TABLE 2.2. Two set of selection criteria, called cuts, used to reject the CR background. The cuts were optimized on the gamma-ray signal from the Crab Nebula for the observing seasons 1995/6 and 2000/1.

2. Apply cuts to reject background.

3. Evaluate rate and significance.

Selection criteria, called cuts, are used to reject cosmic ray events while retaining gamma-ray showers. The criteria are listed in Tab. 2.2 for two periods of operation. The cuts were optimized empirically with data taken on the Crab Nebula to maximize significance of the detection and the gamma-ray rate Reynolds et al. (1993). The $Supercuts1995$ were used with the 109 pixel camera, while $Supercuts2000$ has been used for all periods of observation with the 490 pixel camera. The application of the cuts rejects approximately 99.5% of the cosmic rays. About 60% of gamma-rays pass the geometrical cuts alone, a significant fraction of small $size$ events is eliminated by the cuts on $size$, $max1, 2, 3$ and $length/size$.

After application of the cuts, the gamma-ray rate is evaluated. If observations are taken in the ON/OFF mode, the significance S of the signal, is evaluated from the ratio of source counts N_S to the noise, i.e. the fluctuation σ_{N_S}. This is similar to the signal-to-noise ratio. In the following, N_{ON} and N_{OFF} denote the number of counts in the ON and OFF runs after

all cuts have been applied to the data. Then

$$N_S = N_{\mathrm{ON}} - N_{\mathrm{OFF}} \tag{2.10}$$

and applying error propagation

$$\sigma^2_{N_S} = \sigma^2_{N_{\mathrm{ON}}} + \sigma^2_{N_{\mathrm{OFF}}}. \tag{2.11}$$

Assuming a Poisson distribution for the number of counts received from a steady source

$$S = \frac{N_{\mathrm{ON}} - N_{\mathrm{OFF}}}{\sqrt{N_{\mathrm{ON}} + N_{\mathrm{OFF}}}}. \tag{2.12}$$

Fig. 2.11 shows the distribution of the $alpha$ angle after application of all other cuts for some 2000/1 Crab data. The relatively flat distribution of $alpha$ in the OFF run shows that the background is isotropically distributed, while the ON run shows an excess of events originating from the source located at the center of the camera.
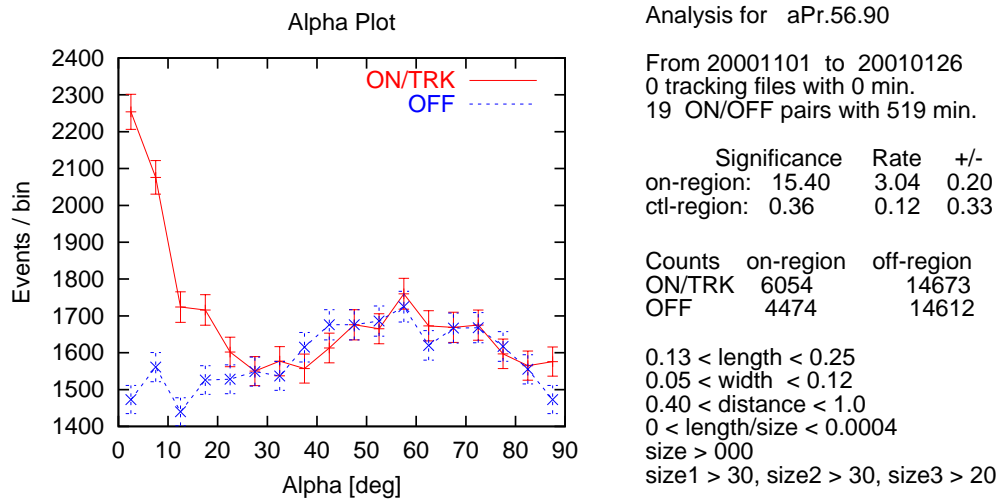
FIGURE 2.11. Distribution of $alpha$ angle for the events in 19 ON/OFF pairs taken on the Crab Nebula in 2000/1. The gamma-ray rate [min^{-1}] together with the significance are displayed for the on-source region $alpha < 15°$, as well as for the control region defined by $20° < alpha < 65°$.

In the case of TRK observations, the expected background count N_{OFF} must be determined differently. For this purpose, OFF source observations with similar elevation and

telescope conditions are used in defining a ratio, ρ, of the number of events in the *source-region* $0° < alpha < 15°$, $M_{\mathrm{src}}(\mathrm{OFF})$, to those in a control region $20° < alpha < 65°$, $M_{\mathrm{ctl}}(\mathrm{OFF})$, with $\sigma_\rho = \rho\sqrt{M_{\mathrm{src}}^{-1}(\mathrm{OFF}) + M_{\mathrm{ctl}}^{-1}(\mathrm{OFF})}$. It is important that the ratio t is calculated from a large number of OFF runs so that the resulting uncertainty in the background estimate is small. The expected background count for a TRK run is given by

$$N_{\mathrm{OFF}} = t\, M_{\mathrm{ctl}}(\mathrm{TRK}), \tag{2.13}$$

$M_{\mathrm{ctl}}(\mathrm{TRK})$ is the number of counts in the control region of the TRK run. The number of signal events is then evaluated similarly as before:

$$N_S = M_{\mathrm{src}}(\mathrm{TRK}) - t\, M_{\mathrm{ctl}}(\mathrm{TRK}) \tag{2.14}$$

and applying error propagation

$$\sigma_{N_S}^2 = \sigma_{M_{\mathrm{src}}}^2 + r^2 \sigma_{M_{\mathrm{ctl}}}^2 + M_{\mathrm{ctl}}^2\, \sigma_t^2, \tag{2.15}$$

where (TRK) has been suppressed for clarity and the significance is given by

$$S = \frac{M_{\mathrm{src}} - t\, M_{\mathrm{ctl}}}{\sqrt{M_{\mathrm{src}} + \rho^2 M_{\mathrm{ctl}} + M_{\mathrm{ctl}}^2\, \sigma_t^2}}. \tag{2.16}$$

There has been some discussion in the literature as to how to correctly calculate the significance when the background count has been scaled. Li and Ma (1983) find that Eq. 2.16 slightly underestimates the true significance when $t < 1$; $t \approx 1/3$ for 10 m data. The correct calculation using the log-likelihood method cannot be done analytically when the tracking ratio has uncertainty, and is therefore difficult to handle in practice.

CHAPTER 3

SPECTRAL ANALYSIS

The measurement of VHE gamma-ray spectra with imaging atmospheric Cherenkov telescopes (IACT) is possible because the Cherenkov light is a good calorimetric component of atmospheric particle showers. IACTs have wide dynamic range between about 50 GeV to 100 TeV; this is limited at low energies by secondary electrons from cosmic rays and at the high end by the low flux of gamma rays received. In principle, the spectrum of other particle types, such as protons and muons, could also be measured, but with a single telescope the energy determination of showers initiated by nuclei is difficult.

The task of measuring gamma-ray spectra with a Cherenkov light imaging telescope can be separated into three parts:

- Generate Monte-Carlo simulations of gamma-ray showers that are as close to the observing conditions as possible, see Sect. 3.1.

- Process the ON, OFF, and simulated (SIM) data in the same way, including sky brightness addition and parameterization, see Sect. 2.4.

- Estimate the gamma-ray spectrum through comparison of the ON-OFF data with simulations, see Sect. 3.2.

3.1   Simulations

Computer simulations are used to predict the response of an Imaging Air Cherenkov Telescope (IACT) to the Cherenkov light produced by VHE gamma-ray air showers. The simulation is split into three sequential components

1. Production of an atmospheric particle shower from a VHE gamma ray.

2. Cherenkov light emission by the charged particles and tracing the emitted light to the telescope.

3. Optical and electronic processing by the telescope.

In this work, a set of simulations typically consists of 500,000 gamma-ray showers with energies chosen randomly from a power law spectrum. The calculations were carried out on a 20-node Beowulf cluster at Iowa State University. The computation time is about 5 days during which about 130 MB of final pixel-level data is produced. Intermediate data of particle showers and Cherenkov photons are discarded.

3.1.1   Particle Shower Production

Simulations are an essential tool to study the interaction of cosmic and gamma rays with particles in the atmosphere. These air shower simulation programs use, and in some cases extrapolate far beyond, the available measurements of cross-section to create secondary particles from the primary cosmic or gamma ray. These secondaries, in turn, are propagated through the atmosphere where they may participate in any number of interactions; bremsstrahlung, pair production, multiple Coulomb scattering, and ionization losses are some of the more common ones for gamma-ray primaries. Typically, 500,000 showers are simulated.

Some air shower simulation programs in use today in the field of IACTs are KASCADE (Kertzman and Sembroski, 1994), CORSIKA (Heck et al., 1998), and MOCCA (Hillas, 1985b). The level of sophistication, especially for hadronic interactions, and execution speed, varies greatly between these. The cross sections for the interactions of gamma rays have been measured up to center-of-momentum energies of 200 GeV only, but QED is much better understood than QCD and not much is left open to extrapolation. For gamma-ray simulations, particles in the shower are tracked until they fall below the threshold for production of Cherenkov light.

Here, Monte-Carlo simulations of particle showers are carried using the two versions of the KASCADE code. The original version, referred to as $kascade3$, has been used by Mohanty et al. (1998). A slightly modified version, $kascade7$, is available as part of the Grinnel-ISU package (GrISU, 2004) but has not seen a detailed comparison to the previous version until this work. The main changes are in updated bremsstrahlung and pair production routines, and adjustment of the Earth's magnetic field vector. Through simulations of 1 TeV gamma rays, incident vertically 50 m from the telescope, it was found that the first two changes decrease the Cherenkov light received by 9% each, while the change in the magnetic field decreases the intensity by 5%.

In the spectral analysis, described in Sect. 3.2.4, the primary gamma-ray energy is reconstructed from the amount of light received and the impact distance of the shower. The simulated gamma rays are used to calibrate this dependence; a decrease in the calculated shower intensity means that measured gamma rays will be reconstructed with a higher energy. As the magnetic field effects the lateral distribution of Cherenkov photons, a simple scaling cannot be derived by looking at one energy and impact distance only.

3.1.2 Cherenkov Light Production

Cherenkov light is emitted from charged particles traveling faster than the speed of light in the medium. In the simulation, Cherenkov photons are produced from the shower particle tracks according to Eq. 3.6. The Cherenkov light production code has essentially remained the same since 1995, with the addition of photon emission timing in the GrISU code.

The number of photons detected by a Cherenkov telescope varies with the distance from the shower core. This lateral distribution can be mapped out by placing the telescope at increasingly larger radial distance, the impact distance, from the shower core. The impact distance is measured in a plane perpendicular to the telescope axis, and should not be confused with the angular $distance$ parameter derived from shower images. Fig. 3.1 shows that the Cherenkov photon density on the ground is a function of zenith angle. For vertically

incident gamma-rays, a significant amount of Cherenkov light is received out to about 120 m; this distance increases with increasing zenith angle because the shower is further away and spreads over a larger area. Simulations were carried out with both, $kascade3$ and $kascade7$, the later producing about 30% less Cherenkov light on the ground independent of elevation.
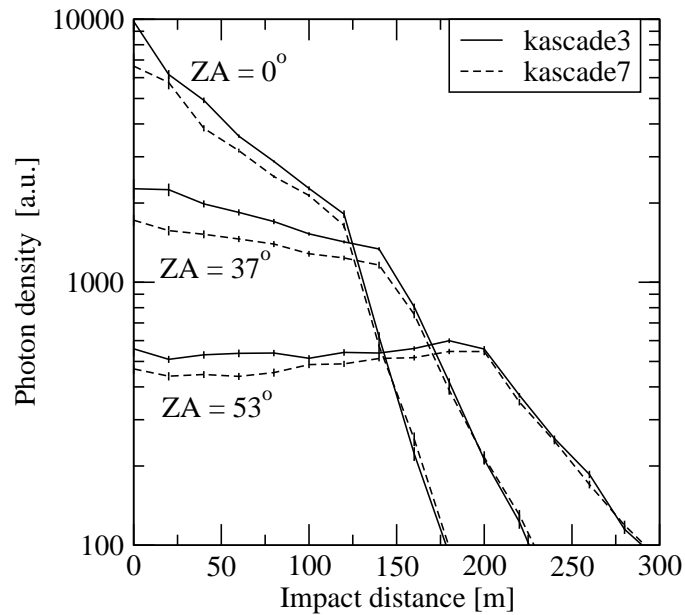
FIGURE 3.1. Lateral distribution of the Cherenkov light recorded by the 10 m telescope from simulated 1 TeV gamma-ray primaries. The vertical axis is in units of dc recorded by the 10 m telescope. The Cherenkov photon density is approximately 1 dc = 0.023 photons m^{-2}. Simulations were carried out with $kascade3$ (*solid lines*) and $kascade7$ (*dashed lines*).

Another factor influencing the number of detected Cherenkov photons is the field of view (FOV) of the camera. Cherenkov photons are emitted at high elevations with a very low Cherenkov angle, $\approx 0.8°$, while at sea level the emission angle is about $1.4°$. With increasing gamma-ray energy, the shower develops further down in the atmosphere and hence Cherenkov photons are imaged further out in the FOV. Fixing at one energy, Fig. 3.2 shows the increase in the number of collected photons with a larger FOV.
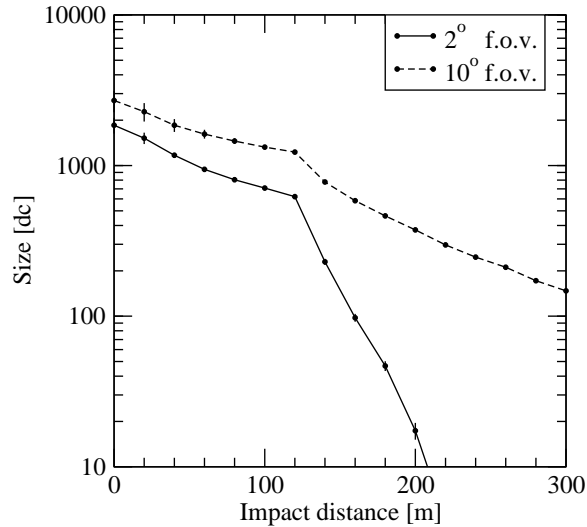
FIGURE 3.2. Lateral distribution of the Cherenkov light recorded by the 10 m telescope with a 2° (*solid line*) and 10° (*dashed line*) field of view. Gamma-ray showers were simulated with primary energy of 0.3 TeV using $kascade3$. The vertical axis is in units of dc recorded by the 10 m telescope. The Cherenkov photon density is approximately 1 dc = 0.023 photons m^{-2}.

3.1.3 Telescope

The model of the telescope in the GrISU simulation consists of ray tracing the Cherenkov photons to the front of the PMT, followed by production and propagation of photoelectrons through the analog/digital electronics chain. The optics are modeled precisely up to the light cones, which are simply represented by an effective increase in the photosensitive area of the PMT cathode. The electronics is modeled at the single photoelectron level, including a multiplicity trigger with a coincidence time window set at the actual width of 40 ns. The simulated trigger does not, however, include a pattern trigger installed in the telescope in 1999. As the pattern trigger mostly suppresses NSB and coincidences due to afterpulsing in the PMTs, this would seem at first not be effect the simulation much. However, close to the trigger threshold the simulations are necessarily inaccurate in triggering on low energy events and a minimum $size$ is imposed to eliminate events in this uncertain trigger region. With the cuts used in the analysis, this effects the trigger rate by less than

Pair	Elevation	Throughput	Rate [min^{-1}]	Bkg. Rate [min^{-1}]
5106/4969	82°/81°	0.91/0.91 ±0.07	5.57 ± 0.51	−0.07 ± 0.30
5108/4982	75°/75°	0.87/0.88 ±0.06	9.47 ± 0.62	0.54 ± 0.38
5109/4988	70°/70°	0.86/0.87 ±0.07	11.45 ± 0.68	0.32 ± 0.37
5110/5144	64°/66°	0.80/0.80 ±0.08	14.01 ± 0.74	0.58 ± 0.42
5111/5237	60°/57°	0.78/0.71 ±0.08	14.97 ± 1.64	−0.18 ± 1.15

TABLE 3.1. Flare data of Mrk 421 on 7 May 1996.

1%. In the conversion of photoelectrons to digital counts, a calibration constant is needed; it can be measured directly by inspection of the electronics or by indirect measurements, see Sect. 3.3.

The telescope simulation used by Mohanty et al. (1998) did not perform ray tracing or photon arrival timing in the trigger decision. Instead, the telescope was modeled with a 10 m aperture and the arrival direction was convoluted with a Gaussian point spread function. All photons were counted as belonging to the shower. As nice as this simplicity is, for an array of telescope operating in parallel, such as the future VERITAS array, photon timing is important in making a trigger decision. Though only a single 10 m telescope is used for the measurement, the new, more complete, GrISU detector code is used for this work.

3.1.4 Comparison of Gamma-Ray Simulations with a Strong Flare of Mrk 421

The purest sample of gamma rays measured to date with the 10 m telescope comes from a flare of Mrk 421 observed on May 7, 1996 (Gaidos et al., 1996). At its peak the flux was up to ten times brighter than the Crab Nebula. This data set is used here in a comparison with simulated gamma rays. Simulated gamma rays should produce image parameters similar to those measured from real gamma rays.

The Mrk 421 flare data consist only of TRK data, OFF runs were selected based on similarity in elevation, throughput, and number of events that pass $Quicklook$ cuts in the off-region, $20 < alpha < 65$. A summary of the data is given in Tab. 3.1, the lightcurve is shown in Fig. 3.3.
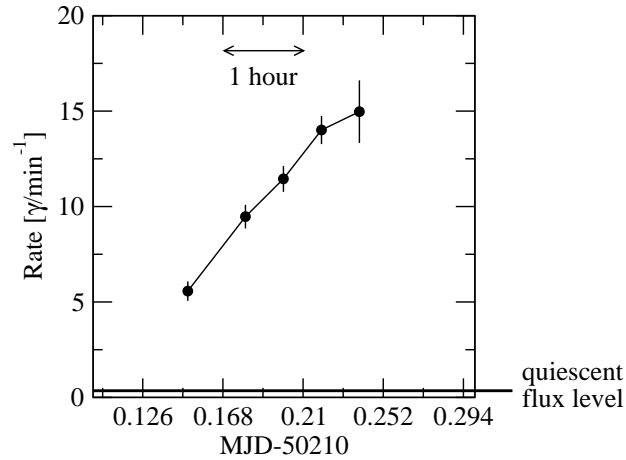
FIGURE 3.3. Gamma-ray lightcurve of Mrk 421 on 7 May 1996. The quiescent flux level, shown by a *thick line*, is about 0.1-0.3 gamma/min (Gaidos et al., 1996).

Histograms of several image parameters are shown in Fig. 3.4 for the measured raw ON and OFF data sets. While events in the raw data are mostly due to cosmic rays, the gamma-ray signal is very strong and an event excess in the ON data is clearly visible for $alpha$ <20°and to some extend in the $length$ and $width$ histogram as well. To increase the signal-to-noise ratio, a set of loose cuts was applied to reject more background events: $alpha$ <18°, $length$ <0.4°, $width$ <0.25°, 0.3°< $distance$ <1.2°, $length/size$ < 0.00085 °/dc, and $max2$ > 65 dc. After applying these cuts, the gamma-ray excess is more easily visible, see Fig. 3.4.

The measured gamma-ray excess before and after cuts is compared to simulations in Figs. 3.5 and 3.6. The simulations were carried out with $kascade3$, the PMT quantum efficiency (a) Sect. 3.3, and the parameters listed in Tab 3.7, see also Sect. 3.4.2. Simulations using $kascade7$ produced essentially the same results.

Focusing first on the uncut distributions, generally good agreement is visible for all but the $length/size$ distribution. At large values, the measured $length/size$ histogram is dominated by the signal from single muons. These particles produce large shower images with little light in them. Thus, the measured negative excess at large $length/size$ probably
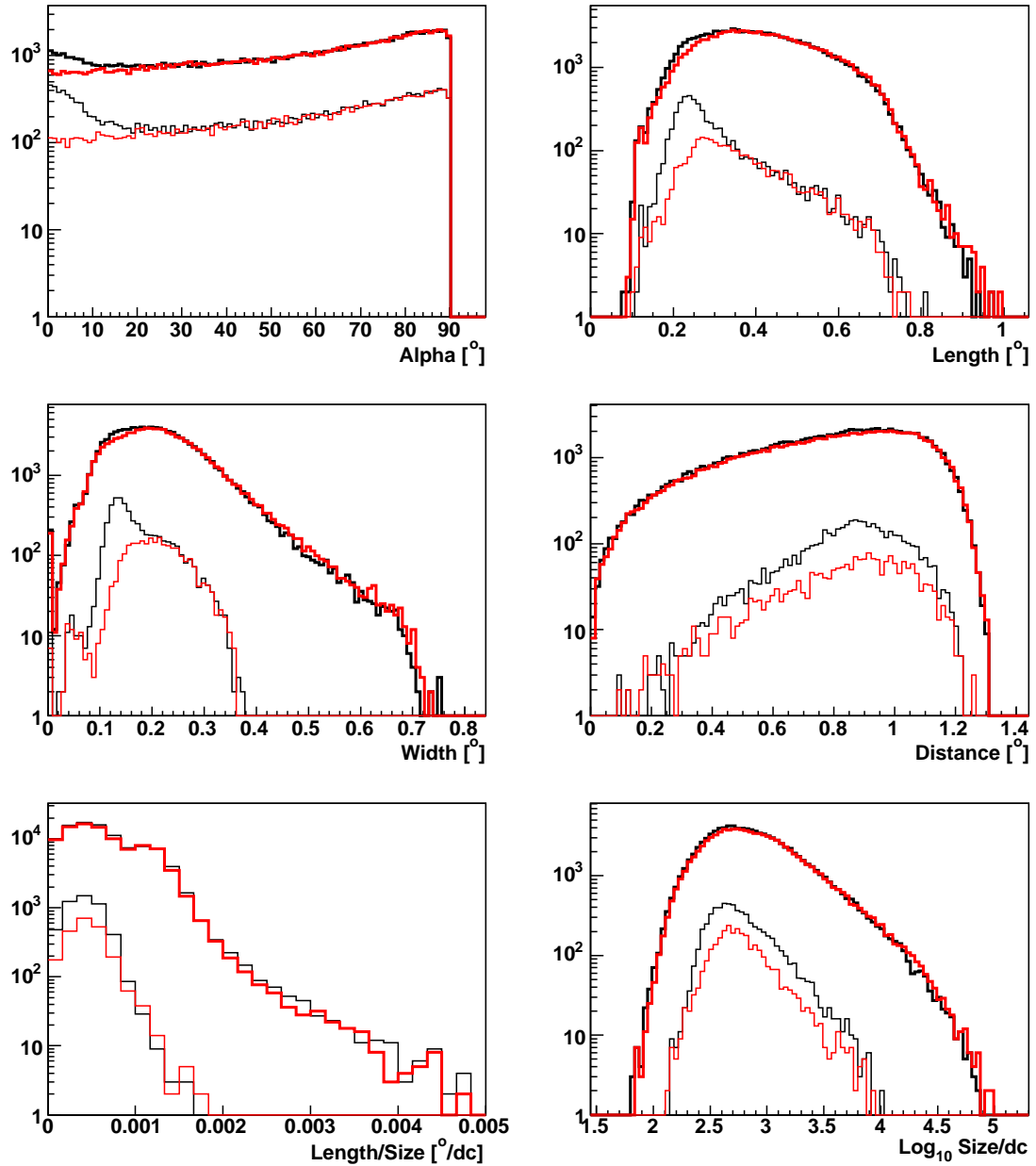
FIGURE 3.4. Histograms of parameters derived from raw data (*bold*) and after applying s set of loose cuts (*thin*) described in the text. ON data are shown in *black*, OFF data in *red*. For the *thin lines*, the parameter plotted in the histogram was excluded from the cuts.

indicates a muon excess in the OFF data and is not relevant in comparing the gamma-ray signal. A Kolmogorov-Smirnov test reveals that the $distance$ distribution agrees with simulation at a probability level of 0.27, the $length$ distribution at 0.002, and all others at less than 1×10^{-5}. This is not surprising as a large fraction of CR events are present in the data.

The gamma-ray spectrum was measured to be -2.57 ± 0.17 with combined statistical and systematic errors (Zweerink et al., 1997), while the simulation here assumes a -2.5 spectrum. The histograms in Figs. 3.5 and 3.6 show an average over all triggered energies. However, Fig. 3.7 shows that some of the mean shower parameters vary with the primary gamma-ray energy. Therefore, perfect agreement between the measured and simulated parameter distributions is not expected.

However, when loose cuts are applied, differences are visible between the parameters from measured and simulated gamma rays. In particular, the measured $alpha$ distribution is broader compared to the simulation. As Mrk 421 is a point source of gamma rays, this implies that the simulated point spread function of the telescope was too narrow. Also, the measured $width$ distribution is wider than the simulation predicts. The $width$ parameter is a measure of the optics of the telescope, the primary gamma-ray spectrum, and the broadening due to multiple Coulomb scattering. The Coulomb scattering routine was verified in the simulation, and as the measured gamma-ray spectrum is relatively close to the simulated spectrum, this means that the optical aberrations of the telescope were underestimated.

The optical quality is measured by observing how well a star is imaged on the focal plane; the resulting image is called the point spread function (PSF) of the telescope. In 1995/6, the PSF was measured to be 0.12 °full-width half-max (FWHM) at 32° elevation (Lewis, 1990). But the optical abberations were found to change with observing elevation. Image distortions are caused by flexure in the optical support structure; this has been remedied in 2002 with the implementation of a bias alignment, see Sect. C.3. Thus, the real PSF may have been 0.15° - 0.18° at the average observing elevation of 70° for Mrk 421, see Fig. C.5. The optics of the 10 m was simulated here using a 0.14° FWHM PSF; details
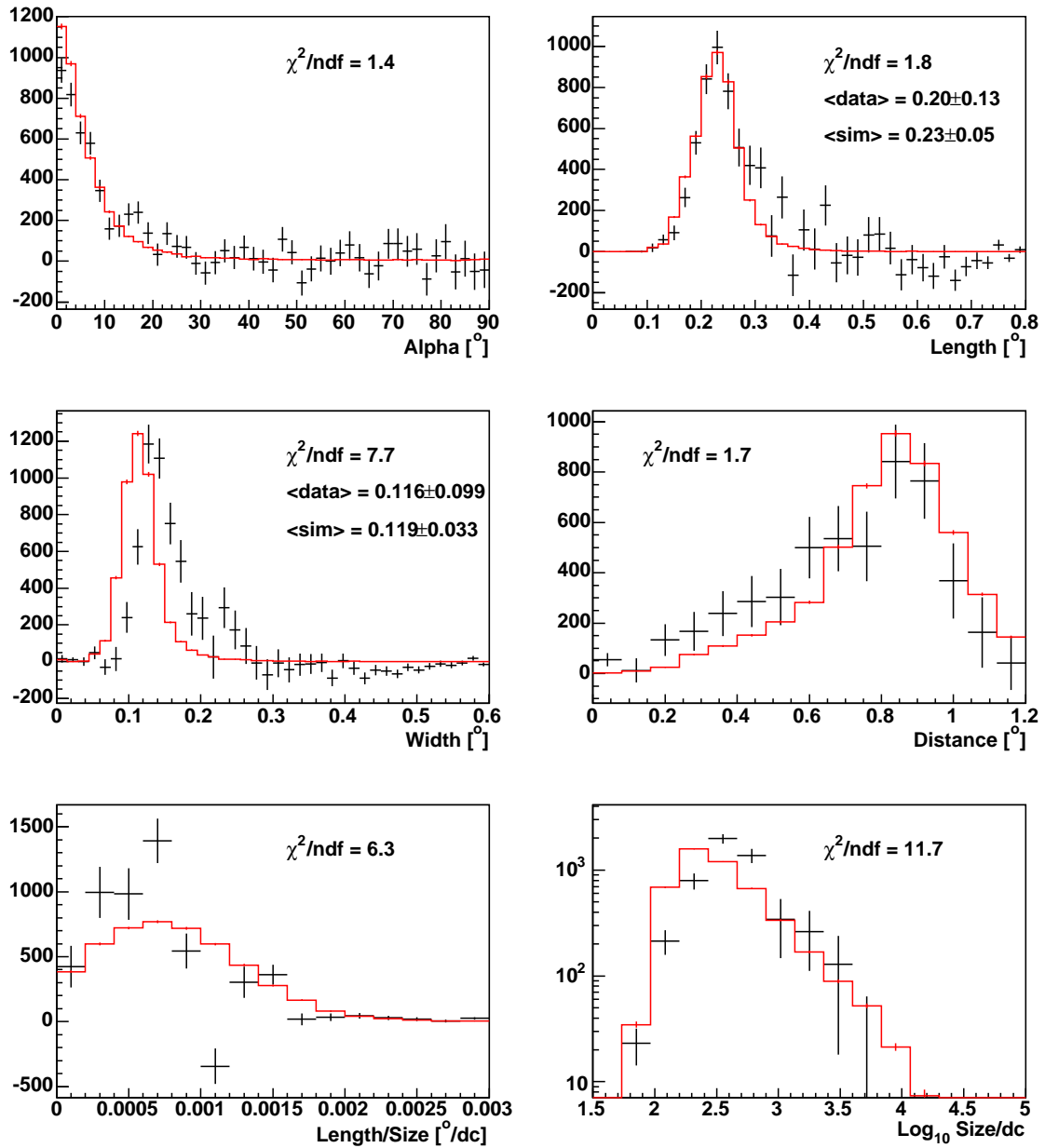
FIGURE 3.5. Histograms of the ON-OFF differences in the raw parameter distributions (*crosses with error bars*). Simulations of gamma rays (*line*) are normalized to the total count of the difference histogram.
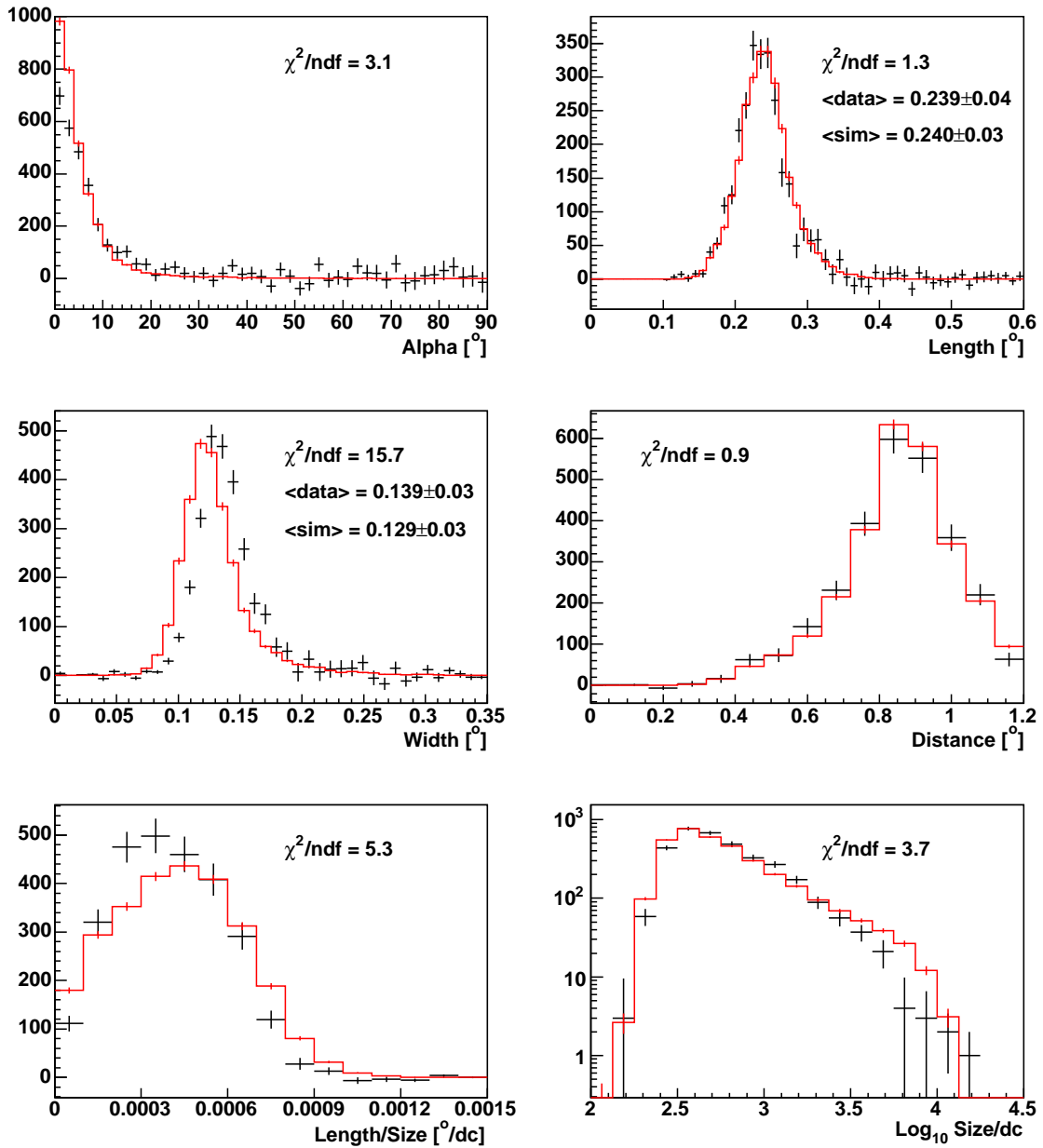
FIGURE 3.6. Histograms of the ON-OFF differences in the cut parameter distributions (*crosses with error bars*). Simulations of gamma rays (*line*) are normalized to the total count of the difference histogram.
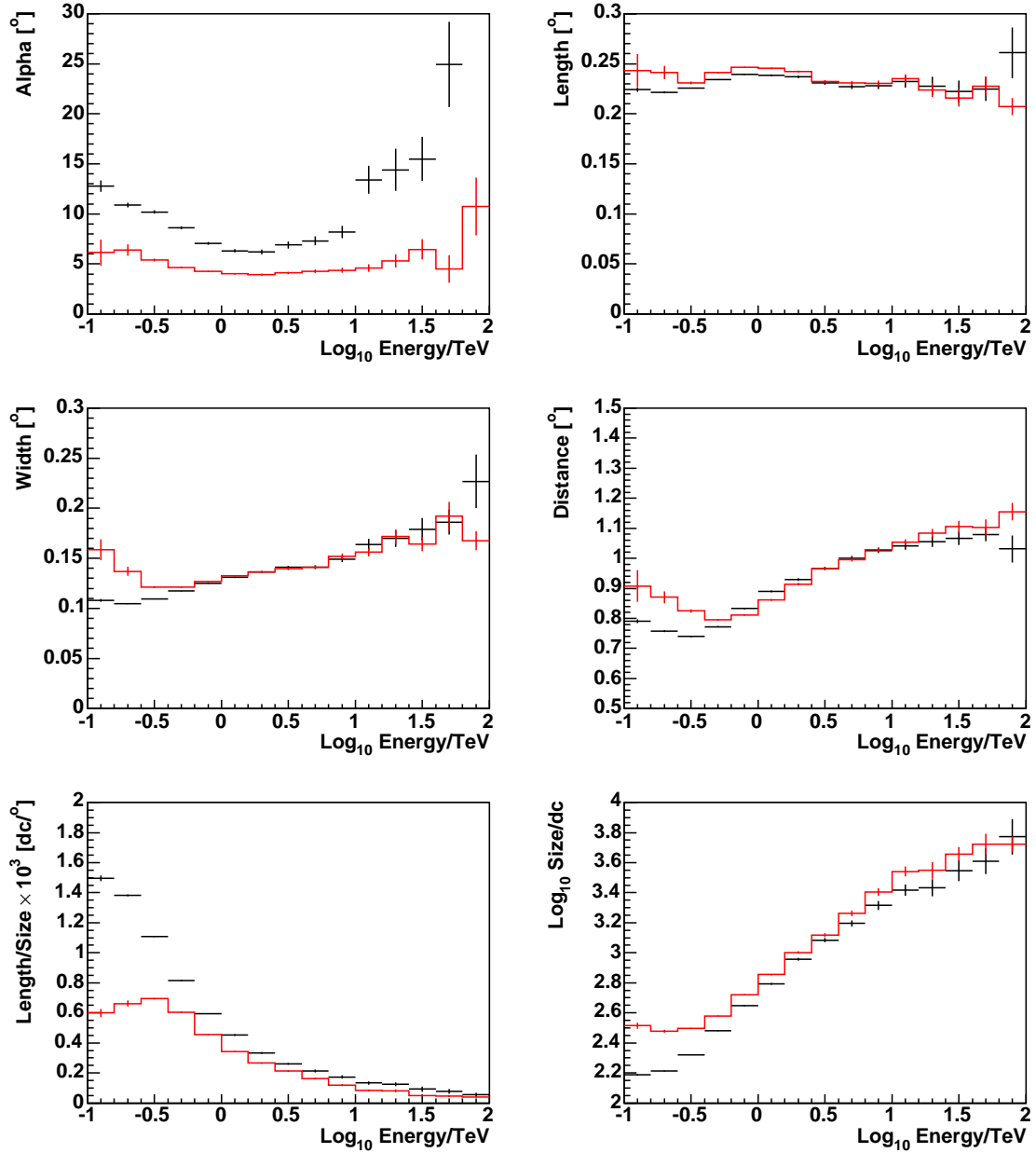
FIGURE 3.7. Variation of the average image parameters with primary gamma-ray energy for all simulated gamma rays (*crosses with error bars*) and those that pass a set of loose cuts described in text (*line*).

on how the simulation of the telescope optics can be checked against direct measurements are given in Sect. C.5. This value is underestimates and it should be possible to achieve better agreement between the simulated and measured $width$ distribution by increasing the PSF in the simulation. The $width$ parameter is the RMS image size and the PSF is an RMS error, so the needed increase of the PSF is the RMS difference between measurement and simulation: $\sqrt{(0.139°)^2 - (0.129°)^2} = 0.05°$. By the same argument it follows that the correct PSF to use in the simulation is $\sqrt{(0.14°)^2 + (0.05°)^2} = 0.148°$, because the PSF is an RMS value.

However, this does not necessitate new simulations because the cut levels are quite broad. The simulated $width$ distribution is used to develop the cut level to discriminate against cosmic ray images in the data, see Sect. 3.2.2. This cut level is chosen at twice the RMS value of 0.03 to $0.06°$, depending on gamma-ray energy, see Fig. 3.8. However, since the difference between the simulation and measurement is only $0.01°$, no significant error is introduced by using the slightly smaller PSF in the simulation.

The measured and simulated $length$ distributions are in agreement; $length$ is a measure of the longitudinal development of the shower

To conclude, the image parameters derived from simulated gamma rays were compared with a very strong gamma-ray flare of Mrk 421. The simulated parameter distributions $alpha$, $length$, $distance$, and $length/size$ are in good agreement with the measured ones. Only the simulated $width$ distribution is systematically too small, indicating that the simulation of the telescope optics was too optimistic. The rejection of background is performed by cuts on $alpha$, $length$, and $width$. As the cuts in the spectral analysis are chosen conservatively at $2\sigma_{RMS}$ centered at the mean, the mismatch in the $width$ distribution is not significant. The energy of an event is calculated from its $size$ and $distance$, independent of $width$ or $length$. Thus, the small difference found here between simulated and actual gamma rays is acceptable and should not distort the reconstructed energy.

3.2 Energy Spectrum Reconstruction

The gamma-ray energy flux is reconstructed through comparison with a Monte-Carlo simulated gamma-ray spectrum. The simulated gamma-ray air showers are used in all steps of the analysis:

- Identify images produced by gamma rays and reject cosmic-ray initiated showers.

- Estimate the energy of the primary gamma ray from the properties of the recorded light.

- Determine the gamma-ray flux.

Usually only one set of simulated gamma rays is needed to accomplish all steps. It is essential to the technique that the simulated spectrum be close in shape to the measured spectrum. Usually, a power-law spectrum with differential index of -2.5 is simulated initially. This can then be adapted to other shapes through a weighting procedure.

3.2.1 Raw Spectrum

The gamma-ray spectrum is measured from the difference in the on-source and off-source energy spectra. The raw spectra before cuts are due to 95% from proton showers, with He and heavier nuclei constituting the remainder (besides the very small amount of gamma rays) (Mohanty, 1995). Because the primary cosmic-ray spectrum is constant and well known, it could in principle be used to evaluate the stability of the atmosphere. To do this in detail requires the reconstruction of the cosmic ray energy, which is difficult with a single telescope because the fragmented images of hadronic showers produce large fluctuations in the received light intensity. Using simulations, the energy resolution of proton showers was estimated to be about twice as uncertain, RMS($\Delta \log E$)≥ 0.3, as for gamma rays. Instead, the only use of the raw spectrum is as a simple measure of the relative throughput, described in Sect. 2.3.

3.2.2 Background Rejection

Cosmic rays produce Cherenkov images that are more fragmented due to the hadronic cascade that produces many penetrating particles. This is an important difference to the more compact Cherenkov images from gamma rays. Software selection criteria, called cuts, are applied to the parameters $width$, $length$, and $alpha$ to eliminate most of the cosmic-ray background. These cuts scale with $size$ so that the fraction of gamma rays passing the cuts is independent of $size$ (Mohanty et al., 1998).

Fig. 3.8 illustrates how the cuts are derived for simulations done at 70° elevation for the camera in the 1995/6 observing season. The cuts are later used in deriving the spectrum of the Crab Nebula, Sect. 3.4.3. To begin, preliminary cuts are applied to reduce the amount of data and to reduce the uncertainty in the trigger response near threshold: $max2 > 65$ dc, $length/size < 0.00085°$/dc, $0.31°< distance < 1.1°$, and $alpha < 15°$. The $length/size$ cut is used to reject single muons. The parameter distributions are then binned in equally spaced $\log(size)$ bins and the mean, m, and standard deviation of the distribution, σ, are calculated in each bin. The mean and standard deviation are fitted with a second order polynomial fit in $\log(size)$. For $length$ and $width$, the cuts include the parameter space $m \pm t \times \sigma$, while for $alpha$ it is of the form $0°< alpha < m + t \times \sigma$, where t is the cut tolerance. The tolerance is usually chosen at the 2-σ level so that about 90% of the simulated gamma rays pass all cuts relatively independent of $size$.

The application of the $size$-dependent cuts on the raw parameter distributions of Crab Nebula observations is shown in Fig. 3.9. Together, these cuts reject most of the cosmic ray background, but explicit background subtraction though an OFF-source observation is still performed. The constant cut level of $Supercuts1995$, illustrated in the figure by a *dotted* line, is optimized to the energy region where the most gamma rays are collected by the telescope which is close to the triggering threshold.
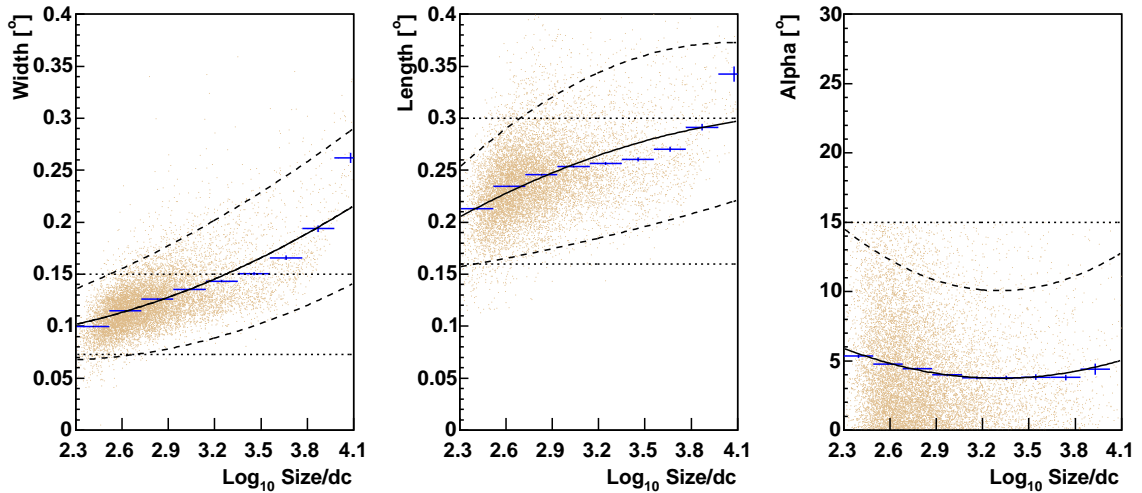
FIGURE 3.8. Simulated gamma-ray parameter distributions of *length*, *width*, and *alpha* and derived cuts versus $\log(size)$ after application of loose spectral cuts. The *dots* are simulated events, the *blue crosses* show the mean, while the *solid lines* show the polynomial fit through the mean. *Dashed lines* show the actual cut chosen at a tolerance of two standard deviations around the mean. *Dotted lines* show cut level of $Supercuts1995$.

3.2.3 Gamma-Ray Trigger Rate and Collection Area

The collection area of a Cherenkov telescope represents the area over which gamma rays trigger the telescope. The collection area specifies the efficiency with which gamma rays of different energy are detected by the telescope. The collection area is much larger than the physical mirror size because Cherenkov photons from gamma-ray showers that reach the telescope are produced 5 - 20 km higher up in the atmosphere, depending on the primary particle's energy. With a typical $3°$ field of view and a 10 km shower height, this corresponds to a theoretically possibly area in excess of 200,000 m^2. However, light attenuation in the atmosphere and other inefficiencies limit this to about 1/2 to 1/4 of this value.

To determine the collection area, gamma-ray showers were simulated with an impact distance of typically 300 m. This corresponds to an area of $A_0 = \pi(300 \text{ m})^2$. Let the number of events that were simulated with a true energy E and fall within a bin width
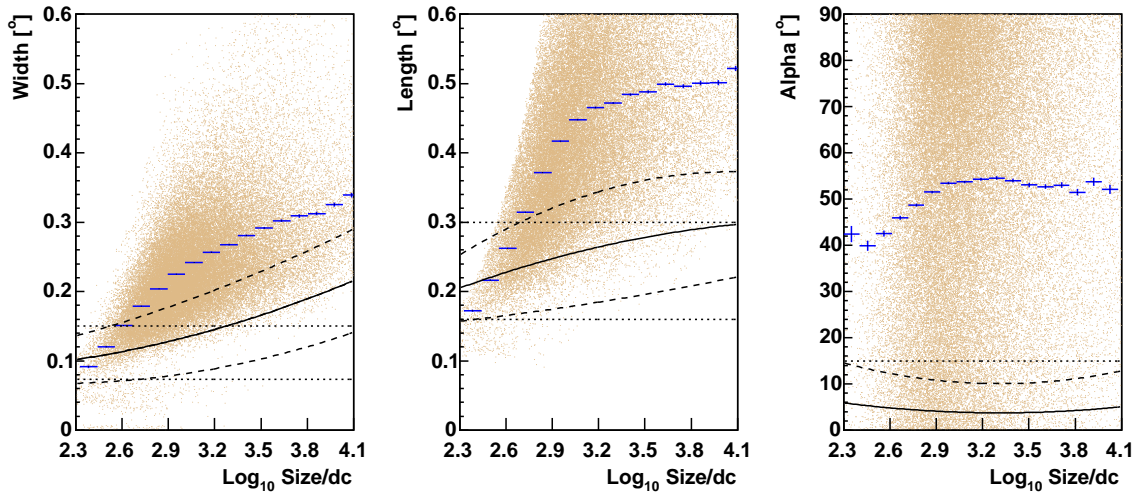
FIGURE 3.9. Raw parameter distributions of *length*, *width*, and *alpha* of Crab Nebula observations taken in 1995/6 at around 70° elevation. The *dots* are measured events, the *blue crosses* show the mean of the data. The mean value of simulated gamma rays is shown with *solid lines*. *Dashed lines* show the gamma-ray cut for the spectral analysis. *Dotted lines* show the cut level corresponding to $Supercuts1995$.

$\Delta \log(E)$, be called $I(E)$. Let $T(E)$ be the number of events that cause a trigger in the telescope with energy E and fall within the same bin width $\Delta \log(E)$. The effective area, $A(E)$, on the ground over which the telescope triggers occur is then given by

$$A(E) = A_0 \frac{T(E)}{I(E)}. \tag{3.1}$$

Gamma rays were simulated coming from a -2.5 power law spectrum and observed at an elevation of 70° with the 1995/6 camera configuration. The raw trigger rate is shown in Fig. 3.10. Also shown is the rate of events passing spectral cuts and $Supercuts1995$. The peak of the trigger rate is often called the "energy threshold", and lies at 0.56 TeV for spectral cuts and at 0.74 TeV with $Supercuts1995$. The peak energy for $Supercuts1995$ is higher because a minimum $size$ of 400 dc ($\simeq$ 400 pe) is required, Tab. 2.2 , while the spectral cuts only use $max2 > 65$ dc. The peak trigger rate moves to higher energies with increasing zenith angle of the observation due attenuation in the atmosphere and the greater

distance to the shower maximum.
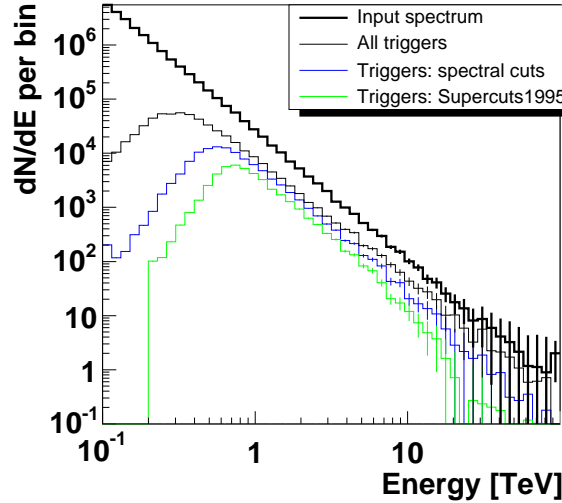
FIGURE 3.10. Trigger rate (*thin black line*) for gamma rays observed at 70° elevation from a -2.5 power law input spectrum (*bold line*). Also shown are the trigger rate after application of spectral cuts (*blue line*) and after $Supercuts1995$ (*green line*)

The collection areas corresponding to Fig. 3.10 are shown in Fig. 3.11.

3.2.4 Energy Estimation

The initial gamma-ray energy is estimated from the measured $size$ and $distance$ of the shower image. The estimated energy, E_{est}, is determined from the polynomial (Mohanty et al., 1998):

$$\log E_{est} = a_1 + a_2 \times \log S + a_3 \times D + a_4 \times (\log S)^2 + a_5 \times D^2 + a_6 \times D \times \log S, \quad (3.2)$$

where $S \equiv size$ and $D \equiv distance$. The coefficients of this polynomial, a_i, are determined by fitting the true energy of simulated gamma rays to their image parameters. The fit is performed by minimization of both the rms difference between the true and estimated energy $\sqrt{\sum (\log E - \log E_{est})^2 / n}$ as well as of the bias $\sum (\log E - \log E_{est})/n$, where n is the number of events. In performing the fit, the bias is emphasized by a factor of 10 over
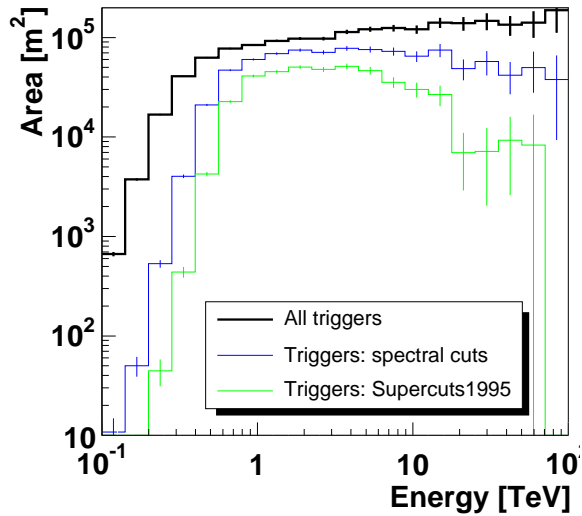
FIGURE 3.11. Collection area for gamma-rays observed at $70°$ elevation. in for spectral cuts (*bold line*) and $Supercuts1995$ cuts (*thin line*).

the χ^2 difference. It is important for the energy estimator to be bias free, so that during the flux calculation the number of events binned in estimated energy bins is equal to the number of events with the same true energy and no distortions are introduced in the energy calibration. The fit is performed over a limited energy range where the relation between E and $size$ is approximately linear; this is not the case very close to the trigger threshold, where fluctuations in the shower development are large, and at very high energies, where most of the shower light lies outside of the limited field of view of the camera.

As an example, Fig. 3.12 shows the result of estimating the energy for simulated gamma rays at $70°$ elevation during the 1995/6 observing season. The energy resolution is discussed in Sect. 3.2.5.

3.2.5 Energy Resolution

The energy resolution is the probability distribution for measuring an energy E_{est} when the true energy is E. This is measured from Monte-Carlo simulations by comparing the true energy with the estimated energy. Fig. 3.12 shows in the middle graph the residuals, $\log E-$
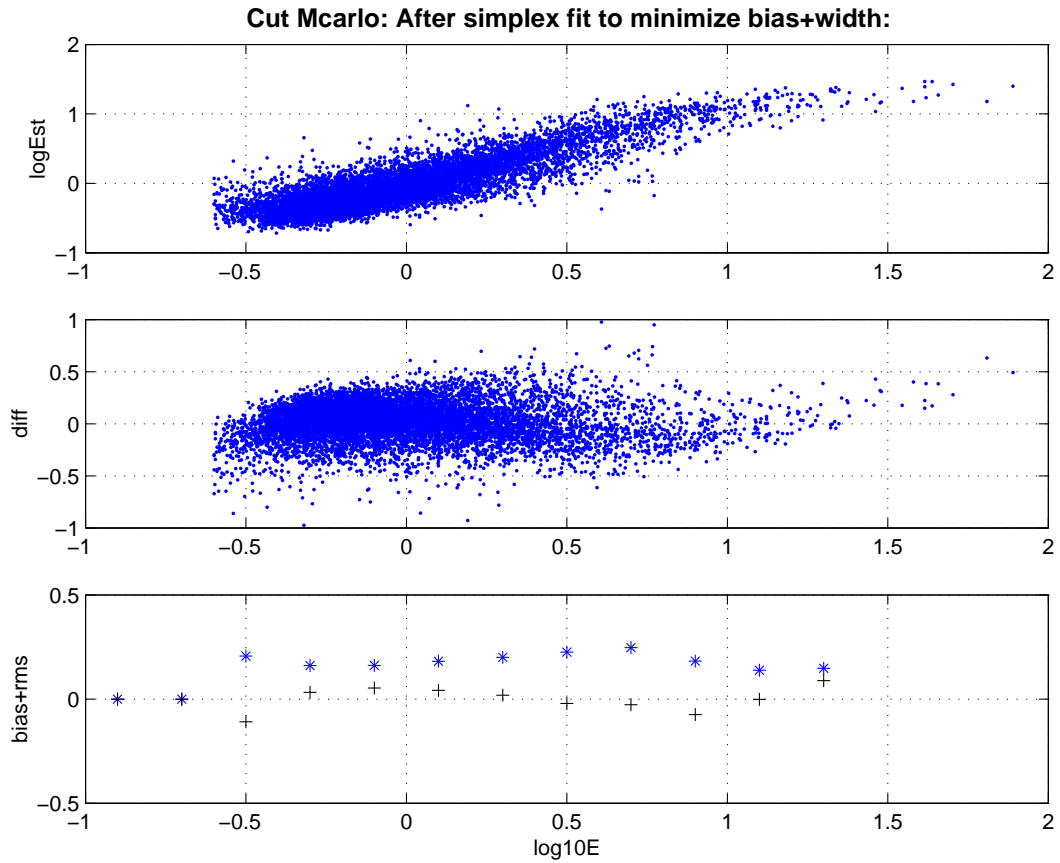
FIGURE 3.12. *Top:* Estimated energy vs. true energy of simulated events. *Middle:* Residuals of the fit. *Bottom:* RMS deviation of $(\log(E) - \log(E_{est})$ shown by (*) and bias (+).

$\log E_{est}$, and in the lower portion the mean and RMS difference with energy. They are relatively energy independent and histograms over the complete energy range of $(\log E_{est} - \log E)$ and of $(E_{est} - E)/E$ are shown in Fig. 3.13.

The energy resolution in logarithmic energy space is approximately normally distributed, reduced $\chi^2 = 2.3$, and has a Gaussian width of 0.17 and mean 0.025. The corresponding RMS value is 0.18. Traditionally the energy resolution is measured by $(E_{est} - E)/E$. This is shown in Fig. 3.13 together with two fitted functions. A Gaussian, width = 0.28, reduced $\chi^2 = 13$, and a Breit-Wigner distribution of width 0.21, reduced $\chi^2 = 19$. These distributions do not fit the energy resolution well due to the long tail at

large overestimated energies. The RMS($\Delta E/E$) is 0.51.

To summarize, the energy resolution is best described by a Gaussian in logarithmic energy space and for this work it will be quoted by its RMS value only.
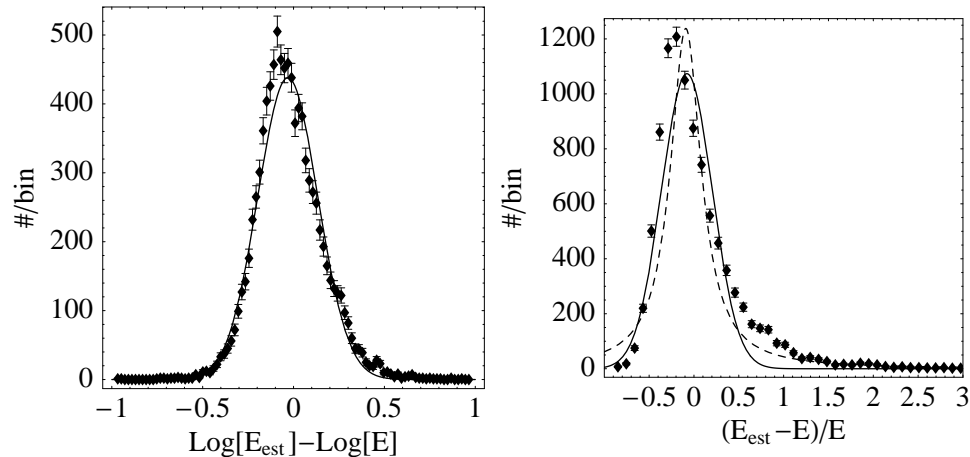
FIGURE 3.13. *Left:* Histogram of $(\log E_{est} - \log E)$ fitted with a Gaussian (*solid line*). *Right:* Histogram of $\Delta E/E$ over the energy range from 0.25-25 TeV fitted with a Gaussian (*solid line*) and with a Breit-Wigner function (*dashed*). See text for explanation.

The energy resolution varies slowly with energy as shown by the RMS value in the lower panel in Fig. 3.12. The energy resolution increases with lower elevations as showers tend to be smaller and more fully contained in the camera.

3.2.6   Flux and Spectrum Determination

The method of reconstructing the gamma-ray flux [$L^{-2}\,T^{-1}\,E^{-1}$] was outlined in Mohanty et al. (1998). It uses a modified collection area that implicitly contains the energy resolution function without recurse to folding the spectrum with the resolution function. However, the method differs from that described in (Mohanty et al., 1998) by binning events based on their estimated energy and not based on $size$ alone.

The following is a description of this method: The gamma-ray flux, $F_m(E)$, from a source is reconstructed by binning the excess number of events received from the source,

$N(E_{est})$, during a time, t, in bins of width $\Delta \log(E)$. This is multiplied by the fraction of events per unit area that trigger the telescope, called the modified area.

The modified area is calculated from the number of events, $I(E)$, that were simulated with a true energy E and fall within a bin width $\Delta \log(E)$ and the number of events, $T(E_{est})$, that cause a trigger within that bin and have an estimated energy $E_{est} = E$. This is then divided by the area, A_0, that showers were thrown over. Therefore, the flux is given by

$$F_m(E) = \frac{N(E_{est})}{t \, \Delta \log(E)} \times \frac{I(E)}{A_0 T(E_{est})} \tag{3.3}$$

$$F_m(E) = \frac{N(E_{est})}{A_0 \, t \, (k \times E)} \times \frac{I(E)}{T(E_{est})}, \tag{3.4}$$

where $k \equiv 2 \sinh(\ln 10 \, \frac{\Delta \log(E)}{2})$ is the bin width in linear space, explained in Appendix F. An example of the collection area and the modified area is shown in Fig. 3.14.
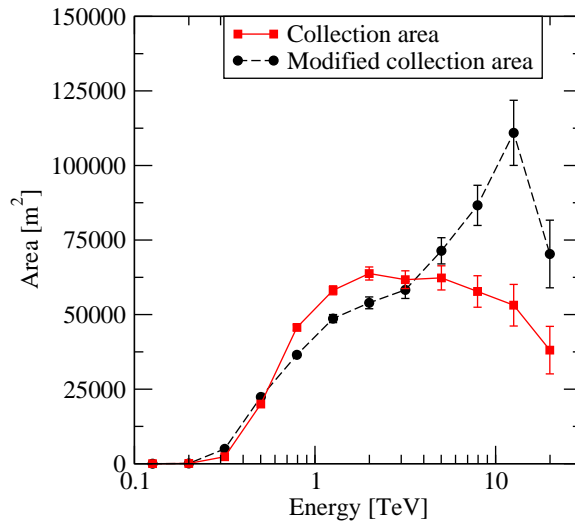
FIGURE 3.14. Collection area (*solid line*) and modified collection area (*dashed line*) for gamma rays observed at $70°$ elevation with the 1995/6 camera configuration.

The bin width is chosen as small as possible while still maintaining a good signal-to-noise ratio. Scott (1979) determine that this optimal bin width is

$$\Delta \log(E) = 2 \times 9\pi^{1/6} \sigma N^{-1/3} = 3.5 \frac{\sigma}{N^{1/3}}, \tag{3.5}$$

Simultaneous parameters	Confidence level			
	40%	68.3%	90%	95%
1	0.27	1.00	2.70	3.84
2	1.02	2.30	4.61	5.99
3	1.87	3.53	6.25	7.81

TABLE 3.2. By increasing χ^2 from its minimum value by the stated amount, the confidence level of 40%, 68.3%, 90%, and 95% is reached. This is listed for 1, 2, and 3 simultaneously fitted parameters.

where σ is the Gaussian energy resolution width and N is the total number of events: ON-OFF after cuts.

A spectrum, usually a simple power-law, is then fitted to the measured flux. The spill over of events into nearby bins depends on the energy spectrum; this is accounted for by the term $\frac{I(E)}{T(E_{est})}$ which corrects for the number of misidentified events in each energy bin. Therefore, if the simulated spectrum deviates from the measured spectrum, a new spectrum is simulated that is equal in shape to the measured spectrum and the analysis is then repeated. This iterative method of calculating the flux usually converges within one iteration. The method works well for power-law spectra, but care must be taken for spectra with a sharp cut-off feature. These might lead to unphysical fluctuations in the spectrum on scales smaller than the energy resolution.

The statistical error in the fitted power law is determined by the χ^2 method. The 2 parameters, flux and spectral index, are varied about their optimum value until the desired increase in χ^2 is reached (Lampton et al., 1976; Avni, 1976). In this way a χ^2 map is produced with probability content determined from the cumulative χ^2 distribution with 2 degrees of freedom. Tab. 3.2 lists in the second row the increase in χ^2 required to reach confidence interval (CI) levels of 40%, 68.3%, 90%, and 95%. Also shown in the table are the corresponding entries when one or three parameters are fitted simultaneously.

The systematic uncertainty on the spectrum is determined by varying the cut tolerance, t, within reasonable bounds: between 1.5 and 2.5. In addition, the dc/pe ratio is allowed

to vary by its uncertainty. Then, to evaluate the systematic uncertainty of the gamma-ray spectrum, the spectral analysis is carried out again with the new parameters.

3.3 Absolute Calibration using Cosmic-Ray Muons

One way of calibrating the light intensity received by the PMTs of the telescope in terms of the digitized signal, is through the light recorded from muon events (Vacanti et al., 1994; Jiang et al., 1993). Single muons are produced by interactions of cosmic rays of energy 1-100 GeV with the upper atmosphere. The mean lifetime of muons is 2.2 μs in their rest frame which allows them to reach sea level before decaying if they travel near the speed of light. The energy threshold above which muons and electrons produce Cherenkov light at a particular height in the atmosphere is shown in Fig. 3.15. Above threshold, muons that are incident nearly parallel to the telescope axis and impact on the telescope aperture, are imaged as a ring. Fig. 3.16 shows an actual muon ring corresponding to this type of event. The total amount of light, $size$, detected from such a muon is comparable to that from a high-energy gamma-ray initiated shower. However, the light from muons is spread over very many of pixels, while gamma rays produce much more compact images with only a few tens of pixels containing all the light.

The recorded brightness can be calibrated in terms of the absolute number of incident photons using muons, because the number of Cherenkov photons emitted by a muon is proportional to the angular radius of the ring image. In other words, by comparing the measured photon count in a muon image with the expected count derived from the measured angular radius of the muon ring, the light throughput of the telescope can be calibrated.

Electrons, though copiously produced by cosmic rays in the atmosphere, do not produce a ring image because they do not travel in a straight line for very long. Instead, they are deflected by multiple Coulomb scattering as well as by the Earth's magnetic field and lose energy through bremsstrahlung. The first two effects change the position of the ring, while the latter decreases the ring radius. This makes electron images not at all ring-like, but
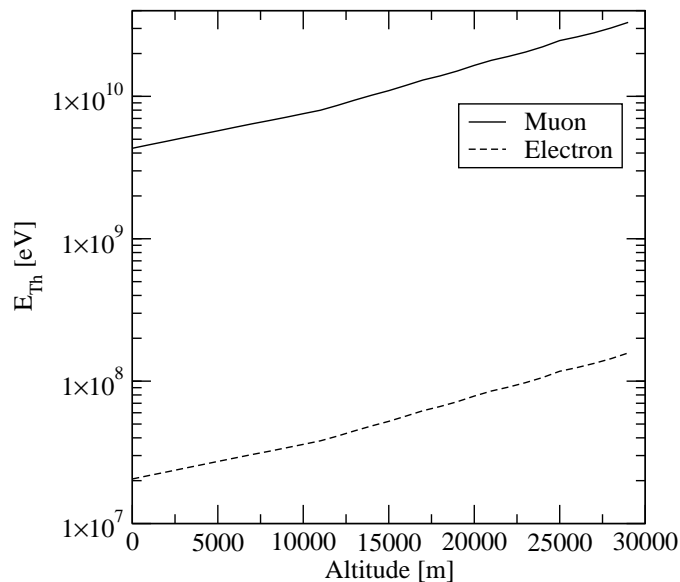
FIGURE 3.15. The minimum energy required for muons (*solid*) and electrons (*dashed*) to emit Cherenkov light.

more like large low-density spots.

An advantage of using muons to calibrate the light throughput, is that it is a single factor that scales the light intensity to be expected from gamma-ray showers. Using muons, the calibration includes to first order everything local to the telescope: the local atmosphere within 400 m of the reflector, the mirror reflectivity, the light cone efficiency, the PMT quantum efficiency, cable loss, impedance mismatch, and slight timing offsets that effect the charge integration. Though a best effort is made to include all parts of the telescope in the Monte-Carlo simulation, the lack of information on the variation with time of all these components necessitates the use of an overall scaling factor in the interpretation of the image brightness. Usually, the calibration is expressed in terms of the ratio of the number of photoelectrons (pe) produces by the PMT photocathode to the digital read-out, measured in digital counts, dc, called the dc/pe factor. This calibrates only the electronic part of the detector; it does not include the changes in the light collecting portion of the telescope. Thus, it should be kept in mind that the muon calibration method does not produce a dc/pe
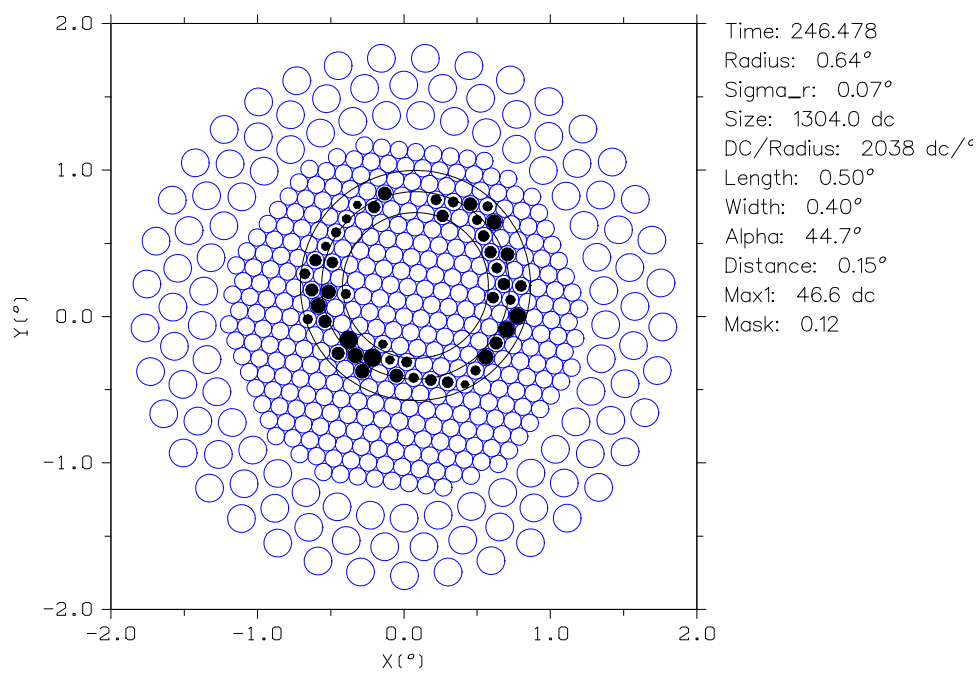
FIGURE 3.16. A muon event recorded with the 490 pixel camera. The amount of light measured by each PMT measured is represented by a filled circle such that a full circle corresponds to the brightest pixel. The amount of light in the brightest pixel is listed as the $Max1$ value in the legend. Also shown is a fitted circle together with its measured radial extend σ_r. See text for more details.

ratio, but rather the overall light-to-dc factor. However, an attempt is made to take account of the optics and thus to derive a dc/pe ratio.

The disadvantage of a muon calibration comes from the somewhat different received spectrum of Cherenkov light from local muons compared to gamma-ray initiated showers 10 km higher in the atmosphere. The somewhat uncertain optical extinction and PMT response in the ultra-violet (UV) region from 250 nm$< \lambda < 300$ nm, leads to a systematic error, see Sect. 3.3.4. Another shortcoming for diagnostic purposes is the inclusive nature of the muon calibration. For example, it is not possible to distinguish between deterioration of the light cones or the electric cables, but separate tests must be performed.

The straightforward way to determine the dc/pe ratio is by direct measurement of all components involved: from PMTs to the ADC module; this was explained in Sect. 2.2.4.

Another method to determine the dc/pe ratio is to measure single electron peaks for each PMT. This is done by starting with a very high gain where it is easy to see individual photoelectrons and interpolating the dc value back to the actual operating voltage where single pe are lost in the noise.

3.3.1 Model of Cherenkov Light Production by Muons

The differential number of Cherenkov photons, N_γ, emitted per path length l, azimuthal angle ϕ, and wavelength λ is given by (Leo, 1994)

$$\frac{\mathrm{d}^3 N_\gamma}{\mathrm{d}l \, \mathrm{d}\lambda \, \mathrm{d}\phi} = \frac{\alpha}{\lambda^2}(1 - \frac{1}{\beta^2 n[\lambda]^2}), \tag{3.6}$$

where β is the speed of the charged particle, α is the fine structure constant, and n is the index of refraction. The factor $1/(\beta n[\lambda]) = \cos[\theta]$ is the cosine of the measured Cherenkov angle. The index of refraction at 2.3 km elevation varies between 200 nm and 600 nm from 1.0003 to 1.00025, introducing a variation of the maximum Cherenkov angle θ between 1.4 ° and 1.28°. This variation is not very significant since an average is taken over many hundred of photons over a small range of elevations. As only complete muon rings are used here, the Cherenkov light comes from less than 500 m above the telescope. The variation
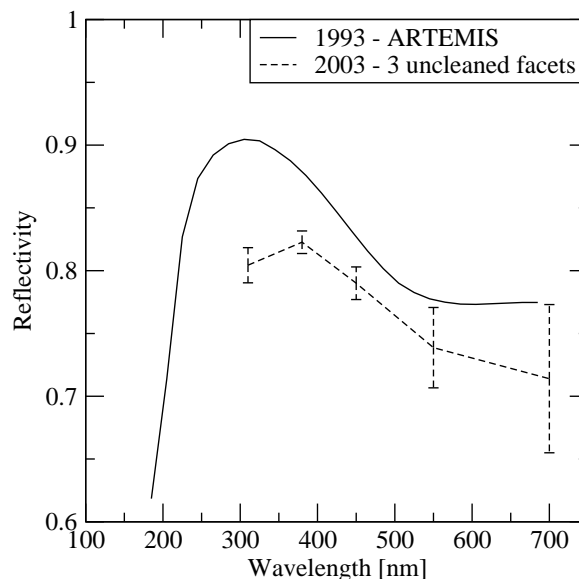
FIGURE 3.17. Mirror reflectivity measurement with freshly coated facets (*solid line*) and in 2003 for three uncleaned facets (*dashed line*). The entire telescope was recoated in 1998-9.

of the index of refraction over this altitude is negligible as well. Atmospheric absorption of Cherenkov light occurs mainly in the ultra-violet below 250 nm, see Fig. 3.24. Its detailed effect will be included in Sect. 3.3.3; here it will only serve as a lower limit of integration λ_{min}. An uncertainty of ± 50 nm is assumed in the lower limit. The conversion from the number of incident photons N_γ to photoelectrons (pe) ejected at the PMT photocathode is performed by integrating over the mirror reflectivity $M(\lambda)$, Fig. 3.17, and the PMT quantum efficiency $QE(\lambda)$. Fig. 3.18 shows QE specifications for the 1" Hamamatsu R1398 and the 1/2" R647-25 with UV-glass window and bialkali photocathode. Though, the photocathode is supposed to be same for both PMTs, slightly different specifications are in existence. The reason(s) for the differences are unclear. Therefore, both, quantum efficiencies a) and b), will be used in the calibration to explore the range of systematic uncertainty caused by them. As the upper limit of integration, $\lambda = 700$ nm will be used because the quantum efficiency is near zero at this wavelength.

Additional photon losses in the telescope and camera are due to missing facets and
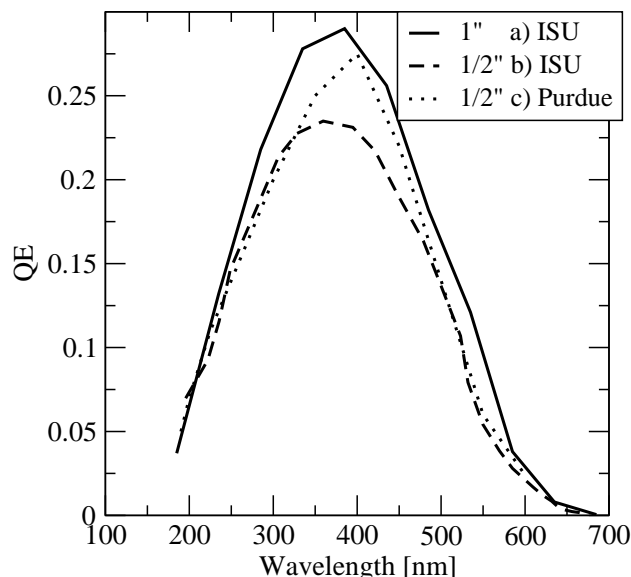
FIGURE 3.18. PMT quantum efficiencies for the 1" Hamamatsu R1398 and 1/2" R647-25 with UV-glass window and bialkali photocathode. Source of measurement indicated in parentheses.

the PMT arrangement. There are always 11 facets missing and the camera support arms obscure about 1 m^2, for a total loss of $11 * 0.372 \, \text{m}^2 + 1.0 \, \text{m}^2 = 5 \, \text{m}^2$. Fig. 3.17 shows that the mirror reflectivity had dropped by about 5% in 2003 relative to freshly coated mirrors. These two effects reduce the effective mirror area of $\pi(5\text{m}))^2 = 78.5\text{m}^2$ by about 12%. To minimize dead space between PMTs, they are tightly packed in a hexagonal pattern. Light cones cover the empty space between the PMTs to reflect some of the photons into the photocathode that would otherwise have been lost. A detailed account of the geometrical losses at the camera is presented in Tab. 3.3 for the 109 and 379 PMT cameras. The efficiency of the light cones was determined by comparing the cosmic ray spectrum from 10 min zenith runs with and without light cones. In all, excluding $M[\lambda]$ and $QE[\lambda]$, a photon randomly incident on the telescope with the 109 (379) camera has a $L = 69\%$ (48%) chance of being detected.

	109 PMT Camera	379 PMT Camera
PMT spacing	33 mm	15 mm
Area per pixel	943 mm^2	195 mm^2
Cathode radius	12.55 mm	5.2 mm
Cathode area	495 mm^2	85 mm^2
Throughput increase with cones	1.27	1.24
Effective cathode area	623 mm^2	106 mm^2
Effective cathode radius	14.14 mm	5.8 mm
Focal plane coverage	78%	54%
Geometrical light cone efficiency	0.28	0.18

TABLE 3.3. Arrangements of the 109 pixel and the inner 379 pixels of the 490 PMT cameras. The area on the photocathode that is covered with photoelectric material is smaller than the physical diameter of the PMT. The light cones increase the effective area of the photocathode.
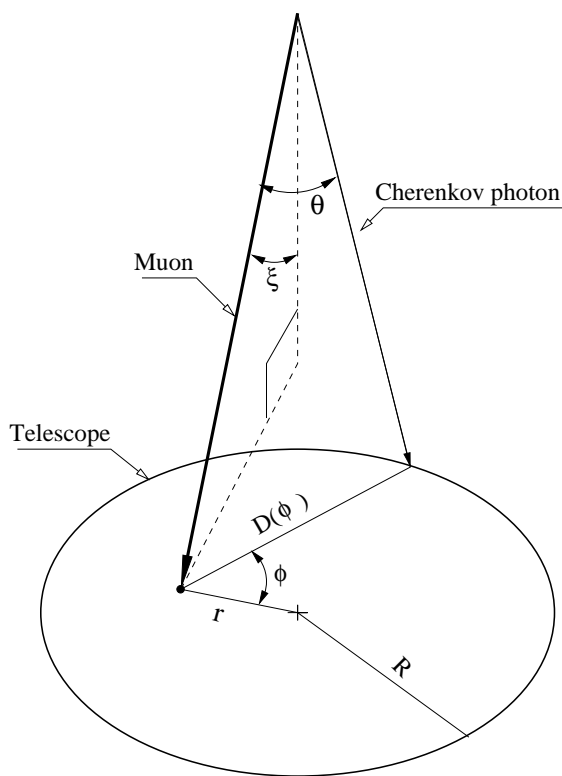
FIGURE 3.19. Impact geometry of a muon that can be imaged as a complete ring. Whether or not it is imaged as a complete ring depends on the f.o.v. of the camera. The angle at which Cherenkov photons are emitted relative to the direction of the muon is θ.

The number of photoelectrons is given by

$$\frac{d^3pe}{dl\, d\lambda\, d\phi} = L\, \alpha\, \sin[\theta]^2 \frac{M[\lambda]QE[\lambda]}{\lambda^2}. \tag{3.7}$$

Performing the integral over λ with the mirror reflectivity $M[\lambda]$ measurement of newly coated mirrors and the PMT quantum efficiencies a) and b):

$$K \equiv \int_{250\text{nm}\pm 50\text{nm}}^{700\text{nm}} \frac{M[\lambda]\, QE[\lambda]}{\lambda^2} d\lambda \tag{3.8}$$

$$K_a = 448272 \pm 95000 \text{ pe/m}, \ K_b = 375201 \pm 85000 \text{ pe/m},$$

where the error comes from the uncertainty in λ_{min}. The integral over the path length l depends on the radius of the telescope $R = 5\text{m}$, the impact parameter, r, and the angle of incidence ξ with respect to the telescope normal, see Fig. 3.19.

$$pe = K\, L\, \alpha\, \sin[\theta]^2 \int_0^{2\pi} d\phi \int_0^{l[\phi]} dl. \tag{3.9}$$

Consider only complete rings, then the impact parameter $r < R$. The integral over $l[\phi]$, the path length from which Cherenkov emission is captured by the telescope, is evaluated by the law of sines

$$\frac{D[\phi]}{\sin[\theta]} = \frac{l[\phi]}{\sin[\pi - \theta + \xi]}$$

where $D[\phi]$ is the distance in the plane of the telescope which captures radiation from the particle. Since $\theta < 1.3°$ and $\xi < 0.5°$ for the 10 m telescope, this can be simplified in the small angle approximation to

$$l[\phi] = \frac{D[\phi]\cos[\theta]}{\sin[\theta]}. \tag{3.10}$$

$D[\phi]$ is likewise found by the law of sines, see Fig. 3.20

$$\frac{D[\phi]}{\sin[\gamma]} = \frac{R}{\sin[\phi]} = \frac{r}{\sin[\alpha]},$$

with

$$\gamma = \pi - \phi - \alpha, \ \alpha = Sin^{-1}[\frac{r}{R}\sin[\phi]].$$

So that

$$D[\phi, r] = R\frac{\sin[\gamma]}{\sin[\phi]} = \sqrt{R^2 - r^2 \sin[\phi]^2} + r \cos[\phi], \tag{3.11}$$

and

$$pe = K\,L\,\alpha\,\sin[\theta]\,\cos[\theta]\int_0^{2\pi} \mathrm{d}\,\phi\sqrt{R^2 - r^2 \sin[\phi]^2} + r \cos[\phi]. \tag{3.12}$$

The integral over ϕ can be expressed as

$$pe = K\,L\,\alpha\,\sin[\theta]\,\cos[\theta]\,4\,R\,\mathrm{E}[\frac{r^2}{R^2}], \tag{3.13}$$

where E is the complete elliptical integral. The impact location of the muon on the telescope, r, can be estimated by the azimuthal photon distribution in the camera, requiring a more lengthy calculation and parameterization of the light asymmetry. Instead, here the impact location is averaged to make this calculation simple and tractable:

$$\langle pe \rangle = \frac{\int_0^R r\mathrm{d}r pe[r]}{\int_0^R r\mathrm{d}r} \tag{3.14}$$

$$\langle pe \rangle = K\,L\,\alpha\,\sin[\theta]\,\cos[\theta]\frac{16R}{3} \tag{3.15}$$

Eq. 3.15 predicts that the total number of photoelectrons that the camera should have received is proportional to the muon ring radius θ. The data acquisition system records events with a charge-to-digital converter. The $size$, measured in digital counts, dc, is proportional to the number of photoelectrons, pe. For each muon ring, the ratio dc/pe can be calculated from the measured $size$ and θ.

3.3.2 Selection of Muon Rings

Muons can be selected from the data using selection cuts on the standard parameters $length$, $width$, and $length/size$. However, this is not very efficient and manual verification of the images is still necessary. To facilitate the selection of muons with high efficiency, the following algorithm was developed.
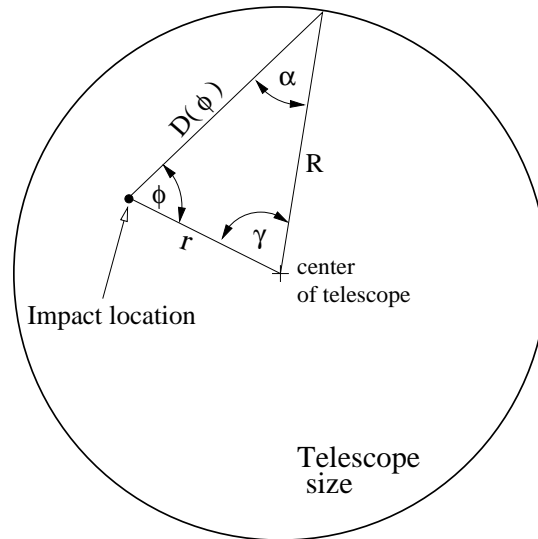
FIGURE 3.20. Angles used in the computation of $D[\phi]$.

1. Pedestal subtraction and flat fielding of all pixels, as described in Sect. 2.4.1. The resulting signal is in each pixel, i, is $v_i = (s_i - ped_i)g_i$.

2. Calculate the pedestal noise level for each pixel σ_i.

3. Cleaning: keep image pixel if $v_i > P \times \sigma_i$. Also, keep those pixels that are neighbors to i and have a signal larger than $B \times \sigma_i$. All other pixels are set to 0. The cleaning thresholds, P and B, are discussed below.

4. Make a binary image (1/0) using all picture and boundary pixels.

5. Create 45 ring masks of various sizes and positions. A mask consists of the values +1 within the ring and -1 outside.

6. Multiply the image with each mask. Keep the image if (binary picture * mask)/(number of pixels within ring) > 0.1.

7. Fit a circle to the binary image, with origin located at a distance ξ° from the center, Cherenkov angle θ, and RMS σ_θ, see Fig. 3.19.

8. Keep the image if: a) it is fully contained in the camera: $\xi + \theta + \sigma_\theta < 1.1°$, b) $\theta > 0.4°$, c) there is at least one pixel in each octant of the ring, and d) at least half of the pixels fall within $\theta \pm \sigma_\theta$.

9. Sum all pixel values v_i that fall within $\theta \pm 2\sigma_\theta$ and correct for the fraction of PMTs turned off.

An example of a muon-ring image selected with this algorithm is shown in Fig. 3.16, along with the fitted parameters. The distribution of $size$ vs. θ is shown in Fig. 3.21 of muons found in nineteen runs taken during the observing season 2000/1 on the Crab Nebula. A linear fit results in $size = (1956 \pm 20)\theta$ and $\chi^2_{red} = 1.17$, where the intercept (0,0) was chosen to correspond to the physical condition of no Cherenkov light emitted by muons at or below their threshold energy. Relaxing this condition and allowing for non-zero intercept results in the fit $size = (-5\pm110)dc+(1950\pm150)\theta$ and $\chi^2_{red} = 1.18$. This fit is compatible with zero intercept, but the error on the slope is much larger and hence only the fit with zero intercept will be used.

The muon selection algorithm was developed and optimized iteratively by comparison with a set of muon events that were selected by eye. Several comments on the algorithm are:

- The purpose of applying 45 ring-shaped masks to the image and testing for overlap is a 5 times speed increase over fitting a circle to each image.

- A circle is fitted by calculating the mean distance of the pixels from some origin. The best fit is achieved by picking a new origin until the variance of the distance distribution is minimized. The final sum of pixel values depends slightly on the width of the ring considered. Decreasing the width to $\theta \pm 1\sigma_\theta$ causes a 5% drop in the $size$. Likewise, increasing the thickness to $\theta \pm 3\sigma_\theta$ causes a 5% rise in the $size$.

- The image cleaning uses picture/boundary cleaning thresholds, P and B, different from the standard $Supercuts$ values of 4.25 and 2.25. Here, the thresholds are op-
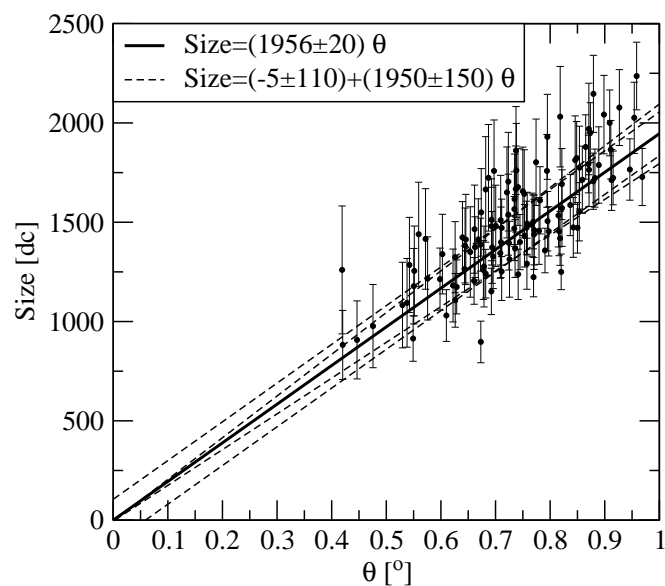
FIGURE 3.21. Distribution of *size* vs. Cherenkov angle for muons found in 19 observations of the Crab Nebula during the 2000/1 observing season. Also shown is a linear fit with zero intercept (*solid line*). For a linear fit with non-zero intercept, the 68% confidence interval of independent parameter variations of the intercept and slope are shown by *dashed lines*.
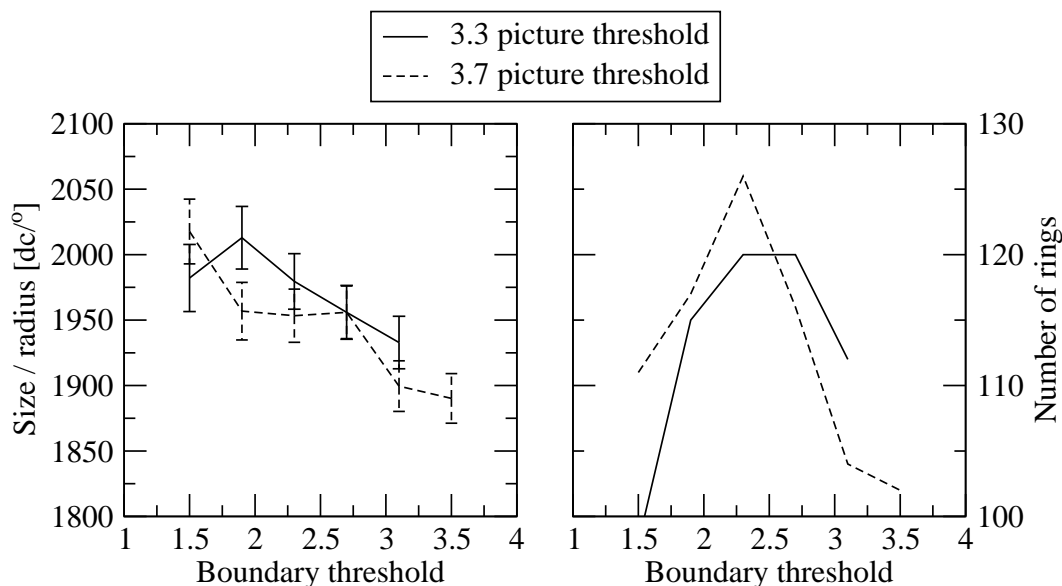
FIGURE 3.22. *Left:* Variation of the $size/radius$ ratio with picture/boundary thresholds of muon events identified in 8.5 hours of observations taken on the Crab Nebula during the 2000/1 observing season. *Right:* Variation of the number of muon rings with picture/boundary thresholds.

timized to selected the greatest number of muon rings while not picking up noisy pixels. Cherenkov light from muons is spread over a much larger angular area than the compact images of Cherenkov light produced by gamma-rays, hence muon images require lower cleaning thresholds to effectively detect them.

Fig. 3.22 shows the effect that varying the cleaning thresholds has on the number of selected muon events and on the $size/°$ ratio. For this purpose, muon events were searched for in nineteen observations taken on the Crab Nebula during the 2000/1 observing season. A larger range of picture thresholds was explored, but for clarity on the two best picture thresholds are shown. Based upon the highest number of identified muon events, the thresholds will be set at $P = 3.7$ and $B = 2.5$ for all future muon selections. Additional detail on the optimization of the thresholds is presented in Sec. 3.3.3.

Year	QE	dc/pe from Eq. 3.15	dc/pe from simulations	Measured
1995/6	a)	0.74±0.17	0.84±0.07	1.05±0.10
1995/6	b)	0.89±0.20	0.95±0.08	
2000/1	a)	1.86±0.42	2.6±0.19	3.3±0.3
2000/1	b)	2.68±0.61	3.1±0.22	

TABLE 3.4. dc/pe calibrations for 1995/6 and 2000/1 for two different PMT quantum efficiencies a) and b) shown in Fig. 3.18. The measured values are explained in Sect. 2.2.4 and Tab. 2.1

Shown in Tab. 3.4, column 3, is the dc/pe ratio calculated for the 1995/6 and 2000/1 observing seasons using quantum efficiencies a) and b). As an example, the calculation for 1995/6 a) is shown in Eq. 3.16. The error estimate of Eq. 3.15 stems mainly from the assumed 20% uncertainty in the lower wavelength cutoff.

$$\frac{dc}{pe} = \frac{780 \pm 20 \ dc/^{\circ}}{1050 \pm 241 \ pe/^{\circ}} = 0.74 \pm 0.17. \tag{3.16}$$

3.3.3 Simulation of Muon Events

The theoretical model presented in Sect. 3.3.1 does not take into account atmospheric extinction or different arrival directions. Instead of including those in a very detailed analytical model, the GrISU simulation package (GrISU, 2004) was used to determine the calibration. Because this is the same software used to simulate gamma-ray showers, it has the advantage that if for example the telescope had too few mirrors in the simulation, the muon calibration would correct for this automatically.

By specifying a muon as the initial particle in the KASCADE shower program, both the Cherenkov photon production and the telescope model are included in the calibration. This makes the calibration specific to the particular simulation used. Gamma-ray simulations then need to be carried out with the same program.

The parameters used to simulate muons are listed in Tab. 3.5. Muons produce the same amount of Cherenkov light with $kascade3$ and $kascade7$. This is because they do not

Energy range		4 GeV - 9 GeV
Differential index		-1.65
Number of throws		5,000
Zenith angle		0°
Initial depth		663 g/cm^2
Final depth		763 g/cm^2
Slice thickness		0.05 g/cm^2
Impact range		0 m - 5 m
Angular spread		0.5°
Night sky background		101 pe/(ns m^2 sr)
Trigger threshold	1995	2-fold, each > 67 mV
	2000	3-fold, each > 32 mV
Mirror reflectivity		0.95
PMT radius		14.14 mm ?WHAT ABOUT 2000?

TABLE 3.5. Parameters used in the Monte-Carlo simulation of muon showers.

produce a large number of secondaries and almost all of the Cherenkov light is produced by the initial muon. Again, an optimization of the picture/boundary thresholds was attempted to maximize the number of muon rings while remaining unaffected by noise. This was done for both years and for both QEs in Fig. 3.18 a) and b). For 2000/1 and QE a), the $size/°$ dependence on the boundary cleaning threshold for simulated and real muon rings is shown in Fig. 3.23. Both, simulated and real events show a fall in $size/°$ with increasing boundary threshold. This is due to preferentially thinner rings being selected. The number of simulated muon events selected by the procedure shows a slight peak using the values $P = 3.7$ and $B = 2.5$ as before. The dc/pe calibration is presented in Tab. 3.4. The error estimate includes statistical error, and systematic errors of 5% for the ring width, see above discussion of the muon selection algorithm, and 5% for the picture/boundary thresholds. The latter is a conservative estimate on the systematic error introduced by choosing different thresholds, see Fig. 3.22.
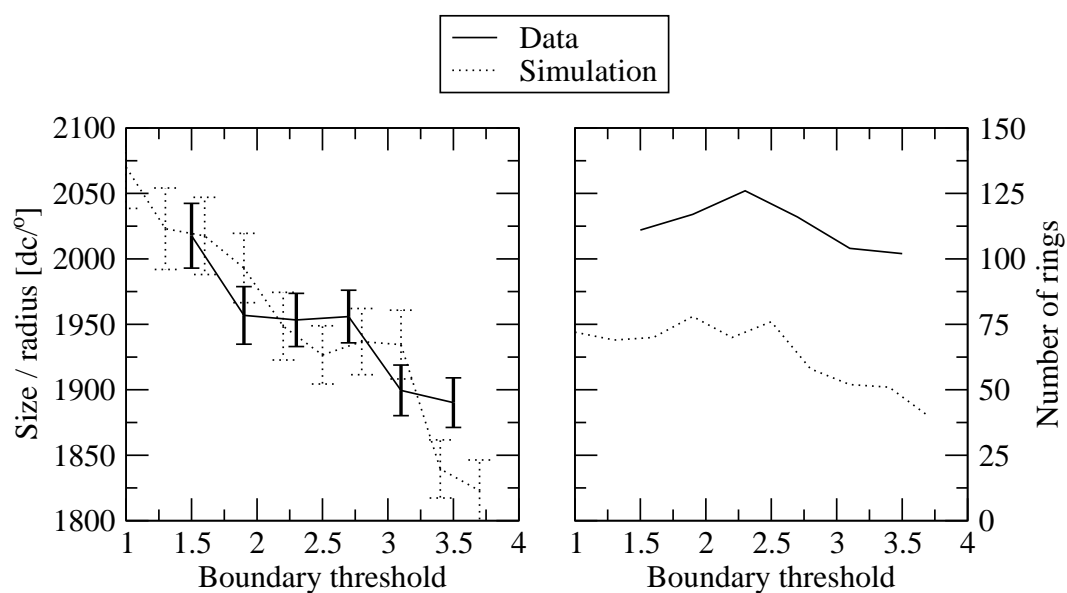
FIGURE 3.23. *Left:* Variation of the $size/radius$ ratio with boundary threshold of muon events elected from real data (*solid*) and of simulated muon events (*dotted*). *Right:* Variation of the number of muon rings with boundary threshold identified in the data (*solid*) and in the simulations (*dotted*). The picture threshold has been fixed at 3.7 for both graphs.
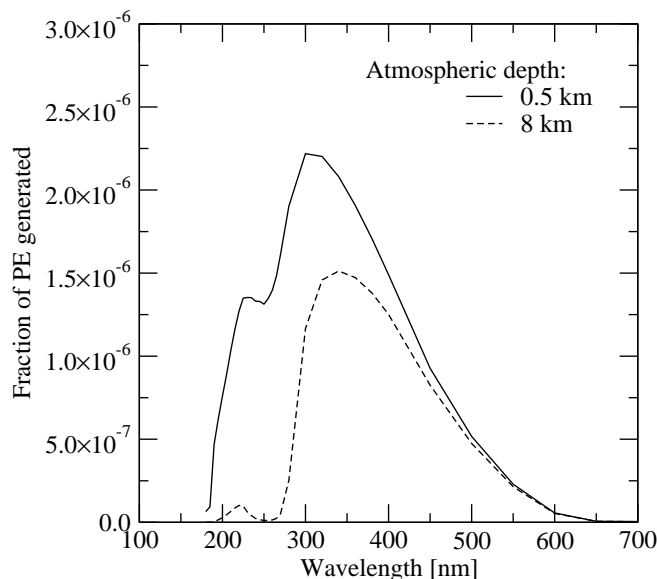
FIGURE 3.24. The fraction of Cherenkov photons that generate a photoelectron after transversing the atmosphere for 0.5 km (solid) and 8 km (dashed).

3.3.4 Difference to Cherenkov Light from Gamma Rays

A problem associated with using muon rings to calibrate the detector, is that the detector receives a higher fraction of UV Cherenkov light from muons than from gamma-rays. This is due to less atmospheric extinction for the shorter path length. The distance muon-generated Cherenkov light travels is less than 500 m, while simulations show that Cherenkov light from gamma-rays travels between 5 and 15 km. This introduces a large difference in the spectrum of Cherenkov light received by the telescope. This would not be a problem if the atmospheric extinction, PMT quantum efficiency, and mirror reflectivity were well known. However, since these are less well known below 270 nm, the calibration is prone to systematic errors. Fig. 3.24 shows the fraction of photoelectrons generated by photons of different wavelengths that travel 0.5 km, i.e. a muon-like spectrum, and 8 km, a gamma-ray like spectrum. The curves were produced by folding the atmospheric extinction with the PMT quantum efficiency and the mirror reflectivity.
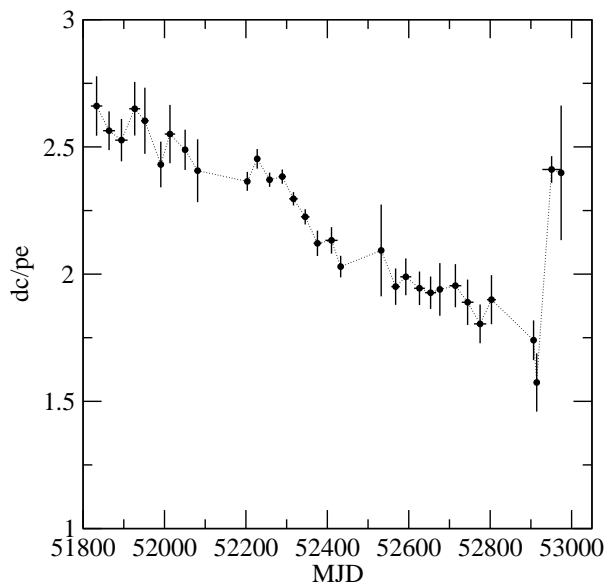
FIGURE 3.25. The dc/pe ratio from September 2000 through November 2003 calibrated for PMT quantum efficiency a).

3.3.5 Calibration from 2000 to 2003

From September 2000 through November 2003, the dc/pe ratio is shown in Fig. 3.25 for $kascade3$ and QE a). The dc/pe ratio dropped from 2.7 ± 0.15 to 1.65 ± 0.15. In Oct. 2003, the PMT gain was again raised to close to its initial value, by increasing the high voltage by 40 V. This raised the signal significantly above the electronic noise and made the system more stable. The drop in the gain is mainly due to deterioration of the last dynode. After operation for approximately 2600 hours during that time, it is expected that the output current reduces by 0.7 ± 0.1 (Ham, 2002). As the muon calibration method includes the optical light throughput by default, variations in the dc/pe ratio may also stem from weathering of the mirrors and light cones whose performance is kept fixed in the simulation.

3.4 The Crab Nebula Spectrum

The Crab Nebula serves as the standard candle in VHE gamma-ray astronomy; no flux or spectral variations have been detected by various groups CITE, CITE. Because the spectrum of two new sources will be measured in the following chapters for which new gamma-ray simulations must be carried out, the spectrum of the Crab Nebula will be derived for observations spanning the same period of time. This will be a check against possible errors in the simulation. The two sources for which new spectra will be measured are 1ES 1959+650 and 1ES 2344+514, treated in chapters 4 and 5, respectively.

Though only two new source spectra will be measured from data taken in 1995 and 2002, the VHE spectrum of the Crab Nebula will be derived for three observing seasons: 1995/6, 2000/1, and 2001/2. The telescope was operating in a stable condition in 2000/1 and a large number of Crab Nebula observation were taken. This makes the data set ideal for comparison between the shower simulation codes $kascade3$ and $kascade7$. Also, the camera configuration was changed from 109 to 490 pixels between 1995 and 2000, so that new detector parameters can be verified with this data. Between 2000/1 and 2001/2, a loss in telescope sensitivity was noticed. To correct for this, a calibration presented in Sect. 3.3 was applied to the simulations and was verified by measuring the Crab Nebula spectra for the 2001/2 season.

3.4.1 Observations

For 1995/6, all A weather data is considered. However, in 2000/1, Crab data taken under all weather conditions are included to increase the gamma-ray signal. The Crab data were taken above 56°elevation in stable weather conditions. Criteria for stability are raw rate fluctuations of less than 1.5 sec^{-1} and throughput values in line with "A" weather observations. A summary of the data is given Tab. 3.6.

	1995/6	2000/1	2000/1
Weather	A	A	all
Exposure (hr)	1 7.9	8.6	12.3
Rate (γ/min)	1.56 ± 0.06	3.0 ± 0.2	3.2 ± 0.2
Significance (σ)	25.3	15.4	18.5
$\sigma/\sqrt{\mathrm{hr}}$	6.0	5.2	5.5

TABLE 3.6. Summary of data taken on the Crab Nebula in the observing seasons 1995/6 and 2000/1.

Zenith angle		$20°$
Energy range		0.1 TeV - 100 TeV
Impact range		0 m - 300 m
Differential spectral index		-2.5
Number of throws		500,000
Initial depth		1 g/cm^2
Final depth		763 g/cm^2
Slice thickness		0.05 g/cm^2
Source extension		$0°$
Night sky background		101 pe/(ns m^2 sr)
Trigger threshold	1995/6	2-fold, each > 40 mV
	2000/1/2	3-fold, each > 32 mV

TABLE 3.7. Parameters used for the gamma-ray simulation. The first three entries are chosen according to the zenith angle of the observations and to give optimal coverage in energy and impact distance.

3.4.2 Simulation Details

Gamma-ray simulations were produced with both $kascade3$ and $kascade7$, with the parameters listed in Tab. 3.7. The dc/pe ratio is calibrated with muons, see Sect. 3.3.3. For $kascade7$, two PMT quantum efficiencies are used in the simulations: a) ISU values used in all publications and b) the values distributed with GrISU, see Fig. 3.18. Both are manufacturer specifications, but it is not known why they are different.

3.4.3 Spectrum in 1995/6 and 2000/1

Before proceeding with the spectral analysis, preliminary cuts were applied to the data and the simulations. To remove the low energy triggering region in 2000/1, the required minimum value of the largest three pixel was 50 dc, 45 dc, and 40 dc. To improve the energy resolution of the events, the angular $distance$ is restricted between 0.4° and 1.0°, see Fig. 2.10. Also, $alpha$ was restricted to less than 45°. The rms energy fit difference $log[E] - log[E_{est}]$ is 0.19, with energy resolution $rms(\frac{\Delta E}{E}) = 0.58$ and an average bias of 0.02. For the 1995/6 data, the following cuts were applied: $size_2 > 65\ dc$, $length/size < 0.00085$, $0.31° < distance < 1.1°$, and $alpha < 15°$. Here, the rms energy fit difference $log[E] - log[E_{est}]$ is 0.17, with energy resolution $rms(\frac{\Delta E}{E}) = 0.48$ and an average bias of 0.02. The spectra for 1995/6 and 2000/1 with PMT quantum efficiency a) are shown in Fig. 3.26. Statistical errors as well as two kinds of systematic errors are given. Systematic errors are explored by varying the dc/pe calibration within the tolerance given in Tab. 3.4 and by varying the cut tolerance by $\pm 0.5\sigma$ for $length$, $width$, and by $+5°$ for $alpha$. The statistical error includes the 63% CI for a fit with two independent parameters defined by $\chi^2_{min} + 2.3$. The best-fit to the spectrum between 320 GeV and 13 TeV for 1995/6 is

$$\frac{dN}{dE\ dt\ dA} = (4.2 \pm 0.3_{stat} \pm 0.4_{dc/pe} \pm 0.3_{cut}) \times 10^{-7}$$
$$E^{-2.38 \pm 0.08_{stat} \pm 0.02_{dc/pe} \pm 0.02_{cut}} \frac{1}{\text{TeV m}^2\ \text{s}}, \tag{3.17}$$

with χ^2_{min}/ndf = 3.2/(9-2), where the number of degrees of freedom is abbreviated with ndf. For 2000/1, the best-fit between 320 GeV and 13 TeV is

$$\frac{dN}{dE\ dt\ dA} = (2.8 \pm 0.2_{stat} \pm 0.4_{dc/pe} \pm 0.3_{cut}) \times 10^{-7}$$
$$E^{-2.49 \pm 0.09_{stat} \pm 0.03_{dc/pe} \pm 0.01_{cut}} \frac{1}{\text{TeV m}^2\ \text{s}}, \tag{3.18}$$

with χ^2_{min}/ndf = 5.3/(9-2). A summary of the Crab gamma-ray spectrum between 320 GeV and 13 TeV is presented in Tab. 3.8. Shown are the results for the two years, each calculated with both, $kascade3$ and $kascade7$. For the latter, two different PMT quantum efficiency curves were used. Also listed are published results by Whipple and HEGRA.
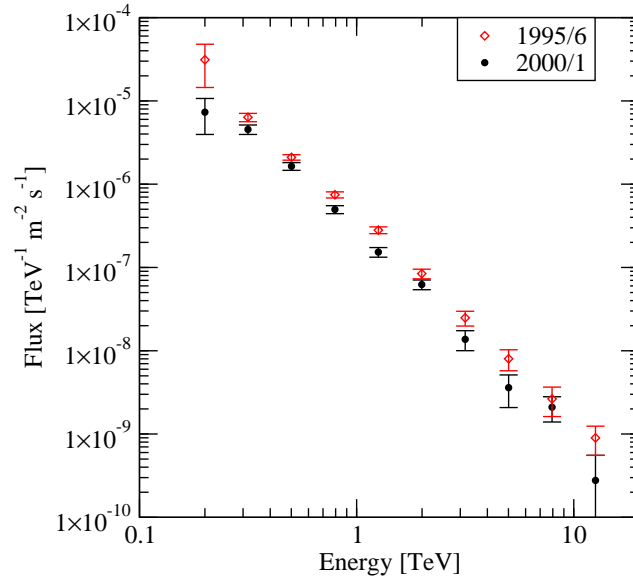
FIGURE 3.26. Gamma-ray spectrum of the Crab Nebula in 1995/6 and 2000/1 using quantum efficiency curve a).

	1995/6	2000/1
$kascade3$, **QE a)**	$(4.2 \pm 0.3) \times 10^{-7} E^{-2.38 \pm 0.03}$	$(2.8 \pm 0.2) \times 10^{-7} E^{-2.49 \pm 0.09}$
$kascade7$, **QE a)**	$(5.4 \pm 0.3) \times 10^{-7} E^{-2.42 \pm 0.08}$	$(3.5 \pm 0.3) \times 10^{-7} E^{-2.51 \pm 0.09}$
$kascade7$, **QE b)**	$(5.4 \pm 0.3) \times 10^{-7} E^{-2.40 \pm 0.08}$	$(3.8 \pm 0.3) \times 10^{-7} E^{-2.51 \pm 0.09}$
Whipple[a]	$(3.12 \pm 0.40) \times 10^{-7} E^{-2.57 \pm 0.12}$	
HEGRA[b]		$(2.79 \pm 0.52) \times 10^{-7} E^{-2.59 \pm 0.08}$
Whipple 1989[a]	$(3.41 \pm 0.25) \times 10^{-7} E^{-2.38 \pm 0.10}$	

TABLE 3.8. Gamma ray spectrum of the Crab Nebula between 320 GeV to 13 TeV in 1995/6 and 2000/1 as determined using different simulations. The errors for the spectra calculated here are statistical only, while those of other publications include statistical plus systematic errors. The HEGRA spectrum was taken between 1 TeV and 20 TeV.

[a]Mohanty et al. 1998

[b] Aharonian et al. 2000b

The spectral index is in good agreement between both years and the different simulations. However, the flux constant is systematically higher in 1995/6 than in 2000/1. A decrease in the TeV gamma-ray flux from the Crab Nebula is unlikely. This leaves as the cause for a decreasing flux constant a systematic error in the dc/pe calibration. An increase in the dc/pe ratio decreases the flux constant. This is because if a simulated shower at the same energy makes a brighter image, the same measured shower now looks more like a simulated shower with lesser energy. The 109 camera was not very sensitive to muons and only the very brightest triggered the camera. However, this is unlikely the cause of the disagreement as the discriminator threshold in the simulation was set at the same level as the hardware trigger.

Both shower simulations reconstruct the spectral index of the Crab Nebula spectrum correctly; the difference is within the statistical error. However, the flux constant calculated with $kascade7$ is consistently higher than with $kascade3$. This means that $kascade7$ increases the estimated shower energy by 10% and this must be taken into account as an additional systematic error. Further investigation into the changes are in progress.

3.4.4 Spectrum in 2001/2

Of interest for the analysis of the blazar 1ES 1959+650 flare in June 2002 is the contemporaneous Crab Nebula spectrum. Unfortunately, this is not possible as the Crab Nebula is only visible until April with decreased elevations beginning in February. By requiring the dc/pe calibration to be approximately constant for all data, Fig. 3.25 shows that the time period is restricted to October through January. The $Quicklook$ analysis of the selected 39 pairs in A weather is shown in Fig. 3.27. The unusually large 2.7σ excess in the *ctl*-region ($20° < alpha < 65°$) builds up steadily in time; it is not correlated with raw rate or pedestal fluctuations, or with throughput. The dc/pe calibration was performed with muon rings from the same 39 Crab ON/OFF pairs. Its value of $2.38 \pm 0.02 dc/pe$ is compatible within month-to-month variations from October through January, shown in Fig. 3.25. The fit

Alpha Plot

Analysis for aPR.56.90_OctJan

From 20011015 to 20020115
0 tracking files with 0 min.
39 ON/OFF pairs with 1075 min.

Significance Rate   +/-
on-region: 25.18   2.91   0.12
off-region: 2.72   0.51   0.19

Counts   on-region off-region
ON/TRK 9296   20832
OFF   6165   20281

0.13 < length < 0.25
0.05 < width < 0.12
0.40 < distance < 1.0
0 < length/size < 0.0004
size > 0, size1 > 30
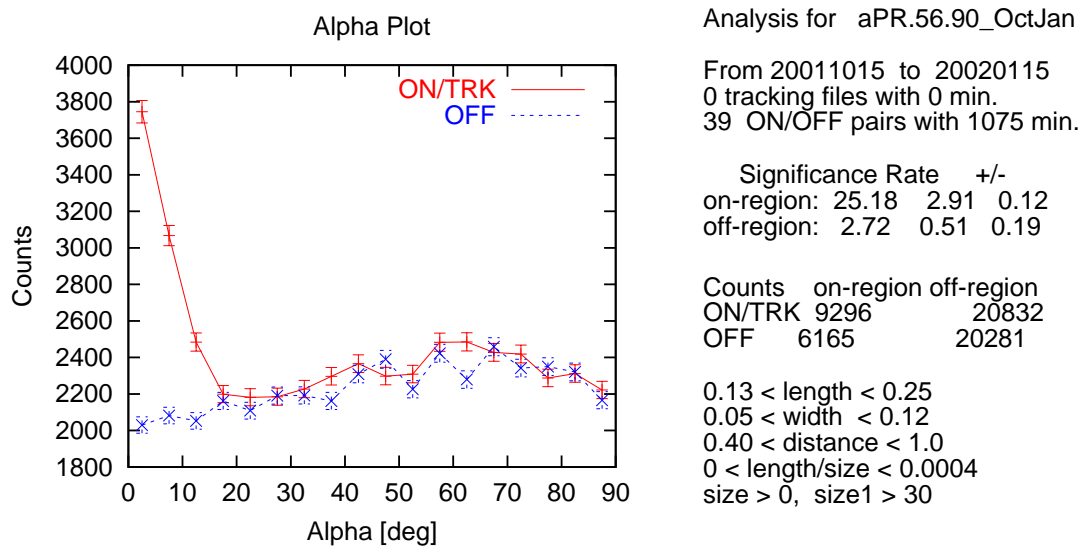
FIGURE 3.27. *Quicklook* analysis of the Crab data taken in 2001/2.
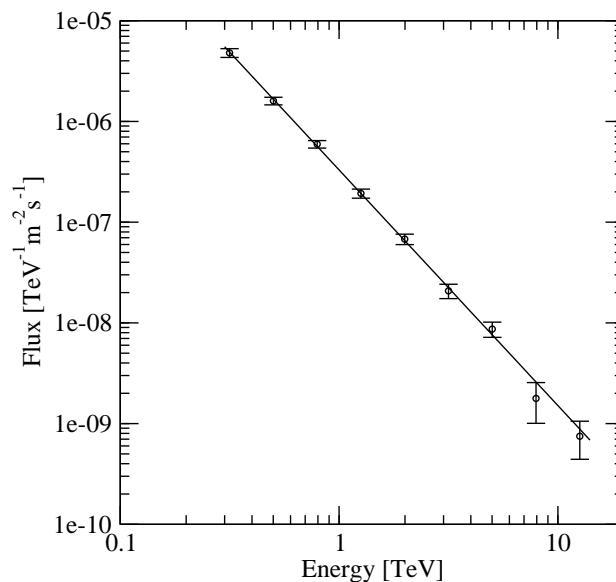
FIGURE 3.28. Differential spectrum of the Crab Nebula during 2001/2.

of the energy estimation function was done between 250 GeV and 20 TeV with an rms difference $log[E] - log[E_{est}]$ of 0.19, energy resolution $rms(\frac{\Delta E}{E}) = 0.62$ and an average bias $log[E] - log[E_{est}]$ of 0.005. The spectrum of the Crab Nebula, Fig. 3.28, can be fitted with a power law between 312 GeV and 13 TeV by

$$\frac{\mathrm{d}N}{\mathrm{d}E \, \mathrm{d}A \, \mathrm{d}t} = (3.3 \pm 0.2_{st}) \times 10^{-7} E^{-2.34 \pm 0.07_{st}} \frac{1}{\mathrm{TeV} \, \mathrm{m}^2 \, \mathrm{s}}, \qquad (3.19)$$

with $\chi^2_{min}/ndf = 2.6/(9 - 2)$. Only statistical errors have been calculated; the systematic uncertainty of the flux constant is estimated as ± 0.6 and that of the index ± 0.04. Thus, the spectrum is in agreement with other years, see Sect. 3.4.3.

CHAPTER 4

FLARE SPECTRUM OF 1ES 1959+650

The BL Lac object, 1ES 1959+650 (1ES 1959), at a redshift of 0.047, is the super massive black hole at the center of a galaxy, shown in Fig. 4.1. It was discovered in 1993 by comparing the X-ray/radio/optical fluxes of objects in the *Einstein* IPC Slew Survey (Schachter et al., 1993). 1ES 1959 was first detected at VHE energies by the Utah Seven Telescope Array in mid-1998 (Nishiyama et al., 1999). During May 2002, it was seen in a flaring state in the VHE energy regime for the first time by the Whipple Observatory (Weekes et al., 2002). During the following two months, the object was intensely monitored by the VERITAS (Holder et al., 2003b,a) and HEGRA collaborations (Aharonian et al., 2003b). Overlapping with the VHE observations were radio, optical, and X-ray observations (Schroedter et al., 2003; Horns et al., 2002; Krawczynski et al., 2003, 2004). See App. E for an updates to the analysis presented in (Schroedter et al., 2003).
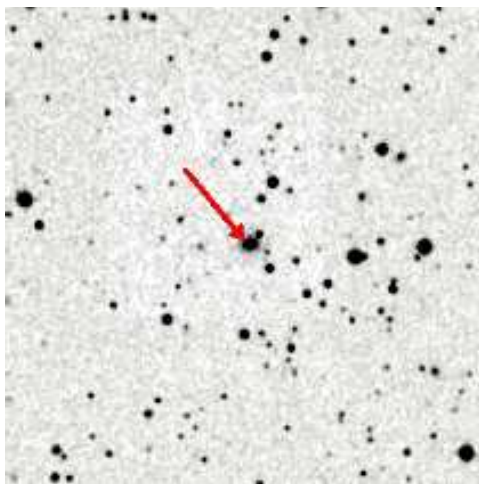
FIGURE 4.1. Optical image of 1ES 1959 (indicated by arrow) on a 6' by 6' field of view.

4.1   History and Spectral Energy Distribution

1ES 1959 is classified as a high-frequency peaked BL Lac with an X-ray to radio flux ratio $\log F_{1keV}/F_{5GHz} > 5.5$ (Urry et al., 2000). The host galaxy of 1ES 1959 is elliptical with a half-width half-max radius of $r_e = 6.64 \pm 0.13$ kpc, assuming H_0=50 km s^{-1} Mpc^{-1} and q_0=0 (Urry et al., 2000). The host galaxy size was determined from a fit of emission from a point source, 1ES 1959, plus an elliptical galaxy convolved with the point spread function of the telescope. The central black hole mass was derived from stellar velocity dispersion measurements to be $10^{8.09}$ M$_\odot$(Woo and Urry, 2002).

The spectral energy distribution of 1ES 1959 is shown in Fig. 4.2. Across the entire spectrum it is an unresolved point source. Infrared and optical radiation from the host galaxy, shown by a thick line and labeled "Galaxy light" in Fig. 4.2, are relatively weak compared to the emission from the jet. Near-contemporaneous data across the entire spectrum for the VHE flare on 4 June is shown by *open squares* in Fig. 4.2. At radio wavelengths, the flux level did not change during the flare compared to archival data.

During two X-ray flares in 2000, a correlation was seen between the hardness ratio and the flux (Giebels et al., 2002). This suggests that the steady emission is due to the large-scale relativistic jet, while the flares are due to knots or hot spots as are commonly seen in the jets of non-aligned AGN. The EGRET 95% confidence level upper limit for 1ES 1959 is 1.62×10^{-7} cts cm^{-2} s^{-1}, E$>$ 100 MeV (Hartman et al., 1999). The peak response for most sources detected with EGRET lies at around 300 MeV, so we derive an upper limit at 300 MeV of about 7.8×10^{-11}erg cm^{-2}.

4.2   Lightcurve in 2002

Observations on 1ES 1959 were taken with the Whipple 10m telescope from 16 May 2002 through 8 July 2002 (UT) for a total of 36 hrs. The light curve derived from a tracking (TRK) analysis with $Supercuts2000$ applied is shown in Fig. 4.3. Holder et al. (2003a) applied a correction to the integral gamma-ray rate to account for the loss of telescope
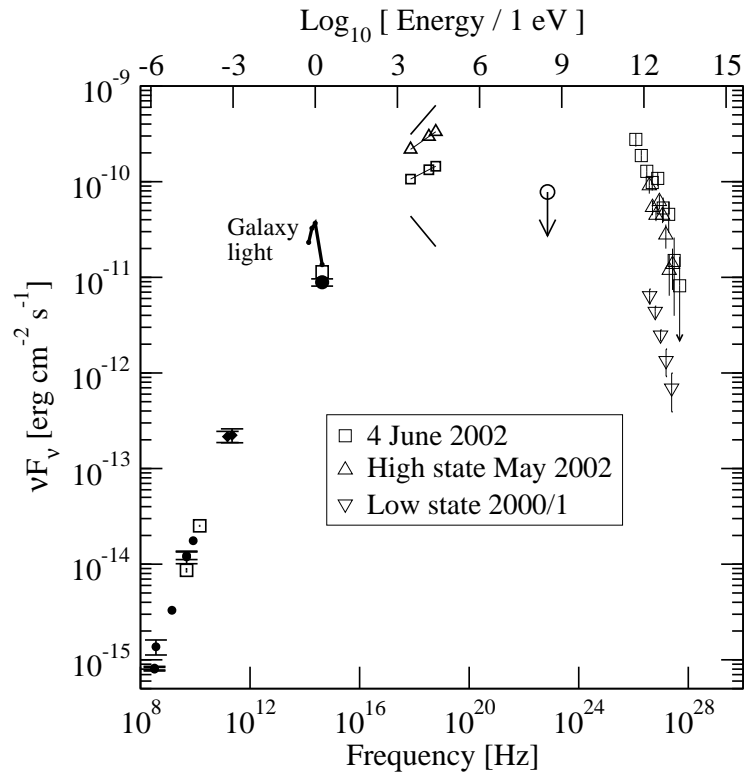
FIGURE 4.2. Spectral energy distribution of 1ES 1959 along with the VHE spectrum obtained with the Whipple telescope. Data taken from the following sources: 325 MHz radio data from (Rengelink et al., 1997), 365 MHz from Texas radio survey (Douglas et al., 1996), 1.4 GHz from Greenbank (White and Becker, 1992), 4.85 GHz from Greenbank (Gregory and Condon, 1991), 8.4 GHz from VLA (Patnaik et al., 1992), galaxy photometry at millimeter wavelength from (Stevens and Gear, 1999), galaxy photometry (*thick line and points*) at K, H, and J-bands from 2MASS (Jarrett et al., 2003), galaxy and nucleus R-band photometry obtained with Hubble Space Telescope and corrected for interstellar reddening (Urry et al., 2000). *Open squares* indicate measurements (nearly) contemporaneous with the VHE flare on 4 June flare (Krawczynski et al., 2004), *triangles up* indicate the time averaged spectrum in May while the source was in a high state (> 0.5 Crab). Also shown are two other X-ray spectra from Krawczynski et al. (2004) that indicate the range of spectra observed during flares in May (*upper curve*) and during a quiescent VHE state in mid June (*lower curve*). The upper limit at 300 MeV is from EGRET (Hartman et al., 1999) averaged over several years. The VHE gamma-ray spectrum during the quiescent state in 2000/1 and during flaring in May 2002 are taken from (Aharonian et al., 2003b). The VHE flare spectrum on June 4 is derived in this work.

sensitivity that was based on the measured background rate. Here, no correction is applied to the data, but for the spectral analysis the simulations are calibrated using the measured brightness of muon rings, see Sect.. 3.3.
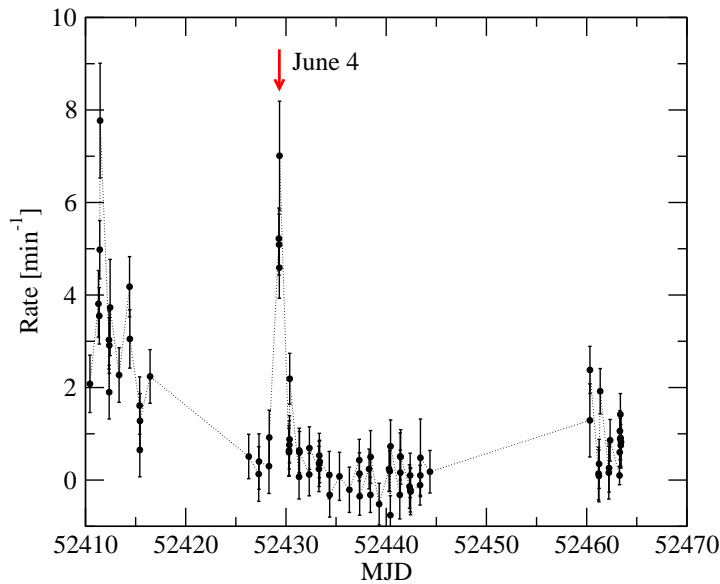
FIGURE 4.3. Rate of gamma rays with energy greater than 670 GeV detected from 1ES 1959 during May through July 2002.

4.3 Flare and Background Data

The spectrum will be derived for the gamma-ray flare observed on the night of 4 June 2002, 52429 MJD. The detailed lightcurve is shown in Fig. 4.4. During the 2 hours of observations, no strong evidence for variability was found; the χ^2 probability for constant emission is 8% (Holder et al., 2003a).

Holder et al. (2003a) also found that this gamma-ray flare had developed in less than seven hours, the fastest change observed for this source in any waveband. Simultaneous RXTE observations at the time of the VHE gamma-ray flare did not reveal any change in the 2-10 keV flux or the 3-25 keV photon index (Krawczynski et al., 2003). The presence of a VHE gamma-ray flare without X-ray activity cannot be modeled by a single electron
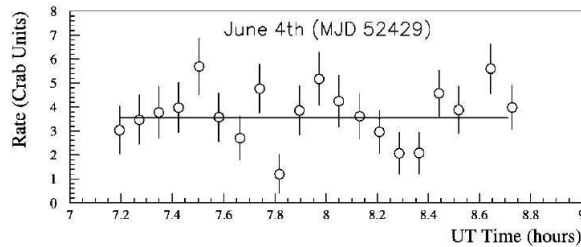
FIGURE 4.4. The gamma-ray rate for the flare night in 5 minute binning, taken from Holder et al. (2003a). The rates have been corrected for zenith angle of observation and relative telescope efficiency as described there.

population, but requires a two-component model (Krawczynski et al., 2003). This the first example of an "orphan" gamma-ray flare.

The flare data consists of 4 on-source observations without immediately following off-source observations. This tracking (TRK) mode of observations is used when a strong signal is measured and the systematic error arising from non-contemporaneous off-source (OFF) observations is expected to be small. Total on-source exposure time was 92 minutes.

The selection of OFF runs was based on their similarity to the TRK runs in date, elevation, throughput, pedestal fluctuation. In particular, OFF files were taken within 1 month of the TRK observation, within $5°$ of elevation, throughput factor within 0.05, and pedestal fluctuations less than or equal to the TRK run.

A summary of the tracking data together with the selected non-contemporaneous off-source observations is given in Tab. 4.1. The table shows in the third column the throughput factor for the TRK and OFF runs; this is the background event rate due to cosmic rays measured relative to a reference run with clear night sky. The raw gamma-ray rate derived with $Supercuts2000$, Tab. 2.2, and not corrected for throughput or elevation is shown in column four. Additionally, the last column shows how well the TRK and OFF runs are matched to each other; it is the statistical significance of background events between the ON and OFF observation. These events are not part of the gamma-ray signal and were selected according to the criteria given in Tab. 4.1. The background events cover the entire

energy range considered in the spectral analysis. For a good match, the significance is required to be less than 1.5-σ. For all four pairs the combined excess is 0.58-σ, meaning the TRK and OFF runs are well matched to each other.

TRK/OFF[a]	Elevation	Throughput	Rate[b]	Match[c]
22353/595	46°/50°	0.51/0.52 ±0.04	4.82 ± 0.67	-0.60
22354/609	48°/51°	0.55/0.54 ±0.06	4.35 ± 0.68	-0.02
22355/458	51°/52°	0.59/0.57 ±0.05	5.37 ± 0.66	1.19
22356/231	52°/54°	0.60/0.64 ±0.05	7.32 ± 1.18	0.77
		Total	5.11 ± 0.37	0.58

TABLE 4.1. Detailed look at flare data of 1ES 1959 on 4 June 2002.
[a] Run number.
[b] Gamma-ray rate per minute after $Supercuts2000$, see Tab. 2.2.
[c] Significance of the cosmic ray event excess between the TRK and OFF run. Events selected for this purpose are not part of the gamma-ray signal and should provide a relatively unbiased estimate of the similarity between the observation conditions. The criteria that define this control region are: 20°$< alpha <$65°, 0.4°$< distance <$1.0°, $max1 > 50$ dc, $max2 > 45$ dc, and $max3 > 40$ dc.

4.3.1 Sky Quality

The weather was rated "B-" for the night because of wispy clouds before sunset. Usually, such high cirrus clouds do not have a large effect on the gamma-ray detection rate. The raw rate was stable for all runs and the throughput, Fig. 4.5, falls in line with A weather observations during May and June, though the throughput in May was generally higher than in June.

4.4 Description of the Monte-Carlo Simulation

Simulations of gamma-ray initiated atmospheric showers and detection by the telescope were carried out with the Grinnell-ISU (GrISU) package, based on Kertzman and Sembroski (1994) and described in part in Mohanty et al. (1998). The parameters used to produce the simulations are the same as listed in Tab. 3.7, with the exception of energy
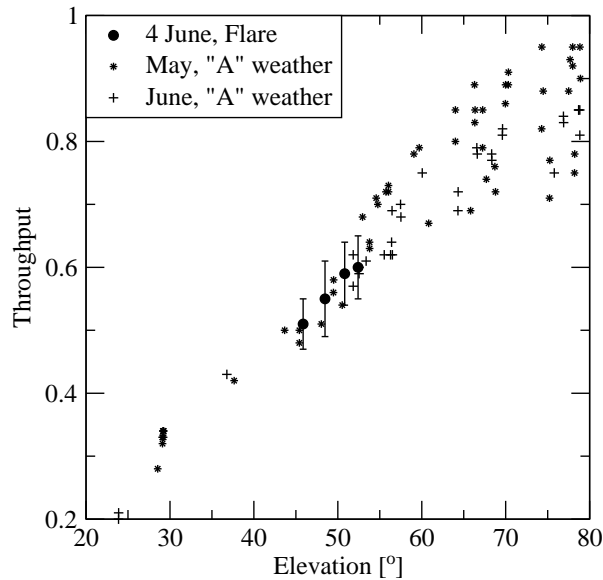
FIGURE 4.5. Throughput of flare data and "A" weather data in May and June.

range: 0.15 TeV$<$E$<$100 TeV and zenith angle, 41°. The light-to-digital counts conversion of the telescope was calibrated by comparison of simulated muon rings with those found in contemporaneous 1ES 1959 data, see Sect. 3.3. Its value of 2.10 ± 0.05 dc/pe is in agreement[1] with 2.03 ± 0.05 dc/pe determined for the entire month of June, see Fig. 3.25.

To improve the energy resolution in the spectral analysis and to reduce bias due to uncertainties around the triggering threshold the following loose cuts were applied to the simulations and the data: $0.4° < distance < 1.0°$, $max1 > 50$ dc, $max2 > 45$ dc, $max3 > 40$ dc, $alpha < 35°$. For a Crab-like spectrum with differential index -2.5, the differential and integral trigger rates are shown in Fig. 4.7. The peak trigger rate occurs at an energy of 0.82 TeV for the spectral cuts, described below, and 0.87 TeV with $Supercuts2000$. With these cuts, 90% of the triggers occur above 0.62 TeV and 0.67 TeV, respectively. The collection area, shown in Fig. 4.7, reaches 10% of its maximum value of 126,000 m^2 at an energy of about 560 GeV for the spectral cuts.

---

[1]This factor includes changes of the telescope optics. As these are not part of the electronics chain, the dc/pe value derived here cannot be compared directly with other published calibrations.
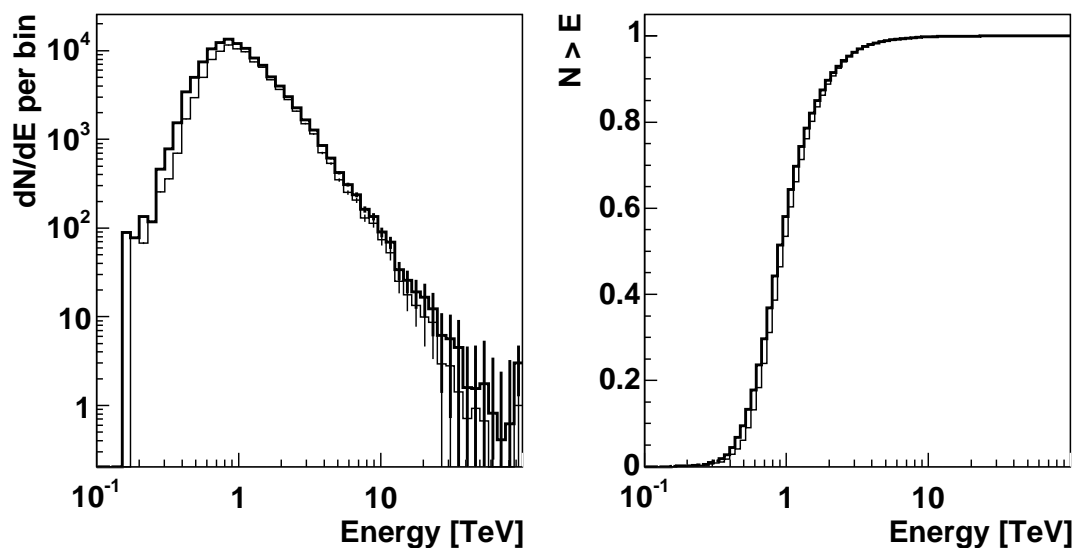
FIGURE 4.6. *Left:* Trigger rate from a source with spectral index -2.5 after spectral cuts (bold) and $Supercuts2000$ (thin). *Right:* Integral trigger rate normalized to 1.
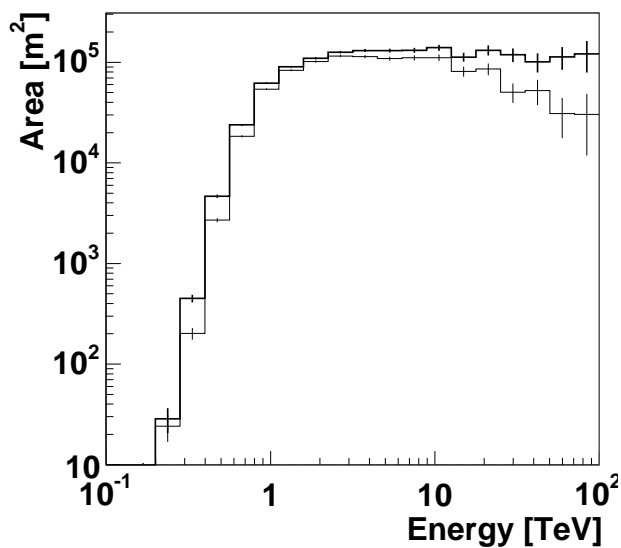
FIGURE 4.7. Collection area of gamma-rays at 49° elevation in May/June 2002 for spectral cuts (bold line) and $Supercuts2000$ (thin line).

4.5   Event Selection and Energy Estimation

The spectral analysis is a combination of both, method 1 and 2 by Mohanty et al. (1998), see Sect. 3.2 and Petry et al. (2002). The method consists of deriving $size$-dependent cuts on $length$, $width$, and $alpha$, shown in Fig. 4.8, and fitting an energy estimation function to the measured $size$ and $distance$ of simulated gamma rays. About 89% of the simulated gamma rays pass all cuts relatively independent of $size$. The fit results in an energy resolution of $rms(\Delta \log E) = 0.17$, $rms(\Delta E/E) = 0.48$, and $bias(\Delta \log E) = 0.015$. The fit was performed over the energy range from 0.4 TeV to 40 TeV. The lower limit is a combination of the collection area fall-off with decreasing energy and the energy resolution at that point: 0.56 TeV$/(1+0.48) \approx 0.4$ TeV. A cut-off at the upper limit is necessary because of poor event statistics of the Monte-Carlo simulation.
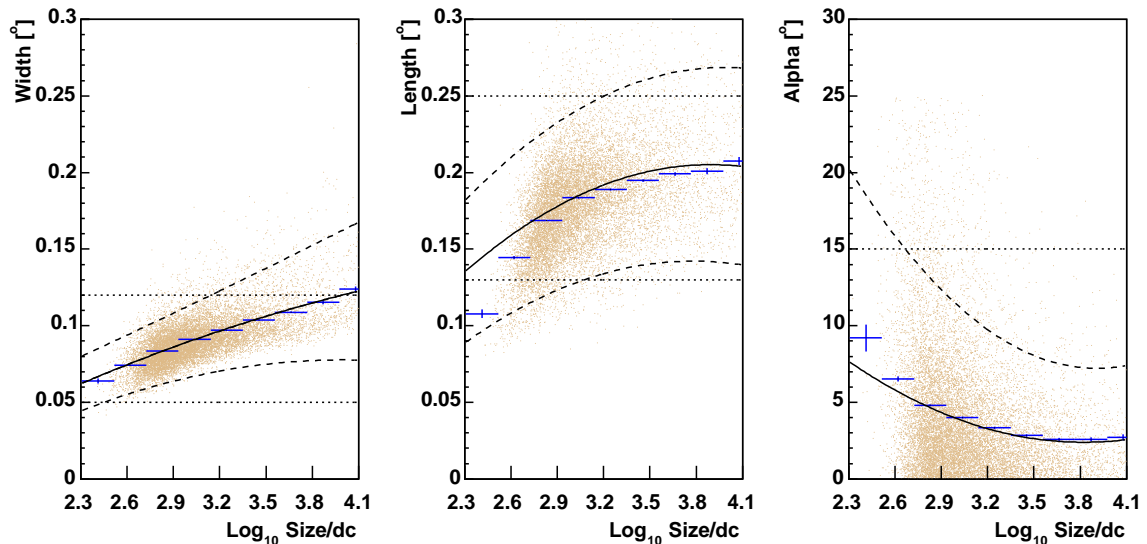
FIGURE 4.8. Parameter distributions and cuts versus $\log(size)$ from Monte-Carlo simulation at $49°$ elevation after application of loose spectral cuts. The *dots* are simulated events, the *blue crosses* show the mean, while the *solid lines* show the polynomial fit through the mean. *Dashed lines* show the actual cut chosen at a tolerance of two standard deviations around the mean. *Dotted lines* show cut level of $Supercuts2000$.

4.5.1   Spectral Reconstruction

To fit a functional form to the spectrum, the signal excess is binned with logarithmic width about equal to the energy resolution: $\Delta(\log E) = 0.2$ (Scott, 1979; Mohanty et al., 1998) with the lowest bin starting at $\log E = -0.4$ as discussed in Sect. 4.5 .

4.6   Flare Spectrum

For 1ES 1959, the number of excess events in each energy bin passing all cuts is shown in Tab. 4.2.

Energy [TeV]	ON [events]	OFF [events]	ON-OFF [events]	S [σ]	Flux [TeV^{-1}m^{-2}s^{-1}]
0.50	136	50	86±14	6.3	$(6.89\pm1.10)\times10^{-6}$
0.79	205	81	124±17	7.3	$(1.86\pm0.26)\times10^{-6}$
1.26	183	79	104±16	6.4	$(5.06\pm0.79)\times10^{-7}$
2.00	136	57	79±14	5.7	$(1.54\pm0.27)\times10^{-7}$
3.16	93	27	66±11	6.0	$(6.76\pm1.14)\times10^{-8}$
5.01	35	11	24±7	3.5	$(1.32\pm0.38)\times10^{-8}$
7.94	17	4	13±5	2.8	$(4.51\pm1.61)\times10^{-9}$
12.59	4	1	3±2	1.3	$(5.92\pm4.36)\times10^{-10}$
19.95	1	0	1±1	1.0	$(1.28\pm1.29)\times10^{-10}$
Total	810	310	500±33.5	14.9	

TABLE 4.2. Statistics in each energy bin for the flare data.

Fig. 4.9 shows the flare spectrum with statistical error bars. The systematic uncertainty stems from the combined statistical and systematic uncertainty of the dc/pe calibration, estimated at 10%, see Sect. 3.3.3, and from the chosen cut tolerance, t. To explore the uncertainty arising from the cut tolerance, t will be varied around 2 ± 0.5. The power law fit to the spectrum over the energy range from 0.5 TeV to 20 TeV including statistical (st) and systematic (sy) uncertainties is given by

$$\frac{\mathrm{d}N}{\mathrm{d}E\,\mathrm{d}A\,\mathrm{d}t} = (1.03 \pm 0.07_{st} \pm 0.1_{sy}) \times 10^{-6} E^{-2.73\pm0.08_{st}\pm0.05_{sy}}\ \frac{1}{\mathrm{TeV\ m^2\ s}}, \qquad (4.1)$$

with $\chi^2_{min}/ndf = 7.5/(9-2)$. The χ^2 probability that this data would randomly arise from the power-law fit is 0.29. The statistical error represents the 68% confidence interval (CI) for a fit with one free parameter and the other parameter frozen at its optimum value. The 68% CI with two simultaneous free parameters, defined by $\chi^2_{min} + 2.3$, is shown in Fig. 4.10 along with two other probability contours. Though the χ^2 value of the fit is acceptable, a power law fit exponential cut-off is also explored, shown in Fig. 4.9 by a dashed line. This cut-off parameterization has been frequently used to characterize the absorption of VHE gamma rays by extragalactic light. Though the attenuation follows an exponential shape $e^{-\tau}$, the optical depth τ does not vary linearly with energy so that a cut-off found with this simple parameterization should be interpreted as evidence for absorption, but not as a physically quantitative statement. The power law fit with exponential cut-off is

$$\frac{\mathrm{d}N}{\mathrm{d}E\,\mathrm{d}A\,\mathrm{d}t} = (1.10 \pm 0.09 \pm 0.05) \times 10^{-6}\, e^{-E/13 \pm 7 \pm^{\infty}_{2} TeV}\, E^{-2.44 \pm 0.14 \pm^{0.05}_{0.24}}\, \frac{1}{\text{TeV m}^2\, \text{s}}, \quad (4.2)$$

with $\chi^2_{min}/ndf = 4.4/(9-3)$, a χ^2 probability of 0.62. The F-test probability of obtaining this lower χ^2 value randomly over the power law fit is 66%. The improvement over a pure power law is not significant, but from Fig. 4.9 a slight downturn of the flux above 10 TeV is noticeable. The 95% asymptotic CI of the cut-off energy as the only free parameter ranges extends to 31 TeV, past the the available data. This, together with the systematic uncertainty of $\pm^{\infty}_{2}$, leads to the conclusion that no statement can be made about the existence of an exponential cut-off.

The selection of OFF runs for this analysis was based on several reasonable, but ad-hoc criteria. To check the validity and possible systematic errors arising from this choice, two other sets of OFF runs were also used in the spectral analysis. One set consisted of OFF data that was well matched to the TRK runs by using $Supercuts 2000$ with $20° < alpha < 65°$ instead of the cuts described in Tab. 4.1. These cuts restrict the events to a slightly higher energy range. The fitted power law spectra with and without exponential cut-off were found to be compatible within statistical uncertainties. Another set of OFF runs was composed of 1ES 1959 TRK runs that had little or no signal in them, but were otherwise similar to the
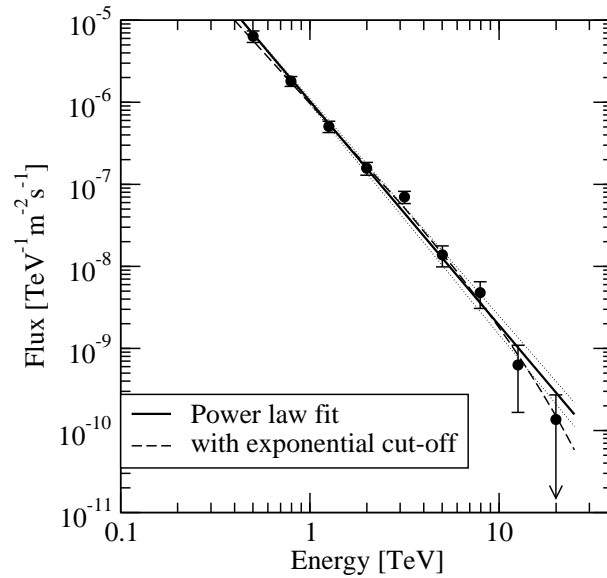
FIGURE 4.9. Differential flux spectrum of 1ES 1959 on 4 June 2002 together with a power-law fit (solid) and a power-law fit with exponential cut-off (dashed). Dotted lines on the power law fit show the CI obtained by varying both parameters to their individual 68% confidence interval.

June 4 data. This resulted in a similar spectral index, but with a reduced flux constant as the OFF runs had a small amount of signal in them.

The HEGRA collaboration measured the spectrum of 1ES 1959 during its quiescent phase from 2000 through 2001 and during major outbursts in May and July 2002 (Aharonian et al., 2003b). While 1ES 1959 was in a flaring state during 6 nights in May and July 2002, they derived a spectrum of $(7.4 \pm 2.2) \times 10^{-7} E^{-2.83 \pm 0.22}$ TeV^{-1}m^{-2}s^{-1}, χ^2_{red}(d.o.f.) = 1.9 (6) between 1.5 TeV and about 10 TeV, shown in Fig. 4.11. Though the HEGRA spectrum was derived over a different time period and excludes the June 4 flare, it is compatible with the spectrum of the "orphan" flare on June 4. The HEGRA spectrum is also compatible with the Whipple 10 m spectrum measured during flaring activity in May 2002 (Daniels et al., 2004).

HEGRA also fitted a power law with exponential cut-off to the data: $(5.6 \pm 1.6) \times 10^{-7} e^{-E/(4.2 \pm 1.5 TeV)} E^{-1.83 \pm 0.23}$ TeV^{-1}m^{-2}s^{-1}, χ^2_{red}(d.o.f.) = 1.7 (5). The cut-off energy
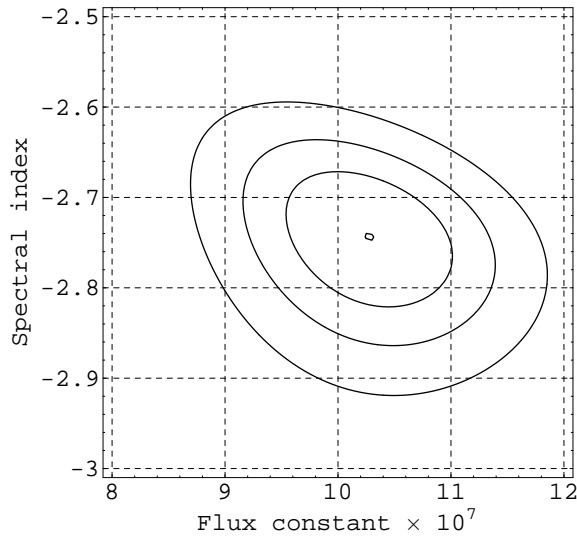
FIGURE 4.10. Confidence regions for the power law fit without exponential cut-off with probability content of 40%, 68%, and 90% for the simultaneous values of the spectral index and flux constant. Contour lines are drawn at χ^2_{min}+1, 2.3, and 4.6.

measured by HEGRA is statistically compatible with no cut-off at all and thus with the Whipple spectra.

During the quiescent phase, the spectrum was measured by HEGRA to be $(7.8 \pm 2.5) \times 10^{-8} E^{-3.18 \pm 0.25}$ TeV^{-1}m^{-2}s^{-1}, χ^2_{red}(d.o.f.) $= 0.22$ (3), or with a power law with exponential cut-off and fixed spectral index $(6.0 \pm 2.2) \times 10^{-8} e^{-E/(2.7 \pm 1.1 TeV)} E^{-1.8}$ TeV^{-1}m^{-2}s^{-1}, χ^2_{red}(d.o.f.) $= 0.65$ (3).

On a final note, Vassiliev (2000) introduced a smooth parameterization of the optical depth so that an analytic form of the EBL density can be derived. With the functional form of the EBL spectrum proposed there, the 1ES 1959 spectrum is described by $\exp(-13.77 \pm 0.07 - (2.60 \pm 0.14) \log E - (0.08 \pm 0.08) \log^2 E)$ TeV^{-1}m^{-2}s^{-1}, χ^2_{red}(d.o.f.) $= 6.01$ (6); the statistical errors are for the 68% confidence interval of independent parameter variations. The effect of absorption is represented by the two last coefficients, they describe the change in power law and the curvature. The curvature term is compatible with the mean value of
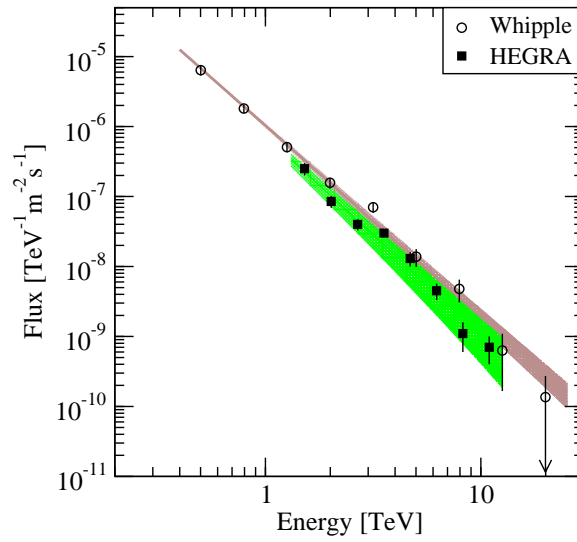
FIGURE 4.11. 1ES 1959 spectra measured for two different flares by the Whipple and HEGRA collaborations.

0.17 suggested by Vassiliev from the flare spectra of Mrk 421 and Mrk 501 and less than the upper limit of 0.3 derived through direct optical EBL measurements at 3.5μm.

CHAPTER 5

FLARE SPECTRUM OF 1ES 2344+514

The BL Lac object 1ES 2344+514 (1ES 2344), shown in Fig. 5.1, has been monitored by
the Whipple collaboration since 1995 (Catanese et al., 1998). The object was observed
in a flaring state during the night of 20 December, 1995, with a significance of 5.3 σ, the
strongest flare from this object measured to date. At a redshift of 0.044, it is one of five
active galactic nuclei (AGN) detected by the Whipple collaboration. Recently, the HEGRA
collaboration reported an independent confirmation of this source (Tluczykont et al., 2003).
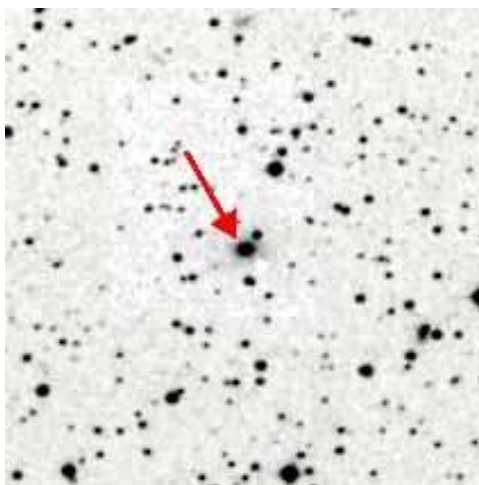
FIGURE 5.1. Optical image of 1ES 2344 (indicated by arrow) on a 6' by 6' field of view.

5.1 History and Spectral Energy Distribution

1ES 2344 (position J1950: RA 23h44m36.26s, DEC 51d25m37.4s (Patnaik et al., 1992))
was detected by the Einstein Slew Survey (Elvis et al., 1992) in the energy range 0.2-4 keV.

The survey was constructed from data collected during the HEAO-2 mission from 1978-1981. 1ES 2344 was identified as a BL Lac object from (1) its distinctive radio/optical/X-ray flux, (2) the absence of emission lines with observed equivalent width greater than 5Å, and (3) a CA II "break strength" smaller than 25% (Perlman et al., 1996). These criteria define an object with strong nonthermal emission which almost completely masks the thermal emission from the surrounding host galaxy. The host galaxy of 1ES 2344 is elliptical with a half-width half-max radius of $r_e = 7.12 \pm 0.02$ kpc, assuming H_0=50 km s^{-1} Mpc^{-1} and q_0=0 (Urry et al., 2000).

The non-contemporaneous spectral energy distribution of 1ES 2344 is shown in Fig. 5.2. Across the entire spectrum, 1ES 2344 is an unresolved point source, a central black hole of mass $10^{8.80\pm0.16}$ M$_\odot$ derived from stellar velocity dispersion measurements (Barth et al., 2003). The earliest radio data was obtained by the University of Texas Radio Astronomy Observatory at 365 MHz during a sky survey from 1974-1983 (Douglas et al., 1996). Radio observations followed at 1.4 GHz in 1983 (Condon and Broderick, 1985), at 4.85 GHz in 1987 (Becker et al., 1991) (Gregory and Condon, 1991) (Perlman et al., 1996), and at 8.4 GHz in 1990 by the VLA (Patnaik et al., 1992).

In the optical and far-infrared, observations of 1ES 2344 are masked by the thermal emission coming from the host galaxy. The total photometry by the 2 Micron All Sky Survey (Jarrett et al., 2003) and by HST (Urry et al., 2000), label "Galaxy light" in Fig. 5.2, lie well above the value expected by pure synchrotron emission from the jet. Observations with the Hubble Space Telescope (HST) in 1996 measured a R-band brightness of the nucleus of 16.83±0.05 mag from a fit of a point source plus galaxy convolved with the point spread function of the telescope (Urry et al., 2000). During continued monitoring through 1998, the R-band brightness varied from 16.47 mag (Nilsson et al., 1999), and 17.00 mag (Falomo and Kotilainen, 1999), indicating optical variability. An optical monitoring program in 2000/1 by Xie et al. (2002) found short time scale variability to be weak, with maximum intraday variability of $\Delta V = 0.18$ mag, $\Delta R = 0.1$ including galaxy light. A relatively large brightness decrease of 0.35 mag was observed in the V-band over 2 weeks
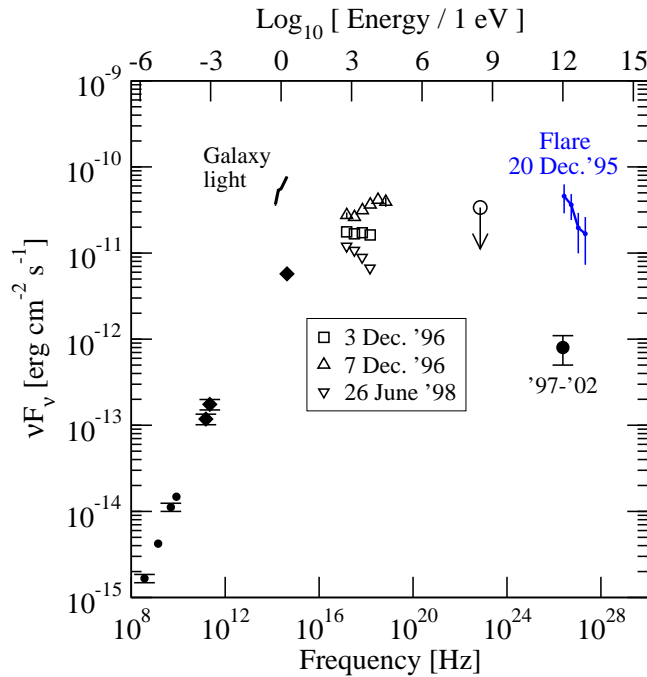
FIGURE 5.2. Spectral energy distribution of 1ES 2344 along with the VHE spectrum obtained with the Whipple telescope. Data taken from the following sources: 365 MHz from Texas radio survey (Douglas et al., 1996), 1.4 GHz from Greenbank (White and Becker, 1992), 4.85 GHz from Greenbank (Gregory and Condon, 1991), 8.4 GHz from VLA (Patnaik et al., 1992), galaxy photometry at millimeter wavelength from (Stevens and Gear, 1999), galaxy photometry at K, H, and J-bands from 2MASS (Jarrett et al., 2003), galaxy and nucleus R-band photometry obtained with Hubble Space Telescope and corrected for interstellar reddening (Urry et al., 2000). X-ray observation by BeppoSAX (Giommi et al., 2000), upper limit at 300 MeV from EGRET (Hartman et al., 1999). Quiescent VHE gamma ray flux during the period 1997-2002 from HEGRA (Tluczykont et al., 2003) and .

in January 2001.

1ES 2344 showed X-ray variability on the time scale of hours in the 0.1 - 10 keV energy band during a week-long campaign in 1996 by the BeppoSAX satellite (Giommi et al., 2000). A follow-up observation in 1998 found 1ES 2344 to be in a very low state, implying a frequency shift by a factor of 30 or more of the peak synchrotron emission. This suggested the interpretation that two distinct electron populations contribute to the synchrotron emission; one steady low-energy component, the other extending from soft to hard X-rays with

rapid time variability. During the 1996 X-ray campaign, near-simultaneous VHE observations by the Whipple observatory did not result in a detection.

The EGRET 95% confidence level upper limit for 1ES 1959 is 6.98×10^{-8} cts cm^{-2} s^{-1}, E> 100 MeV (Hartman et al., 1999). The peak response for most sources detected with EGRET lies at around 300 MeV, so we derive an upper limit at 300 MeV of about 3.4×10^{-11} erg cm^{-2}.

The detection of VHE gamma rays from 1ES 2344 in December 1995, was first reported by the Whipple collaboration at the 1997 International Cosmic Ray Conference (Catanese et al., 1997). Though the detection was at the 6 σ level, it was considered tentative because follow-up observations through 1997 did not detect further evidence for a signal nor had other observatories reported the object to be in a high state. Monitoring from 1998 to 2000 however, showed again a small positive excess (Badran, 2001), but no flares were detected at VHE or X-ray energies. Recently, the HEGRA collaboration reported an independent confirmation of this source (Tluczykont et al., 2003). A summary of the VHE observations is given in Tab. 5.1. An earlier unpublished measurement of the VHE gamma-ray spectrum covering the entire 1995/6 observing season yielded a spectrum of $(1.14 \pm 0.50) \times 10^{-7} E^{-2.29 \pm 0.43}$ TeV^{-1} m^{-2} s^{-1}, statistical error only, with $\chi^2/ndf = 3.2/2$ (Bussons-Gordo, 1998a,b).

5.2   Flare and Background Data

The flare data consists of the 4 pairs summarized in Tab. 5.2 with lightcurve shown in Fig. 5.3. The total on-source exposure time was 110 minutes. The table shows in the third column the throughput for the ON and OFF runs, the background event rate due to cosmic rays relative to a reference run with clear night sky. The gamma-ray rate derived with $Supercuts95$ is shown in column four; this reanalysis is in agreement with Catanese et al. (1998). The last column shows how well the ON and OFF runs are matched, it is the significance of the ON-OFF excess with events characterized by $20° < alpha < 65°$ and

Date	Reference	Exposure [hr]	S^a [σ]	Integral Flux [$\times 10^{-7}$ m $^{-2}$s^{-1}]	E_{thresh} [TeV]
1995/6	Catanese et al. 1998	20.5	5.8	1.7 ± 0.5	0.35
20 Dec. 1995	Catanese et al. 1998	1.85	5.3^b	6.6 ± 1.9	0.35
1996/7	Catanese et al. 1998	24.9	0.4	$< 0.82^c$	0.35
Dec. 1997	Aharonian et al. 2000a	15.8	NA	$< 0.29^d$	1.0
1997-2002	Tluczykont et al. 2003	72.5	4.4	0.08 ± 0.03	0.8
1998	Konopelko et al. 1999	23.8	3.3^b	$< 0.09^e$	1.0
2000	Badran 2001	3.1	2.4	1.1 ± 0.1^d	≈ 0.4

TABLE 5.1. Worldwide VHE measurements of 1ES 2344.
^{a} statistical excess, ^{b} part of the data listed in the above entry, ^{c} 99.9% C.L. upper limit, ^{d} 99% C.L. upper limit, ^{e} statistical error only.

passing a set of loose cuts, see Tab. 5.2. This control (*ctl*) region is excluded from the gamma-ray analysis and the significance gives an indication of the statistical compatibility between the ON and OFF runs over the entire energy range considered in the spectral analysis. A good match is especially important for the last run which was taken without an immediate off-source observation. A separate OFF run was selected from 16 February, 1996 that was found to match well in elevation, throughput, pedestal fluctuation, and is relatively bias-free in the *ctl*-region.
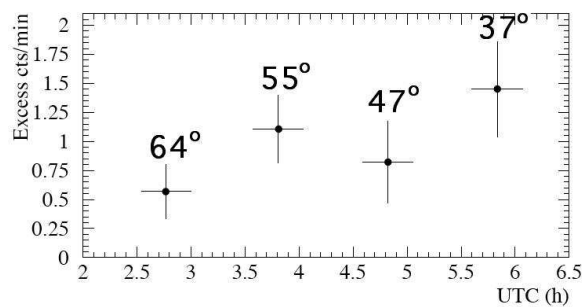
FIGURE 5.3. VHE gamma-ray lightcurve for 20 Dec. 1995, Figure taken from Catanese et al. (1998)

ON/OFF[a]	Elevation	Throughput	Rate[b]	Match[c]
4022/3	64°	0.77/0.78 ±0.08	0.70 ± 0.28	-0.70
4024/5	55°	0.68/0.71 ±0.08	1.04 ± 0.378	-1.33
4026/7	47°	0.52/0.57 ±0.05	0.91 ± 0.42	-0.98
4028/4490	37°/36°	0.45/0.41 ±0.04	1.54 ± 0.47	0.86
		Total	1.14 ± 0.20	-0.82

TABLE 5.2. Detailed look at data of 1ES 2344 taken on 20 Dec. 1995.
[a] Run number.
[b] Gamma-ray rate per minute after $Supercuts$1995, see Tab. 2.2.
[c] Significance of the event excess for the TRK run over the OFF run for a subset of the data that is otherwise excluded from the gamma-ray spectral analysis. This should provide a relatively unbiased estimate of how well the TRK and OFF runs match. The criteria that define this *ctl*-region are: $20°< alpha <65°$, $0.31°< distance <1.1°$, $size > 65$ dc, and $length/size < 0.00085$ °/dc.

5.2.1 Sky Quality

The weather was rated "A" by the observers; this is confirmed by the overlap of the throughput value with other "A" weather observations made from October 1995 through April 1996 shown in Fig. 5.4.

5.3 Description of the Monte-Carlo Simulations

The observations cover a wide range of elevation with relatively low gamma-ray rate. To obtain the most optimized cuts and to maintain an accurate energy calibration, the data is combined at two average elevations of $41°$ and $58°$. The Monte-Carlo simulations of gamma-ray initiated atmospheric showers and subsequent detection by the telescope were carried out with the Grinnell-ISU (GrISU) package.

At $58°$ elevation, the parameters used to produce the simulations are the same as listed in Tab. 3.7, with the exception of zenith angle. At $41°$ elevation simulations were carried out over the energy range 0.3 TeV$<$E$<$100 TeV and a larger impact range of up to 350 m.

The light-to-digital counts conversion of the telescope was calibrated by comparison
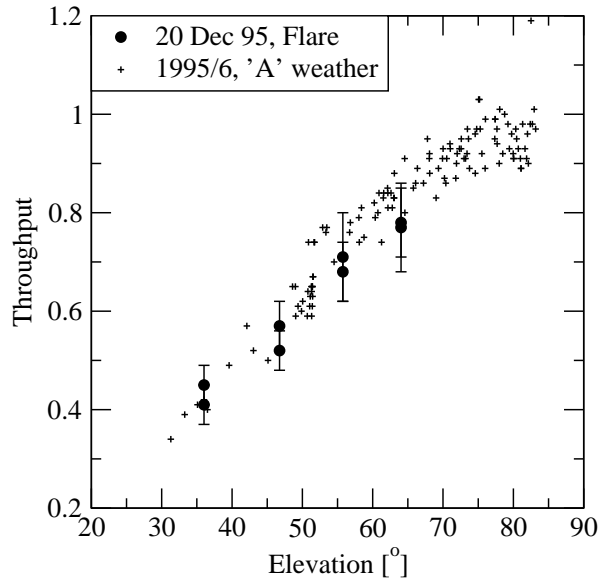
FIGURE 5.4. Throughput of 1ES 2344 flare data and "A" weather observations in 1995/6. For clarity, the error bars are only shown for the flare data.

of simulated muon rings with those found in contemporaneous Crab Nebula data, see Sect. 3.3. Its value of 0.84 ± 0.07[1] digital counts (dc) per photo electron (pe) is constant over observing season, see Sect. 3.3.

To improve the energy resolution of the spectral analysis and reduce bias due to uncertainties around the triggering threshold the following loose cuts were applied to the simulations and the data: $0.31°< distance <1.1°$, $length/size <0.00085$ °/dc, $max2 > 65$ dc, and $alpha < 25°$.

At $41°$, the differential and integral trigger rates are shown in Fig. 5.6 for a Crab-like spectrum with differential index -2.5. The peak trigger rate occurs at an energy of 1.4 TeV for spectral cuts, described below, and 2.1 TeV with $Supercuts1995$. With these cuts, 90% of the triggers occur above 1.05 TeV and 1.67 TeV, respectively. The collection area, shown in Fig. 5.5, reaches 10% of its maximum value of 170,000 m^2 at an energy of about 1.1 TeV for spectral cuts.

[1]This factor includes changes of the telescope optics. As these are not part of the electronics chain, the dc/pe value derived here cannot be compared directly with other published calibrations.

At 58°, the differential and integral trigger rates are shown in Fig. 5.6 for a Crab-like spectrum with differential index -2.5. The peak trigger rate occurs at an energy of 0.69 TeV for spectral cuts and 1.1 TeV with $Supercuts1995$. With these cuts, 90% of the triggers occur above 0.48 TeV and 0.75 TeV, respectively. The collection area, shown in Fig. 5.5, reaches 10% of its maximum value of 136,000 m^2 at an energy of about 0.51 TeV for spectral cuts.

5.4   Event Selection and Energy Estimation

The spectral analysis is described in Sect. 3.2 At 41°, the energy resolution is $rms(\Delta \log E) = 0.15$, and the bias is $bias(\Delta \log E) = 0.018$. The fit was performed between $E = 0.8$ TeV and 40 TeV, the lower limit is a combination of the collection area falloff with decreasing energy and the energy resolution at that point: 1.07 TeV/(1+0.39)≈ 0.8 TeV. A cut-off at the upper limit is necessary because of poor event statistics of the Monte-Carlo simulation.

At 58°, the fit results in $rms(\Delta \log E) = 0.15$, energy resolution $rms(\Delta E/E) = 0.45$ and $bias(\Delta \log E) = 0.012$. The fit was performed between $E = 0.4$ TeV and 25 TeV, the lower limit is chosen at 0.51 TeV/(1+0.45)≈ 0.4 TeV.

The selection of gamma rays from the data is done by imposing cuts on the parameters $width$, $length$, and $alpha$. These "extended cuts", or spectral cuts, are derived from the Monte-Carlo simulation and scale with $size$ so that the fraction of gamma rays selected is roughly $size$ independent. Fig. 5.7 shows the parameter distributions and the mean value after loose cuts up to the largest $size$ observed in the data[2]. At 41°, 86% of the simulated gamma rays pass all cuts shown in Fig. 5.7, relatively independent of $size$ and at 58°, 87% pass all cuts. The simulations at 58° are limited by statistics at high energies, making the cuts somewhat inefficient. In particular, the upturn of the $alpha$-cut is unphysical, but it still remains below 15°, the canonical value of $Supercuts$.

---

[2]The largest $size$ for the 41° data is $10^{3.9}$ dc and $10^{4.0}$ dc for the 58° data.
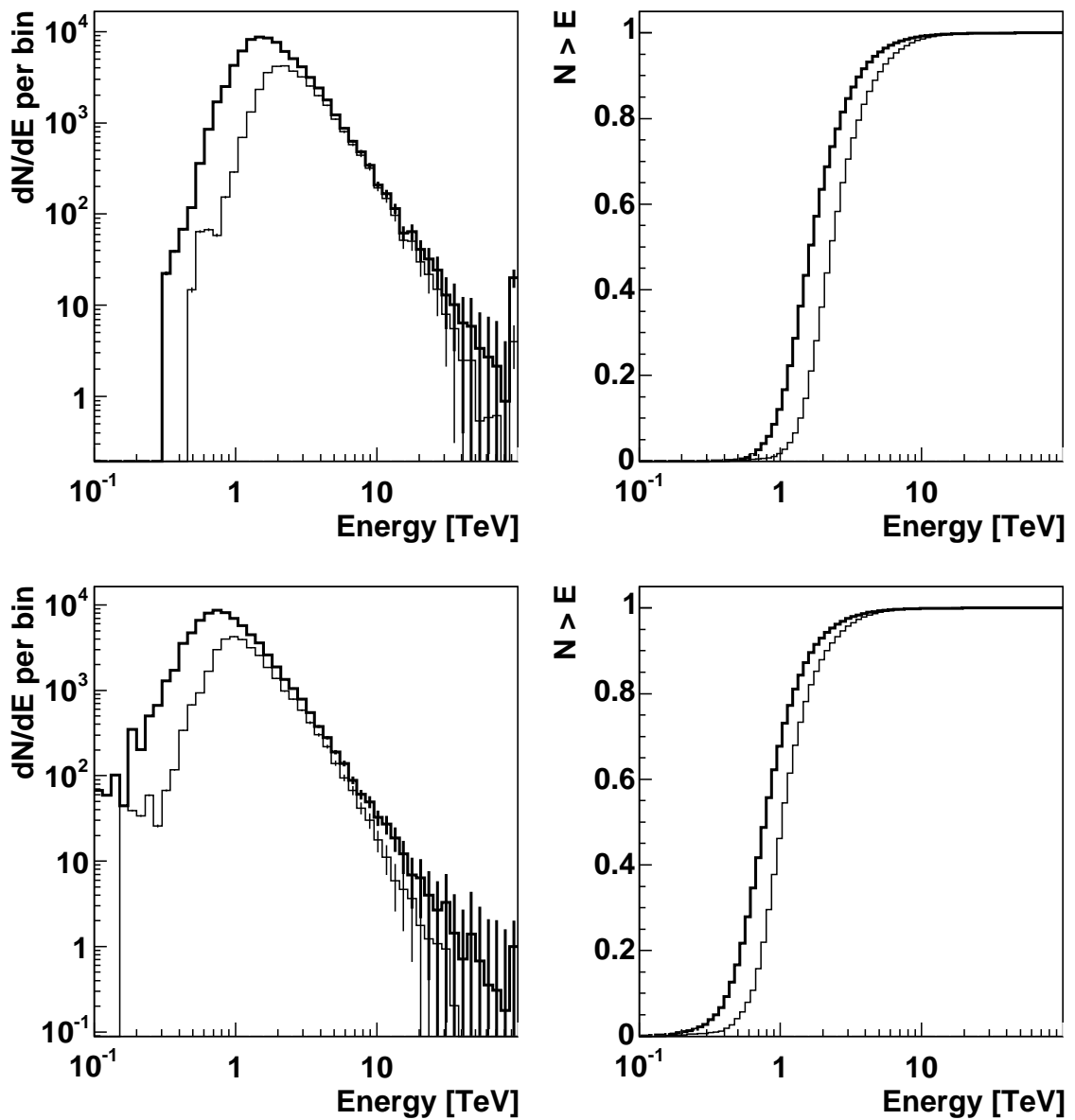
FIGURE 5.5. *Left*: Trigger rate at $41°$ elevation (*top*) and $58°$(*bottom*) due to a Crab-like spectrum after spectral cuts (bold) and $Supercuts1995$ (thin). *Right*: Integral trigger rate normalized to 1.

5.4.1 Spectral Reconstruction

To fit a functional form to the spectrum, the excess is binned in logarithmic energy bins.

Because of the very small signal, the bin width is chosen at twice the energy resolution
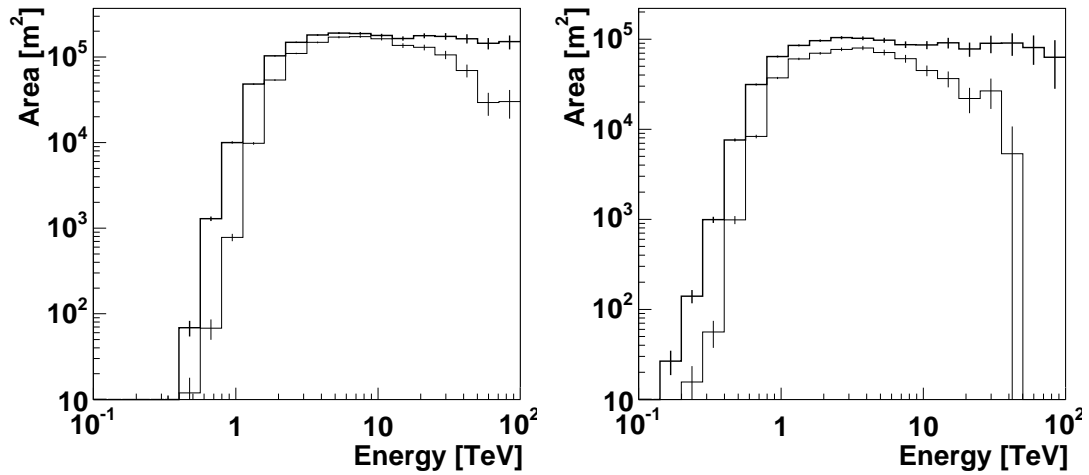
FIGURE 5.6. Collection area of gamma-rays at $41°$elevation (*left*) and at $58°$ elevation (*right*) in 1995 for spectral cuts (bold line) and $Supercuts1995$ cuts (thin line).

$\Delta(\log E) = 0.3$ (Petry et al., 2002).

5.5 Flare Spectrum

For 1ES 2344, the number of excess events in each energy bin after all cuts is shown in Tables 5.3 and 5.4 for the two elevation ranges. Flux upper limits are given if the gamma-ray significance is less than 1 σ in the energy bin. The upper limits are at the 98% confidence level and calculated according to the method described in (Helene, 1983).

The spectra for the two data sets centered around $41°$ and $58°$ elevation are shown in Fig. 5.8. The error bars show the statistical error only.

The power law fit to the $41°$ spectrum over the energy range from 0.8 TeV to 12.6 TeV is given by

$$\frac{\mathrm{d}N}{\mathrm{d}E \, \mathrm{d}A \, \mathrm{d}t} = (5.1 \pm 1.0_{st} \pm 1.2_{sy}) \times 10^{-7} E^{-2.54\pm0.17_{st}\pm0.07_{sy}} \frac{1}{\mathrm{TeV \ m^2 \ s}}, \quad (5.1)$$

with $\chi^2_{min}/ndf = .2/(4-2)$. The χ^2 probability for this data to randomly arise from the power-law fit is 0.9. The statistical error represents the 68% confidence interval (CI) for a
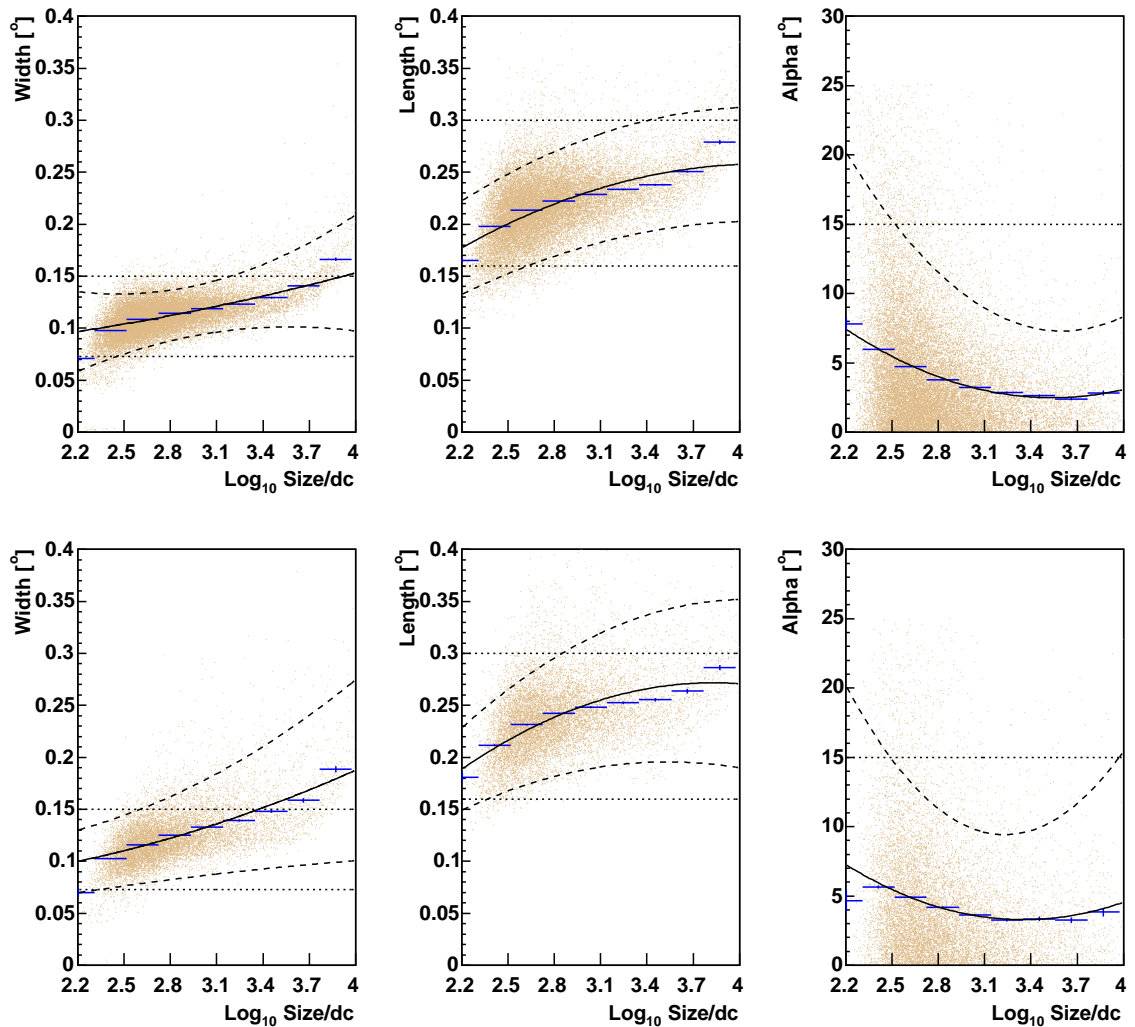
FIGURE 5.7. Parameter distributions and cuts versus $\log(size)$ from Monte-Carlo simulation after application of loose spectral cuts. *Top*: 41° elevation, *bottom*: 58° elevation. The *dots* are simulated events, the *blue crosses* show the mean, while the *solid lines* are the polynomial fit through the mean. *Dashed lines* show the actual cut chosen at a tolerance of two standard deviations around the mean. *Dotted lines* show cut level of $Supercuts1995$.

fit with one free parameter while the other parameter frozen at its optimum value. The 68% CI with two simultaneous free parameters, defined by $\chi^2_{min} + 2.3$, is shown in Fig. 5.9.

The systematic errors are shown in Fig. 5.9 by crosses. They were estimated by varying the cut tolerance, t, from its nominal value of 2, between 1.5 and 2.5, and by varying the

Energy [TeV]	ON [events]	OFF [events]	ON-OFF [events]	S $[\sigma]$	Flux $[\mathrm{TeV}^{-1}\mathrm{m}^{-2}\mathrm{s}^{-1}]$
1.12	55	30	25±9	2.7	$(3.64\pm1.34)\times10^{-7}$
2.24	86	51	35±12	3.0	$(7.24\pm2.42)\times10^{-8}$
4.47	35	20	15±7	2.0	$(9.82\pm4.85)\times10^{-9}$
8.91	14	6	8±4	1.8	$(2.11\pm1.19)\times10^{-9}$
17.78	7	4	3±3	0.9	$<1.19\times10^{-9}$
35.48	0	2	-2±1	-1.4	$<1.43\times10^{-10}$
Total	197	113	84±17.6	4.8	

TABLE 5.3. Statistics in each energy bin for the flare data near 41° elevation. Upper limits are given at the 98% confidence level.

Energy [TeV]	ON [events]	OFF [events]	ON-OFF [events]	S $[\sigma]$	Flux $[\mathrm{TeV}^{-1}\mathrm{m}^{-2}\mathrm{s}^{-1}]$
0.56	63	38	25±10	2.5	$(1.29\pm0.51)\times10^{-6}$
1.12	83	63	20±12	1.7	$(1.27\pm0.77)\times10^{-7}$
2.24	39	42	-3±9	-0.3	$<3.91\times10^{-8}$
4.47	22	19	3±6	0.5	$<1.46\times10^{-8}$
8.91	8	7	1±4	0.3	$<3.62\times10^{-9}$
Total	220	174	44±19.8	2.2	

TABLE 5.4. Statistics in each energy bin for the flare data near 58° elevation. Upper limits are given at the 98% confidence level.

energy calibration by ±10%, see Sect. 3.3.3. The uncertainty in the energy calibration is the most significant contribution to the uncertainty in the flux constant. For example, a 10% change in the energy calibration leads to a 25% (30%) change in the flux constant if the spectrum has a differential index of -2.5 (-3.0). In addition, due to the large range of elevation covered, a small systematic uncertainty on the order of 10-15% should be allowed for when comparing the two spectra measured (Krennrich et al., 1999). The spectral index is mostly effected by varying the cut tolerance. It should be noted that the systematic error evaluated in this way is smaller than the statistical error. This means that a good estimate of the systematic error is not possible with this method, nevertheless is does indicate the relative importance of the two sources of error.
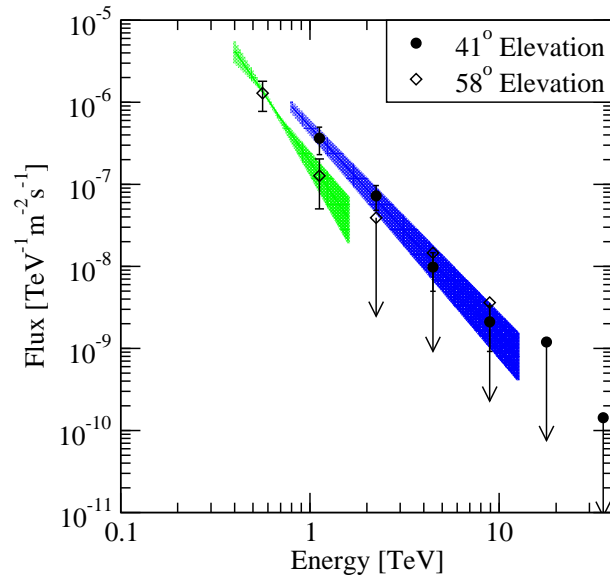
FIGURE 5.8. Differential flux spectrum of 1ES 2344 on 20 December 1995. Observations around 41° (circles) and 58° (diamonds) elevation are shown together with power law fits (solid lines). Shaded regions show the CI of the power law fits and were obtained by varying both parameters to their individual 68% confidence interval.

The power law fit to the 58° spectrum over the energy range from 0.4 TeV to 1.6 TeV is given by

$$\frac{\mathrm{d}N}{\mathrm{d}E\,\mathrm{d}A\,\mathrm{d}t} = (1.9 \pm 0.6_{st} \pm 0.6_{sy}) \times 10^{-7} E^{-3.3 \pm 0.7_{st} \pm 0.7_{sy}} \frac{1}{\mathrm{TeV}\,\mathrm{m}^2\,\mathrm{s}}, \quad (5.2)$$

and the confidence interval contours are shown in Fig. 5.9.

As the spectral indexes of the two spectra are compatible, it would be possible to adjust the flux of the 58° spectrum so that it overlaps, in a least-squares sense, with the spectrum at 41° elevation. This would make the flux constant for one of the spectra a free parameter. However, as the statistical significance of the spectrum at 58° is very small compared to the spectrum at 41°, combining the two would result in an, at best, marginal improvement of the statistical error of the spectral index. Therefore, the spectral measurement of 1ES 2344 derived here, is best represented by the 41° spectrum alone.
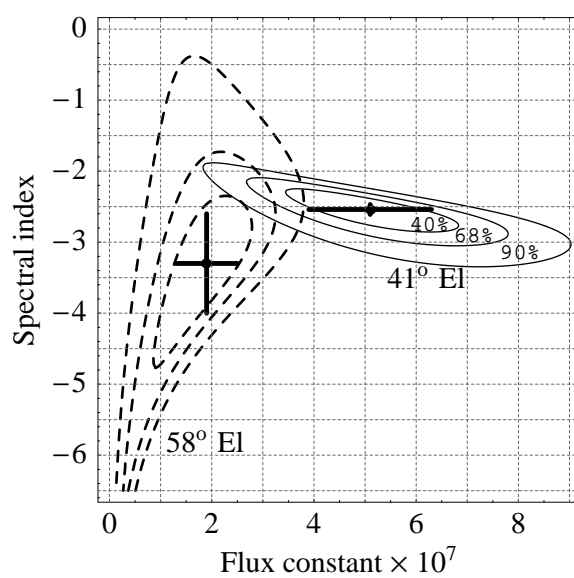
FIGURE 5.9. Confidence regions with probability content of 40%, 68%, and 90% for the simultaneous values of the spectral index and flux constant. Contour lines are drawn at χ^2_{min}+1, 2.3, and 4.6. Confidence regions corresponding to spectrum at 41° (*solid lines*) and at 58° (*dashed lines*). Also shown are the systematic error on the flux constant and spectral index (*crosses*)

CHAPTER 6

ABSORPTION OF VHE PHOTONS BY THE EXTRAGALACTIC BACKGROUND LIGHT

In determining the gamma-ray source spectrum it is important to consider what interactions gamma rays participate in as they travel through space and how this modifies the spectrum. The following section will outline the contribution and relative importance of the radiation and matter densities to the absorption of gamma rays.

6.1 Propagation of VHE Gamma Rays through Space

As photons propagate through space, they may interact with other particles and are redshifted due to the cosmological expansion. Photon interactions in order of relative importance from low to high energies are: (1) Photoelectric effect, (2) Compton scattering, (3) Pair production, and (4) Photon-photon scattering. Neglected here are nuclear reactions like $\gamma + n \rightarrow p + e$ because the cross section and the matter density is very small relative to the photon density. Unlike charged particles, photons do not suffer from deflection by magnetic fields, ionization or bremsstrahlung interactions. This makes them, along with neutrinos, very penetrating and ideal for astrophysical observations.

6.1.1 Magnetic Fields

Though the propagation of photons is not directly effected by magnetic fields except at extremely high energies, VHE photons may produce secondary photons whose propagation direction depends on the presence of a magnetic field because of its effect on their progenitors. The secondaries are the result of pair production by a VHE photon on the extragalactic background light (EBL) and subsequent Compton up-scattering of the EBL photons by the e^+ and e^-. This modifies the VHE spectrum in three ways: (1) the secondary photons are of

lesser energy where they pile up, (2) their direction has changed making the source appear larger at lower energies, and (3) secondary photons arrive somewhat later than the primary photons because of the path difference and slower propagation speed (Biller, 1995). However, if the intergalactic magnetic field strength is of order $> 10^{-13}$ G, then even for the nearest blazar Mrk 421, essentially all secondary gamma rays are redirected out of the primary beam and hence would not produce observable secondary photons. The strength of the extragalactic magnetic field is very uncertain, it could be as large as 10^{-9} G or as small as 10^{-20} G or even 10^{-29} G (Wang et al., 2004) if it were generated during the cosmological QCD or electro weak phase transition. (See Han and Wielebinski (2002) for a review of cosmic magnetic fields.) (Biller, 1995) found that the time lag between primary and secondary photons, produced by the electron/positron pair traveling at less than the speed of light, would be easily observable by the spectrum first hardening then softening followed by a return to the initial spectrum. As BL Lacs observed at TeV energies are highly variable objects that produce VHE flares on time scales of 15 min (Gaidos et al., 1996) and no such spectral variation has been observed, it is highly unlikely that secondary photons are currently being observed. However, as the secondary photons have energy of $1/1000(E_\gamma/1\text{TeV})^2$ (Wang et al., 2004), simultaneous observations of flares covering the GeV to TeV region by GLAST and VERITAS may be able to constrain the intergalactic magnetic field.

6.1.2 Photoelectric Effect

The photoelectric effect describes the ejection of a bound electron from an atom by a photon. The outgoing electron has kinetic energy $K.E. = h\nu - B.E.$, where $B.E.$ is the binding energy of the electron. The binding energy generally ranges from 5 eV to 100 keV, it is 13.6 eV for Hydrogen. At $E_\gamma = m_e$ the cross section is of order $\alpha^4 r_e^2 = 2 \times 10^{-38}$ m^2 and proportional to $\nu^{-3.5}$ and Z^5. Thus, at TeV energies this contribution is negligible.

6.1.3 Compton Scattering

Compton scattering is the interaction of a free electron with a photon. Because the density of free electrons in intergalactic space is much less than the density of photons and atoms, the effect is negligible.

6.1.4 Pair Production

The importance of pair production on the propagation of VHE gamma rays was first noted by Nikishov (1962). Pair production, $\gamma_{TeV} + \gamma_{IR} \rightarrow e^+ + e^-$, can occur if the total energy in the center-of-momentum frame is $\geq 2m_e$; for example, a 1 TeV gamma-ray colliding with an infrared 1 eV photon. The opacity of the entire extragalactic photon spectrum for high-energy cosmic rays was explored by Lieber et al. (1965); Gould and Schréder (1967). They found that absorption of UHE gamma rays occurs mainly by the CMB, see also (Gould and Schréder, 1966; Jelley, 1966).

For VHE gamma rays, photons with wavelengths between 1μm and 50μm are most important. The mid-infrared energy density in the Solar neighborhood is ~ 10 eV/cm^3, in the Galaxy $\sim 10^{-2}$ eV/cm^3, and in extragalactic space about half that (Dwek and Slavin, 1994). The nearest VHE blazar, Mrk 421, is located at a distance of 130 Mpc while the size of the Galaxy is ~ 10 kpc and that of the Solar neighborhood is $\ll 1$ pc. Thus, the extragalactic background light produces the most absorption for extragalactic sources. Unfortunately, it is difficult to measure and the wavelength dependence is not well known, so that VHE source spectra cannot be accurately reconstructed. The current status of EBL measurements is given in Sect. 6.2.

VHE gamma-ray absorption may also occur near the source itself, either by pair production on optical light emitted from the accretion disk of the blazar or by dense clouds in the line of sight. If gamma-ray absorption occurs external to the source by the uniformly distributed EBL, then the spectra should contain an absorption feature that depends only on the redshift of the blazar. If however, a significant amount of absorption occurs close to the

source, then gamma-ray absorption may vary in connection with source activity in the optical region and thus indicating that it is not caused by the extragalactic photon background. Simultaneous optical and VHE observations may provide more information.

6.2   Measurements and Constraints on the EBL

The measurement of the EBL is important for VHE gamma-ray astronomy as well as for the modeling of star formation and galaxy evolution. Current measurements of the EBL are summarized in Fig. 6.1. The optical to near-IR emission, peaking in the 1 μm region and extending to 20 μm is due to direct star light, while molecular clouds and dust reprocess the optical light and emit in the IR to far IR region producing the second peak, $\lambda \approx$ 20-300 μm. Hauser and Dwek (2001) comprehensively reviewed measurements and implications of the cosmic infrared background.

The optical to far-infrared EBL is difficult to measure because it is dwarfed by the much brighter foregrounds caused by night-sky glow, diffuse dust in the Galaxy, and the zodiacal light caused by interplanetary dust, see Fig. 2.4. For example, emission by the zodiacal dusk peaks in the 25 μm region, orders of magnitude above the low EBL density in this wavelength. In the case of ground- or rocket-based observations, instrumental emission also plays a significant role. This is complicated by the fact that the only characteristic upon which a detection of the EBL can be based is that it has to be isotropic. These difficulties have precluded ground- and rocket-based measurements from detecting the EBL at all.

Direct measurements are possible in the two windows of least foreground around 1 μm and >100 μm (Hauser and Dwek, 2001). Recently, the Cosmic Background Explorer (COBE) satellite with its two instruments the Diffuse Infrared Background Experiment (DIRBE) and the Far Infrared Spectrometer (FIRAS), has detected the EBL at 140 μm and 240 μm, see Fig. 6.1. The possible detections at 60 μm and 100 μm (Finkbeiner et al., 2000) are viewed as too high and are more controversial, requiring revised galaxy evolution models with larger dust content (Blain and Phillips, 2002). The FIRAS measurement (Fixsen

et al., 1998) shows that the CIB can be characterized between 125 μm and 2000 μm by a modified blackbody spectrum of the form $(1.3\pm0.4)\times10^{-5}(\nu/\nu_0)^{0.64\pm0.12}I_\nu(18.5\pm1.2K)$, with $\nu_0 = c/100\mu m$. The isotropic optical and near-IR emission detected with the Japanese IRTS satellite is considerably higher than integrated light from galaxies and theoretical predictions (Matsumoto, 2000).

Lower limits on the EBL density are placed by adding the flux per unit area received from all galaxies down to a given flux limit. As galaxies are only one source contributing to the EBL, these galaxy counts represent a lower limit on the total EBL (Franceschini et al., 1991; Armand et al., 1994; Pozzetti et al., 1998). In the mid-IR region, where the foreground is particularly bright, Elbaz et al. (2002) were able to place a lower limit on the 15 μm EBL density.

Upper limits can be placed on the EBL from direct measurements with minimal background subtraction (Hauser et al., 1998). Also, upper limits can be derived from fluctuations in the measured light distribution, see Kashlinsky et al. (1996); Kashlinsky and Odenwald (2000).

6.2.1 Upper Limits from Observations of VHE Blazars

A new method of deriving upper limits on the EBL density comes from the spectra of VHE gamma-ray blazars. As explained in Sect. 1.4, if one knew the intrinsic spectrum of blazars, the EBL density could be derived from the measured attenuation of VHE gamma rays. Stecker et al. (1992) suggested that simultaneous GeV to TeV measurements would be able to determine intrinsic source spectrum and the EBL density. They applied this method to infer an upper limit on the density through the non-detection of VHE gamma rays from an strong GeV gamma-ray source, 3C 279.

The critical assumptions in deriving EBL upper limits are the intrinsic source spectrum and the spectrum of EBL photons. Vassiliev (2000) laments the assumptions used to by some authors to derive upper limits. For example, the upper limits on the EBL derived by
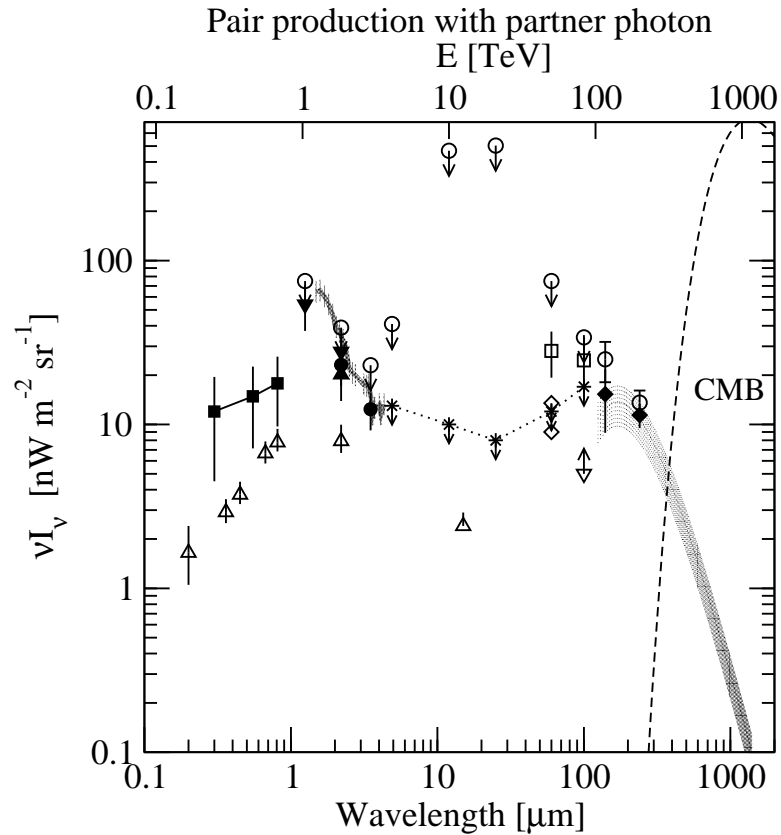
FIGURE 6.1. Spectral energy distribution of the EBL. The top axis indicates the most likely energy of the partner photon to participate in pair-production with the EBL. The flux measurements and limits are taken from (Hauser et al., 1998) (*open circles*), (Finkbeiner et al., 2000) (*open squares*). Upper limits from fluctuation analysis by Hauser and Dwek (2001) using the data from Kashlinsky et al. (1996); Kashlinsky and Odenwald (2000) (*stars*). Tentative detection by (Miville-Deschênes et al., 2002) (*open diamonds*). (Lagache et al., 1999) (*filled diamonds*), (Dwek et al., 1998) (*open triangle pointing down*), (Fixsen et al., 1998) (*shaded region)* near the CMB. Galaxy counts corresponding to lower limits are shown with *open triangles pointing up* and are at 0.2μm from (Armand et al., 1994), from 0.36 μm to 2.2 μm from (Pozzetti et al., 1998), and at 15 μm from (Elbaz et al., 2002). In the infrared, the *filled circles* are from (Wright and Reese, 2000), *filled triangle pointing up* from (Wright, 2001), and *filled triangles pointing down* from (Cambrésy et al., 2001). In the optical, the *filled squares* are from (Bernstein et al., 2002). The *grey line* in the optical/infrared is from (Matsumoto, 2000). The cosmic microwave background (CMB) is shown by a *dashed line*.

Stecker and de Jager (1993) conflicted with later measurements. Therefore, the limits were revised (Stecker and de Jager, 1998) with a new EBL model and they predicted intrinsic power law source spectra. In another case, Dwek and Slavin (1994) used the spectrum of Mrk 421 to determine the EBL spectrum. Any claim to determine the EBL from just one VHE gamma-ray spectrum is certainly over-optimistic. A more conservative approach was taken by Stanev and Franceschini (1998), where a flare of Mrk 501 in 1997 was used to place upper limits on a piecewise-flat EBL, in a νF_ν representation. Biller et al. (1998) used this idea and derived upper limits with the assumption of an intrinsic power law with differential index -2, for Mrk 421 and Mrk 501. In both cases, the intrinsic spectrum was not well justified: the intrinsic spectrum was not specified by Stanev and Franceschini (1998) and the flux normalization was not specified by Biller et al. (1998). Mrk 501 was also used to derive upper limits on normalization of two EBL shapes extending from 3×10^{-3}- 3×10^{-1} eV by Funk et al. (1998). However, this region of the EBL is not covered by VHE gamma rays and it is unclear what the impact of this upper limit is. In summary, the claims of upper limits through VHE gamma-ray observations have been over-optimistic and one should be very cautious when deriving new ones.

However, this does not mean that VHE gamma-ray spectra cannot be used to derive upper limits on the EBL. A new approach of deriving upper limits on the EBL density uses certain reasonable constraints on the intrinsic source spectrum; such as that it should not rise exponentially with energy and be consistent with the X-ray synchrotron peak (Renault et al., 2001; Aharonian et al., 2003a; Krennrich and Dwek, 2003; Dwek and Krennrich, 2004).

6.3 Extinction due to Pair Production

Consider a single VHE gamma ray of energy, E, coming from a distant extragalactic source. If the gamma ray makes a collision with another particle, it will not propagate in a straight line and is lost to the observer who is several Mpc away. Pair production is the

most likely type of inelastic collision in extragalactic space as the photon density, though varying with wavelength, is much higher than the matter density. For the pair production to occur, the total energy available must be greater than $2m_e$. For VHE gamma rays with energy between 100 GeV and 20 TeV, the low energy photon must be in the range from 10 eV to 0.05 eV. The absorption of VHE gamma rays is described by a very simple rate equation involving only the channel

$$\gamma_{TeV} + \gamma_{ir} \rightarrow e^+ + e^-.$$

The number of VHE gamma rays, N, with energy E changes per unit time, $\mathrm{d}t$, as

$$\frac{\mathrm{d}N(E)}{\mathrm{d}t} = -N(E)\lambda_{\gamma\gamma\rightarrow e^+e^-}(E). \tag{6.1}$$

Eq. 6.1 is solved by expressing $\mathrm{d}t$ in terms of the distance $\mathrm{d}l$ traveled by the photon: $\mathrm{d}l/\mathrm{d}t = c$. For small redshift, $z << 1$, the relation $\mathrm{d}l/\mathrm{d}z = c/H_0$ holds so that the number of gamma rays at redshift z is given by

$$N(z, E) = N_0(E)\, e^{-H_0^{-1}z\,\lambda(E)}. \tag{6.2}$$

This defines the optical depth

$$\tau(z, E) = H_0^{-1}z\,\lambda(E). \tag{6.3}$$

The Hubble constant $H_0 = 71 \pm 4$ km s^{-1} Mpc^{-1} (Bennett et al., 2003) with $c/H_0 = 1.3 \cdot 10^{26}$ m. See Sect. 6.3.1 for an extension of this formalism to cosmological distances.

The momentum distribution averaged pair production rate, λ, in units of T^{-1}, is

$$\lambda(E) \equiv \langle\sigma v_{rel}\rangle = \int \mathrm{d}^3p\, f(p)\, \sigma(\sqrt{s})\, v_{rel} \tag{6.4}$$

$$= \int \mathrm{d}\Omega \int p^2\, \mathrm{d}p\, f(p)\, \sigma(\sqrt{s})\, v_{rel} \tag{6.5}$$

$$= 2\pi c \int_{-1}^{+1} \mathrm{d}x\, (1 - x) \int_{\frac{2m^2}{E(1-x)}}^{\infty} p^2\, \mathrm{d}p\, f(p)\, \sigma(\sqrt{s}), \tag{6.6}$$

where $\mathrm{d}\Omega \equiv \mathrm{d}(cos\theta)\mathrm{d}\phi$, $cos\theta \equiv x$ is the angle between the incoming particles, and $\sqrt{s}$ is the total energy. The lower limit of the $\mathrm{d}p$-integral is equal to the minimum photon

energy required for pair production so that the cross section is completely integrated over. The relative speed between the interacting particles is $v_{rel} = c(1 - x)$. The comoving photon momentum distribution of the EBL is given by $f(p)$ $[E^{-3}L^{-3}sr^{-1}]$. Eq. 6.6 can also be written in terms of the particle density per energy per volume by substituting $n(\epsilon) \equiv 4\pi p^2 f(p)$ and making the replacement $p \to \epsilon$. Measurements and models of the EBL are presented in Sect. 6.2.

From Eq. 6.6 it can be seen that if the photon density, $n(\epsilon)$, is independent of ϵ, then the optical depth is independent of the gamma-ray energy: i.e. $\lambda(E) \propto n$ only. This corresponds to an energy density $dn/d\epsilon \propto \epsilon^{-1}$. On a νF_ν plot, such an EBL spectrum would fall as λ^{-1} and is quite possible in the optical / near-IR portion.
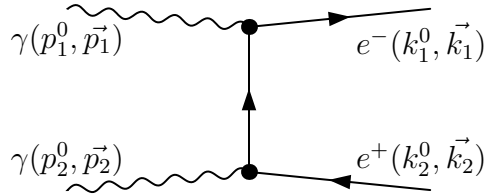
FIGURE 6.2. Schematic of electron/positron pair production by photons.

The spin-averaged pair production cross section, σ, shown in Fig.6.3, is given (Breit and Wheeler, 1934; Landau and Lifshitz, 1989) by

$$\sigma(v_e) = \frac{1}{2}\pi r_e^2 (1 - v_e^2)((3 - v_e^4) \log\left(\frac{1 + v_e}{1 - v_e}\right) - 2v_e(2 - v_e^2)), \qquad (6.7)$$

where $r_e = \frac{\alpha\hbar}{m_e} = 2.8 \times 10^{-15}$ m is the classical electron radius and v_e is the speed of the electron or positron in the center-of-momentum (CM) frame. Because the pair production cross section is proportional to $[M^{-2}]$, pair production of muons and tau-particles is strongly suppressed relative to electrons. The speed, v_e, is given in terms of the incoming
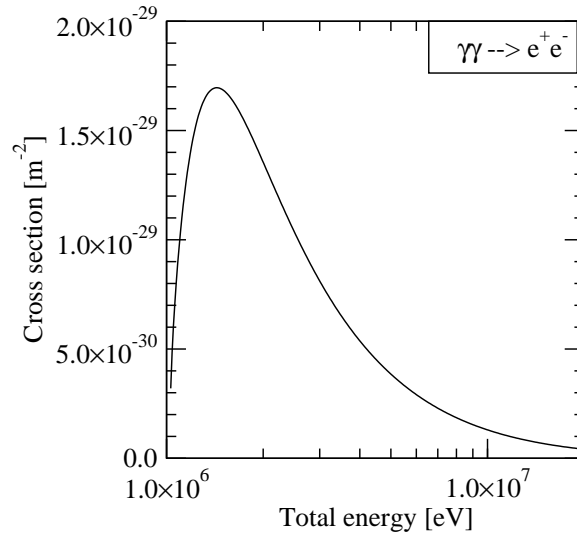
FIGURE 6.3. Pair production cross section.

photon energies and the angle between them by[1]

$$v_e = \sqrt{1 - \frac{2m^2}{Ep(1 - cos(\theta))}}, \tag{6.9}$$

with $m = 0.511 MeV$ for electrons.

6.3.1 Extension to Large Redshift

At arbitrary redshift, z, the optical depth is given by

$$\tau(z_0, E) = \int_0^{z_0} dz \frac{dl}{dz} \int d^3p \, f(z, p) \, \sigma(\sqrt{s}) \, v_{rel}. \tag{6.10}$$

---

[1]See Fig. 6.2. The energy of the electron, k_1^0, needs to be expressed in terms of the initial photon energies. This can be done by evaluating the kinematic invariant $s \equiv (p_1 + p_2)^2$ in the lab frame for the two photons and in the CM frame for the pair. The photons have 4-momenta $(p_1^0, \vec{p_1})$ and $(p_2^0, \vec{p_2})$. Then, $s_i = 2p_1 \cdot p_2 = 2p_1^0 p_2^0 (1 - cos\theta)$, where θ is the angle between them. The 4-momenta of the electron-positron pair in the CM frame are $(k_1^0, \vec{k_1})$ and $(k_1^0, -\vec{k_1})$. Then, $s_f = (k_1^0 + k_1^0, 0)^2 = 4(k_1^0)^2$. Because $s_i = s_f$, $(k_1^0)^2 = (1/2)p_1^0 p_2^0 (1 - cos\theta)$.

$$v_e = \frac{|\vec{k_1}|}{k_1^0} = \frac{\sqrt{(k_1^0)^2 - m^2}}{k_1^0} = \sqrt{1 - \frac{m^2}{(k_1^0)^2}} = \sqrt{1 - \frac{2m^2}{p_1^0 p_2^0 (1 - cos(\theta))}}, \tag{6.8}$$

However, evaluating Eq. 6.10 for large redshift is difficult because the EBL density evolution with redshift is not well known. The absorption of 10-500 GeV gamma rays at redshift < 3 including an evolving EBL was investigate in (Salamon and Stecker, 1998)

In the no-evolution (NE) model, it is assumed that the spectral properties of galaxies are constant in a co-moving frame. The starlight contribution since the formation of galaxies is then summed up to the current epoch (Biller, 1995). The term 'no evolution' refers to the spectra of young and old galaxies being the same.

A further simplification that is valid out to $z \lesssim 0.4$ (Kneiske et al., 2002), is that the EBL does not evolve at all and changes are only due to the expansion of the universe, i.e. the EBL density changes from $n(p)$ to $n(p)(1 + z)^3$. In addition, the gamma-ray energy increases by a factor of $(1 + z)$. However, the energy of EBL photons is not redshifted, as the gamma-rays interact with EBL photons that are co-moving with their local frame of reference. More sophisticated models, such as the NE models, take the contribution of redshifted EBL photons into account. However, simply de-reddening the EBL, as some authors do, is incorrect as the EBL comes from more or less constant light sources since z_{max}. Galaxies were not intrinsically brighter at higher z. At the moment, the evolution model is irrelevant as all blazars detected so far at very high energies are at $z < 0.15$. Implications of the EBL evolution on the gamma-ray absorption from blazars are discussed in (Kneiske et al., 2004).

For a homogeneous and isotropic universe with a Robertson-Walker-Friedman metric the distance-redshift relation is (Stecker, 1971)

$$\frac{\mathrm{d}l}{\mathrm{d}z} = \frac{c}{H_0(1 + z)^2(1 + \Omega z)^{1/2}}. \tag{6.11}$$

The total mass-energy density has been measured by Bennett et al. (2003) as $\Omega = 1.02 \pm 0.02$, implying a flat and expanding universe. With these substitutions the optical depth is

given by

$$\tau(z_0, E) = \frac{2\pi c}{H_0} \int_0^{z_0} \mathrm{d}z (1+z)^{1/2} \int_{-1}^{+1} \mathrm{d}x \, (1-x) \int_{\frac{2m^2}{E(1+z)(1-x)}}^{\infty} p^2 \, \mathrm{d}p \, f(p) \, \sigma(v_e), \quad (6.12)$$

and the electron speed is given by $v_e = \sqrt{1 - \frac{2m^2}{Ep(1-x)(1+z))}}$.

The difference in using Eq. 6.12 and the simpler Eq. 6.6 to calculate the optical depth is less than 10% for the furthest detected VHE blazar H 1426 at $z = 0.129$. In subsequent calculations Eq. 6.6 is used.

6.3.2 Recovering the Source Spectrum

With respect to the emitted spectrum by the source, the measured flux level is modified by:

1. Distance: The measured flux with respect to reference distance d_0 is reduced by d_0^2/d_L^2, where $d_L(z)$ is the luminosity distance calculated in the appropriate cosmo-logical model.

2. Rate: The time interval between successive arriving photons is Doppler shifted by $\Delta t \to \Delta t(1+z)$.

3. Energy: The energy of arriving photons is redshifted by $E \to E/(1+z)$. Also, the energy bin width is decreased by $\Delta E \to \Delta E/(1+z)$

4. Optical depth: The fraction of gamma rays that are not absorbed through pair pro-duction on the EBL is $e^{-\tau(E_m)}$.

The measured flux, F_m, is then given in terms of the flux emitted by the source, F_e, by

$$F_m(E_m) = \frac{\Delta N_m(E_m)}{\Delta E_m \Delta A_m \Delta t_m} \tag{6.13}$$

$$= e^{-\tau(E)} \frac{\Delta N_e(\frac{E_e}{1+z})}{\frac{\Delta E_e}{1+z} \times (\frac{d_L}{d_0})^2 \Delta A_e \times (1+z)\Delta t_e} \tag{6.14}$$

$$= e^{-\tau(E_m)} \left(\frac{d_0}{d_L}\right)^2 \frac{\Delta N_e(\frac{E_e}{1+z})}{\Delta E_e \Delta A_e \Delta t_e} \tag{6.15}$$

$$= e^{-\tau(E_m)} \left(\frac{d_0}{d_L}\right)^2 F_e(E_m) \tag{6.16}$$

with $E_m = E_e/(1 + z)$.

6.3.3   Example: Monoenergetic EBL

The sensitivity of the gamma-ray spectrum to absorption by the EBL is best illustrated by the toy model of a monoenergetic EBL, i.e. one that consists only of photons with one energy. The absorption probability per unit length is given by

$$\lambda(E, \epsilon) = n(\epsilon)\frac{c}{2} \int_{-1}^{+1} \mathrm{d}x \ (1 - x) \ \sigma(v_e),$$ (6.17)

where the constant $\rho(\epsilon)$ is the co-moving photon density $[L^{-3}]$. Note that the only dependence on the EBL energy ϵ is through $v_e = c(1 - x)$. The absorption probability per unit length is plotted in Fig. 6.4 for various EBL energies ranging from infrared to UV: the density is taken uniformly as 1 cm^{-3}. Though gamma-ray absorption is most likely when $\sqrt{Ep} \approx 2m_e$, there is significant absorption of gamma rays with energy half to four times as much.

In general, knowledge of the optical depth is not sufficient to unambiguously determine both the shape and magnitude of the EBL density. If the EBL flux is known over a finite wavelength region, an infinite number of shapes are possible because of the limited energy resolution of this method. The energy resolution is limited by the width of the pair production cross-section and the isotropic EBL photon distribution, see Eq. 6.12. If one assumes a shape for the spectrum with only the overall normalization left as a free parameter, it is possible to determine the best fit EBL flux through a χ^2 minimization between the measured and modeled optical depths. However, this still relies on knowing the intrinsic blazar spectrum, a feat not easily accomplished. Nevertheless, by making reasonable assumptions on the intrinsic flux, this method has been widely used to derive upper limits for power-law EBL spectra. Whether the EBL spectrum is a power law remains questionable.

To avoid specifying the EBL spectral shape, upper limits on the EBL density can be derived for a monochromatic EBL density. Eq. 6.17 shows that in this case the EBL density, n, can be taken out of the integral, greatly simplifying the calculation. As explained
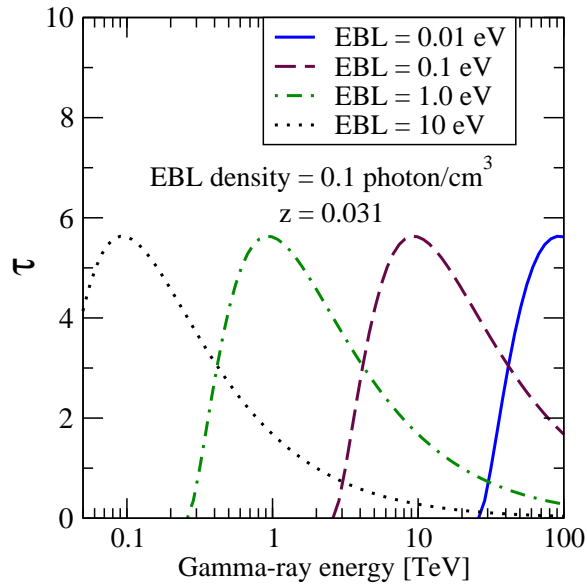
FIGURE 6.4. Absorption probability of a VHE gamma ray by a monoenergetic EBL of energy $\epsilon = 0.01$ eV (123 μm, solid), 0.1 eV (12.3 μm, dashed), 1.0 eV (1.23 μm, dash-dot-dot), and 10 eV (123 nm, dotted). The EBL photon density is 1/cm^3.

below, this can then be used to derive upper limits on the EBL density if upper limits, or measurements, of the optical depth are available.

A monoenergetic EBL absorbs VHE gamma rays with energy spread shown in Fig. 6.4. Conversely, contributions to the absorption of gamma rays with a single energy, E, come from a range of EBL wavelengths. EBL photons with energy $\epsilon = 4m_e^2/E$ are most effective in the absorption of gamma rays, but EBL photons with energy half to four times higher contribute significantly as well. Physically, we know that the EBL spectrum is extended. However, if we suppose the EBL is monochromatic and we ignore the contribution of other wavelength to the absorption of gamma rays, then the EBL density at that single wavelength will have to be much larger to reproduce a measured optical depth, than if other wavelengths are allowed to contributed as well. This means that the EBL density needed in reproduce a measured optical depth is greatest, if there are only photons with one wavelength; i.e. they have to do all the absorption. If the spectrum were extended, then the contributions by EBL

photons with other wavelengths to the total absorption reduces the density required at each wavelength.

There remains the question, what EBL wavelength is used in attenuating the gamma rays? As a monochromatic EBL will always provide upper limits on the true density, those EBL photons that are most efficient in absorbing gamma rays should be used. This will give the lowest upper limits on the monochromatic EBL density. Fig. 6.4 shows that EBL photons with energy $\epsilon = 4m_e^2/E$ produce the highest optical depth. If we did not chose $\epsilon = 4m_e^2/E$, the monochromatic EBL density needed to reproduce the measured optical depth would have to be substantially higher. This would still produce upper limits, but not the lowest possible ones.

The measured optical depth, τ_m, given by Eq. 6.3 can be expressed in terms of the monochromatic EBL density using Eq. 6.17:

$$\frac{\tau_m}{zH_0^{-1}} = n(\epsilon)\frac{c}{2}\int_{-1}^{+1} \mathrm{d}x\,(1-x)\,\sigma(v_e) \tag{6.18}$$

$$\rightarrow n(\epsilon) = \frac{\frac{\tau_m H_0}{z}}{\frac{c}{2}\int_{-1}^{+1}\mathrm{d}x\,(1-x)\,\sigma(v_e)}, \tag{6.19}$$

so that the upper limit (UL) is given by

$$n_{\mathrm{UL}}\left(\frac{4m_e^2}{E}\right) = \frac{\frac{\tau_m(E)\,H_0}{z\,c}}{1.4\times 10^{-29}\mathrm{m}^2}. \tag{6.20}$$

Eq. 6.20 gives the upper limit on the monoenergetic EBL density as a function of the measured optical depth, τ_m.

As an example, Fig. 6.5 shows the steps in going from three measured optical depth for gamma-rays coming from a source at redshift 0.031, to the derived monochromatic EBL densities. These monochromatic lines reproduce the measured optical depth at the measured gamma-ray energy, but additional absorption is produced by the finite width of the cross section.
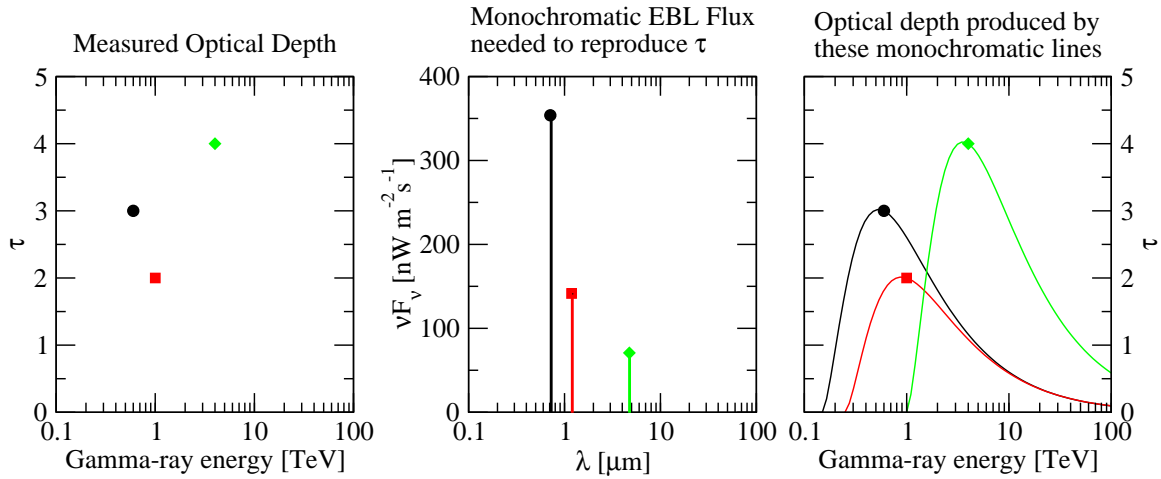
FIGURE 6.5. Illustration of the method used to derive upper limits on the EBL density through monochromatic lines. From the hypothetical measured optical depth (*left*), the monochromatic EBL intensity is calculated (*middle*). As a check on the method, the (*right*) graph shows the optical depth produced by each monochromatic EBL line. Note that the optical depth derived from each monochromatic line overestimates the measured optical depth everywhere except at the measured gamma-ray energy.

6.3.4 Example: Thermal EBL

Following the simple model of Nikishov (1962), the infrared photon gas is assumed to be isotropic and in thermal equilibrium at temperature $T = 0.5~eV$, but with density reduced by a factor γ_ρ. With this assumption, the momentum distribution function is given by

$$f(p) = \frac{2}{(2\pi\hbar c)^3}\frac{\gamma}{e^{p/T} - 1},\tag{6.21}$$

where γ_ρ is the phase space occupancy. Nikishov (1962) assumed an infrared photon energy density of 1×10^5 eV/m³, which requires $\gamma_\rho = 1.86 \times 10^{-14}$. Such a rarefied gas is highly unlikely to be in kinetic equilibrium[2] and a more realistic photon density is pursued in Sect. 6.3.5. The probability that a VHE gamma ray is absorbed by this photon gas is shown in Fig. 6.6 together with the effect this has on a power-law source spectrum. Compared to the measured EBL shown in Fig. 6.7, the photon density is too high by a factor of 5-100

---

[2]Kinetic equilibrium means that the density of states is given by the Bose-Einstein distribution.

depending on the wavelength. Though this model is obviously incorrect, it does illustrate that the bump in the EBL around 1 μm comes from direct star light, while the peak at longer wavelengths comes from preprocessing of this star light by dust and gas.
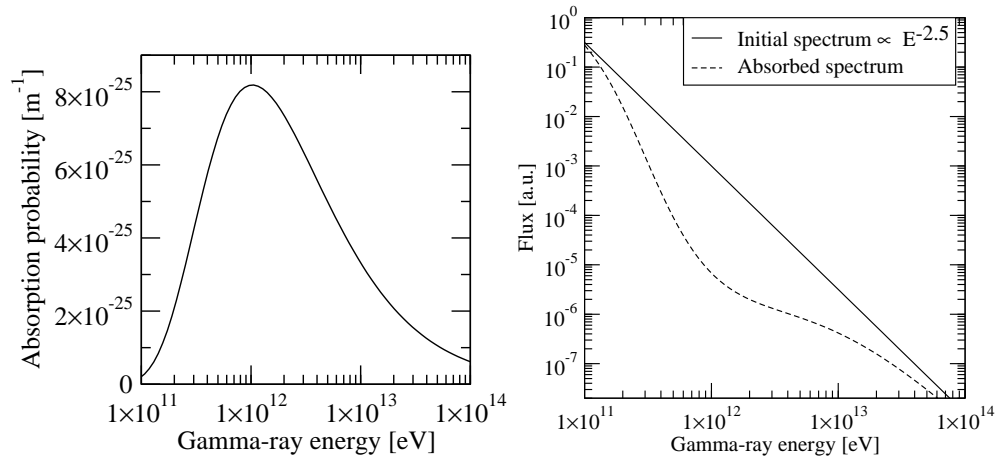
FIGURE 6.6. *Left:* Probability that a VHE gamma ray is absorbed by a thermal IR background at temperature T = 0.5 eV (5800 K), but with reduced energy density of 0.1 eV/cm^3. *Right:* Power law emission spectrum with differential index -2.5 (*solid line*) and the observed absorbed spectrum for a source at $z = 0.047$ (*dashed line*).

6.3.5 A Realistic EBL Model

Primack et al. (2001) presented a model for the EBL that was used by Aharonian et al. (2003a) and is shown in Fig. 6.7. Although Primack et al. has proposed a number of models, this is referred to as the Primack model in the following. With the exception of giving an estimate of the optical depth at low gamma-ray energies in Sect. 6.5, the Primack model will be used solely as a base-line comparison.

The optical depth corresponding to this model is shown in Fig. 6.8. From the optical depth, the monochromatic EBL density is derived according to Eq. 6.20 and shown in Fig. 6.8.
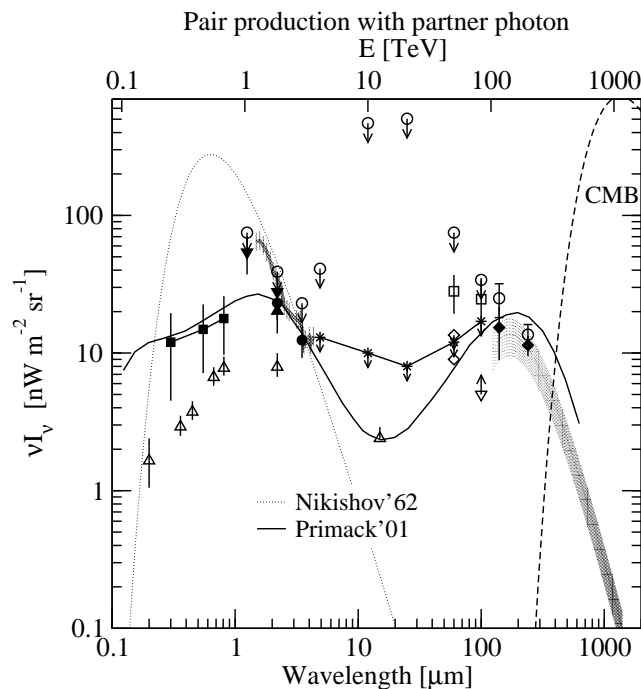
FIGURE 6.7. The Primack model (*solid line*) and the blackbody EBL model of Nikishov (1962) (*dotted line*) together with measurements and upper limits as shown in Fig.6.1.
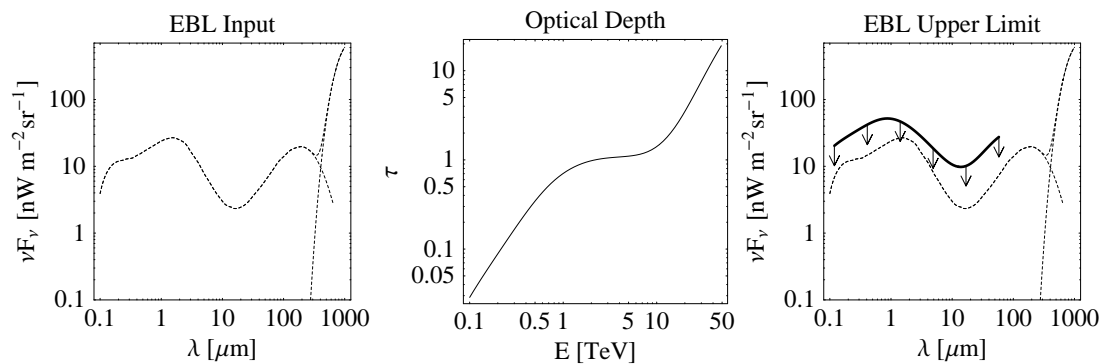
FIGURE 6.8. *Left:* Primack EBL model (*dashed line*). *Middle*: Predicted optical depth for gamma rays coming from Mrk 421 (z=0.031). *Right*: Monochromatic EBL density (*solid line*) derived from the optical depth displayed in the middle graph. This represents an upper limit on the EBL density and is derived solely from the optical depth.

6.4 Comparison of Blazar Spectra

The observed VHE spectra of Mrk 421 and Mrk 501 are best described by a power law with exponential cut-off at low redshifts (Krennrich et al., 2001). A more complicated structure may be present in the spectrum of furthest object, H 1426+428 (Petry et al., 2002; Aharonian et al., 2003a); this should be treated with caution because of limited statistics and systematic errors from combining the spectra from two collaborations. The brightest flare spectra for each of the six blazars were discussed in Sect. 1.3 and are shown in Fig. 6.9. The similarity of the spectra suggests that we make the zeroth order assumption that the same process is responsible for the VHE emission in all these AGN.

The power-law spectral index of each AGN flare spectrum is shown in Fig. 6.10. Because some curvature is present in the spectra of Mrk 421 and Mrk 501, the spectral index is measured at two energies to estimate the systematic error arising from this choice. In both cases, the increasingly steep spectrum with redshift is well fitted by a linear function with spectral index at z=0 of -1.7$\pm$0.1 and 2.0$\pm$0.1. The reduced χ^2 of the fits are 5.6 and 1.4 when the index is measured at 1 TeV and 2 TeV, respectively.

This result is consistent with uniform attenuation by the EBL. Fig. 6.11, *left*, shows the attenuation predicted by the Primack model. Also shown is the spectral slope at 1 TeV due to the absorption; it becomes steeper for more distant sources. Assuming that all blazars have the same intrinsic spectrum, the source spectrum at zero redshift is then obtained by choosing an intrinsic power-law index so that the χ^2 difference is minimized between the measured index-redshift slope and predicted slope, Fig. 6.12*right*. The spectral index at zero redshift predicted in this way is -1.62 and -2.2, when the power law fits are performed at 1 TeV and 2 TeV, respectively. Considering the large degree of uncertainty in choosing an energy at which to measure the spectral index, Fig. 6.11 implies that the intrinsic spectral index is on the order of -2 to -1.8. This is consistent with the spectral index that is obtained when the spectrum is fitted by a power-law modified with an exponential cut-off feature for Mrk 421 and Mrk 501. The power law spectral index for flares of these objects is in the
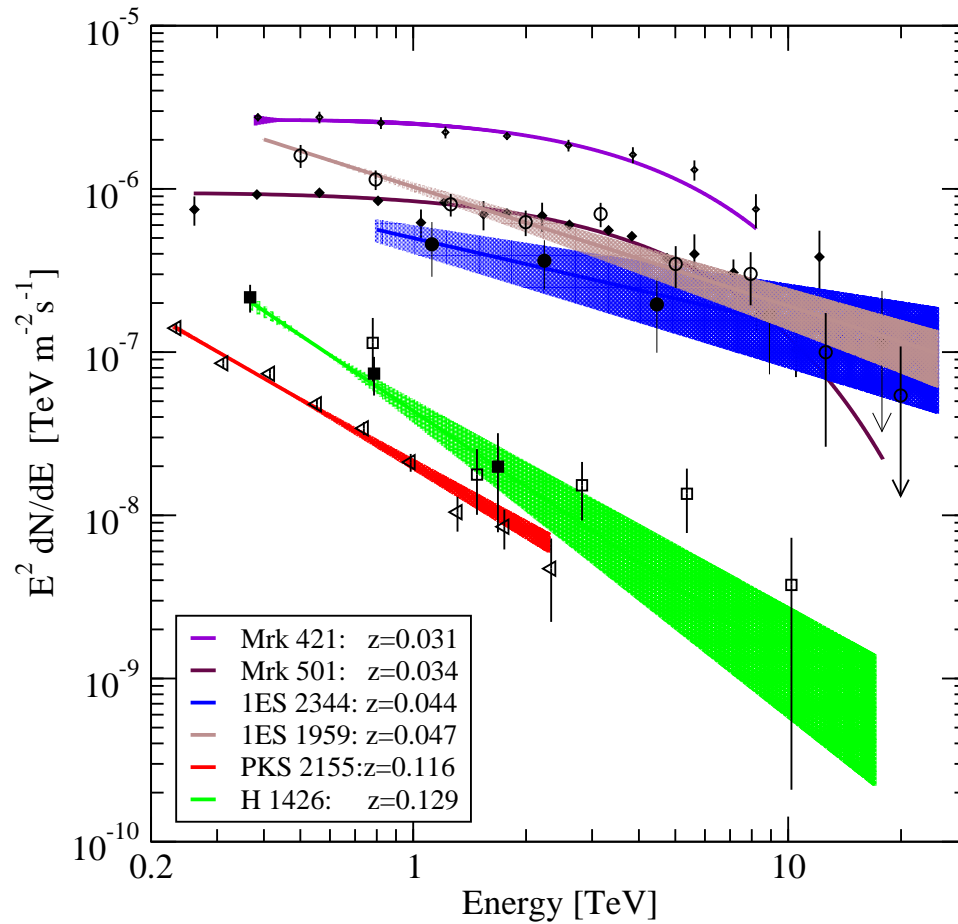
FIGURE 6.9. The very high energy flare spectra of six AGN. The shaded region shows the fit and 68% CI for 2 independent parameters. Mrk 421 from Krennrich et al. (2002) (*violet diamonds and line*), Mrk 501 from Samuelson et al. (1998) (*maroon diamonds and line*), 1ES 2344+514 (*full circles and blue shaded region*), 1ES 1959+650 (*open circles and brown shaded region*), H.E.S.S. spectrum of PKS 2155-413 in 2003 (*left triangles and red line*) courtesy of Wystan Benbow (Raue, 2004), H 1426+428 from Petry et al. (2002) (*filled squares and green region*) and Aharonian et al. (2003a) (*open squares*).

range from -1.9 to -2.1 with cut-off energy around 4 TeV consistent between both blazars and independent of flux state (Krennrich et al., 2002; Aharonian et al., 2002b).

It should be noted that the predicted spectral steepening with increasing redshift depends on the shape of the EBL. As Fig. 6.11 shows for the Primack EBL model, there is a leveling-off at high energies, not a simple power law with exponential cut-off as sup-
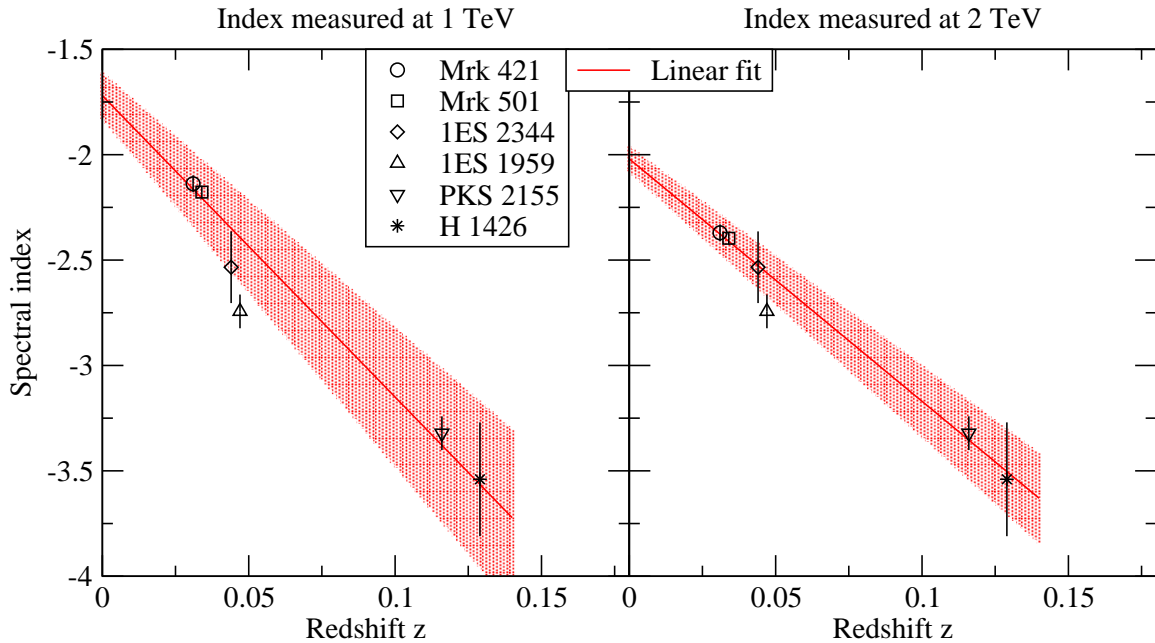
FIGURE 6.10. Spectral index of power law fits to the hardest measured flare spectra versus distance of the VHE blazars. The index was measured at 1 TeV (*left*) and at 2 TeV (*right*) for the curved spectra of Mrk 421 and Mrk 501. A linear fit to the data is shown in each case.

posed above. The cut-off energy in this case would be referring to the initial downturn at ≈ 0.6 TeV. At higher energies, the flux is so far diminished that measurements with VHE telescopes do not yield a statistically significant result. Note that if the optical depth is independent of energy, as is the case for $\nu F_\nu(\lambda) \propto \lambda^{-1}$, no change occurs at all in the spectrum with increasing redshift. In the Primack model this is almost the case between 2 TeV and 5 TeV, corresponding to the 2 - 5 μm EBL.

6.5   Upper Limits on the EBL Density from the Spectra of Blazars

The physical mechanism for production of the VHE gamma-ray peak is generally accepted as being due to inverse Compton up-scattering of UV/X-ray seed photons on high energy electrons. The intrinsic spectrum of the source is thus smooth and concave downwards; no physical mechanism has been proposed that would produce an exponential rise with energy
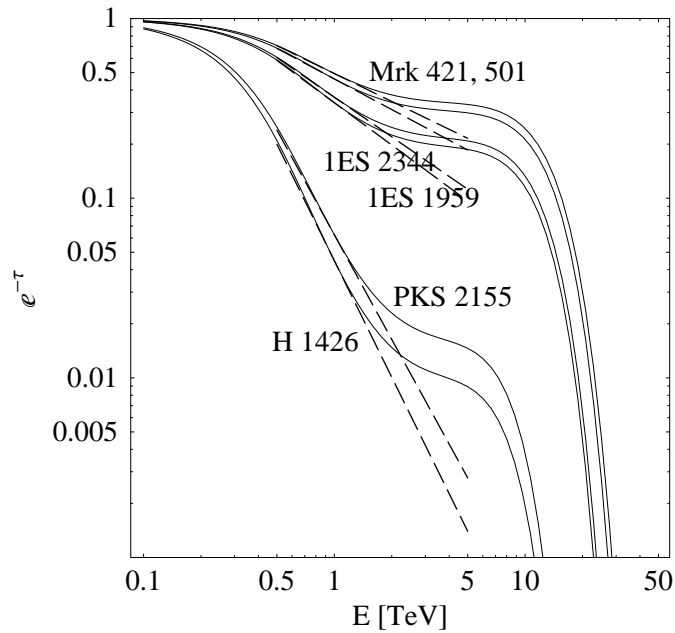
FIGURE 6.11. Illustration of power law spectra measured at 1 TeV from the attenuation predicted by the Primack mode. The attenuation, $e^{-\tau}$ (*solid lines*), is shown for the blazars (*top to bottom, solid lines*) Mrk 421, Mrk 501, 1ES 2344, 1ES 1959, PKS 2155, and H 1426. The *dashed lines* show the power-law spectra at 1 TeV. These become steeper with increasing source distance. No attenuation occurs at $z = 0$, the horizontal line at the top of the figure which corresponds to the intrinsic source spectrum and could be any reasonable shape.

or emission-like line features.

To determine the amount of absorption present in a measured spectrum requires a priori knowledge of the intrinsic source spectrum. Though the mechanism for VHE gamma-ray production has been modeled, important details that determine the source spectrum are not known: What is the mechanism? What is the electron or proton spectrum? What is the magnetic field? What is the opacity in the vicinity of the source for gamma-rays to escape?

To place upper limits on the EBL density, the following simple assumption will be made: The intrinsic spectral index of all blazars equals -1.8; this has been motivated in Sect. 6.4. If the spectrum has not been measured down to 0.2 TeV, the flux at that energy
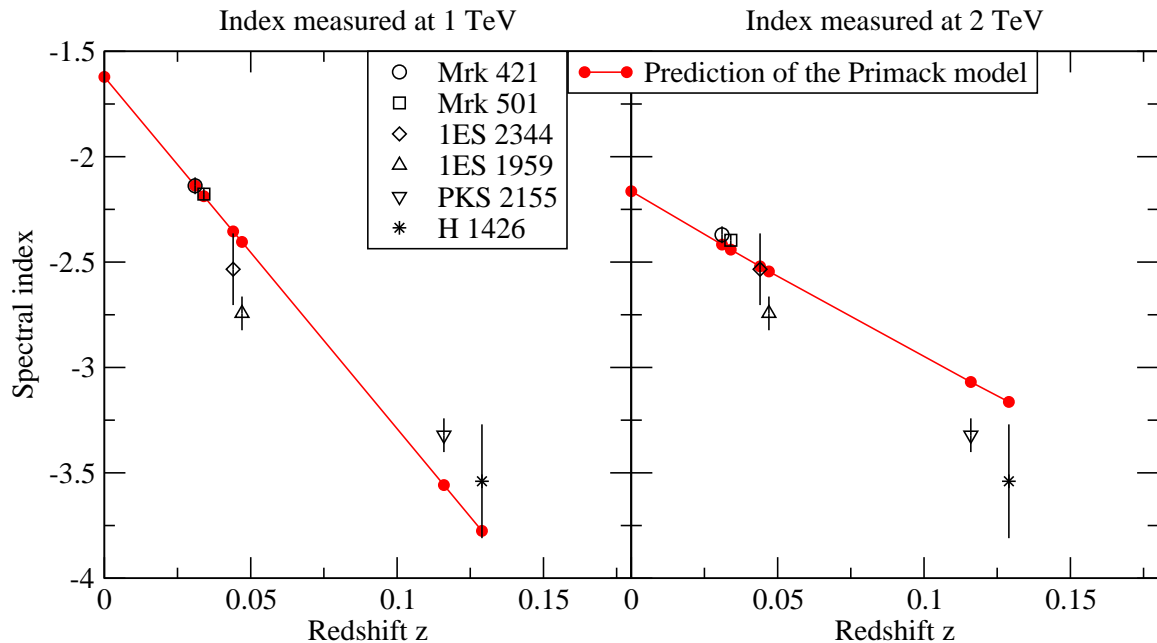
FIGURE 6.12. Spectral index of power law fits to the hardest measured flare spectra versus distance of the VHE blazars. The index was measured at 1 TeV (*left*) and at 2 TeV (*right*) for the curved spectra of Mrk 421 and Mrk 501. The prediction of the Primack model for the steepening of the spectra is shown by *connected red dots*. The predicted index was evaluated at each source distance and produces an almost linear relationship. For the Primack model, the spectral index at zero redshift is a free parameter and is derived from a best-fit to the data. The reduced χ^2 for the fit in the *left* figure is 5.7 and 4.3 for the *right* figure.

can be predicted from a power law fit extrapolated from higher energies, and the small amount of absorption present already at 0.2 TeV is estimated from the Primack model.

The assumed spectral index of -1.8 is very hard and cannot extend indefinitely. Harder spectra are, in principle, possible, but physically the energy output must decrease with energy at some point. Thus, there should be some downward curvature in the intrinsic VHE spectrum, so that by using a power law fit from higher energies, where the spectrum is steeper, to extrapolate down to 0.2 TeV will likely overestimate the expected flux from the source. The amount of absorption present at 0.2 TeV is calculated from the Primack model. The exact value of the optical at 0.2 TeV becomes less important at higher energies;

already at 1 TeV it contributes only 10% to the total optical depth. For example, the optical depth at 0.2 TeV for Mrk 421 is 0.9 ± 0.4, where the error estimate comes from the EBL measurement at 0.3 nm by Bernstein et al. (2002).

The expected flux for each blazar is shown in Fig. 6.13 by a dashed line. The absolute flux levels have been adjusted to the distance of Mrk 421 using an inverse square law and show that the power output of the sources is similar. The optical depth is the ratio of expected flux to measured flux with the addition of the optical depth at 0.2 TeV

$$\tau = \ln\left(F_e/F_m\right) + \tau(z, E = 0.2\,\mathrm{TeV}) \tag{6.22}$$

and does not dependent on the overall normalization of the flux level. The optical depth calculated in this way for the six blazars is shown in Fig. 6.14. Also shown in the figure is the optical depth calculated in the Primack model for comparison with the measured values.

The monochromatic EBL flux derived from each blazar spectrum under the above assumptions is shown in Fig. 6.15. For comparison, the value of the monochromatic flux as calculated from the Primack model is shown in the figure as well. For the most part, the monochromatic flux values derived here agree with the Primack model; this suggests that the true EBL density is close to this model. Differences between the sources in the derived monochromatic flux are likely caused by the intrinsic flare spectra not being pure power laws. Because of the large distances to the blazars it is highly unlikely that non-uniformities in the EBL could give rise to the observed differences. The limits derived from Mrk 421 and Mrk 501 are the lowest. To bring them higher and in line with the other sources, their intrinsic spectra would need to be slightly harder than -1.8. The good agreement of the flux values derived for H 1426 with the Primack model is not surprising because this model was used by the HEGRA collaboration to explain the intrinsic spectrum being a pure power law spectrum (Aharonian et al., 2003a). The systematic uncertainty in absolute energy calibration is 10%, directly corresponding to a 10% uncertainty in the EBL wavelength in Fig. 6.15.
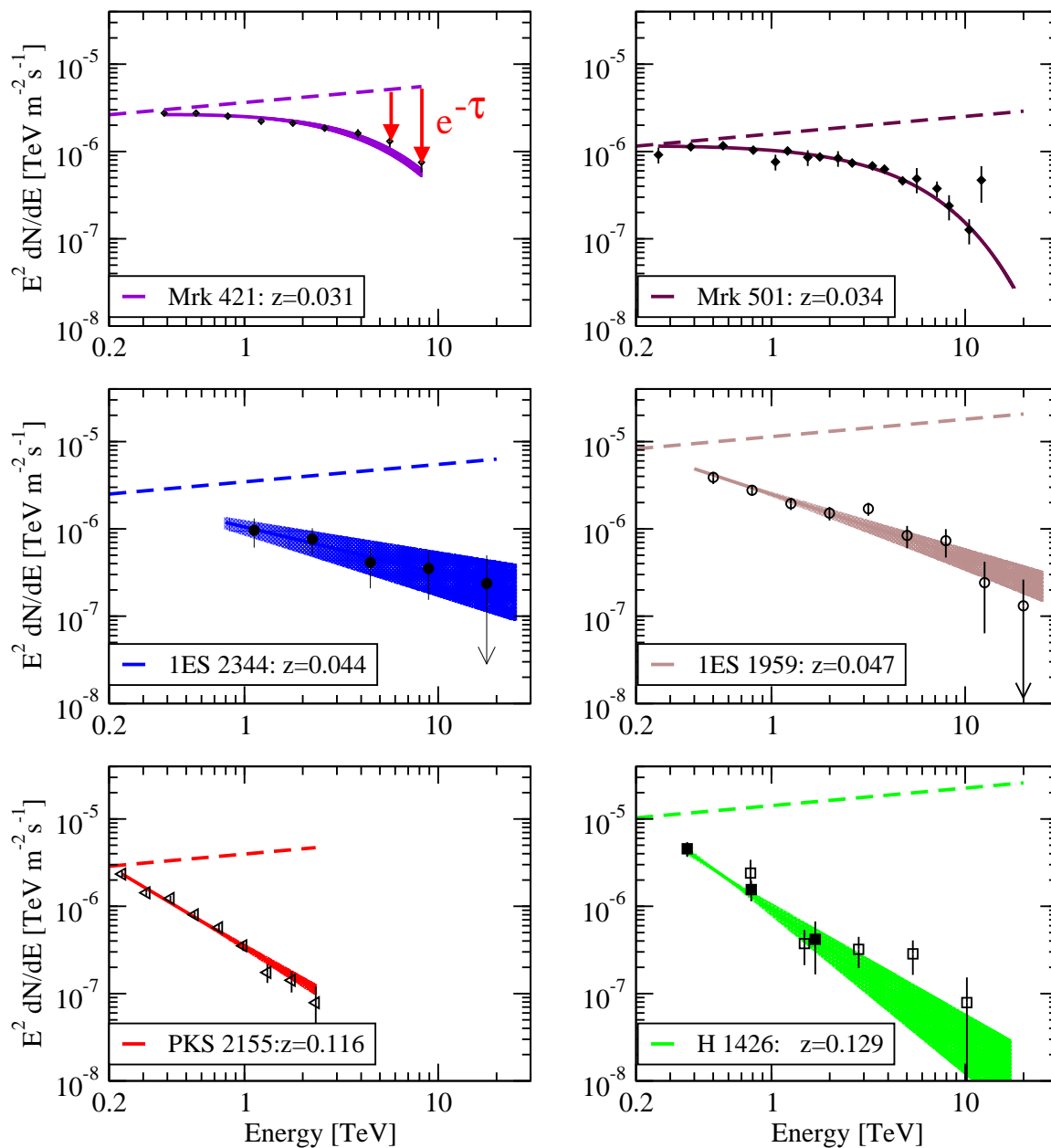
FIGURE 6.13. The very high energy flare spectra of six AGN. The flux for each source is adjusted with an inverse square law to the same distance as Mrk 421. Shown by the *dashed line* in each case is the assumed source spectrum with differential index -1.8; they are normalized to the measured, or predicted, flux at 0.2 TeV. The *top left* graph indicates the effect of the optical depth in attenuating the flux at two energies.

Fig. 6.16 shows the derived 98% confidence level upper limits together with other EBL measurements and limits shown previously in Fig. 6.1. The range of upper limits from the six sources is indicative of the systematic error of this method. The systematic error stemming from the optical depth at $E = 0.2$ TeV is not shown. It is about 5% at 1 TeV and decreases with wavelength.

The mid-IR limits on the EBL are monotonously decreasing with wavelength and above the limits inferred from fluctuation-analysis of the EBL by Hauser and Dwek (2001).

The upper limits in the optical to near-IR are in conflict with the detections claimed by (Matsumoto, 2000). An increase in the upper limits in this region would be achieved if the intrinsic source spectrum had a bump in the 0.7-2 TeV region or if the optical depth at 0.2 μm is substantially higher. The measured gamma-ray spectra are very flat in this energy region and it would be an unlikely coincidence if a high EBL flux were to exactly attenuate a high gamma-ray flux to produce a featureless (flat) gamma-ray spectrum.

Matsumoto (2000) argues that his measurements are inconsistent with galaxy evolution models and much higher than what can be accounted for by the observation of galaxy populations. Already at 2.2 μm the flux is higher than that claimed by (Wright, 2001) from COBE and 2MASS data. It appears that zodiacal emission modeling is the main uncertainty and responsible for the large fluxes.
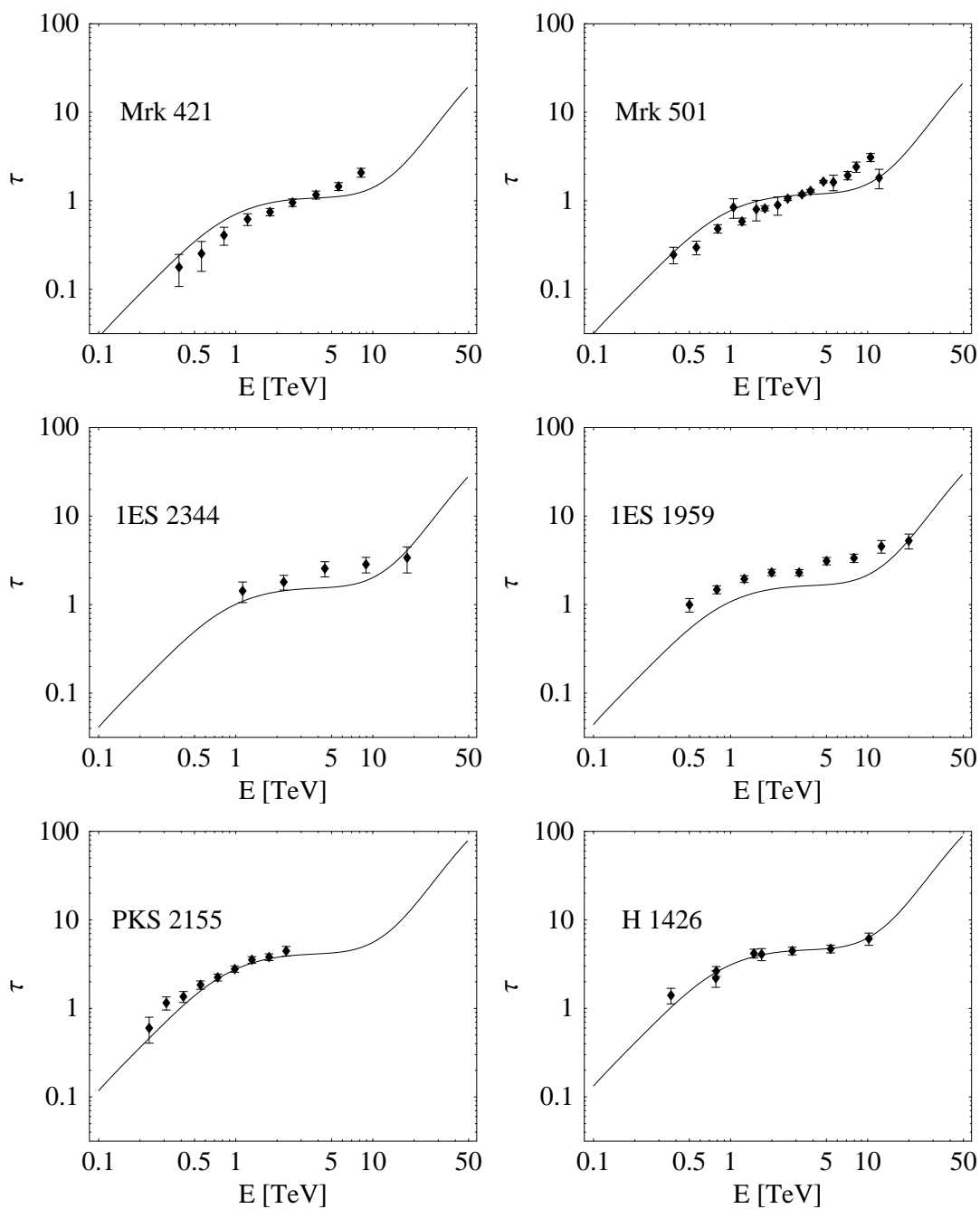
FIGURE 6.14. The optical depth (*data points with error bars*) derived according to Eq. 6.22 from the differences in Fig. 6.13 between measured and assumed flux. For comparison, the optical depth derived from the Primack model is shown by a *solid line*.
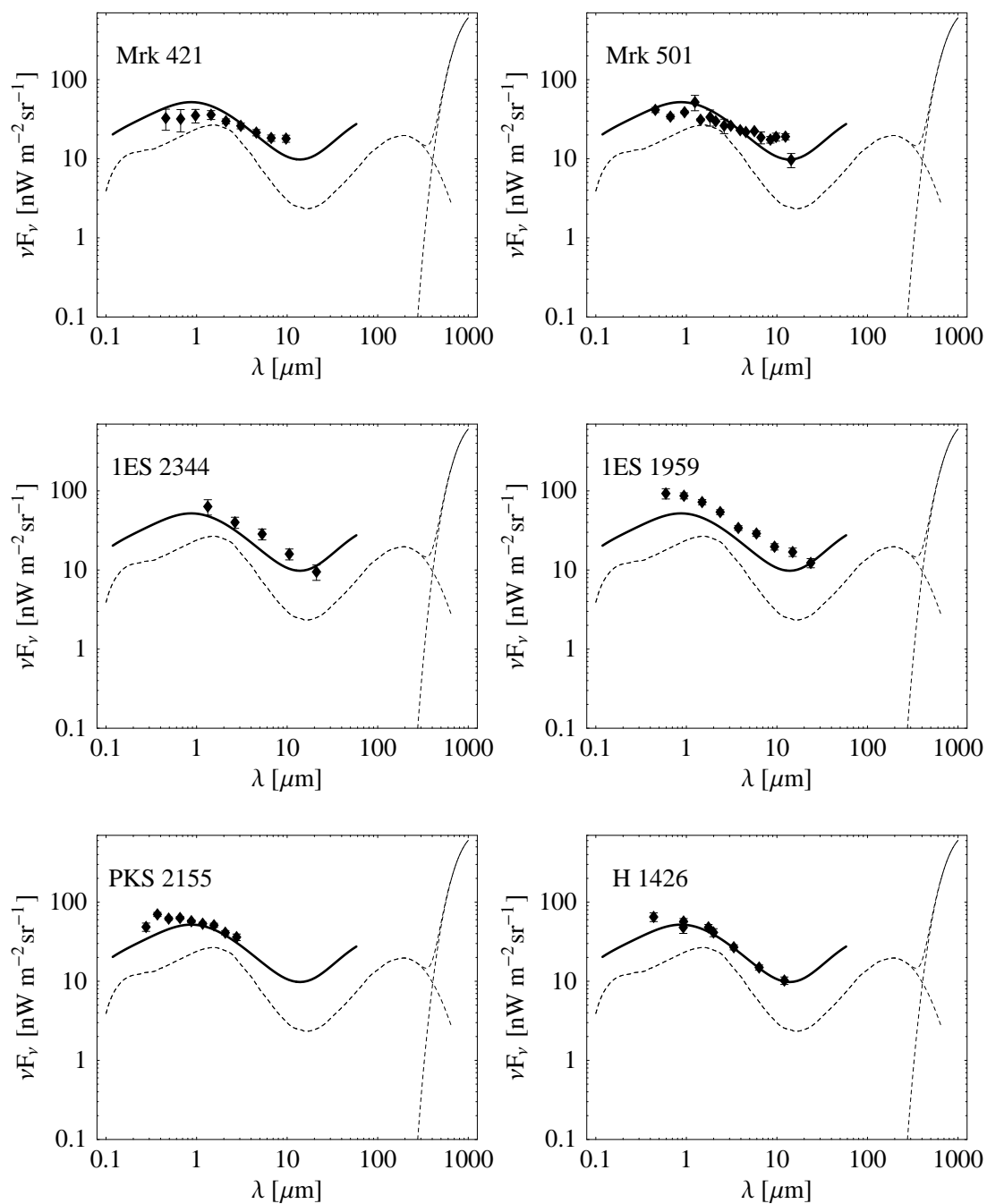
FIGURE 6.15. The monoenergetic EBL flux derived from the spectra of AGN (*points with error bars*). Also shown for comparison is the monochromatic flux (*thick line*) derived from the Primack EBL model (*thin dashed line*).
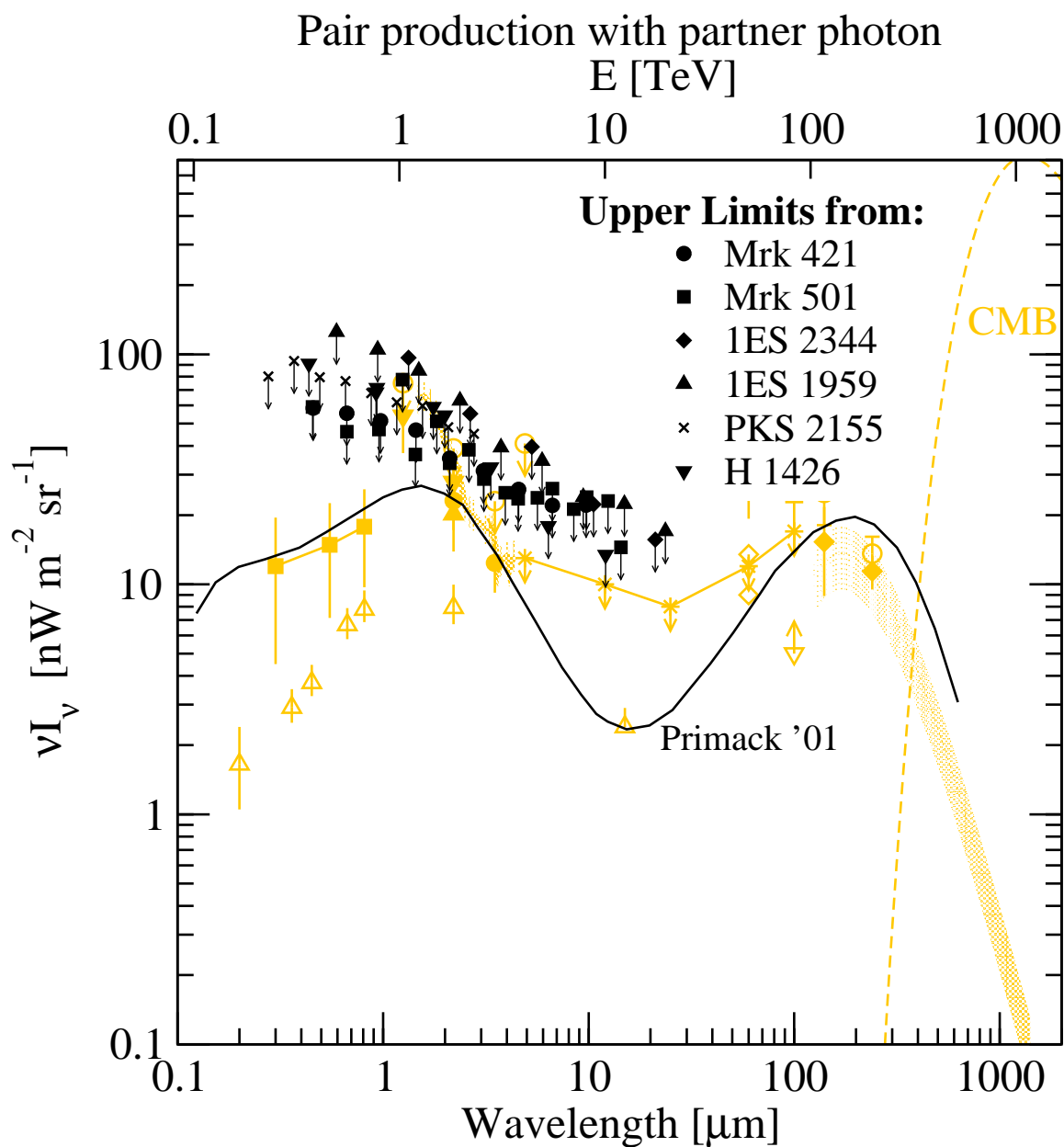
FIGURE 6.16. 98% confidence level upper limits of the EBL flux (*black points with error bars*). Measurements and limits from other publications are shown in *yellow*, see also Fig. 6.1. The model by Primack et al. (2001) is shown for comparison by a *solid line*. The top axis indicates the most likely energy of the partner photon to participate in pair-production with the EBL.

CHAPTER 7

CONCLUSIONS

Observational very high energy gamma-ray astronomy has made great progress in the last few years. Initially, gamma-ray astronomy was motivated by the mysterious origin of cosmic rays, but the detectors at that time were not sensitive enough to measure this. Now, with the advent of arrays of imaging Cherenkov telescopes with low energy thresholds and very good angular resolution, this underlying goal may be pursued again.

In the meantime, very high energy gamma-ray astronomy has established itself as an independent field with the detection of galactic and extragalactic sources, two of which have not been detected at other wavebands. A total of six extragalactic objects have been detected so far. They are BL Lac objects, a sub-group of active galactic nuclei characterized by intense nonthermal radiation. The VHE spectra of two of these, 1ES 1959+650 and 1ES 2344+514, were measured in this work. Similar to the other four BL Lacs detected, their VHE spectrum and flux level is highly variable and shows a broadband spectrum characterized by two emission peaks: one in X-ray, the other at GeV to TeV energies. For one of these, 1ES 1959+650, simultaneous observations were carried out at other wavelengths and for the first time, a VHE flare without increased X-ray flux level, was recorded. For the other object, 1ES 2344+514, no simultaneous X-ray observations were taken, making further modeling impossible.

TeV gamma rays are very penetrating and can shine through most of the dust in the Galaxy. But, on cosmological distances, pair production with optical and infrared extragalactic radiation attenuates the flux. At first, this may seem to be only a negative effect. The extragalactic background light (EBL) arises from galaxy formation and is difficult to measure directly because of bright foreground radiation originating within the Solar system. VHE gamma-ray astronomy can establish important upper limits on the density of

the EBL. If one can somehow guess what the source spectrum is, then one can infer the EBL density from the measured attenuation in the spectra. As the VHE spectra of BL Lac object are very similar, the zeroth order assumption was made (and justified) in this work that they are actually the same; differences in attenuation arising solely due to the different distances to the objects. The upper limits derived here are not very constraining, but they do question one particular set of EBL measurements that are very high in the near infrared waveband. Galaxy formation models are typically not able to reproduce this high density.

The analysis of VHE spectra is still being developed; in part because of the new array of four telescopes, VERITAS, being built at the moment. Monte-Carlo simulations are used in this work and changes in the simulation software had not seen a comparison to the previous version until this work. Differences were identified that impact the energy reconstruction. A method was developed to calibrate the absolute energy scale by automatically identifying cosmic-ray muons recorded by the telescope.

7.1 Limitations in Determining the EBL with VHE Gamma-Ray Spectra

Only upper limits on the EBL density were derived in this work. To do better and measure the EBL density, requires knowledge of the intrinsic and the absorbed source spectra over at least a decade of energy with very good accuracy. Reduced error bars on the measured spectrum will be achieved with the new generation of telescopes coming online now. However, the mechanism for production of VHE gamma rays, and hence the intrinsic source spectrum, is still under considerable debate. Unless a theoretical model is accepted or a "standard candle" at cosmological distances is identified with a well understood gamma-ray spectrum, the spectra from all these sources will only provide upper limits on the EBL flux. Only through further observation at all wavelengths will the gamma-ray production mechanism be understood. The GLAST satellite, to be launched in 2006, will cover the energy range from 0.1-100 GeV. Together with the low threshold of about 100 GeV for the

new arrays of imaging Cherenkov telescope such as HESS, VERITAS, and CANGAROO, simultaneous flux measurements can be performed over almost six decades in energy.

APPENDIX A

GLOSSARY

Adapted from Fegan (2004).

ACT — *Atmospheric CherenkovTelescope*, ground-based gamma-raydetection technique utilizing the production of Cherenkovradiation by charged secondaries (largely $e^{\pm}$) in the extensive air-showers that result from interaction of the primary in the atmosphere.

AGN — *Active Galactic Nucleus*, a galaxy with a powerful central core which is typically more luminous than the stars of the host galaxy combined. AGN are sub-categorized by their observational characteristics, such as the strength of radio emission, variability and presence or absence of broad emission line. In the unified theory of AGN, emission is the result of accretion onto a super-massive black hole, the various classes arising largely through differences in the orientation with respect to the line of sight of the observer.

Blazar — Sub-class of AGN characterized by strong radio emission, extreme variability, polarization at radio and optical wavelengths, and strong continuum emission. Blazars are classified as either FSRQ or BL Lac objects, distinguished by the presence (FSRQ) or absence (BL Lac) of absorption and emission lines. It is thought that blazars are AGN with a jet emanating from the core, oriented in the direction of the observer. They have a two peaked emission spectra, with correlated synchrotron and inverse-Compton components.

BL Lac — A type of blazar characterized by the absence of absorption and emission lines which makes the determination of redshift difficult. Their featureless spectra at optical wavelengths mean that BL Lacs are usually identified at x-ray or radio energies. Traditionally BL Lacs have been classified as low-frequency (LBL) or high-frequency (HBL) depending on the energy of the peak of synchrotron emission. There is probably a sequence of intermediate BL Lacs which are more difficult to identify as they do not stand out at radio or x-ray energies. All extragalactic VHE gamma-raysources detected to date are extreme

HBLs.

CANGAROO — *Collaboration between Australia and Nippon for a Gamma Ray Observatory in the Outback*, arguably the most contrived of astronomical acronyms. An ACT experiment operating in the Australian outback. The group is upgrading their single telescope to an array of four 10 m instruments.

CGRO — *Compton Gamma-Ray Observatory*, second in NASA's program of "great observatories". Launched in 1991 with four experiments covering the energy range from 60 keV to 30 GeV, it operated for nine years.

Chandra — Third of NASA's "great observatories", an x-ray instrument named for Subrahmanyan Chandrasekhar (1999-present).

DAQ — *Data Aquisition System*.

DSA — *Diffusive Shock Acceleration*, acceleration of a charged particle which repeatedly crosses of a shock-front due to scattering in the plasma.

EBL — *Extragalactic Background Light*, usually refers to the optical / infrared component of the diffuse radiation permeating the universe.

EGRET — *Energetic Gamma-Ray Experiment Telescope*, an instrument on the CGRO satellite, which operated in the energy range of 30 MeV to 30 GeV. The most successful gamma-raymission to date, its many achievements included a catalog of 271 point sources. EGRET sources are conventionally prefixed by 3EG.

erg — unit of energy in the CGS system equaling 10^{-7} J.

HBL — see BL Lac.

HE — *High Energy*, in the context of this work, refers to the energy range accessible to satellite based gamma-rayinstruments, 30 MeV to 30 GeV.

HEGRA — *High-Energy Gamma Ray Astronomy*, European ACT and air-shower array experiment on La Palma. The HEGRA group were the first to successfully employ the stereoscopic technique to discriminate between gamma-raysand cosmic-rays.

IACT — *Imaging Atmospheric Cherenkov Telescope*.

IC — *inverse-Compton* scattering.

ISM — *Interstellar Medium*, low density material that permeates the regions between stars in the galaxy.

LBL — see BL Lac.

MC — *Monte Carlo*.

Mid-IR — *5-80μm*.

NSB — *Night Sky Background*, consists of star light and the faint glow produced by charged particles in the upper atmosphere.

PMT — *Photo-Multiplier Tube*.

PSR — prefix used frequently to designate pulsars, e.g. PSR 1959+650, pulsar at sky coordinates $\alpha = 19^h 59^m$, $\delta = +65.0°$.

Plerion — A supernova remnant with a central object.

PWN — *Pulsar Wind Nebula*, synchrotron nebula or plerion. A supernova remnant which is being resupplied with high energy electrons by a central pulsar. The electrons cool quickly through synchrotron emission. For example: The Crab Nebula.

ROSAT — *Röntgen Satellite*, a German-US x-ray satellite which operated from 1990 to 1999. Its principal instrument, denoted HRI, operated in the energy range of 0.12 keV to 2.4 keV. The main aim mission was the first all-sky survey with a sensitivity 1000 higher than that of UHURU. ROSAT sources are conventionally prefixed by RX or 1RXS.

RXTE — *Rossi X-ray Timing Explorer*, NASA x-ray satellite (1995-present).

SAX or Beppo-SAX, *Satellite per Astronomia X*, an Italian x-ray satellite (1996–2002).

SED — *Spectral Energy Distribution*, the power an instrument would receive as a function of frequency, given the assumption that its bandwidth is proportional to the frequency.

SNR — *Super Nova Remnant*, hot material thrown off as blast wave in supernova explosion. Shocks formed in interaction with ISM may give rise to particle acceleration, possibly resulting in a population of charged particles with energies up to 10^{15} eV.

RMS — *Root Mean Square*, Describes the width of a distribution. For a Gaussian distribution, if the mean is zero, the Gaussian width equals the RMS value.

TeV — *Terra Electron-Volts*, unit of energy equivalent to $\sim 1.6 \times 10^{-7}$ J and 1.6 erg.

VHE — *Very High Energy*, in the context of this work, the energy range of 300 GeV to 30 TeV, accessible to ground-based gamma-rayinstruments.

VLA — *Very Large Array*, interferometer consisting of 27 radio telescopes, each with 25 m diameter, near Socorro, NM. The array has four configurations, the largest of which spans an area of diameter 35 km.

XMM-Newton — *X-ray Multi-Mirror* mission, a high resolution, x-ray instrument operated by the European Space Agency (1999-present).

XRB — *X-ray Binary*, a binary system consisting of a pulsar and a large companion star. Often they are sub-classified as high-mass (HMXB) or low-mass (LMXB).

APPENDIX B

THEORY OF CHERENKOV RADIATION

The theory and applications of Cherenkov radiation are discussed in detail by Jelly (1958). Only, the essential results are summarized here. Cherenkov radiation is emitted by a charged particle if it travels through a medium faster than the speed of light in that medium. The speed of light in a medium is a collective effect and describes how fast information can travel. In an approximation, dipole radiation occurs from the polarization of the dielectric medium when a charged particle traverses it faster than the medium can respond to the electric field [1]. The speed of light, c_n, in a medium of refractive index, n, is given by

$$c_n = c/n, \tag{B.1}$$

where c is the speed of light in vacuum. A particle traveling at speed v faster than c_n, but less than c, produces an electromagnetic shock wave, similar to a super-sonic shock wave in air or water. From Huygen's construction of constructive interference, see Fig. B.1, the opening angle of the conical wave front is

$$\cos(\theta) = c_n/v. \tag{B.2}$$

The limits on θ are defined by $\cos(\theta) \leq 1$ and $v < c$, that means $c_n \leq v < c$. The refractive index of air at sea level is 1.000285, varying slightly with wavelength, resulting in a maximum opening angle of about $1.37°$.

The number, N_γ, of Cherenkov photons emitted per units wavelength λ, per distance l traveled by the charged particle, and per azimuthal angle ϕ is (Leo, 1994)

$$\frac{\mathrm{d}^3 N_\gamma}{\mathrm{d}l\,\mathrm{d}\lambda\,\mathrm{d}\phi} = \frac{\alpha}{\lambda^2}(1 - \frac{c^2}{v^2 n[\lambda]^2}). \tag{B.3}$$

---

[1]This is related to the density effect, but here the emitted radiation is considered and not the energy loss of the charged particle.
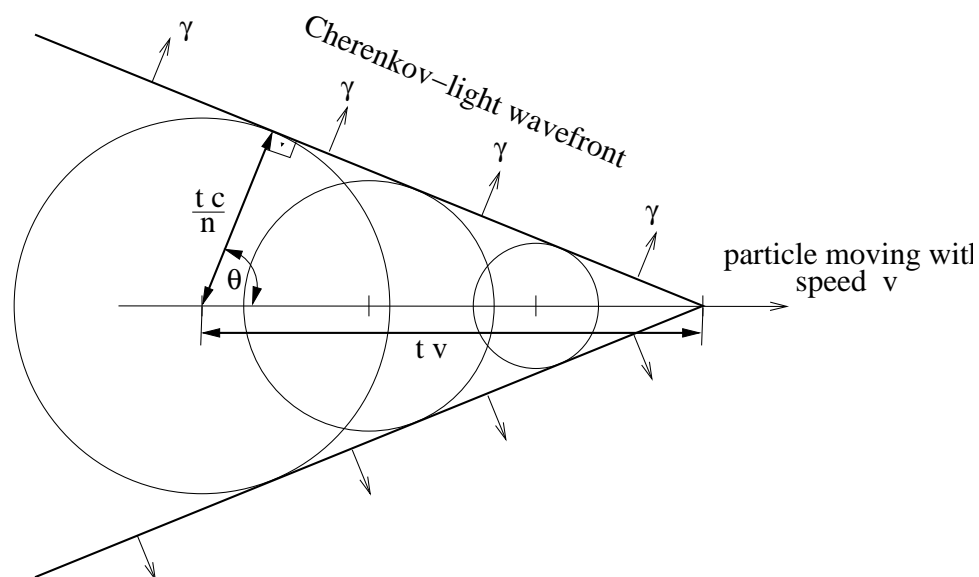
FIGURE B.1. Constructive interference of the emitted radiation wavefronts occurs along a cone of opening angle θ. During a time, t, the particle moves a distance tv, while the radiation front advances by tc_n, hence $\cos(\theta) = c_n/v$.

For a typical optical detector that detects wavelengths between 350 nm and 550 nm, this corresponds to $47500 \sin^2(\theta)$ γ/m, or about 30 γ/m in air. This also means that energy loss due to Cherenkov radiation is negligible compared to bremsstrahlung radiation and ionization losses (Blackett, 1948).

APPENDIX C

OPTICS OF THE 10 M TELESCOPE

This study of the telescope optics was carried out to (1) improve the optical quality of the telescope and (2) determine the parameters to use in the simulation of the telescope optics with GrISU.

C.1   Optical Properties

The Whipple 10 m telescope consists of a spherical optical support structure (OSS) with 10 m diameter. The radius of the OSS is 7.3 m and it supports about 240 spherical mirrors each of 7.3 m focal length and hexagonal in shape. A comprehensive review of the optical properties along with a comparison to a parabolic telescope, is given by Lewis (1990).

C.2   Alignment

The 240 facets on the 10m telescope are aligned so that light from a star is focused to a common point. However, the size of the 10 m telescope makes it impossible to access and adjust the facets while the telescope is pointing at a star since the mirror must be adjusted from the front. Therefore, the telescope is aligned in the stow position. For a spherical mirror, the incident and reflected rays of light are coincident with each other if they pass through a point located along the optical axis at a distance twice the focal length, the $2f$ point. The facets on the 10 m telescope are arranged on a sphere, see Fig. C.1. This means an alignment can be performed by positioning a laser at the $2f$ point and adjusting a facet so the beam is reflected back to the $2f$ point.

Located at the $2f$ point, a distance of 14.6 m for the Whipple 10m telescope, is the alignment instrument. The alignment instrument consists of a steerable laser on a pan-tilt
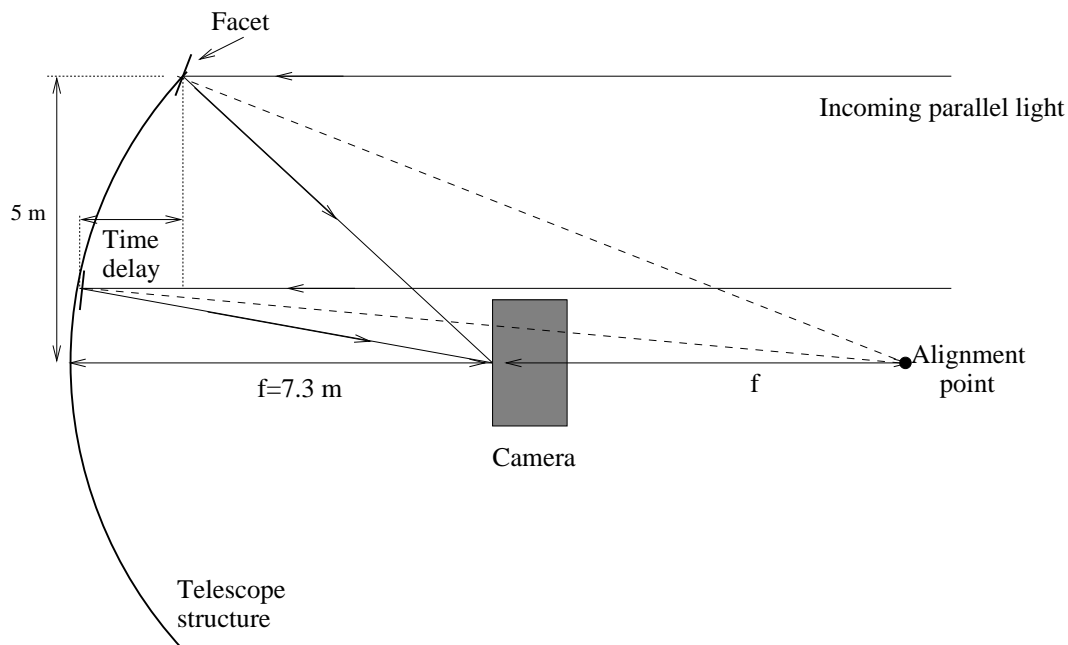
FIGURE C.1. Ray diagram for alignment of facets. There are about 240 facets on the telescope, but only two facets are shown for illustrative purposes. Laser alignment of the innermost facets is not possible as the line-of-sight from the $2f$ point is obscured by the focal box.

unit (PTU) and a CCD camera. The telescope axis is pointed at the prism; a properly aligned facet will point the laser directly back to the $2f$ point of the spherical telescope.

To verify the quality of the alignment, stars are directly imaged on the focal plane. For that, a paper screen is put in front of the PMT camera and the telescope is pointed at stars at various elevations. Ideally, a star is imaged as a single point with Gaussian width equal to the blur size of an individual facet. However, deformations of the telescope structure and the facet mounts result in misaligned facets and cause additional blurring. The images of stars recorded in this way are referred to as the point spread function (PSF) of the telescope.

C.3 Bias Alignment

The Whipple 10 m reflector was built in 1968 and designed to make high energy gamma-ray observations with light detectors of $1°$ diameter. The measured point spread function (PSF) was $0.12°$ to $0.15°$ with a simple light detector at the focus. The current Whipple camera, which is heavier than the reflector was designed for by a factor of two, has pixels of $0.12°$ diameter; ideally the PSF of the reflector should have a FWHM less than this. Measurements of the PSF with the heavier camera showed a width of $0.18°$ above elevations of $60°$ where most observations are made. A study of the optical properties of the reflector showed two causes of light spreading: gross deformation of the optical support structure and individual facet motion. These effects can be lessened by a bias alignment, i.e., intentional misalignment of the facets in the horizontal position where the alignment is performed so as to give an optimized image over the operating range of elevation from $50°$ to $90°$.

The motion of each facet with respect to the positioner axis was measured with telescope elevation. For that, a laser was clamped on a facet and the positions of the laser spots on the PMT camera was recorded. The arrows in Fig. C.2 show the facet tilt that occurs when the telescope moves from $0°$ to $30°$, $60°$, and $90°$ elevation. The deformation of the OSS occurs mainly around vertical structural elements. Also, a general vertical shift is visible; this is somewhat compensated by the vertical motion of the PMT camera with respect to the positioner axis. In addition, the average decentering is subtracted before the bias alignment is done.

C.4 Point Spread Function

The image on the focal plane generated by a star, a point source, is called the point spread image (PSI). Point spread images obtained without and with a bias alignment are shown in Figs. C.3 and C.4. The average full-width half-max (FWHM) of the light distribution with elevation is shown in Fig. C.5. The FWHM was determined from a fitted 2-d Gaussian to
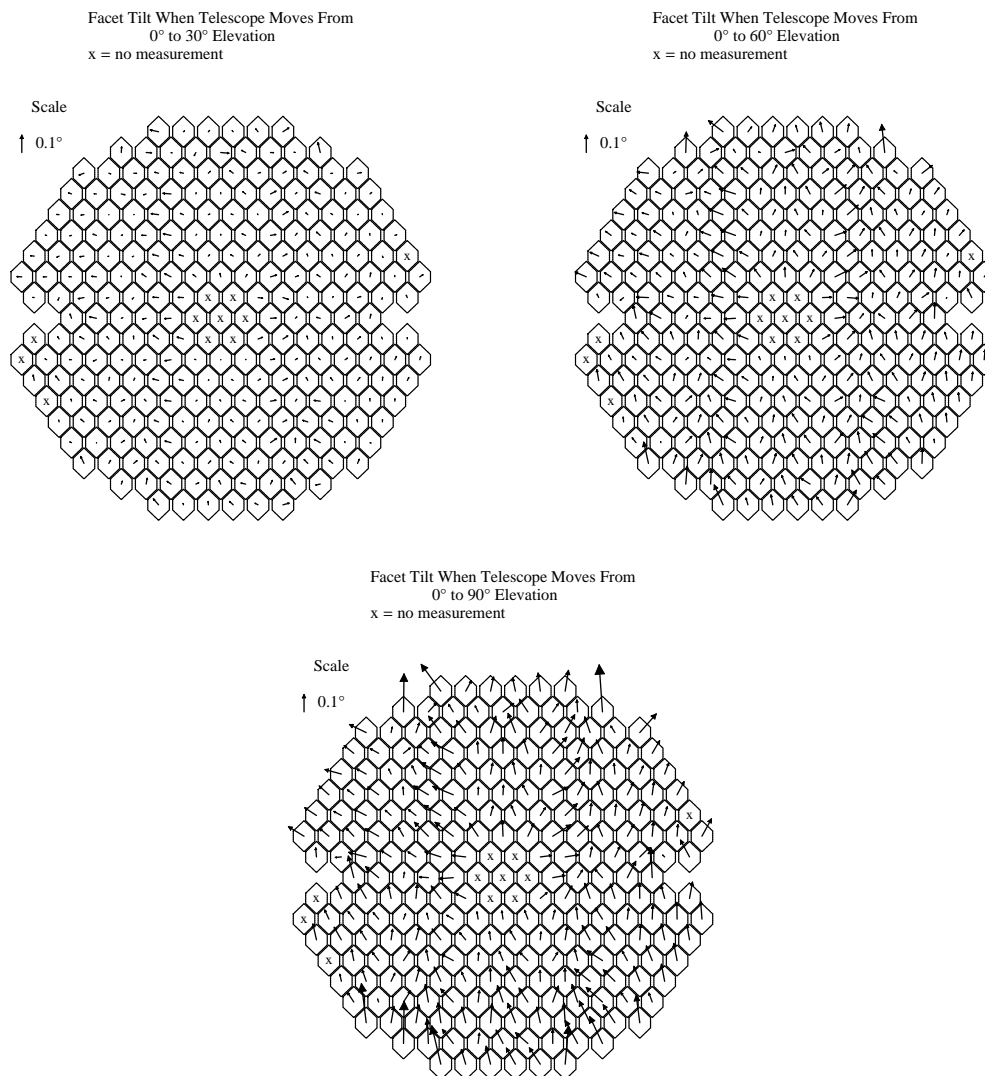
FIGURE C.2. Tilt of mirror facets when telescope is pointed from elevation 0° to 30°, 60°, and 90°.

the PSI.

C.5   Simulation of the Telescope Optics

An important parameter for the telescope simulation with $grisudet$ is how well the light from a star is focused by all mirrors on the telescope. One way to compare the telescope
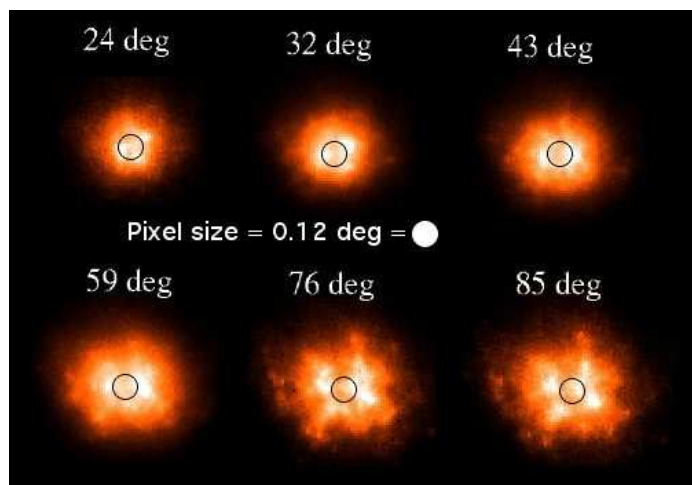
FIGURE C.3. Point spread images at various elevations without biased mirror alignment. Measurement on 17 October 2001.
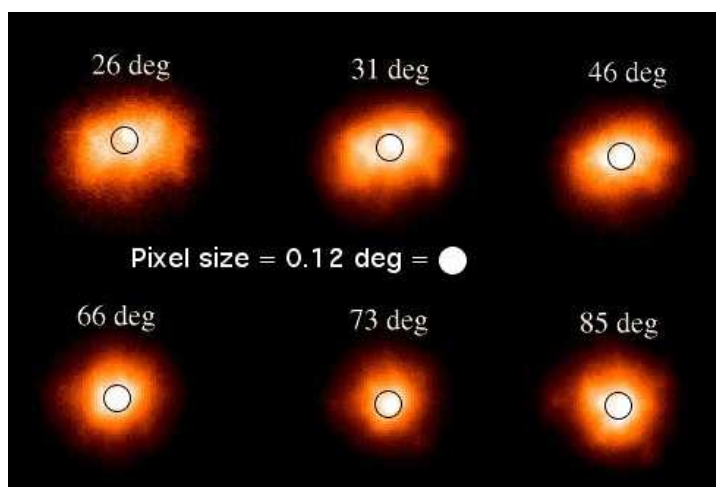
FIGURE C.4. Point spread images when mirrors are aligned with bias offsets. Measurement from 7 February 2002.

simulation with measurement is by plotting the radial brightness profile of the PSI. For the measured PSI the image center was identified by fitting a 2-d Gaussian profile and averaging the brightness at a given distance from the center. The simulated PSI was generated by randomly throwing photons at the telescope and ray tracing them to the focal plane. The PSI brightness profile with and without bias alignment is shown in Fig. C.6 for low and
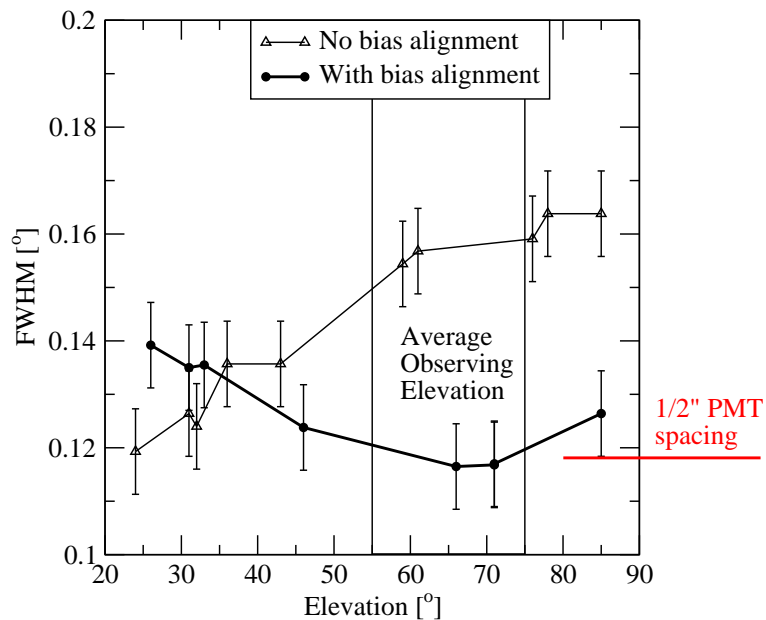
FIGURE C.5. Measured point spread function without (thin) and with (thick) bias alignment.

high elevations. When the mirrors are not bias aligned, the image breaks apart horizontally into two sections. Simulated brightness profiles are shown in Fig. C.7 alongside two measured profiles without bias alignment and in Fig. C.8 with two measured profiles with bias alignment. The bias alignment markedly improves containment to a single PMT. Without bias alignment the measured radial profile cannot be fitted with two global parameters anymore because the PSI falls apart into at first two and at higher elevation four separate parts.
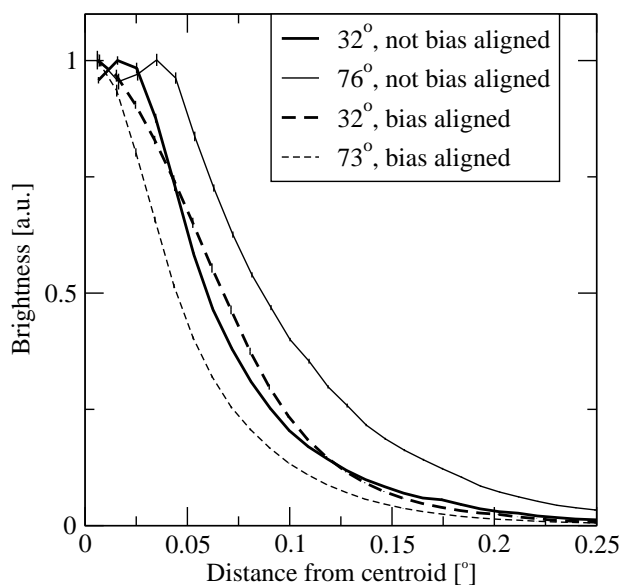
FIGURE C.6. Radial brightness profile of point spread images taken at elevation of $32°$ and $76°$ before bias alignment and after bias alignment at elevations of at $32°$ and $73°$.

FIGURE C.7. Simulated brightness profiles with the default values in $grisudet$ (thick line) and for two other cases that produce a better fit. Gray lines show the point spread image profiles without bias alignment at elevation of $32°$ and $76°$. Vertical line at $0.06°$ indicates radius of 1/2" PMTs.
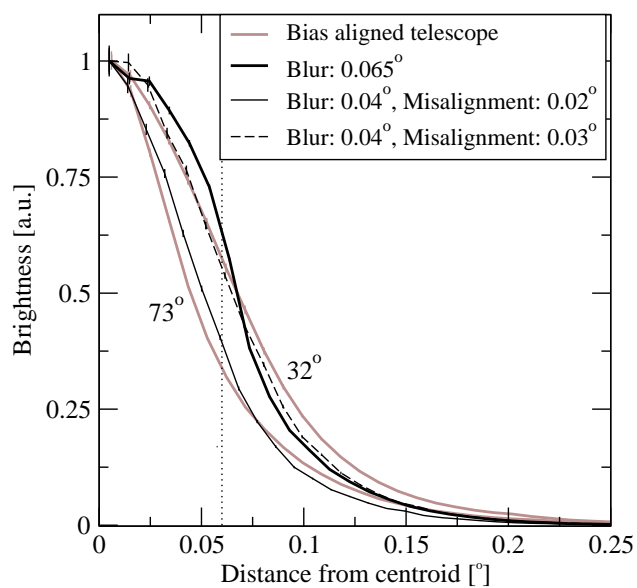
FIGURE C.8. Simulated brightness profiles with the default value $grisudet$ (thick line) and two other cases that produce a better fit. Gray lines show the point spread image profiles with bias alignment at elevations of 32° and 73°. Vertical line at 0.06° indicates radius of 1/2" PMTs.

APPENDIX D

OPTICAL SPECTRA OF MRK 421 DURING EARLY 2002

To study if external photons from the surrounding galaxy could be the seed photons for production of VHE gamma rays, simultaneous observations were taken with the Whipple 10 m telescope and the FAST spectrograph on the 60" Whipple telescope from January to April 2002. Fig. D.1 shows the integrated spectrum If, for example, a Hydrogen emission line becomes visible only during periods of of intense VHE emission, it may be a sign that seed photons are not due to synchrotron radiation, but a nearby cloud. In particular, the correlation between the VHE flux and H_α, was measured. Data were taken with typical integration times of 3x10 min per night, a few times per week and when flaring was reported by 10 m telescope. Unfortunately, a good signal-to-noise ratio on the opitcal spectra required combining data from an entire month for a total of about two to four hours exposure, Fig. D.2. This prevents a correlation to be established between the short time scale VHE flare and the optical activity. On month-long time scale, no variation in the strength and equivalent width of the H_α line was found, even though some VHE flare was seen for Mrk 421. Fig. D.3 shows the VHE lightcurve for this period together with the monthly averages. The elevation range that this data was taken over is shown in Fig. D.4. As most of the data lies at high elevations, the energy threshold for detection of gamma rays is about the same for all data.
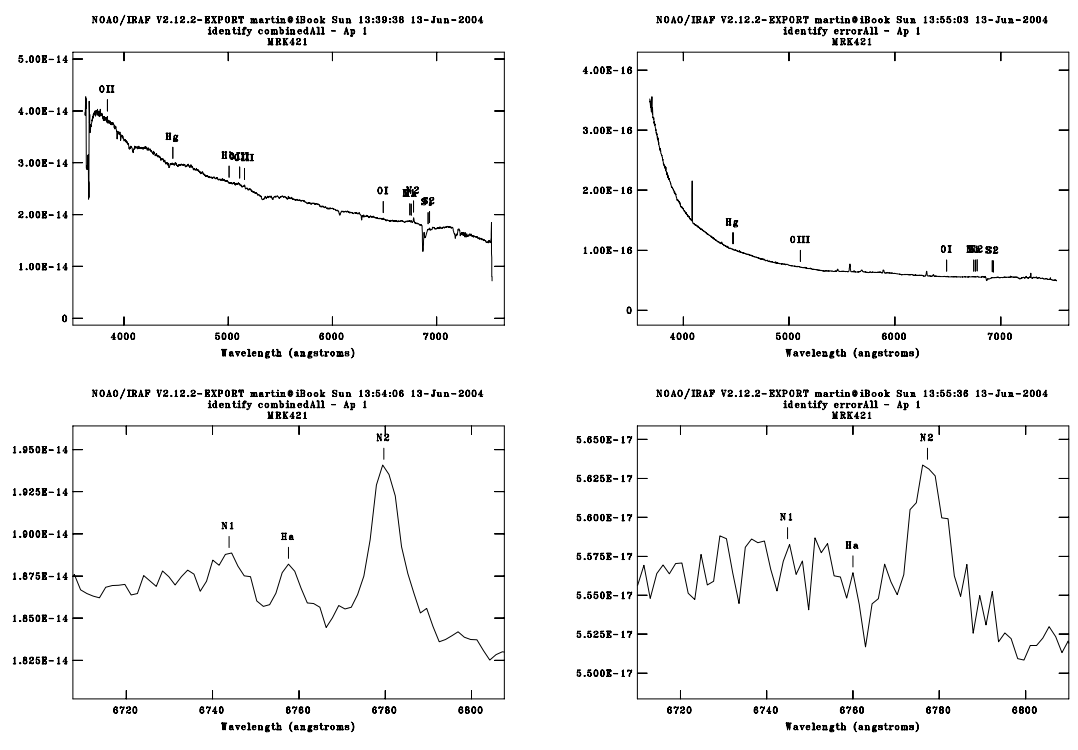
FIGURE D.1. Optical spectrum of Mrk 421 integrated from January through April 2002. Shown in the *top left* is the flux calibrated spectrum [erg s^{-1} Å^{-1}] together with the rms error (*top right*). A clope up of the region around H_α is shown in more detail at the *bottom left* together with the rms error (*bottom right*).
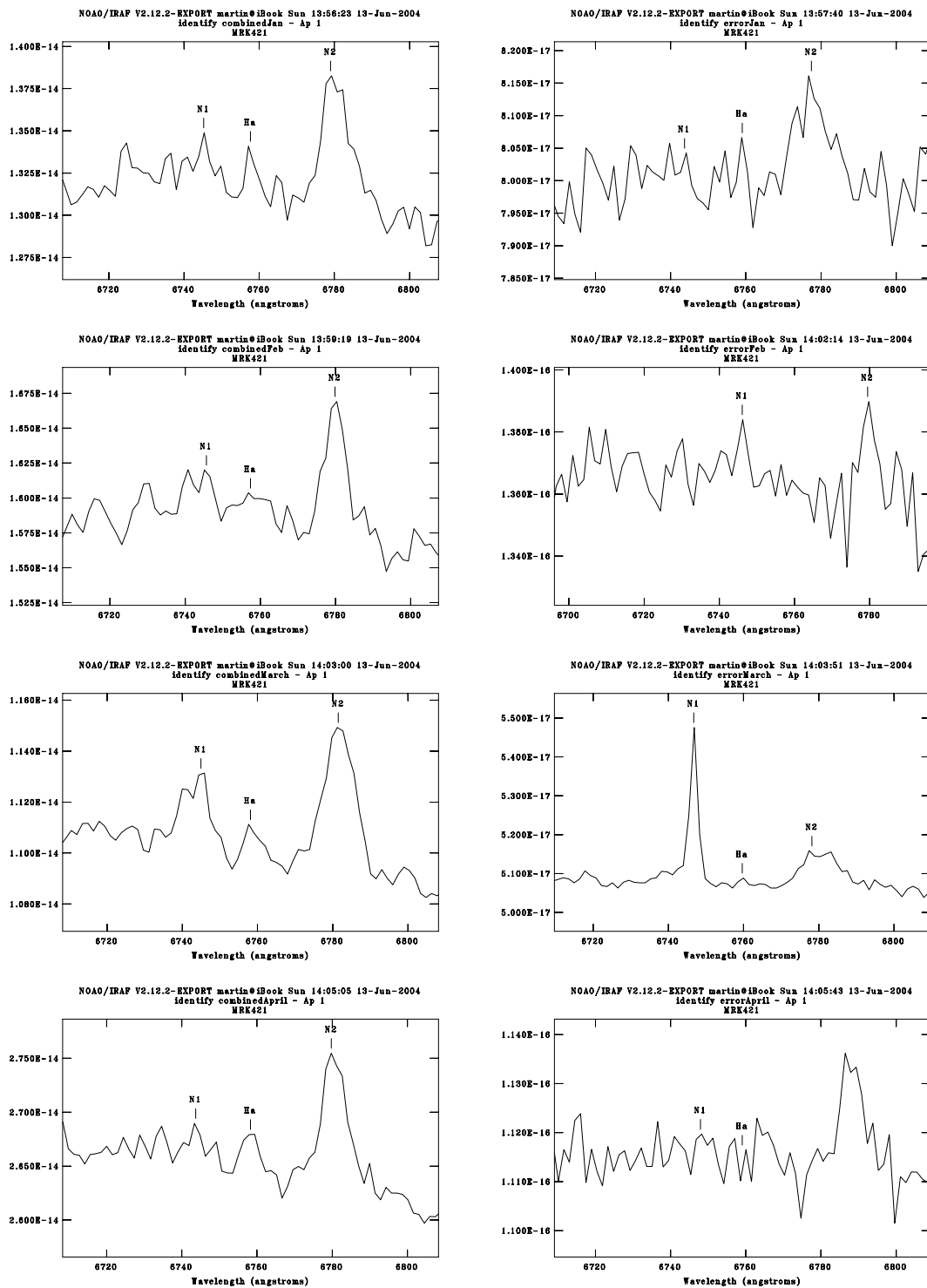
FIGURE D.2. Monthly optical spectra of Mrk 421 (*left*) and RMS errors (*right*) in units of [erg s^{-1} Å^{-1}] during January (*top*), February (*second row*), March (*third row*), and April (*bottom*) of 2002.
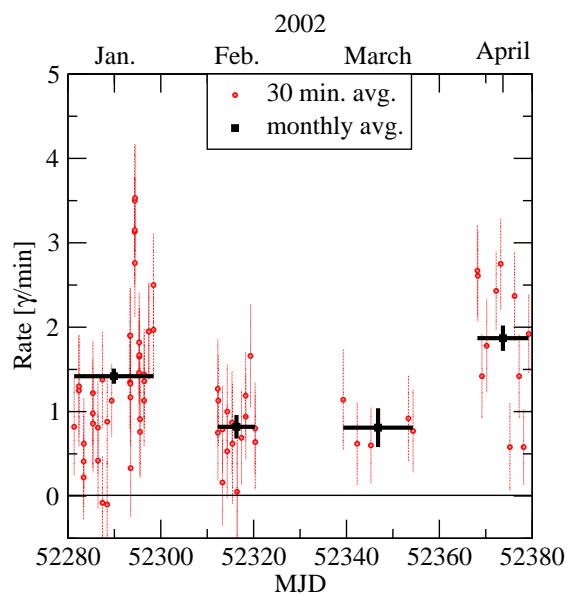
FIGURE D.3. Gamma-ray rate during January through April 2002 of Mrk 421 on a run-by-run basis (*red data points*) and on a monthly time scale (*black thick data points*).
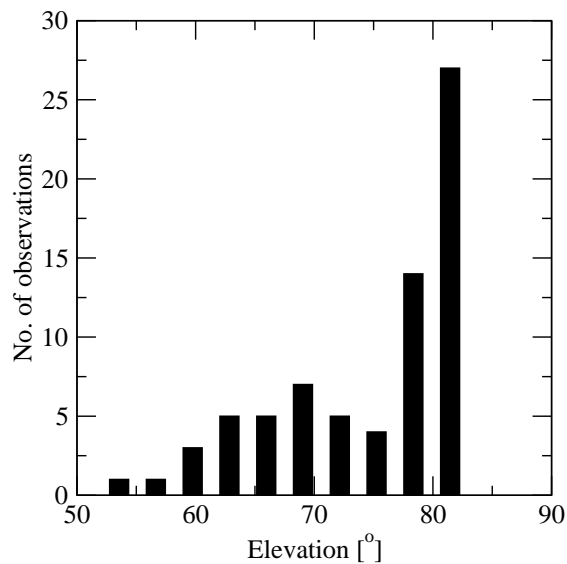
FIGURE D.4. Elevation distribution of data taken during January through April 2002 on Mrk 421.

ADDENDUM ON THE CORRELATION OF OPTICAL AND X-RAY LIGHTCURVES FOR 1ES 1959+650 DURING SPRING 2002

The results of multiwavelength observations for 1ES 1959+650 consisting of optical, X-ray, and VHE gamma-ray data were presented by Schroedter et al. (2003). Based on the data available at that time, evidence was presented for a correlation between the X-ray emission and the R-band optical photometry; with the optical component lagging by five days, Figs E.2 and E.3. Some time later, additional optical data became available and prompted a reanalysis. With the increased data set, the X-ray / optical correlcation could not be confirmed anymore. The nine addional R-band observations cover the time after MJD 52438. The complete lightcurves for the three energy bands is shown in Fig. E.1.

To test if a correlation exists between two sets of data, one can start with the zeroth order assumption of a linear correlation between two variables x and $y = a + bx$ or equally well between y and $x = a' + b'y$. The linear correlation coefficient (LCC) is defined as (Bevington, 1992)

$$\mathrm{LCC} = \sqrt{bb'}. \tag{E.1}$$

The LCC = 1 for complete correlation and both b and b' are zero for no correlation. The statistical significance of the signal was evaluated through comparison with 100 time-randomized versions of the data. As none of the VHE, X-ray, and optical data points were taken truly simultaneously, the points in the lightcurves were binned in 24 hr increments. Also, the possibility of arbitrary time-lags between the energy bands was allowed for in the analysis. Additional detail can be found in Schroedter et al. (2003).

Using this method, the LCC for different time lags between the optical and X-ray bands was calculated, see Fig. E.2. The most significant correlation occurs for a five day optical
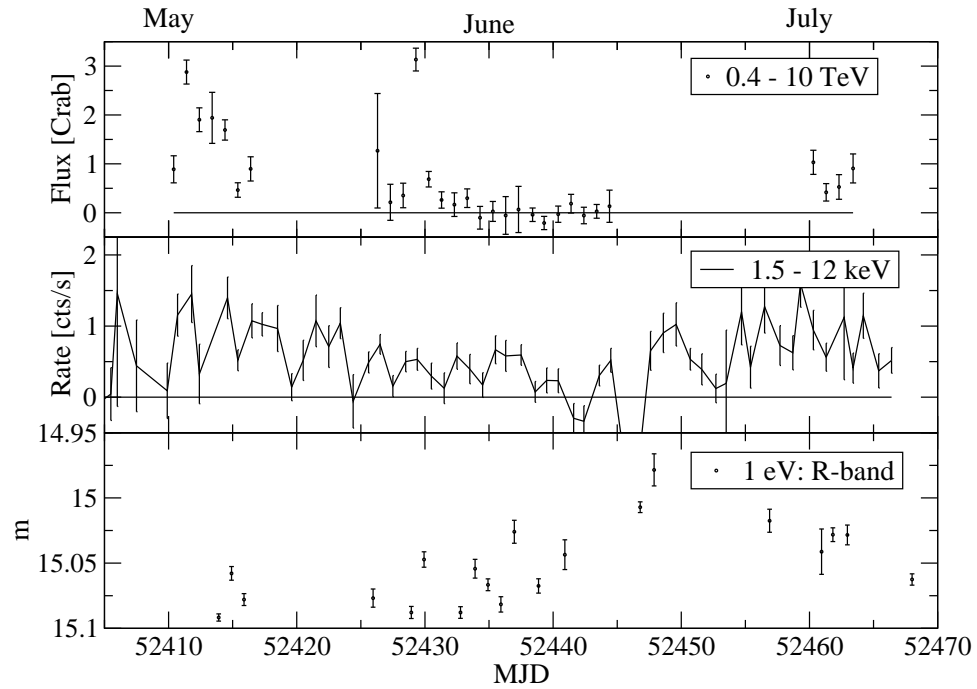
FIGURE E.1. Lightcurve of VHE, X-ray, and R-band brightness during May - July 2002.

time lag, the probability for this to occur randomly is 9×10^{-6}. With the new data (*bottom plot*) the correlation goes away. Fig. E.3 shows that the additional optical data is not correlated with the X-ray data anymore.

Though, the correlation dissappeared with the additional data, it should be kept in mind that for almost 2 months there was a correlation. Blazars have a rapidly varying lightcurve across the entire spectrum; thus it is not unexpected that one finds correlations from time to time.
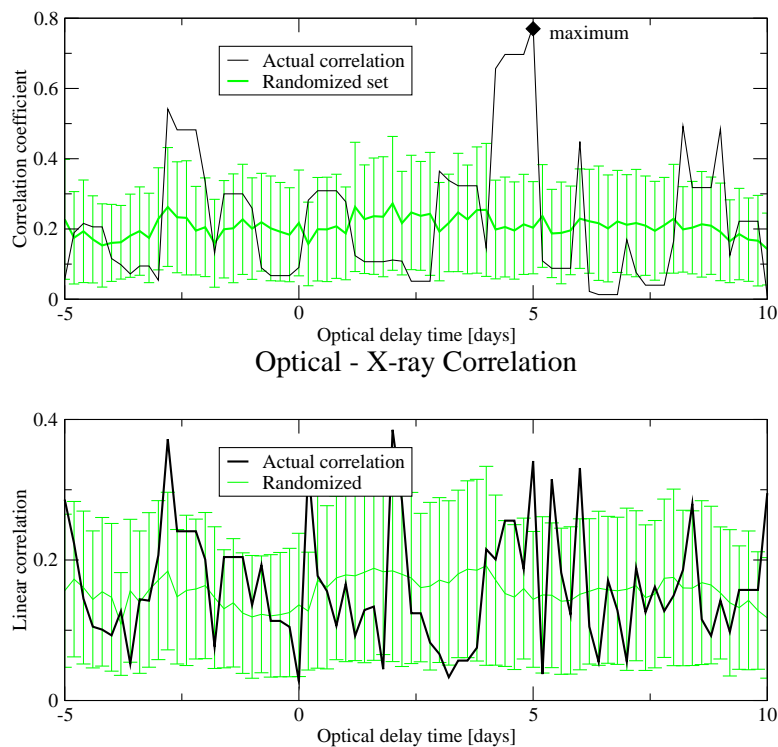
FIGURE E.2. *Left*: Optical - X-ray correlation before MJD 52438. *Right*: Correlation with all data.
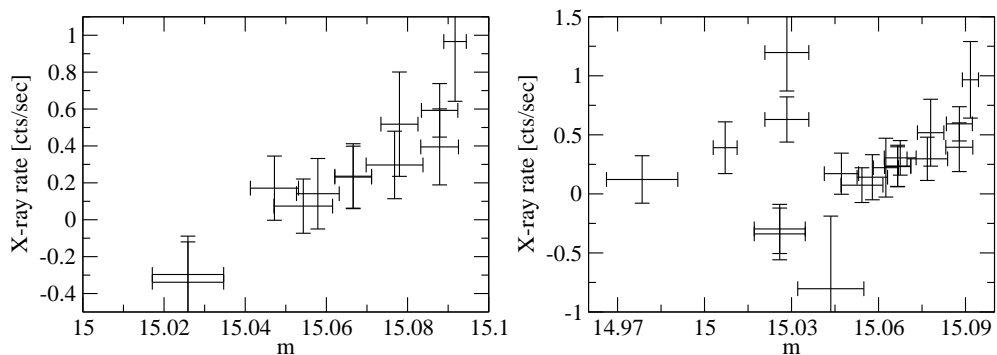
FIGURE E.3. *Left*: Optical vs. X-ray brightness with 5-day offset before MJD 52438, *Right*: Correlation with all data.

LOGARITHMIC AND LINEAR BINNING OF HISTOGRAMS

In the calculation of the flux, the conversion between logarithmically spaced bins to linearly spaced bins is needed; i.e. $\frac{\Delta N}{\Delta E} \rightarrow \frac{\Delta N}{\Delta log(E)}$. Let bins be equally spaced logarithmically with separation $\Delta \log(E)$ and centered at $\log Ec_a$, $\log Ec_b$, etc., see Fig. F.1. Then the linear bin width, ΔE is given by

$$\Delta E = b - a \;\; = \;\; 10^{\log Ec_a + \frac{\Delta \log(E)}{2}} - 10^{\log Ec_a - \frac{\Delta \log(E)}{2}} \tag{F.1}$$

$$= \;\; 2Ec_a \sinh(\ln 10 \, \frac{\Delta \log(E)}{2}) \tag{F.2}$$

$$= \;\; Ec \times k, \; k \equiv 2 \sinh(\ln 10 \, \frac{\Delta \log(E)}{2}). \tag{F.3}$$
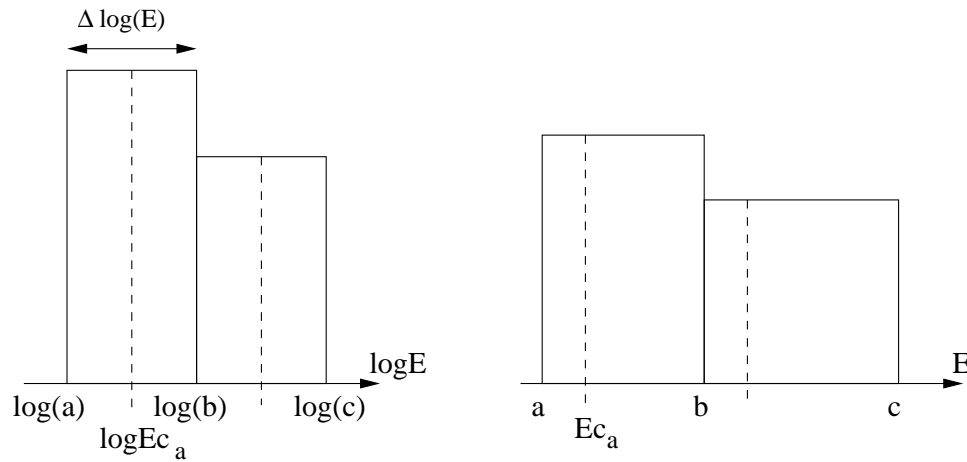
FIGURE F.1. Illustration of the conversion between logarithmically spaced and linearly spaced bins.

REFERENCES

Aharonian F, Akhperjanian A, Barrio J, et al. TeV gamma rays from the blazar H 1426+428 and the diffuse extragalactic background radiation. *Astronomy & Astrophysics*, 384:L23–L26, Mar. 2002a.

Aharonian F, Akhperjanian A, Beilicke M, et al. Variations of the TeV energy spectrum at different flux levels of Mkn 421 observed with the HEGRA system of Cherenkov telescopes. *Astronomy & Astrophysics*, 393:89–99, Oct. 2002b.

Aharonian F, Akhperjanian A, Beilicke M, et al. Observations of H1426+428 with HEGRA. Observations in 2002 and reanalysis of 1999&2000 data. *Astronomy & Astrophysics*, 403:523–528, May 2003a.

Aharonian F, Akhperjanian A, Beilicke M, et al. Detection of TeV gamma-rays from the BL Lac 1ES 1959+650 in its low states and during a major outburst in 2002. *Astronomy & Astrophysics*, 406:L9–L13, July 2003b.

Aharonian F, Akhperjanian A, Beilicke M, et al. An unidentified TeV source in the vicinity of Cygnus OB2. *Astronomy & Astrophysics*, 393:L37–L40, Oct. 2002c.

Aharonian FA, Akerlof CW. Gamma-Ray Astronomy with Imaging Atmospheric Cerenkov Telescopes. *Annual Review of Nuclear and Particle Science*, 47:273–314, 1997.

Aharonian FA, Akhperjanian AG, Barrio JA, et al. HEGRA search for TeV emission from BL Lacertae objects. *Astronomy & Astrophysics*, 353:847–852, Jan. 2000a.

Aharonian FA, Akhperjanian AG, Barrio JA, et al. The time averaged TeV energy spectrum of MKN 501 of the extraordinary 1997 outburst as measured with the stereoscopic Cherenkov telescope system of HEGRA. *Astronomy & Astrophysics*, 349:11–28, Sept. 1999.

Aharonian FA, Akhperjanian AG, Barrio JA, et al. The Energy Spectrum of TEV Gamma Rays from the Crab Nebula as Measured by the HEGRA System of Imaging Air Cerenkov Telescopes. *Astrophysical Journal*, 539:317–324, Aug. 2000b.

Aharonian FA, Konopelko AK, Völk HJ, et al. 5@5 - a 5 GeV energy threshold array of imaging atmospheric Cherenkov telescopes at 5 km altitude. *Astroparticle Physics*, 15:335–356, Aug. 2001.

Aharonian HESSCF. Very high energy gamma rays from the direction of Sagittarius A*. *ArXiv Astrophysics e-prints*, Aug. 2004. astro-ph/0408145.

Amenomori M, Ayabe S, Cao PY, et al. Observation of Multi-TEV Gamma Rays from the Crab Nebula using the Tibet Air Shower Array. *Astrophysical Journal Letters*, 525: L93–L96, Nov. 1999.

Armand C, Milliard B, Deharveng JM. Far-ultraviolet diffuse background and galaxy counts. *Astronomy & Astrophysics*, 284:12–16, Apr. 1994.

Atkins R, Benbow W, Berley D, et al. TeV Gamma-Ray Survey of the Northern Hemisphere Sky Using the Milagro Observatory. *Astrophysical Journal*, 608:680–685, June 2004.

Avni Y. Energy spectra of X-ray clusters of galaxies. *Astrophysical Journal*, 210:642–646, Dec. 1976.

Badran HM. Recent Observations of 1ES2344+514 Using the Whipple Gamma-Ray Telescope. In *AIP Conf. Proc. 587: Gamma 2001: Gamma-Ray Astrophysics*, pages 281–+, 2001.

Barth AJ, Ho LC, Sargent WLW. The Black Hole Masses and Host Galaxies of BL Lacertae Objects. *Astrophysical Journal*, 583:134–144, Jan. 2003.

Becker RH, White RL, Edwards AL. A new catalog of 53,522 4.85 GHz sources. *Astrophysical Journal Suppl. Ser.*, 75:1–229, Jan. 1991.

Beilicke M et al. Detection of the PSR B1259-63 binary pulsar at TeV energies with the H.E.S.S. telescopes. In *Presentation at 3rd Conf. on Frontier Science: Physics and Astrophysics in Space, Villa Mondragone*, 2004a.

Beilicke M et al. Investigation of the PSRB1259-63 field of view H.E.S.S. In *Heidelberg Gamma-Ray Meeting, AIP Conference Proceedings*, 2004b.

Beilicke M, Götting N, Tluczykont M. Observation of the giant radio galaxy M87 with the HEGRA Cherenkov telescopes. *New Astronomy Review*, 48:407–410, Apr. 2004c.

Bennett CL, Halpern M, Hinshaw G, et al. First-Year Wilkinson Microwave Anisotropy Probe (WMAP) Observations: Preliminary Maps and Basic Results. *Astrophysical Journal Suppl. Ser.*, 148:1–27, Sept. 2003.

Berge D et al. Observations of the SNR RX J1713.7-3946 with H.E.S.S. In *AIP Proc. Gamma 2004, Heidelberg*, 2004.

Bernlöhr K, 1999. http://www.mpi-hd.mpg.de/hfm/CosmicRay/ShowerDetection.html.

Bernlohr K. Impact of atmospheric parameters on the atmospheric Cherenkov technique*. *Astroparticle Physics*, 12:255–268, Jan. 2000.

Bernstein RA, Freedman WL, Madore BF. The First Detections of the Extragalactic Background Light at 3000, 5500, and 8000 Å. I. Results. *Astrophysical Journal*, 571:56–84, May 2002.

Bevington PR. *Data reduction and error analysis for the physical sciences*. McGraw-Hill, 2nd edition, 1992.

Biller SD. Implications of modified AGN spectra due to absorption by infrared photons. *Astroparticle Physics*, 3:385–403, Aug. 1995.

Biller SD, Buckley J, Burdett A, et al. New Limits to the Infrared Background: Bounds on Radiative Neutrino Decay and on Contributions of Very Massive Objects to the Dark Matter Problem. *Physical Review Letters*, 80:2992–2995, Apr. 1998.

Blackett PMS. A possible contribution to the night sky from the Cerenkov radiation emitted by cosmic rays. In *The Emission Spectra of the Night Sky and Aurorae, International Conference of the Physical Society, London*, pages 34–+, 1948.

Blain AW, Phillips TG. The 60-μm extragalactic background radiation intensity, dust-enshrouded active galactic nuclei and the assembly of groups and clusters of galaxies. *Royal Astronomical Society, Monthly Notices*, 333:222–230, June 2002.

Blumenthal GR, Gould RJ. Bremsstrahlung, Synchrotron Radiation, and Compton Scattering of High-Energy Electrons Traversing Dilute Gases. *Reviews of Modern Physics*, 42: 237–271, 1970.

Boettcher M, Dermer CD. Reverberation mapping of the central regions of active galactic nuclei using high-energy γ-ray observations. *Astronomy & Astrophysics*, 302:37–+, Oct. 1995.

Bond IH, Hillas AM, Bradbury SM. An island method of image cleaning for near threshold events from atmospheric Čerenkov telescopes. *Astroparticle Physics*, 20:311–321, Dec. 2003.

Bradbury SM, Burdett AM, D'Vali M, et al. Whipple Telescope observations of the Crab Nebula with a Pattern Selection Trigger. In *Proc. 26th International Cosmic Ray Conference*, volume 5, pages 263–, 1999.

Breit G, Wheeler JA. Collision of Two Light Quanta. *Physical Review*, 46:1087, 1934.

Buckley JH, Akerlof CW, Biller S, et al. Gamma-Ray Variability of the BL Lacertae Object Markarian 421. *Astrophysical Journal Letters*, 472:L9+, Nov. 1996.

Bussons-Gordo J. *Derivation of the TeV Gamma-Ray Spectrum of Three Active Galaxies: Mrk 421, Mrk 501, and 1ES 2344+514*. PhD thesis, University College Dublin, July 1998a.

Bussons-Gordo J. The TeV Energy Spectrum of the Active Galaxies 1ES 2344+514 and Markarian 501. In *Proceedings 16th ECRS, July 20-24*, pages 379+, 1998b.

Cambrésy L, Reach WT, Beichman CA, et al. The Cosmic Infrared Background at 1.25 and 2.2 Microns Using DIRBE and 2MASS: A Contribution Not Due to Galaxies? *Astrophysical Journal*, 555:563–571, July 2001.

Catanese M, Akerlof CW, Badran HM, et al. Discovery of Gamma-Ray Emission above 350 GeV from the BL Lacertae Object 1ES 2344+514. *Astrophysical Journal*, 501:616, July 1998.

Catanese M, Boyle PJ, Burdett AM, et al. First Results from a Search for TeV Emission from BL Lacs Out to Z = 0.2. *Proceedings of the 25th International Cosmic Ray Conference (Durban, South Africa), vol. 3, eds. M. S. Potgieter, C. Raubenheimer, and D. J. van der Walt, p. 277. Transvaal, South Africa: Potchefstroom University, 1997.*, 3:277–+, 1997.

Catanese M, Weekes TC. Very High Energy Gamma-Ray Astronomy. *Publications of the Astronomical Society of the Pacific*, 111:1193–1222, Oct. 1999.

Cawley MF. . In *Towards a major Cerenkov Detector*, pages 176+. Universal Academy Press, 1993.

Chadwick PM, Dickinson MR, Dipper NA, et al. TeV gamma rays from PSR 1706-44. *Astroparticle Physics*, 9:131–136, Aug. 1998.

Chadwick PM, Lyons K, McComb TJL, et al. Very High Energy Gamma Rays from PKS 2155-304. *Astrophysical Journal*, 513:161–167, Mar. 1999.

Cheng KS, Ho C, Ruderman M. Energetic radiation from rapidly spinning pulsars. I - Outer magnetosphere gaps. II - VELA and Crab. *Astrophysical Journal*, 300:500–539, Jan. 1986.

Condon JJ, Broderick JJ. A 1400 MHz sky survey. I - Confusion-limited maps covering 7h 30 M less than alpha less than 19h 30m, -5 deg less than delta less than 82 deg. *Astronomical Journal*, 90:2540–2549, Dec. 1985.

Costamante L, Ghisellini G. TeV candidate BL Lac objects. *Astronomy & Astrophysics*, 384:56–71, Mar. 2002.

Costamante L, Ghisellini G, Giommi P, et al. Extreme synchrotron BL Lac objects. Stretching the blazar sequence. *Astronomy & Astrophysics*, 371:512–526, May 2001.

Daniels MK et al. Spectrum of Very High Energy Gamma-Rays from the blazar 1ES 1959+650 during flaring activity in 2002. *to be submitted in Astronomy & Astrophysics*, 2004.

de Naurois M, Holder J, Bazer-Bachi R, et al. Measurement of the Crab Flux above 60 GeV with the CELESTE Cerenkov Telescope. *Astrophysical Journal*, 566:343–357, Feb. 2002.

Dermer CD, Schlickeiser R, Mastichiadis A. High-energy gamma radiation from extragalactic radio sources. *Astronomy & Astrophysics*, 256:L27–L30, Mar. 1992.

Dermer CD, Sturner SJ, Schlickeiser R. Nonthermal Compton and Synchrotron Processes in the Jets of Active Galactic Nuclei. *Astrophysical Journal Suppl. Ser.*, 109:103–+, Mar. 1997.

Douglas JN, Bash FN, Bozyan FA, et al. The Texas Survey of Radio Sources Covering -35.5 degrees < declination < 71.5 degrees at 365 MHz. *Astronomical Journal*, 111: 1945–+, May 1996.

Dwek E, Arendt RG, Hauser MG, et al. The COBE Diffuse Infrared Background Experiment Search for the Cosmic Infrared Background. IV. Cosmological Implications. *Astrophysical Journal*, 508:106–122, Nov. 1998.

Dwek E, Krennrich F. Simultaneous constraints on the spectrum of the extragalactic background light and the intrinsic TeV spectra of Mrk 421, Mrk 501, and H1426+428. *Astrophysical Journal submitted*, June 2004. astro-ph/0406565.

Dwek E, Slavin J. On the determination of the cosmic infrared background radiation from the high-energy spectrum of extragalactic gamma-ray sources. *Astrophysical Journal*, 436:696–704, Dec. 1994.

Elbaz D, Cesarsky CJ, Chanial P, et al. The bulk of the cosmic infrared background resolved by ISOCAM. *Astronomy & Astrophysics*, 384:848–865, Mar. 2002.

Elvis M, Plummer D, Schachter J, et al. The Einstein Slew Survey. *Astrophysical Journal Suppl. Ser.*, 80:257–303, May 1992.

Engstrom RW. *Photomultiplier handbook* . RCA corportion, 1980.

Falomo R, Kotilainen JK. Optical imaging of the host galaxies of X-ray selected BL Lacertae objects. *Astronomy & Astrophysics*, 352:85–102, Dec. 1999.

Fegan SJ. *A very high energy survey of unidentified EGRET sources*. PhD thesis, University of Arizona, 2004.

Finkbeiner DP, Davis M, Schlegel DJ. Detection of a Far-Infrared Excess with DIRBE at 60 and 100 Microns. *Astrophysical Journal*, 544:81–97, Nov. 2000.

Fixsen DJ, Dwek E, Mather JC, et al. The Spectrum of the Extragalactic Far-Infrared Background from the COBE FIRAS Observations. *Astrophysical Journal*, 508:123–128, Nov. 1998.

Fixsen DJ, Mather JC. The Spectral Results of the Far-Infrared Absolute Spectrophotometer Instrument on COBE. *Astrophysical Journal*, 581:817–822, Dec. 2002.

Fossati G, Maraschi L, Celotti A, et al. A unifying view of the spectral energy distributions of blazars. *Royal Astronomical Society, Monthly Notices*, 299:433–448, Sept. 1998.

Franceschini A, Toffolatti L, Mazzei P, et al. Galaxy counts and contributions to the background radiation from 1 micron to 1000 microns. *Astronomy & Astrophysics Suppl. Ser.* , 89:285–310, Aug. 1991.

Funk B, Magnussen N, Meyer H, et al. An upper limit on the infrared background density from HEGRA data on MKN 501. *Astroparticle Physics*, 9:97–103, June 1998.

Gaidos JA, Akerlof CW, Biller SD, et al. Very Rapid and Energetic Bursts of TeV Photons from the Active Galaxy Markarian 421. *Nature*, 383:319–+, 1996.

Galbraith W, Jelley JV. . *Nature*, 171:349, 1953a.

Galbraith W, Jelley JV. Light pulses from the Night Sky and Cerenkov radiation. *Journal of Atmospheric and Terrestrial Physics*, 171:349, 1953b.

Ghisellini G, Celotti A, Fossati G, et al. A theoretical unifying scheme for gamma-ray bright blazars. *Royal Astronomical Society, Monthly Notices*, 301:451–468, Dec. 1998.

Giebels B, Bloom ED, Focke W, et al. Observation of X-Ray Variability in the BL Lacertae Object 1ES 1959+65. *Astrophysical Journal*, 571:763–770, June 2002.

Giommi P, Padovani P, Perlman E. Detection of exceptional X-ray spectral variability in the TeV BL Lac 1ES 2344+514. *Royal Astronomical Society, Monthly Notices*, 317: 743–749, Oct. 2000.

Gould RJ, Schréder G. Opacity of the universe to high-energy photons. *Physical Review Letters*, 16:252–4, Feb. 1966.

Gould RJ, Schréder G. Pair production in photon-photon collisions. *Physical Review*, 155: 1404–7, Mar. 1967.

Gregory PC, Condon JJ. The 87GB catalog of radio sources covering delta between O and + 75 deg at 4.85 GHz. *Astrophysical Journal Suppl. Ser.*, 75:1011–1291, Apr. 1991.

Greisen K. End to the Cosmic-Ray Spectrum? *Physical Review Letters*, 16:748–750, Apr. 1966.

GrISU. Monte-Carlo simulation package for IACTs available at http://cherenkov.physics.iastate.edu/simulations.html, 2004.

Halzen F, Zas E, MacGibbon JH, et al. Gamma rays and energetic particles from primordial black holes. *Nature*, 353:807–815, Oct. 1991.

Manual on Construction and Operating Characteristics. Hamamatsu Corporation, 2002.

Han J, Wielebinski R. Milestones in the Observations of Cosmic Magnetic Fields. *Chinese Journal of Astronony and Astrophysics*, 2:293–324, Aug. 2002.

Harding AK. Pulsar gamma-rays - Spectra, luminosities, and efficiencies. *Astrophysical Journal*, 245:267–273, Apr. 1981.

Hartman RC, Bertsch DL, Bloom SD, et al. The Third EGRET Catalog of High-Energy Gamma-Ray Sources. *Astrophysical Journal Suppl. Ser.*, 123:79–202, July 1999.

Haungs A, Razdan AK, Bhat CL, et al. First results on characterization of Cherenkov images through combined use of Hillas, fractal and wavelet parameters. *Astroparticle Physics*, 12:145–156, Nov. 1999.

Hauser MG, Arendt RG, Kelsall T, et al. The COBE Diffuse Infrared Background Experiment Search for the Cosmic Infrared Background. I. Limits and Detections. *Astrophysical Journal*, 508:25–43, Nov. 1998.

Hauser MG, Dwek E. The Cosmic Infrared Background: Measurements and Implications. *Annual Review of Astronomy and Astrophysics*, 39:249–307, 2001.

Heck D, Knapp J, Capdevielle G,J. N. Schatz, et al. "corsika: A monte carlo code to simulate extensive air showers ". Technical report, Forschungszentrum Karlsruhe Report FZKA 6019, 1998.

Helene O. Upper limit of peak area. *Nuclear Instruments and Methods in Physics Research A*, 212:319–322, Dec. 1983.

Hill DA, Porter NA. Photography of Cerenkov Light from Extensive Air Showers in the Atmosphere. *Nature*, 191:690, 1961.

Hillas AM. The sensitivity of Cerenkov radiation pulses to the longitudinal development of cosmic-ray showers. *Journal of Physics G Nuclear Physics*, 8:1475–1492, Oct. 1982.

Hillas AM. Cerenkov light images of EAS produced by primary gamma. *NASA. Goddard Space Flight Center 19th Intern. Cosmic Ray Conf., Vol. 3 p 445-448 (SEE N85-34862 23-93)*, 3:445–448, Aug. 1985a.

Hillas AM. Cerenkov light images of EAS produced by primary gamma. *19th International Cosmic Ray Conference*, 1:155, 1985b.

Hinton JA. The status of the HESS project. *New Astronomy Review*, 48:331–337, Apr. 2004.

Holder J, Bond IH, Boyle PJ, et al. Detection of TeV Gamma Rays from the BL Lacertae Object 1ES 1959+650 with the Whipple 10 Meter Telescope. *Astrophysical Journal Letters*, 583:L9–L12, Jan. 2003a.

Holder J, Bond IH, Boyle PJ, et al. Observations of 1ES1959+650 with the Whipple 10m Telescope. In *The Universe Viewed in Gamma-Rays*, pages 181–186. Universal Academy Press, 2003b.

Horan D. *The Discovery of TeV Gamma-Rays from the BL Lacertae Object 1H1426+428*. PhD thesis, University College Dublin, 2001.

Horan D, Badran HM, Bond IH, et al. Detection of the BL Lacertae Object H1426+428 at TeV Gamma-Ray Energies. *Astrophysical Journal*, 571:753–762, June 2002.

Horan D, Weekes TC. Extragalactic sources of TeV gamma rays: a summary. *New Astronomy Review*, 48:527–535, Apr. 2004.

Horns D. TeV γ-radiation from Dark Matter annihilation in the Galactic center. *ArXiv Astrophysics e-prints, submitted to Phys. Letters B*, Aug. 2004. astro-ph/0408192.

Horns D, Aharonian FA. The Crab nebula: Linking MeV synchrotron and 50 TeV inverse Compton photons. *ArXiv Astrophysics e-prints*, July 2004. astro-ph/0407119.

Horns D et al. Multi-wavelength Observations of the TeV blazars Mkn 421, 1ES1959+650, and H1426+428 with the HEGRA Cherenkov telescopes and the RXTE X-ray satellite. In *High Energy Blazar astronomy*, 2002. URL `astro-ph/0209454`.

Hurley K. Detection of a Gamma-Ray Burst of Very Long Duration and Very High Energy. *Nature*, 372:652–+, Dec. 1994.

Ioka K, Kobayashi S, Mészáros P. Extended GeV-TeV Emission around Gamma-Ray Burst Remnants and the Case of W49B. *Astrophysical Journal Letters*, 613:L17–L20, Sept. 2004.

Jarrett TH, Chester T, Cutri R, et al. The 2MASS Large Galaxy Atlas. *Astronomical Journal*, 125:525–554, Feb. 2003.

Jelley JV. High energy gamma-ray absorption in space by a 3.5 K microwave field. *Physical Review Letters*, 16:479–81, Mar. 1966.

Jelley JV. Cerenkov Radiation from Extensive Air Showers. In *Progress in Elementary and Cosmic Ray Physics*, pages 41–155, 1967.

Jelley JV, Galbraith W. Light pulses from the Night Sky. *Philosophical Magazine*, 44:619, 1953.

Jelly JV. *Cherenkov Radiation*. New York: Pergamon, 1958.

Jiang Y et al. Absolute calibration of an atmospheric Cherenkov telescope using muon ring images. In *Proceedings of 23rd ICRC, Calgary, Canada*, volume 4, pages 662+, 1993.

Kashlinsky A, Mather JC, Odenwald S. Clustering of the Diffuse Infrared Light from the COBE DIRBE Maps: an All-Sky Survey of C(0). *Astrophysical Journal Letters*, 473: L9+, Dec. 1996.

Kashlinsky A, Odenwald S. Clustering of the Diffuse Infrared Light from the COBE DIRBE Maps. III. Power Spectrum Analysis and Excess Isotropic Component of Fluctuations. *Astrophysical Journal*, 528:74–95, Jan. 2000.

Kertzman MP, Sembroski GH. Computer simulation methods for investigating the detection characteristics of TeV air Cherenkov telescopes. *Nuclear Instrumentation and Methods in Physics Research A*, 343:629–643, 1994.

Kifune T, Tanimori T, Ogio S, et al. Very high energy gamma rays from PSR 1706-44. *Astrophysical Journal Letters*, 438:L91–L94, Jan. 1995.

Kirk JG, Ball L, Skjaeraasen O. Inverse Compton emission of TeV gamma rays from PSR B1259-63. *Astroparticle Physics*, 10:31–45, Jan. 1999.

Kneiske TM, Bretz T, Mannheim K, et al. Implications of cosmological gamma-ray absorption. II. Modification of gamma-ray spectra. *Astronomy & Astrophysics*, 413:807–815, Jan. 2004.

Kneiske TM, Mannheim K, Hartmann DH. Implications of cosmological gamma-ray absorption. I. Evolution of the metagalactic radiation field. *Astronomy & Astrophysics*, 386:1–11, Apr. 2002.

Konopelko A, Kettler J, HEGRA. TeV Gamma-Ray Observations of the BL Lac Object 1ES 2344+514 with the HEGRA System of Imaging Atmospheric Cherenkov Telescopes. In *International Cosmic Ray Conference*, volume 3, pages 426–429, 1999.

Kosack K, Badran HM, Bond IH, et al. TeV Gamma-Ray Observations of the Galactic Center. *Astrophysical Journal Letters*, 608:L97–L100, June 2004.

Krawczynski H, Coppi PS, Aharonian F. Time-dependent modelling of the Markarian 501 X-ray and TeV gamma-ray data taken during 1997 March and April. *Royal Astronomical Society, Monthly Notices*, 336:721–735, Nov. 2002.

Krawczynski H, Hughes S, Horan D, et al. X-Ray and TeV Gamma-Ray Observations of Very Strong Flares from the TeV Blazars 1ES 1959+650 and Markarian 421. *AAS/High Energy Astrophysics Division*, 35:0–+, Mar. 2003.

Krawczynski H, Hughes SB, Horan D, et al. Multiwavelength Observations of Strong Flares from the TeV Blazar 1ES 1959+650. *Astrophysical Journal*, 601:151–164, Jan. 2004.

Krennrich F, Badran HM, Bond IH, et al. Cutoff in the TeV Energy Spectrum of Markarian 421 during Strong Flares in 2001. *Astrophysical Journal Letters*, 560:L45–L48, Oct. 2001.

Krennrich F, Biller SD, Bond IH, et al. Measurement of the Multi-TEV Gamma-Ray Flare Spectra of Markarian 421 and Markarian 501. *Astrophysical Journal*, 511:149–156, Jan. 1999.

Krennrich F, Bond IH, Bradbury SM, et al. Discovery of Spectral Variability of Markarian 421 at TeV Energies. *Astrophysical Journal Letters*, 575:L9–L13, Aug. 2002.

Krennrich F, Dwek E. Intrinsic Spectra of the TeV Blazars Mrk 421 and Mrk 501. In *28th International Cosmic Ray Conference*, 2003. astro-ph/0305418.

Kwok PW. *Very High Energy Gamma Rays from the Crab Nebula and Pulsar*. PhD thesis, University of Arizona, Aug. 1989.

Lagache G, Abergel A, Boulanger F, et al. First detection of the warm ionised medium dust emission. Implication for the cosmic far-infrared background. *Astronomy & Astrophysics*, 344:322–332, Apr. 1999.

Lampton M, Margon B, Bowyer S. Parameter estimation in X-ray astronomy. *Astrophysical Journal*, 208:177–190, Aug. 1976.

Landau LD, Lifshitz EM. *Quantum Electrodynamics*, volume 4. Pergamon Press, 2nd edition, 1989.

Lang MJ, Carter-Lewis DA, Fegan DJ, et al. Evidence for TeV gamma ray emission from TeV J2032+4130 in Whipple archival data. *Astronomy & Astrophysics*, 423:415–419, Aug. 2004.

Le Bohec S, 2002. priv. comm.

Le Bohec S, Badran HM, Bond IH, et al. Observation of M87 at 400 GeV with the Whipple 10 Meter Telescope. *Astrophysical Journal*, 610:156–160, July 2004.

Le Bohec S et al. A new analysis method for very high definition Imaging Atmospheric Cherenkov Telescopes as applied to the CAT telescope. *Nuclear Instruments and Methods in Physics Research A*, 416:425–437, 1998.

Lebohec S, Holder J. The cosmic ray background as a tool for relative calibration of atmospheric Cherenkov telescopes. *Astroparticle Physics*, 19:221–233, May 2003.

Leinert C, Bowyer S, Haikala LK, et al. The 1997 reference of diffuse night sky brightness. *Astronomy & Astrophysics Suppl. Ser.* , 127:1–99, Jan. 1998.

Lemiere A et al. AGN observations with H.E.S.S. In *Heidelberg Gamma-Ray Meeting, AIP Conference Proceedings*, 2004.

Leo WR. *Techniques for Nuclear and Particle Physics Experiments.* Springer Verlag, New York, 2nd edition, 1994.

Lessard RW, Bond IH, Bradbury SM, et al. Search for Pulsed TEV Gamma-Ray Emission from the Crab Pulsar. *Astrophysical Journal*, 531:942–948, Mar. 2000.

Lessard RW, Cayón L, Sembroski GH, et al. Wavelet imaging cleaning method for atmospheric Cherenkov telescopes. *Astroparticle Physics*, 17:427–440, July 2002.

Lewis DA. Optical characteristics of the Whipple Observatory TeV gamma-ray imaging telescope. *Experimental Astronomy*, 1:213–226, 1990.

Li TP, Ma YQ. Analysis methods for results in gamma-ray astronomy. *Astrophysical Journal*, 272:317–324, Sept. 1983.

Lieber M, Milford SN, Spergel MS. Very high energy cosmic gamma rays. *Annales d'Astrophysique*, 28:206–+, Feb. 1965.

Mücke A, Protheroe RJ. A proton synchrotron blazar model for flaring in Markarian 501. *Astroparticle Physics*, 15:121–136, Mar. 2001.

Macomb DJ, Akerlof CW, Aller HD, et al. Multiwavelength Observations of Markarian 421 During a TeV/X-Ray Flare. *Astrophysical Journal Letters*, 449:L99+, Aug. 1995.

Mannheim K. The proton blazar. *Astronomy & Astrophysics*, 269:67–76, Mar. 1993.

Maraschi L, Fossati G, Tavecchio F, et al. Simultaneous X-Ray and TEV Observations of a Rapid Flare from Markarian 421. *Astrophysical Journal Letters*, 526:L81–L84, Dec. 1999.

Maraschi L, Ghisellini G, Celotti A. A jet model for the gamma-ray emitting blazar 3C 279. *Astrophysical Journal Letters*, 397:L5–L9, Sept. 1992.

Masterson C, 2004. priv. comm.

Matsumoto T. Observations of Infrared Extragalactic Background Light. *The Institute of Space and Astronautical Science Report SP No. 14, p. 179-186.*, 14:179–186, Dec. 2000.

Matthews J, Ciampa D, Green KD, et al. Search for diffuse cosmic gamma rays above 200 TeV. *Astrophysical Journal*, 375:202–208, July 1991.

Melia F, Falcke H. The Supermassive Black Hole at the Galactic Center. *Annual Review of Astronomy and Astrophysics*, 39:309–352, 2001.

Miville-Deschênes MA, Lagache G, Puget JL. Power spectrum of the cosmic infrared background at 60 and 100 μm with IRAS. *Astronomy & Astrophysics*, 393:749–756, Oct. 2002.

Mohanty G. *The properties of Very High Energy gamma ray sources observed using the air Cherenkov technique*. PhD thesis, Iowa State University, 1995.

Mohanty G, Biller S, Carter-Lewis DA, et al. Measurement of TeV gamma-ray spectra with the Cherenkov imaging technique. *Astroparticle Physics*, 9:15–43, June 1998.

Muraishi H, Tanimori T, Yanagita S, et al. Search for TeV Gamma Rays from the SNR RXJ1713.7-3946. In *Proc. 26th International Cosmic Ray Conference*, volume 3, pages 500–503, 1999.

Muraishi H, Tanimori T, Yanagita S, et al. Evidence for TeV gamma-ray emission from the shell type SNR RX J1713.7-3946. *Astronomy & Astrophysics*, 354:L57–L61, Feb. 2000.

Neshpor YI, Kalekin OR, Stepanian AA, et al. A new VHE gamma-ray source in the Cygnus constellation. In *Proc. 25th International Cosmic Ray Conference, Rome*, volume 2, page 385, 1995.

Nikishov AI. Absorption of High-Energy Photons in the Universe. *Soviet Physics Jetp*, 14: 393–394, Feb. 1962.

Nilsson K, Pursimo T, Takalo LO, et al. Two-dimensional Photometric Decomposition of the TeV BL Lacertae Objects Markarian 421, Markarian 501, and 1ES 2344+514. *Publications of the Astronomical Society of the Pacific*, 111:1223–1232, Oct. 1999.

Nishiyama T et al. 1ES1959+650. In *26th International Cosmic Ray Conference*, volume 3, pages 370+, 1999.

Ong RA. Very high-energy gamma-ray astronomy. *Physics Reports*, 305:93–202, 1998.

Ozlem C, Ong R. Night sky background and single p.e. rates for veritas. Internal memo, version 1.0, 2002.

Padovani P, Giommi P. The connection between x-ray- and radio-selected BL Lacertae objects. *Astrophysical Journal*, 444:567–581, May 1995.

Patnaik AR, Browne IWA, Wilkinson PN, et al. Interferometer phase calibration sources. I - The region 35-75 deg. *Royal Astronomical Society, Monthly Notices*, 254:655–676, Feb. 1992.

Perlman ES, Stocke JT, Schachter JF, et al. The Einstein Slew Survey Sample of BL Lacertae Objects. *Astrophysical Journal Suppl. Ser.*, 104:251–+, June 1996.

Petry D, Bond IH, Bradbury SM, et al. The TeV Spectrum of H1426+428. *Astrophysical Journal*, 580:104–109, Nov. 2002.

Pomarède D, Badran HM, Behr L, et al. A new optical filter for the ARTEMIS experiment. *Nuclear Instruments and Methods in Physics Research A*, 446:469–489, May 2000.

Pozzetti L, Madau P, Zamorani G, et al. High-redshift galaxies in the Hubble Deep Field - II. Colours and number counts. *Royal Astronomical Society, Monthly Notices*, 298: 1133–1144, Aug. 1998.

Primack JR, Somerville RS, Bullock JS, et al. Probing Galaxy Formation with High-Energy Gamma-Rays. In *High Energy Gamma Ray Astronomy*, volume 558, pages 463–478, 2001. Proceedings of the International Symposium Gamma-2000.

Protheroe RJ, Biermann PL. A new estimate of the extragalactic radio background and implications for ultra-high-energy γ-ray propagation. *Astroparticle Physics*, 6:45–54, 1996.

Punch M, Akerlof CW, Cawley MF, et al. Detection of TeV photons from the active galaxy Markarian 421. *Nature*, 358:477–+, Aug. 1992.

Punch M et al. . In *Proc. 22nd International Cosmic Ray Conference*, pages 464–467, 1991.

Quinn J, Akerlof CW, Biller S, et al. Detection of Gamma Rays with E greater than 300 GeV from Markarian 501. *Astrophysical Journal Letters*, 456:L83+, Jan. 1996.

Raue M, 2004. priv. comm.

Renault C, Barrau A, Lagache G, et al. New constraints on the cosmic mid-infrared background using TeV gamma-ray astronomy. *Astronomy & Astrophysics*, 371:771–778, May 2001.

Rengelink RB, Tang Y, de Bruyn AG, et al. The Westerbork Northern Sky Survey (WENSS), I. A 570 square degree Mini-Survey around the North Ecliptic Pole. *Astronomy & Astrophysics Suppl. Ser.* , 124:259–280, Aug. 1997.

Ressell MT, Turner MS. The Grand Unified Photon Spectrum: A Coherent View of the Diffuse Extragalactic Background Radiation. *Comments on Astrophysics*, 14:323–+, 1990.

Reynolds PT, Akerlof CW, Cawley MF, et al. Survey of candidate gamma-ray sources at TeV energies using a high-resolution Cerenkov imaging system - 1988-1991. *Astrophysical Journal*, 404:206–218, Feb. 1993.

Reynolds PT, Fegan DJ. Neural network classification of TeV gamma-ray images. *Astroparticle Physics*, 3:137–150, Mar. 1995.

Salamon MH, Stecker FW. Absorption of High-Energy Gamma Rays by Interactions with Extragalactic Starlight Photons at High Redshifts and the High-Energy Gamma-Ray Background. *Astrophysical Journal*, 493:547–+, Jan. 1998.

Samuelson FW, Biller SD, Bond IH, et al. The TeV Spectrum of Markarian 501. *Astrophysical Journal Letters*, 501:L17+, July 1998.

Schachter JF, Stocke JT, Perlman E, et al. Ten new BL Lacertae objects discovered by an efficient X-ray/radio/optical technique. *Astrophysical Journal*, 412:541–549, Aug. 1993.

Schroedter M, Falco E, Kurtanidze OM, et al. Multi-Wavelength Observations of 1ES1959+650 in a Flaring State. In *The Universe Viewed in Gamma-Rays*, pages 247–253. Universal Academy Press, 2003. URL `http://xxx.lanl.gov/abs/astro-ph/0301033`.

Scott DW. On Optimal and Data-based Histograms . *Biometrika*, 66:605–10, 1979.

Semenov V, Dyadechkin S, Punsly B. Simulations of Jets Driven by Black Hole Rotation. *Science*, 305:978–980, Aug. 2004.

Sinnis G, Smith A, McEnery JE. HAWC: A Next Generation All-Sky VHE Gamma-Ray Telescope. *ArXiv Astrophysics e-prints*, Mar. 2004. astro-ph/0403096.

Sreekumar P, Bertsch DL, Dingus BL, et al. EGRET Observations of the Extragalactic Gamma-Ray Emission. *Astrophysical Journal*, 494:523–+, Feb. 1998.

Stanev T, Franceschini A. Constraints on the Extragalactic Infrared Background from Gamma-Ray Observations of MRK 501. *Astrophysical Journal Letters*, 494:L159+, Feb. 1998.

Stecker FW. *Cosmic Gamma Rays*. Baltimore: Mono Book Corp., 1971.

Stecker FW, de Jager OC. New Upper Limits on Intergalactic Infrared Radiation from High-Energy Astrophysics. *Astrophysical Journal Letters*, 415:L71+, Oct. 1993.

Stecker FW, de Jager OC. Absorption of very high energy gamma-rays by intergalactic infared radiation: A new determination. *Astronomy & Astrophysics*, 334:L85–L87, June 1998.

Stecker FW, de Jager OC, Salamon MH. TeV gamma rays from 3C 279 - A possible probe of origin and intergalactic infrared radiation fields. *Astrophysical Journal Letters*, 390: L49–L52, May 1992.

Stevens JA, Gear WK. Variations in the broad-band spectra of BL Lac objects: millimetre observations of an X-ray-selected sample. *Royal Astronomical Society, Monthly Notices*, 307:403–412, Aug. 1999.

Stocke JT, Morris SL, Gioia I, et al. No evidence for radio-quiet BL Lacertae objects. *Astrophysical Journal*, 348:141–146, Jan. 1990.

Strong AW, Moskalenko IV, Reimer O. A new determination of the extragalactic diffuse gamma-ray background from EGRET data. *Astrophysical Journalaccepted, astro-ph/0405441*, 2004.

Tanimori T et al. Study of the TeV gamma-ray spectrum of SN 1006 around the NE Rim. In *27th International Cosmic Ray Conference*, 2001.

Tluczykont M, Götting N, Heinzelmann G, et al. Observations of 54 Active Galactic Nuclei with the HEGRA Cherenkov Telescopes. In *International Cosmic Ray Conference*, volume 5, pages 2547+, 2003.

Tsuchiya K, Enomoto R, Ksenofontov LT, et al. Detection of Sub-TeV Gamma Rays from the Galactic Center Direction by CANGAROO-II. *Astrophysical Journal Letters*, 606: L115–L118, May 2004.

Urry CM, Padovani P. Unified Schemes for Radio-Loud Active Galactic Nuclei. *Publications of the Astronomical Society of the Pacific*, 107:803–+, Sept. 1995.

Urry CM, Scarpa R, O'Dowd M, et al. The Hubble Space Telescope Survey of BL Lacertae Objects. II. Host Galaxies. *Astrophysical Journal*, 532:816–829, Apr. 2000.

Vacanti G, Cawley MF, Colombo E, et al. Gamma-ray observations of the Crab Nebula at TeV energies. *Astrophysical Journal*, 377:467–479, Aug. 1991.

Vacanti G, Fleury P, Jiang Y, et al. Muon ring images with an atmospheric Cerenkov telescope. *Astroparticle Physics*, 2:1–11, Feb. 1994.

Valle G. Gamma ray signatures from Galactic neutralino annihilation. *Astronomy & Astrophysics*, 424:765–772, Sept. 2004.

Vassiliev VV. Extragalactic background light absorption signal in the TeV gamma-ray spectra of blazars. *Astroparticle Physics*, 12:217–238, Jan. 2000.

Wang XY, Cheng KS, Dai ZG, et al. Constraining the Origin of TeV Photons from Gamma-Ray Bursts with Delayed MeV-GeV Emission Formed by Interaction with Cosmic Infrared/Microwave Background Photons. *Astrophysical Journal*, 604:306–311, Mar. 2004.

Waxman E. High-Energy Cosmic Rays from Gamma-Ray Burst Sources: A Stronger Case. *Astrophysical Journal*, 606:988–993, May 2004.

Webster. *Webster's encyclopedic unabridged dictionary of the English language*. Random House, New York, new revised edition, 1994.

Weekes T, Dowdall C, Moriarty P, et al. 1ES 1959+650. In *International Astronomical Union Circular*, pages 1–+, May 2002.

Weekes TC. Very high energy gamma-ray astronomy. *Physics Reports*, 160:1–2, Mar. 1988.

Weekes TC. TeV Gamma-ray Observations and the Origin of Cosmic Rays: I. *ArXiv Astrophysics e-prints*, Dec. 2003a. astro-ph/0312179.

Weekes TC. *Very high energy gamma-ray astronomy*. IoP Series in astronomy and astrophysics, ISBN 0750306580. Bristol, UK: The Institute of Physics Publishing, 2003b.

Weekes TC, Cawley MF, Fegan DJ, et al. Observation of TeV gamma rays from the Crab nebula using the atmospheric Cerenkov imaging technique. *Astrophysical Journal*, 342: 379–395, July 1989.

Weinberg S. *Gravitation and Cosmology*. John Wiley & Sons, 1st edition, 1972.

White RL, Becker RH. A new catalog of 30,239 1.4 GHz sources. *Astrophysical Journal Suppl. Ser.*, 79:331–467, Apr. 1992.

Woo J, Urry CM. Active Galactic Nucleus Black Hole Masses and Bolometric Luminosities. *Astrophysical Journal*, 579:530–544, Nov. 2002.

Wright EL. DIRBE minus 2MASS: Confirming the Cosmic Infrared Background at 2.2 Microns. *Astrophysical Journal*, 553:538–544, June 2001.

Wright EL, Reese ED. Detection of the Cosmic Infrared Background at 2.2 and 3.5 Microns Using DIRBE Observations. *Astrophysical Journal*, 545:43–55, Dec. 2000.

Xie GZ, Zhou SB, Dai BZ, et al. Photometric monitoring of 12 BL Lacertae objects. *Royal Astronomical Society, Monthly Notices*, 329:689–699, Feb. 2002.

Zatsepin G, Kuzmin V. *Sov. Phys. JETP Lett.*, 4:78, 1966.

Zweerink JA, Akerlof CW, Biller SD, et al. The TeV Gamma-Ray Spectrum of Markarian 421 during an Intense Flare. *Astrophysical Journal Letters*, 490:L141+, Dec. 1997.